Liquid-Solid Systems out of Equilibrium: Phase-Field Crystal Studies of Solidification, Melting, and Plasticity

Joel M. Berry

Department of Physics
McGill University, Montreal
October 2011

A thesis submitted to McGill University in partial fulfillment of the
requirements of the degree of Ph.D.

Abstract

Dynamic processes in nonequilibrium liquid-solid systems are studied over mesoscopic time scales and atomistic length scales using phase-field crystal (PFC) models. Various freezing and melting transitions are examined in two and three dimensions, and microscopic phenomena responsible for solid-phase plasticity are investigated. A primary focus is on the issue of describing atomistic dynamics over time scales that are generally inaccessible to conventional approaches.

Glass forming dynamics in supercooled liquids near a glass transition are studied numerically, and the central features of the transition, including a number of behaviors previously undemonstrated within PFC / classical density functional theory simulations, are successfully reproduced. A connection between the liquid dynamic correlation length and transition fragility is identified, and a physically motivated time scaling applied to the simulation data is shown to generate qualitative agreement with basic glass transition phenomenology across 12 orders of magnitude in time.

The competing processes of amorphous precursor nucleation and crystallization in diffusion-dominated spinodal and non-spinodal simple liquids are also examined. Melting and premelting transitions in defected body-centered cubic solids are studied numerically, and a localized melting theory based on defect elastic energies is formulated. Basic features of the dynamic phase separation patterns that develop in growing heteroepitaxially strained alloy films are also outlined based on numerical simulations of a binary PFC model. Finally, dislocation dynamics are examined in strained periodic systems. The central features of dislocation glide, climb, and annihilation are shown to naturally emerge within PFC models, and the dynamics of individual dislocations are found to reduce to a simple generalized equation of motion.

Résumé

Des procédés dynamiques dans des systèmes liquide-solide non-équilibrés sont étudiés au cours d'échelles de temps mésoscopiques et d'échelles de longueur atomistiques en utilisant des modèles “phase-field crystal” (PFC). Diverses transitions de congélation et de fusion sont examinées en deux et trois dimensions, et les phénomènes microscopiques responsables de la plasticité des phases solides sont étudiées. Un accent est mis sur la problématique des dynamiques atomistiques au cours d'échelles de temps qui sont généralement inaccessibles aux approches conventionnelles.

Les dynamiques de formation vitreuse dans les liquides metastables surfondus près d'une transition vitreuse sont étudiés numériquement, et les caractéristiques centrales de la transition, y compris un certain nombre de comportements qui n'ont pas été démontrées précédemment par les modèles PFC / simulations de la théorie classique densité fonctionnelle, sont reproduites avec succès. Un lien entre la longueur de corrélation dynamique liquide et la fragilité est identifié, et il est démontré par une normalisation de temps physiquement motivé, appliquée aux données de simulation, qu'il y a une correspondance qualitative avec des bases phénomènes de transition vitreuse sur 12 ordres de grandeurs de temps.

Les procédés concurrentiels de la nucléation de précurseurs amorphes et de la cristallisation dominées par la diffusion dans les liquides simples spinodaux et non-spinodaux sont aussi examinés. Les transitions de fusion et pré-fusion dans des solides cubiques centrés ayant des défauts sont étudiés numériquement, et une théorie de fusion localisée basée sur les énergies élastiques des défauts est formulée. Des caractéristiques de base des motifs de la séparation de phase dynamique qui se développent pendant la croissance des films tendus heteroepitaxiellement sont également etudiés en utilisant des simulations numériques d'un modèle binaire PFC. Enfin, les dynamiques des dislocations sont examinées dans les systèmes périodiques tendus, ainsi il est démontré que les caractéristiques fondamentales des procédés de glisse, d'escalade, et d'annihilation émergent naturellement des modèles PFC.

Acknowledgements

This dissertation was completed with direct and indirect contributions from a number of people and organizations. It will be a difficult task to adequately thank those who have helped me through this process, but I hope that the following lines serve as a beginning.

I would first like to express my deepest gratitude to my thesis advisor, Prof. Martin Grant. Martin has given me time, guidance, encouragement, support, and access to his expertise without lapse over the past years, despite so many other demands on his time as Chair of Physics and then as Dean of Science. His patience, humor, insight, humility, and willingness to let me work with freedom and without unnecessary judgement have been greatly appreciated.

I would also like to express my deepest gratitude to Prof. Ken Elder. Ken gave me the opportunity to pursue my interest in physics as a final year engineering student at a nearby university, and has acted as my unofficial thesis co-advisor while I have studied at McGill. He has contributed heavily to the direction, development, and solution of much of the work presented in this dissertation. He has also set an excellent professional and personal example to which I can only hope to aspire.

To the Grant group postdocs - Dan Vernon, Sami Majaniemi, and Makiko Nonomura: Thank you for the advice, encouragement, and many helpful discussions. I am continually in awe of your ability and knowledge. I would also like to thank the Grant group students that I have had the pleasure of knowing along the way - Cristiano, David, Smiso, Jens, and Dominique.

I have had the fortune as well of learning from and collaborating with Prof. Nik Provatas while at McMaster University, and more recently, of discussing research with Prof. Jörg Rottler at UBC. Of the many excellent and generous professors at McGill, I would like to thank the following for sharing their time with me in class lectures or one-on-one discussions: Prof. Paul Tupper, Prof. Maria Kilfoil, Prof. Jorge Viñals, Prof. Michael Hilke, Prof. Guy Moore, Prof. Dik Harris, and Prof. Zaven Altounian. Juan Gallego deserves a special acknowledgement for expertly solving the large number of supercomputing issues that I brought his way and for humoring my regular requests for more nodes. Thank you as well to the others in the Physics Department who have patiently helped me over the past years: Paula Domingues, Diane Koziol, Louise Decelles, Elizabeth Shearon, Sonia Vieira, Lauren Kay, and Paul Mercure.

To my family: Mom and dad - thank you for letting me grow in my own way and for being so unbelievably supportive. Katie, Rob, Kevin, and Leah - thank you for being such positive sisters and brothers to your strange middle sibling. Tiffany, thank you for making my time in the city of Montreal not just bearable, but genuinely happy. Your belief in me has helped more than you know. Thanks also to some physics-enabled friends: Till, Steve, Carolyn, Alex, Allison, and James.

In addition to the McGill University Physics Department, this research was supported by a Richard H. Tomlinson Fellowship, a Carl Reinhardt Fellowship, a Schulich Graduate Fellowship, and computing resources made available by CLUMEQ/Compute Canada.

Contents

List of Figures

List of symbols

α	Dynamic prefactor related to sound speed
β	Damping rate **or** relaxation function stretching exponent
γ	Mode coupling exponent for relaxation time
$\bar{\gamma}$	Average shear strain
$\dot{\gamma}$	Applied shear strain rate
γ_P	Peierls shear strain barrier for glide
Γ	Diffusive mobility function
$\delta\rho(\vec{r})$	Averaged atomic number density difference field
Δt	Discretized numerical time step
Δx	Discretized numerical grid spacing
ϵ	Applied strain (plasticity) **or** misfit strain (epitaxy)
ϵ_P	Peierls normal strain barrier for climb
η	Additive Gaussian stochastic noise **or** solute expansion coefficient
η_v	Viscosity
θ	Grain boundary tilt angle
θ_w	Critical grain boundary tilt angle for prewetting
λ	First Lamé coefficient
μ	Chemical potential **or** shear modulus **or** aging exponent
$\nu(\vec{r}, t)$	Multiplicative Gaussian stochastic noise variable
ξ_D	Dynamic liquid correlation length
ξ_S	Static liquid correlation length
$\rho(\vec{r})$	Averaged atomic number density field
$\bar{\rho}$	Average atomic number density

ρ_d	Dislocation density
ρ_ℓ	Reference state average atomic number density (DFT)
σ	Poisson's ratio **or** particle packing fraction
σ_{ij}	Linearized stress tensor
$\sigma(q)$	Linear perturbative surface instability growth rate
τ	Structural relaxation time at a given wavenumber
τ_α	Slow structural relaxation time
τ_β	Fast structural relaxation time
τ_ℓ	Structural relaxation time in a localized region
ϕ	Polar angle coordinate **or** crystallinty parameter
$\psi(\vec{r})$	Field theory order parameter
∇	Gradient operator
$\vec{\nabla}\cdot$	Divergence operator
a	Lattice constant **or** mode coupling critical decay exponent
a_{eq}	Equilibrium lattice constant
A	Amplitude of a periodic density configuration
A_0	Second order binary $N-c$ coupling constant
b	Burgers vector **or** mode coupling von Schweidler exponent
B	Bulk modulus
c	Species concentration field
C_n	n-point direct correlation function
d	Dislocation spacing in a grain boundary **or** system dimension
D	Mean square displacement
E	Dislocation elastic energy prefactor
f	Debye-Waller factor / nonergodicity parameter
f_i	Helmholtz free energy density
F	Helmholtz free energy
$F[x]$	Helmholtz free energy functional of field x
$\mathrm{F}(q,t)$	Intermediate scattering / density autocorrelation function
$g^P(R)$	Radial distribution function of most probable configuration
h_c	Strained film critical height dislocation nucleation
$h_{unstable}$	Strained film surface instability onset height

H	Coefficient for negative density penalty function (VPFC)
$\vec{J}$	Flux
k_v	Strained film average growth rate
k_B	Boltzmann's constant
K	Field theory surface energy constant
K_{ijkl}	Elastic constant tensor
$\ell(\theta)$	Effective elastic screening length of a grain boundary
L	Length
L_1	A hydrodynamic operator
L_i	System length in direction i
m	Stress exponent for dislocation glide
m_{eff}	Effective dislocation mass
M	Stochastic noise amplitude / temperature constant
M_γ	Dislocation glide mobility
M_ϵ	Dislocation climb mobility
$n(\vec{r})$	Scaled time- or ensemble- averaged atomic number density field
$\bar{n}$	Average scaled atomic number density
N	Number of particles **or** total number density field
q	Wavenumber
q_0	Wavenumber of the first peak correlation maximum
q_{eq}	Equilibrium wavenumber of a simple lattice structure
q_i	Periodicity constant (PFC)
r	Field theory constant proportional to $T - T_c$
$\bar{r}$	Polar radial coordinate
$\vec{r}$	Position vector
r_m	Value of r at the bulk melting point
r_s	Value of r at a liquid spinodal
r_{sol}	Value of r at the solidus
r_{wet}	Value of r at which a grain boundary wets
r_{AB}	Repulsive interspecies coupling constant
R	Cylindrical radial coordinate
$\bar{R}$	Dimensionless cylindrical radial coordinate

R_0	Zero temperature melt radius at a dislocation core
R_c	Critical solid phase droplet radius for nucleation
R_m	Melt radius at a dislocation core
R_{AB}	Binary lattice parameter variable
R_{CN}	Coordination sphere radius
S	Entropy
$S(q)$	Structure factor
$\mathrm{S}^P(q)$	Structure factor of most probable atomic configuration
t	Time
T	Temperature
$\dot{T}$	Rate of change in temperature
T_0	Vogel-Fulcher divergence temperature
T_c	Critical T (field theory) **or** crossover T (glass formation)
T_g	Laboratory glass transition temperature
T_m	Melting temperature
T_s	Spinodal temperature
u	Field theory bulk energy constant
$\vec{u}$	Displacement vector
u_{ij}	Linearized strain tensor
v	Velocity
$\dot{v}$	Acceleration
v_{ss}	Steady-state dislocation velocity
V	Volume
$V(\vec{r})$	External potential field
z	Coordination number

CHAPTER 1

Introduction

Along with gases, liquids and solids are the most common and familiar states of matter in nature. It is through the manipulation of materials in and between liquid, solid, and gaseous states that most aspects of geological, biological, and technological evolution are realized. Though many natural and man-made materials exist outside of thermodynamic equilibrium and involve structures too complex to be described as uniform, unistate systems, our understanding of the fundamental properties and behaviors of most materials stems from our understanding of simple liquids, solids, and gases in or near equilibrium and the phase transitions between such idealized equilibrium states. Nonetheless, many properties of relatively simple materials, particularly properties associated with nonequilibrium conditions, remain poorly understood from fundamental and/or atomistic viewpoints.

In this dissertation, dynamic processes in classical liquid-solid systems out of equilibrium are examined using descriptions which apply on atomistic length scales and over mesoscopic time scales. Solutions are obtained primarily by computational simulations, though analytic results are derived where possible. The relative distance from equilibrium varies somewhat from topic to topic, but the issue of describing dynamical processes over long time scales is relevant to each problem addressed. In this sense, the label of multiscale modeling - multiscale in time - is applicable, as there will be an underlying goal of moving toward macroscopic times ($t \gtrsim 100$ ns) but not necessarily macroscopic lengths ($10^3 \lesssim$ number of particles $\lesssim 10^7$).

The motivation for developing atomic-scale models with access to large time scales can be illustrated through the example of glass formation. This phase transition poses a major challenge in terms of both numerical modeling and unifying theoretical descriptions. It involves the rapid dynamical slowing of a liquid, such that the relevant structural relaxation times vary from initial $\sim ps$ scales, to the largest measurable scale of years. At the same time, on the atomic length scale, glass forming liquids are driven by local caging processes and dynamically correlated atomic clusters with characteristic lengths on the order of $1 - 1000$ atomic units. Thus it can be argued that one ultimately needs to formulate a description that includes atomistic features on the appropriate length scales, but accesses the full range of relevant times. This is of course not possible, and hopefully it will prove unnecessary, but there is currently a great need to extend the present limitations in time, as access to a wide range of scales often seems to be a necessary condition for new breakthroughs concerning this particular transition. In general, numerically economical atomic-level approaches could provide the basis for an unlimited number of applications in which atomistic details play some irreducible role in larger scale processes.

The central theoretical tool used in all studies presented here is the phase-field crystal (PFC) modeling method [3–5], which can be viewed as a simplified form of classical density functional theory [6–11]. This approach employs nonlinear stochastic partial differential equations to provide a natural description of slow, diffusive dynamics in interacting systems while still maintaining atomic-level resolution, including topological defects, elastic behavior, and plasticity. All of the topics addressed are ones in which the coarse-grained-in-time nature of the PFC approach can be exploited to gain understanding of physical processes that are difficult to simulate using conventional atomistic approaches. In order of presentation, these topics are grain boundary melting, dislocation dynamics, amorphous solidification near a spinodal, anomalous dynamics in glass-forming supercooled liquids, and heteroepitaxial growth of binary alloy thin films.

For each of these phenomena, current theoretical understanding is incomplete, and in some cases fundamentally unclear. Each also possesses some degree of practical relevance to laboratory and industrial applications. One of the primary goals of this dissertation is therefore to gain new physical insight into these problems, which will lead the presentation beyond issues of multiscale modeling and into principles of equilibrium and nonequilibrium statistical physics, continuum mechanics, and theories of topological defects. The other primary goal is to clarify the functional validity of the coarse-grained PFC approach in various scenarios - to better understand its range of behaviors, which classes of systems it most accurately describes, and the types of new phenomena that can be predicted.

1.1 Modeling Materials Classically

A large number of simulation-based approaches are used to model condensed matter systems, far too many to discuss here. A very brief outline of a few selected approaches should be instructive, though, in framing the present PFC-based studies. The conventional atomistic approaches attempt to sample the phase space of a given many-particle system by generating statistical averages at the particle level which can then be related to thermodynamic, structural, or transport properties of the system. Large length and time scales cannot be readily accessed with such methods. Most continuum approaches attempt to reduce the many-particle problem to a generalized mesoscopic or macroscopic description, by integrating out the microscopic degrees of freedom and describing only quantities which vary slowly in time and/or space. Such theories generally include input parameters which must be determined from atomistic simulations or experiments. Figure 1.1 shows a *rough* graphical outline of the length and time scales numerically accessible to selected methods, assuming typical modern computing power.

1.1.1 Atomistic and discrete approaches

Ab Initio Molecular Dynamics

For our purposes any material can be usefully viewed as a combination of nuclei and electrons. The nuclei and the tightly bound core electrons can almost always be treated classically in liquids, but any valence electrons must be treated quantum mechanically [12]. This applies to systems with highly covalent bonding or strong hydrogen bonds. In the ab initio molecular dynamics (MD) method one considers an instantaneous configuration of nuclei, calculates the valence electronic structure quan-

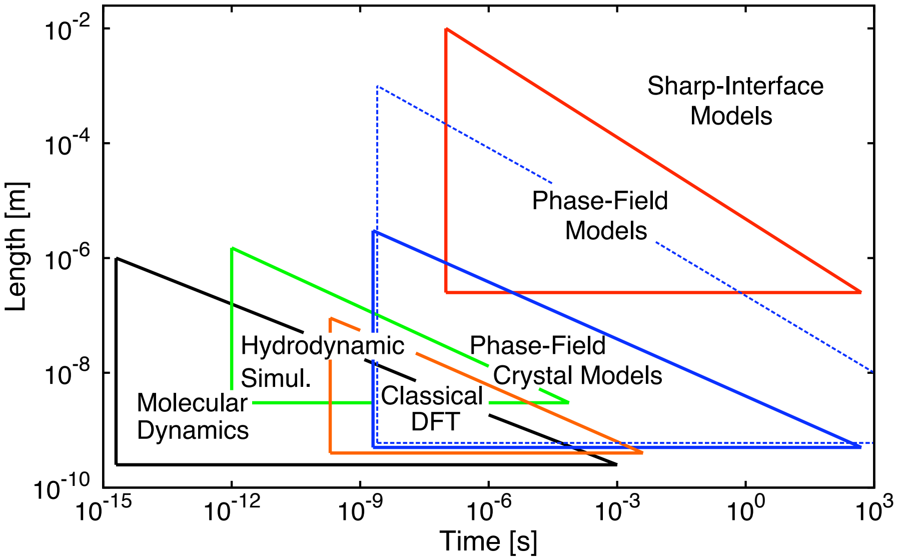

Figure 1.1: Approximate length and time scales numerically accessible to various modeling techniques in three dimensions. The dotted lines represent estimated bounds of the renormalized complex amplitude PFC combined with advanced numerical solution methods. For colloids, multiply L by $\sim 10^3$ and t by $\sim 10^8 - 10^{12}$.

tum mechanically (using *electronic* density functional theory) to determine the forces between nuclei, and then updates the positions of the nuclei using classical equations of motion. The process is iterated to evolve the system in time. Such computations are demanding, severely restricting maximum system sizes and simulation times, but certain systems require a full treatment of this type for a realistic description. The rest of this outline will be limited to classical methods, as quantum mechanical phenomena will not be of particular interest in later chapters.

Classical Molecular Dynamics

The classical approach is usually justified for fluids with filled valence electron shells. The resulting intermolecular forces are relatively weak and can usually be treated in a pair-wise additive manner. Thus a fixed, pre-determined electronic potential can be superimposed upon each nucleic center, and the particle positions can be evolved classically without having to recalculate the quantum valence electronic structure at each iteration. The time step is nonetheless usually limited to $10^{-15} - 10^{-14}s$, meaning that a system with $\sim 10^6$ particles can be simulated for roughly $10^{-9} - 10^{-7}s$ with typical modern computers. Standard classical MD is thus also restricted to the domain of atomically short length and time scales, though longer times can be described in some systems using accelerated MD methods [13].

The basic principle of MD is to map the phase space trajectory of a single system as it evolves in accordance with the rules of classical mechanics. Statistically averaged thermodynamic, structural, or transport properties can be calculated from the atomic level by simulating long times or many independent systems, if it is assumed that ergodicity holds. Since the dynamic evolution is physically consistent, both equilibrium and nonequilibrium situations can be modeled.

Monte Carlo Methods

Monte Carlo (MC) is a complementary approach to MD, in that one samples a system's phase space using a fundamentally statistical approach rather than by explicitly evolving a single system in time. Given an initial configuration, a 'particle' is chosen at random, and a randomly selected test 'movement' is considered from a predetermined set of options. The move will either be accepted or rejected depending on how the energy of the system would be affected, in accordance with the specific MC algorithm employed. Thus configuration space is explored quasi-randomly (the individual movements should be 'small') by repeating the procedure a large number of times. Thermodynamic and structural properties can be computed by averaging over the sampled configurations, which appear on average according to their relative weight in the system's phase space probability density. Since the sequential evolution of the system is not necessarily physical, conventional MC is often limited to studies of static properties in thermodynamic equilibrium. The advantage is that convergence to equilibrium can be dramatically accelerated relative to MD by the allowance of unphysical rearrangements.

1.1.2 Continuum approaches

Classical Density Functional Theory

Classical DFT is an advanced theoretical framework for liquid-solid systems that has been extensively applied to the investigation of simple and complex inhomogeneous fluids and their freezing transitions [6–11]. It has become probably the central theoretical method for studying first-order transitions in classical systems. Liquid and solid states are described by a continuum field $\rho(\vec{r})$ which represents the ensemble- or time-averaged atomic number density. In the liquid state $\rho(\vec{r})$ is uniform, while in the solid state $\rho(\vec{r})$ is inhomogeneous, with localized peaks corresponding to probable atomic lattice positions. Thus the approach is spatially atomistic but within a statistically averaged continuum description.

Phase transitions are described by a suitably chosen thermodynamic free energy functional of $\rho(\vec{r})$, which is constructed from the structural correlations of a reference liquid state near the freezing transition as the only input. Crystallization occurs when the inhomogeneous periodic phase becomes energetically favored over the homogeneous fluid phase below some T, as a result of the preferred correlation structure encoded in the equilibrium liquid structural data. DFT has been extended to describe dynamics (dynamical DFT or DDFT), through equations of motion for $\rho(\vec{r})$ [14–17]. The dynamical theories are generally suited to atomistically resolved studies of mesoscopic dynamic processes, though relatively small system sizes and simulated times are typically required due to the sharp features in the crystalline density peaks.

Generalized Hydrodynamic and Langevin Theories

Hydrodynamics provides a formal method for describing variables in fluid and solid systems which vary slowly in space and time. The full microscopic dynamics is projected onto the space of selected slow variables to obtain a coarse-grained description in terms of the slow field variables only [18]. The resulting description obeys the macroscopic conservation laws (for mass, momentum, and energy in the simplest case) and the symmetries of a given system.

It turns out that hydrodynamic equations often remain accurate to relatively small scales, with gradual deviations as the scale is reduced. Generalized hydrodynamic theories incorporate corrections to maintain validity at even smaller scales, often approaching roughly 10 atomic distances. Hydrodynamic theories require input parameters that must be supplied from more microscopic descriptions, but nonetheless can be applied analytically over a wide range of scales. Numerical implementations are discussed further in Chapter 2.

Phase-Field and Field Theory Methods

Continuum phase-field models and field theories are well-established tools for phenomenologically addressing a wide variety of phase transitions and processes with competing domains separated by interfaces [5, 19–23]. Atomistic lengths and times are neglected in favor of a description in which order parameter fields assume specific constant values which correspond to different 'phases'. The order parameters can represent local concentrations, crystallinity parameters, grain orientations, etc. The internally uniform domains evolve dissipatively in time according to nonlinear partial differential equations, and thus shrink, grow, compete, coarsen, etc, as the thermodynamic driving force is varied (by means of a free energy functional which includes microscopically determined input parameters).

A major motivation for phase-field modeling is to bypass the problem of interface tracking boundary conditions in sharp-interface models (the Stefan problem). The sharp-interface approach also becomes cumbersome when interfaces assume complex shapes or when multiple interfaces meet and interact, while phase-field models naturally allow interaction and evolution of interfaces to virtually arbitrary complexity. Phase-field models are typically applicable in the mesoscopic domain, to problems such as solidification, liquid and solid microstructure pattern evolution, grain growth and coarsening, thin film growth, and solid-state transformations. The lack of atomistic detail excludes certain properties which emerge from small-scale structures, such as elasticity and plasticity. When such effects are desired, their continuum-level equations must be explicitly built in, often at considerable expense in terms of model complexity. Nonetheless, the phase-field approach has considerable value in terms of providing a practical, materials-science-level description of nonequilibrium processes on length and time scales inaccessible to virtually all atomistic theories.

1.1.3 Multiscale modeling

Some materials phenomena involve a wide range of characteristic length and time scales, which may be difficult to reduce to a coarse-grained description without losing essential elements of the underlying physics. Consider the seemingly simple example of a solidifying atomic fluid. The nucleation and growth process involves atomic-scale structure and dynamics at the level of interfaces and fronts, building into micron-scale structures in dendrites and microstructure boundaries, which ultimately determine a sample's macroscopic features and properties. Equilibrium, even locally, is rarely achieved, and the range of important scales is too large to handle with a single theory.

Each of the modeling approaches discussed above is restricted to a characteristic, finite region of frequency-wavenumber space, some more so than others. In numerical studies, the largest scales accessible to any method are generally limited by available computational power. Even if one exploits the applicability of hydrodynamic models at near-atomic scales and performs numerical simulations at such a level, the computations are too demanding to reach any situation even approaching the macroscopic hydrodynamic limit.

Thus, given several approaches with relatively fixed practical bounds in terms of accessible length and time scales, one means of bridging scales is to adopt a multiscale modeling approach. This could involve a relatively straightforward feeding of computed input parameters up the chain from small to large scale approaches. It could also involve explicitly coupling different modeling methods in space and/or time. Multiscale modeling might also be achieved, though with less likelihood, using a single method that can be simulated with extreme efficiency and flexibility.

The multiscale aspect of this dissertation is, in effect, a combination of the first and third scenarios. The intention is to access a broad range of scales in time, more so than in space, using efficiently simulated atomistic models that are coarse-grained in time to various degrees. Specific PFC formulations that effectively coarse-grain either over vibrational time scales or over vibrational and inertial/propagational time scales are employed. A small number of input parameters must in principle be supplied from either experiments or conventional atomistic approaches in both cases. A fuller discussion of the nature of the PFC method and its relation to classical DFT is given in Chapter 2.

1.2 Background, Goals, and Main Findings

The research-based chapters to follow (Chapters 3-7) can each be classified within one of two categories: liquid-solid transitions or crystal plasticity. Some general discussion of the phenomenology for these two topics is given in this section, along with a statement of the goals and main findings concerning each of Chapters 3-7.

1.2.1 Liquid-solid transitions

Most transitions between liquid and solid phases are first-order or discontinuous transitions, though the more complex case of glass formation is also common. First-order transitions are characterized primarily by latent heat and discontinuities in the first derivatives of the free energy, but also by coexisting phases and metastability. Fluctuation effects are generally small, such that mean field theories can often be successfully applied, as opposed to the case of second order or continuous transitions in which fluctuations become large. Nonetheless, first-order transitions are not as well understood as second-order transitions in terms of a robust, widely applicable theoretical framework. This is because the principles of universality, scale invariance, etc which underlie continuous transitions generally do not apply across the spectrum of first-order processes. One finds considerably more dependence on the details of microscopic interactions, and though mean field theories may be applicable, they often need to be carefully constructed for each system if quantitative results are desired.

The first-order transitions of relevance to this dissertation are freezing and bulk melting. Freezing through nucleation and growth of solid phase droplets from the melt, in this case near a liquid phase spinodal, is implied. Bulk melting refers to the corollary of nucleation and growth of liquid phase droplets in a bulk crystal. Due to the lower symmetry of crystals, liquid nucleation can occur through routes other than bulk homogeneous or heterogeneous nucleation above the equilibrium melting temperature T_m. Nucleation (melting) is actually initiated at defects, including surfaces, grain boundaries, dislocations, and vacancies, *below* T_m. These effectively heterogeneous, 'premelting' routes open the possibility of continuous or partially continuous melting transitions which begin below the bulk melting temperature and proceed smoothly as T is raised. Solid phase spinodals may also come into play during melting transitions.

The third type of liquid-solid transition that needs to be discussed here is glass formation, a process whose fundamental nature is still an open subject of research. It is not a first-order transition, though certain thermodynamic quantities, such as the specific heat at constant pressure, do exhibit (cooling rate dependent) semi-discontinuities at the effective transition temperature T_g (see Fig. 1.2). The glass transition is characterized by a rapid but continuous slowing of the liquid dynamics, while the system maintains most of its liquid-like atomic structure. At T_g its structural relaxations become sufficiently slow that the material can be considered a disordered solid or glass. In many ways this solid still resembles a liquid, but one that relaxes with effectively infinite slowness. The enormous span of relevant time scales is demonstrated in Fig. 1.2, where experimental viscosity data for various supercooled liquids are displayed over roughly 17 orders of magnitude [1]. Theories of glass formation can generally be classified as either kinetically- or thermodynamically-driven. It is not clear which picture is most valid, and one possibility is that a successful description will involve some combination of kinetic and thermodynamic driving forces. A more referenced discussion of the literature is provided in Chapter 6.

Chapter 3: Melting and premelting

Motivation and Goals

Interest in premelting at crystalline defects has been stimulated recently in part by visually revealing colloidal studies [2] (Fig. 1.3), but also by traditional materials science issues such as hot cracking induced failure in high temperature processing of metal alloys [24]. The formation of liquid regions below the melting temperature, for example at grain boundaries in polycrystalline materials, can have serious consequences in terms of measurable mechanical properties. There remains a need to formulate a detailed theory or at least to generate new, insightful simulations of the localized melting behavior around defects.

The primary goals of the study described in Chapter 3 are to characterize the melting behavior near dislocations and grain boundaries in a simple three dimensional PFC model as $T \to T_m$ from below, and to take advantage of the quantitative simulation results to develop a simple theory for localized melting and premelting. Another goal is to better understand the conditions under which premelting may occur, as opposed to melting under conditions of liquid-solid coexistence or solid superheating.

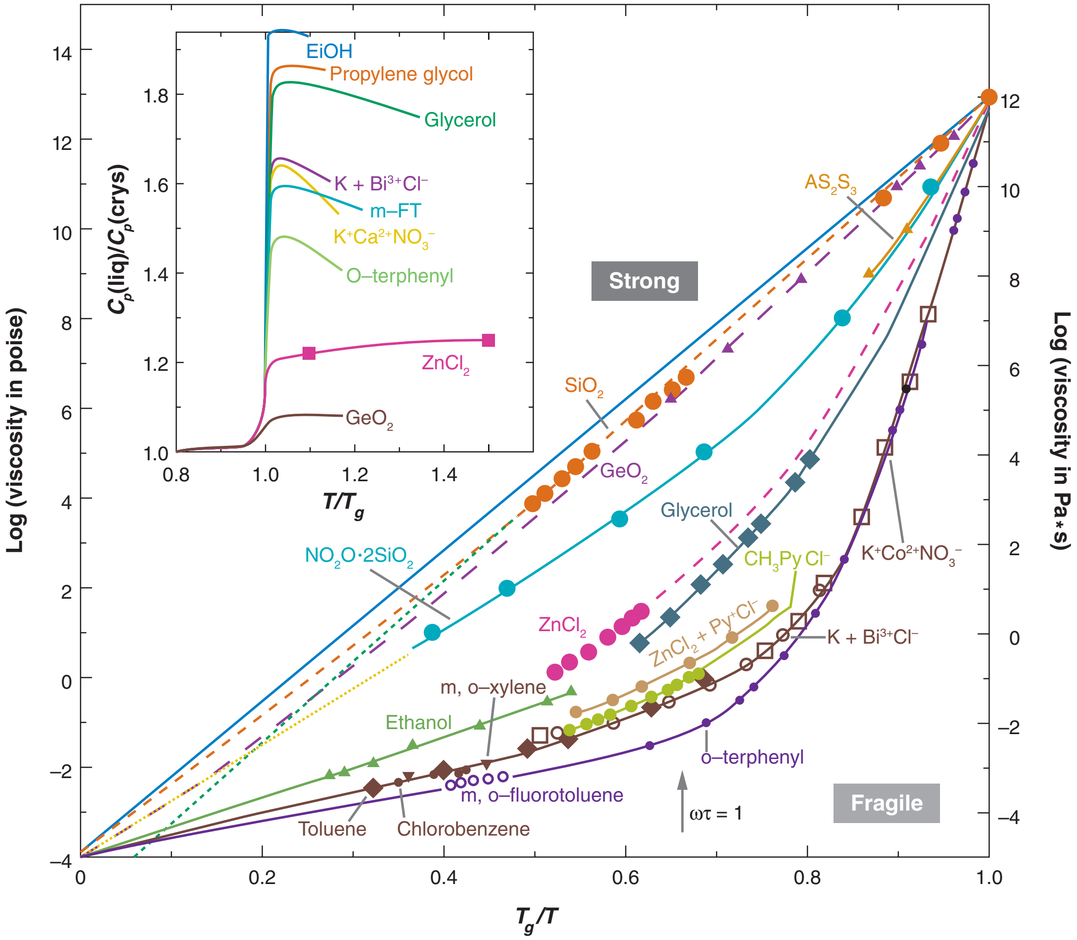

Figure 1.2: Experimental viscosity of glass forming liquids versus inverse temperature, from [1]. Time scales vary from $\sim 1ps$ at the lowest viscosities to $\sim 10^4 s$ at T_g. The inset shows the ratio of liquid and crystal specific heats.

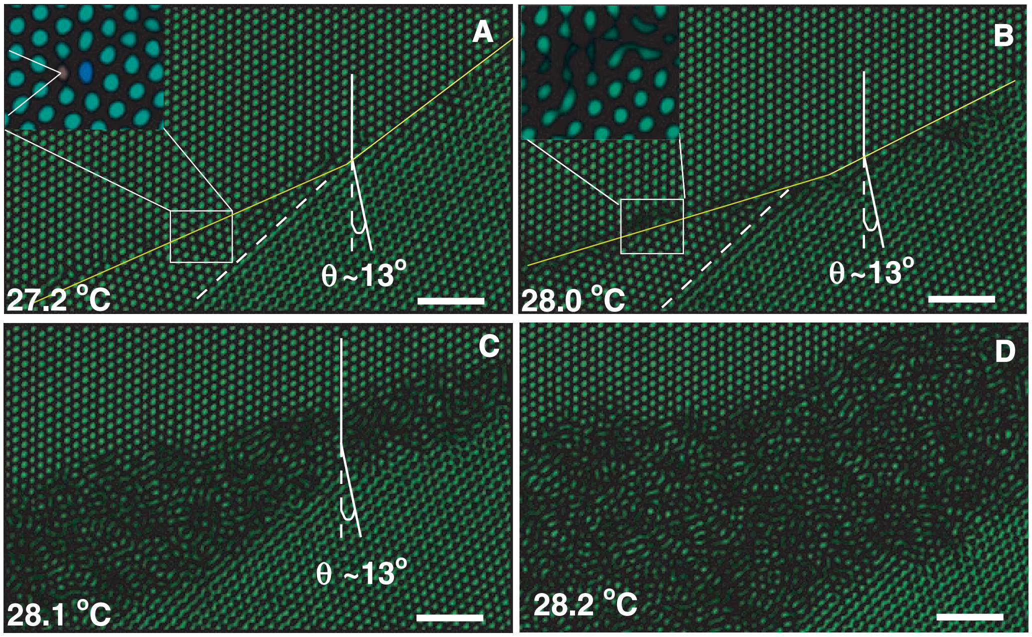

Figure 1.3: Images of premelting at a colloidal crystal grain boundary, from [2]. Scale bars, $5\mu m$.

Main Findings

Simulation results show that the PFC model captures the basic localized defect melting behaviors observed in colloidal experiments. Data are presented for the temperature dependence of the local mean square displacement and melt volume at dislocations and at grain boundaries as a function of boundary angle. A localized theory based on continuum elastic energy expressions for isolated dislocations is developed and shown to describe the simulation results for low to mid angle grain boundaries with semi-quantitative accuracy. High angle grain boundaries are described using an elastic screening approximation, with qualitative accuracy. Ensemble-specific effects are discussed, and the different melting pathways to be expected in the canonical versus grand canonical ensemble are highlighted. It is also demonstrated that premelting is generally enhanced as the bulk melting transition becomes more weakly first order. An approximate expression for the critical grain boundary prewetting angle, as a function of the first-order weakness of the bulk melting transition, is derived.

Chapter 5: Freezing, amorphous nucleation, and spinodals

Motivation and Goals

Though the PFC approach should be well-suited to long-time studies of glassy materials, a useful first step in establishing the model's validity in terms of glass formation would be to understand how disordered solids are created in the simplest version of the model and to characterize some of the properties of the disordered state. Specifically, it is of interest to know whether the transition in the simple model resembles a glass transition or a first-order nucleation process, whether there are signs of glassy dynamics in the supercooled liquid phase (regardless of the answer to the previous point), and whether the resulting glass is suitable for studies of mechanical and other behaviors in amorphous solids. These initial questions are concerned more with PFC validation and model building issues than with questions of new physics in glassy materials. The answers will be useful in Chapter 6, where glass forming (rather than nucleation and spinodal-driven) dynamics are more closely examined and reproduced.

Main Findings

Amorphous solidification is shown to occur through a first-order nucleation and growth process in the purely diffusive three dimensional PFC model. The critical droplet size for the amorphous solid is found in general to be slightly smaller than that of the equilibrium bcc solid. Thus solidification occurs through a two-stage process in which an amorphous precursor phase is first nucleated, and from which the equilibrium bcc phase then nucleates after some cooling rate dependent crystallization time. The structure of the disordered solid is nonetheless consistent with that of known simple glass formers. Critical softening behaviors are also demonstrated as the disordered solid is reheated toward the melting temperature. Finally, liquid spinodal effects are shown to give the appearance of glassy dynamics - moderately stretched exponential decays, a diverging relaxation time, and apparent dynamic heterogeneity - but also a diverging static correlation length and ultimately a discontinuous solidification transition. Thus, a true glass transition is not observed within the standard monatomic PFC model with purely diffusive dynamics.

Chapter 6: The glass transition

Motivation and Goals

The disordered solid states obtained in Chapter 5 provide proof that the PFC free energy contains metastable glassy minima. Such configurations should permit long-time studies of the mechanical properties of glasses, but there would still be great value in correctly capturing the dynamics of the glass transition itself. This would permit long-time studies of the inherently difficult-to-model glass formation process, allowing access to the deeply supercooled regime and contributing to a better understanding of its nature. The goal of Chapter 6 is to build upon the findings of Chapter 5 to construct a PFC model with the dynamic features of a true glass transition in the supercooled liquid phase. The basic questions concern which classes of free energies and equations of motion are most appropriate and whether they can be improved upon to describe Vogel-Fulcher type divergences, two-step relaxation functions, demonstrate agreement with established theoretical and experimental results, and the ability to simulate many additional orders of magnitude in relaxation time. If these issues can be adequately addressed, then one would be in a position to begin investigating some of the fundamental questions related to the physics of the glass transition itself.

Main Findings

Numerical simulations show that a modified nonlinear PFC functional combined with an inertial-diffusive equation of motion produces the fundamental dynamic features of fragile glass formation. This is the first direct evidence, to our knowledge, that DFT-based models are capable of describing such behavior in detail. Vogel-Fulcher divergences, two-step relaxation functions, power law scaling in aging properties, and agreement with established mode-coupling theory (MCT) and experimental results are demonstrated. The success of this description is attributed to the introduction of strong nonlinearities in the free energy and ‘fast’ inertial processes in the dynamics, both of which lead to caging and enhanced dynamic correlation effects. By applying a physically motivated time scaling, the ability to simulate many additional orders of magnitude in relaxation time (12 orders of magnitude in this study) is demonstrated. The first physical insight provided by this new formulation concerns a correlation between liquid fragility and a rapidly growing dynamic correlation length.

Chapter 7: Epitaxial growth

Motivation and Goals

The value of modeling epitaxial growth using the PFC approach was demonstrated in one of the first applications of the model [4]. The entire process of roughening, dislocation nucleation, and relaxation can be naturally modeled with atomistic resolution, without the cusp-like divergences which limit the standard continuum elastic models. The main goal of Chapter 7 is to build upon the findings of these studies concerning monatomic heteroepitaxy, by extending the description to binary systems. In this case the focus is shifted toward outlining the spatial and temporal nature of phase separation in growing alloy films as a function of misfit and relative species mobilities. Another goal is to probe the behaviors and properties of the proposed binary PFC model, which was introduced and applied to various phenomena in the article where much of this work originally appeared [25].

Main Findings

Three general features of phase separation in growing films have been identified from numerical simulations. These concern either lateral or vertical separations. Lateral patterns emerge on the length scale of the surface roughness in which the lower misfit component segregates below surface valleys and the higher misfit component segregates below surface peaks. A vertical separation in which one component accumulates near the film surface is almost always observed. For the case of equal species mobilities, the higher misfit component will be driven toward the surface, but if the lower misfit component has a sufficiently greater mobility, then it will be the one which accumulates most at the surface. Effects such as vertical phase separation at the film-substrate interface and around dislocations are also identified. Finally, selected growth issues in simpler monatomic films are discussed in relation to the predictions of continuum elastic theories. Significant deviations from the continuum limit are demonstrated for relatively small deviations from idealized growth conditions.

1.2.2 Crystal plasticity

Crystalline and polycrystalline solids exhibit a number of generalizable behaviors when subjected to applied strains, and it turns out that most of these behaviors cannot be understood in terms of the properties of perfect crystals. The elastic and plastic responses of crystalline solids are instead a reflection, almost entirely, of internal defect structures and their dynamics. The most relevant defect in terms of plastic flow is generally the dislocation line, the two dimensional analogue of which is studied in Chapter 4.

The multiscale nature of plasticity spans from the relevant structure and dynamics of individual dislocations ($\sim 10^{-12}s$, $\sim 10^{-9}m$) to those that describe the macroscopic features and responses of the material ($\sim 10^{1}s$, $\sim 10^{-2}m$). Atomic-level properties of dislocations and their role in plasticity under extreme deformation rates can be studied, for example, with molecular dynamics simulations. This input can be fed into coarse-grained dislocation dynamics (DD) models [26, 27], which describe length and time scales more relevant to macroscopic materials properties. These models employ continuum-level descriptions of defect stress fields, phenomenological equations of motion for the resulting point and line structures, and pragmatic rules for their interactions with each other. The PFC approach offers an intermediate description which could be used to validate the phenomenology of conventional DD models or as a self-contained mesoscopic approach to plastic behavior, which could be useful for studying specific mesoscale problems at experimentally accessible strain rates.

Chapter 4: Dislocation dynamics

Motivation and Goals

As a model for crystalline solids, the PFC description should capture the basic physical mechanisms and dynamic features of defect motion. The primary goal of Chapter 4 is to quantify at a fundamental level how PFC dislocations respond to applied strains and to the strain fields of other dislocations. The processes of greatest interest are glide, climb, and annihilation. It would also be useful to classify the dynamics of isolated dislocations in terms of simple analytical descriptions, such as the equations of motion for overdamped point masses. This knowledge should help to lay the groundwork for larger-scale plasticity studies, which have since been undertaken.

Main Findings

It is shown that the natural features of dislocation glide, climb, and annihilation are reproduced without any explicit consideration of elasticity theory or ad hoc construction of microscopic Peierls potentials. The Peierls barrier for dislocation glide/climb and the ensuing dynamic behavior are quantified as functions of strain rate, temperature, and dislocation density. It is shown that the dynamics are accurately described by simple viscous motion equations for an overdamped point mass, where the dislocation mobility is the only adjustable parameter. The diffusive dynamical model employed should produce results most applicable to 'soft' systems such as colloidal crystals.

1.3 Dissertation Outline

An introduction to the fundamental principles and equations of PFC modeling is provided in Chapter 2. The first application of the standard monatomic PFC model to melting and premelting at dislocations and grain boundaries is described in Chapter 3. The subject of dislocations is carried into Chapter 4, with an analysis of the diffusive dynamics of individual and paired edge dislocations under applied strains. Chapter 5 shifts the focus to solidification, describing a study of amorphous solidification and crystallization in monatomic PFC systems with diffusion dominated dynamics. In Chapter 6, the dynamics of glass formation in supercooled monatomic and binary liquids are addressed using inertial dynamics and a modified free energy functional. Qualitative agreement with mode-coupling theory [28–30] is demonstrated. A study of strain-driven phase separation in heteroepitaxially grown binary thin films is outlined in Chapter 7, and a summary of results and suggestions for future work is given in Chapter 8. The numerical methods used in these studies are outlined in Appendix A, and several modified PFC formulations, constructed as models for glass formation but eventually set aside in favor of the model described in Chapter 6, are briefly discussed in Appendix B.

1.4 Publications

Much of Chapter 3 has been published in *Physical Review B* [31]. Most of Chapter 4 has been published in *Physical Review E* [32]. Most of Chapter 5 has been published in *Physical Review E* [33]. Portions of Chapter 6 have been published in *Physical Review Letters* [34]. Portions of Chapter 7 have been published in *Physical Review B* [25].

CHAPTER 2

An Introduction to Phase-Field Crystal Modeling

The basic elements and properties of PFC models are outlined in this chapter. Accessible length and time scales are first discussed, followed by an introduction to PFC free energy functionals. The standard functional is examined both from the conventional phase-field viewpoint and from the perspective of classical DFT, wherein PFC models are seen as particularly simple DFTs. Then selected properties of the liquid and solid phases are examined, and extensions to binary systems discussed. Finally, the standard phenomenological and derivable equations of motion for the PFC density field(s) are presented and briefly discussed. Some aspects of the treatment in this chapter are similar to those found in Refs. [5] and [4].

2.1 Relevant Length and Time Scales

Phase-field crystal models are intended to span the spatiotemporal gap in physical modeling between conventional meso/micron-scale continuum phase-field models and atomic-scale models such as molecular dynamics and classical density functional theory (see Fig. 1.1). Ideal applications of the PFC approach will exploit its short-length-scale/long-time-scale description in phenomena where characteristic scales match those of the method. Significant advantages in describing slow atomic-level dynamics during glass formation, crystallization, structural transitions, etc, are in principle obtainable over traditional methods.

Micron-level length scales are also becoming PFC accessible with recent applications of formal spatial coarse-graining techniques (complex amplitude multi-scale expansions) [35–42], combined with advanced numerical methods [38, 43–49]. The amplitude representations are spatially uniform except near lattice defects, and can therefore be simulated over significantly larger length scales. A drawback is that some of the atomic-level information contained in the full PFC description is lost, e.g., Peierls barriers for defect motion may be eliminated, faceted surfaces generally cannot be described, and accuracy is lost near high angle grain boundaries [42]. These amplitude models can in principle be linked with existing phenomenological phase-field models to guide the construction of more accurate phase-field theories and provide insight into their input parameters. By taking the sharp interface limits of the resulting phase-field models, one finally arrives at the fully macroscopic length and time scales described by sharp interface representations [50]. To fully close this chain from atomistic to macroscopic scales, many inconsistencies and technical difficulties still need to be addressed, but the outline of a functional multiscale modeling framework appears to be emerging.

2.2 The PFC Functional

The simplest dimensionless PFC free energy functional for pure systems can be written

$$F_{\mathrm{PFC}}[n(\vec{r})] = \int d\vec{r} \left\{ \frac{n}{2} \left[r + (1+\nabla^2)^2 \right] n + \frac{n^4}{4} \right\} \tag{2.1}$$

where $n \rightarrow n(\vec{r}) + \bar{n}$ is the scaled time- or ensemble- averaged atomistic number density field, $\bar{n}$ is the average value of n, $\vec{r}$ is the spatial coordinate vector, and $r \sim (T - T_c)$ is a constant which controls the distance from the critical point at temperature T_c or $(r, \bar{n}) = 0$. This basic notation will be used in all subsequent chapters.

Equation (2.1), as written, was apparently first studied by Brazovskii [51] as a model for ordering transitions in cholesteric liquid crystals and antiferromagnets, with appropriate reinterpretation of the order parameter n. Swift and Hohenberg expanded on Brazovskii's theory with a specific focus on Rayleigh-Bénard convection [52]. For these reasons Eq. (2.1) is often referred to as the Brazovskii or Landau-Brazovskii free energy (in two dimensions, usually) or the Swift-Hohenberg model (when evolved with nonconserved dynamics).

Elder *et al.* [3, 4] proposed Eq. (2.1) as the basis of a modeling methodology for liquid-solid systems, akin to classical DFT, and applicable to equilibrium and long-time nonequilibrium phenomena. The PFC functional provides an economical framework for modeling both inhomogeneous liquids and solids with naturally emerging elastic and plastic properties. The periodic phases exhibit nonlinear elastic behaviors with atomic-scale interfaces and defect structures analogous to those of crystals. A rapidly growing body of publications has demonstrated that many phenomena involving solids and inhomogeneous liquids are captured by PFC models. These include

- crystal droplet nucleation and growth [38, 53–59],
- dendritic and eutectic solidification [25, 53],
- colloidal solidification [53–55, 60],
- heterogeneous nucleation at walls [61],
- glass formation [33, 34],
- polymorphism and structural phase transformations [53, 62, 63],
- anisotropy in crystalline interfacial energies [37, 53, 54, 56, 64] ,
- heteroepitaxial growth [4, 25, 40, 41, 54, 65–67],
- the Kirkendall effect in binary alloys [68],
- grain boundary energetics [4, 69–71],
- grain boundary melting and premelting [31, 70, 72],
- dislocation pairing in hot grain boundaries [73],
- crystal plasticity and dislocation dynamics [4, 32, 47, 74, 75],
- dislocation avalanches [76],
- dislocation motion in spinodal decomposition [25],
- nonlinear elastic behavior [77, 78],
- structural transformations and sliding friction on atomic surfaces [79–83],
- colloidal patterning on surfaces [55],
- elasticity in liquid crystal-polymer networks [84, 85], and
- phase behavior and dynamics in
  - liquid crystals [86, 87],
  - nonspherical colloids [61], and
  - foams [88].

Further general information on PFC modeling may be found in Refs. [5, 89–91].

2.2.1 Relation to conventional phase-field models

Phase-field and field theory models were described in Chapter 1. The prototypical example is ψ^4 or Landau theory, which provides a phenomenological mean-field description of continuous Ising-like phase transitions between phases of differing symmetry (which are uniform on the level of the order parameter $\psi(\vec{r})$),

$$F[\psi(\vec{r})] = \int d\vec{r}\ \left[\frac{r}{2}\psi^2 + \frac{u}{4}\psi^4 + \frac{K}{2}\left(\nabla\psi\right)^2\right]. \tag{2.2}$$

Here r, u, and K are constants, where $r \sim (T - T_c)$ again controls the distance from the critical point at temperature T_c.

The standard PFC functional is generated by switching the sign of the of gradient term and adding the next even-order gradient term. The fourth-order gradient leads to *periodic* equilibrium solutions for r sufficiently negative, rather than only uniform phases at, e.g., $\psi = 0, \pm\sqrt{r/u}$. Figure 2.1 shows the free energy penalty for inhomogeneities on various length scales for both theories. The ψ^4 penalty grows quadratically with wavenumber q and thus only tolerates relatively large-scale inhomogeneities below the critical point. The PFC penalty by construction encourages structures on the scale of $2\pi/q_0$ for sufficiently negative r (q_0 is the position of the first peak in the PFC direct correlation function, as discussed in the following subsection). The elastic and plastic behaviors which naturally emerge from these periodic structures on all scales are absent in bare ψ^4-like phase-field models.

2.2.2 Derivation from classical density functional theory

Classical DFT, as applied to liquid-solid systems, was introduced in Chapter 1. DFT free energy functionals are often separated into three parts,

$$F[\rho(\vec{r})] = \int d\vec{r}\,[f_{id} + f_{exc} + f_{ext}] \tag{2.3}$$

where $f_{id} = \rho(\vec{r}) \ln\left(\rho(\vec{r})/\rho_l\right) - \delta\rho(\vec{r})$ is the exact entropic, one-body or ideal gas component of the system's free energy, f_{exc} accounts for all higher order, many-body interactions between particles, and $f_{ext} = \rho(\vec{r})V(\vec{r})$ describes the effect of external potentials $V(\vec{r})$ on the system. $\rho(\vec{r})$ is the unscaled averaged atomic number den-

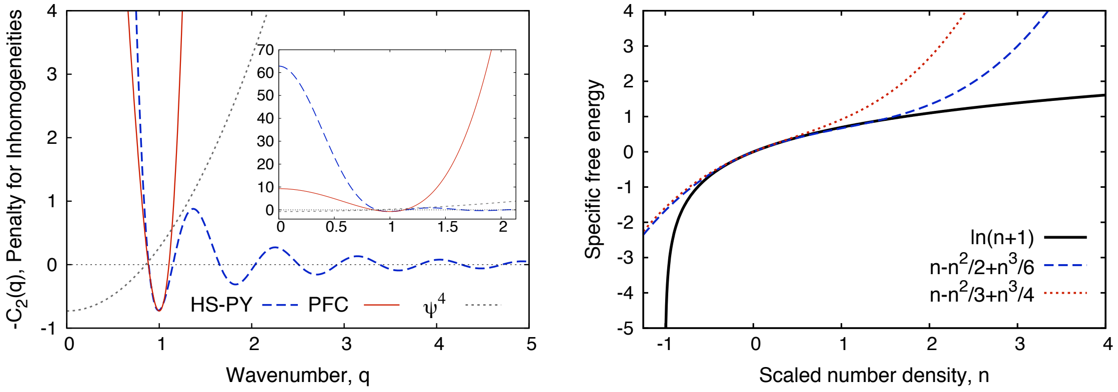

(a) (b)

Figure 2.1: (a) Specific free energy cost for inhomogeneities as a function of wavenumber for hard spheres under the Percus-Yevick (PY) approximation, the corresponding PFC theory, and an example Landau or ψ^4 theory. The PY curve is shown at the hard sphere liquidus, the PFC curve at $r = -0.73$, and the Landau curve below the critical point. The inset shows a wider span in $-C_2(q)$. (b) The logarithmic DFT free energy term and examples of expansions used in PFC models.

sity field, ρ_l is the reference average number density (at the liquidus, usually), and $\delta\rho(\vec{r}) = \rho(\vec{r}) - \rho_l$. The nondimensional form of F given here has been scaled by $k_B T$, where k_B is Boltzmann's constant, and T is temperature. The variational principle of DFT states that F is a unique functional of $\rho(\vec{r})$, that is, $F[\rho(\vec{r})]$ is minimized by the equilibrium density profile $\rho_{eq}(\vec{r})$ and $F[\rho_{eq}(\vec{r})]$ corresponds to the equilibrium canonical free energy.

Obtaining an exact F in DFT is equivalent to calculating a system's partition function, which cannot be done for most realistic systems. Thus, the unknown portion of F is shuffled into f_{exc}, and the various formulations of DFT consist in different approximations for f_{exc}. The form of interest here is a perturbative expansion around $\delta\rho(\vec{r})$ due to Ramakrishnan and Yussouff (RY) [7],

$$F^{\mathrm{RY}}_{exc} = F_{exc}(\rho_l) - \frac{1}{2}\int d\vec{r}\,' \left[\delta\rho(\vec{r})C_2(\vec{r},\vec{r}\,')\delta\rho(\vec{r}\,')\right] + \cdots \tag{2.4}$$

where $C_2(\vec{r},\vec{r}\,') = C_2(|\vec{r}-\vec{r}\,'|) = C_2(r)$ is the two-point direct correlation function of the fluid (assumed isotropic). The Fourier transformed function $C_2(q)$ is related to the structure factor through $S(q) = 1/[1 - \bar{\rho}C_2(q)]$, where $\bar{\rho}$ is the system average number density. The above expansion about the liquid direct correlation functions can be continued, but is usually truncated after $C_2(r)$ for simplicity. Many extensions and alternative formulations of DFT exist [8–10, 92, 93], but the RY functional is still often used as a starting point for semi-quantitative studies.

It has recently been shown that the PFC functional can be viewed as a simplified form of the RY functional [25]. Two approximations are required. First, $C_2(q)$ is gradient expanded in symmetric or even gradients of $n = \rho(\vec{r})/\rho_l - 1$,

$$C_2(q) = \hat{A}_0 + \hat{A}_2 q^2 + \hat{A}_4 q^4 + \ldots \tag{2.5}$$

where $\hat{A}_0$, $\hat{A}_2$, and $\hat{A}_4$ are negative, positive, and negative constants, respectively. This is the simplest physically meaningful form for $C_2(q)$, as it approximates the two-body correlations by a single, smooth, isotropic peak near $q = q_0$ (Fig. 2.1). Such an expansion amounts to a local density approximation, as the full nonlocal $C_2(r)$ term is reduced to a local gradient functional. Next, the $\ln(\rho/\rho_l) = \ln(n + 1)$ term in f_{id} is expanded in powers of n around $n = 0$ and truncated at n^4. Graphical representations of both of these approximations are shown in Fig. 2.1. Higher order correlation functions contribute additional powers of n that will modify the coefficients of the expanded $\ln(n + 1)$ terms [41]. These coefficients are thus generally left as variable parameters, which allows additional flexibility in correcting for the approximate nature of F_{PFC} [94]. Note that the n^3 term resulting from this expansion can always be scaled out; the only two independent variables in this formulation are r and $\bar{n}$.

The single Fourier peak approximation to $C_2(q)$ produces relatively sinusoidal periodic structures, as high-q modes are severely penalized by the PFC $C_2(q)$. The full RY $C_2(q)$ permits subtle high-q effects, resulting in equilibrium density profiles with many contributing modes and much sharper features. DFT crystalline states generally consist of very narrow, almost non-overlapping Gaussian peaks at the atomic lattice positions. The PFC description thus captures the basic symmetries of the crystalline phase but not the small-scale details of the individual density peaks.

The second PFC approximation, the truncated $\ln(\rho/\rho_l)$ expansion, penalizes large values of n more severely than the logarithm. This caps the optimal amplitude of periodic structures near 1, as suggested by Fig. 2.1. The truncated $\ln(\rho/\rho_l)$ expansion may also permit unphysical occurrences of $\rho < 0$ unless explicit penalties are imposed [95] or the density is scaled from ρ to n in such a way that inconsistencies are avoided [63].

The RY-to-PFC approximation therefore results in solid phases with nearly sinusoidal density profiles of amplitude order 1, as opposed to multi-mode, sharply-peaked Gaussian profiles with amplitude $\gg 1$. The advantages are that the properties of the PFC states are generally much easier to compute analytically and that numerical studies can be performed on a much coarser simulation grid than that of the corresponding RY states (approximately eight grid units per PFC lattice spacing as compared to 32-64 grid units per RY lattice spacing, per dimension). Three-dimensional DFT simulations with more than a few hundred or few thousand particles are generally impractical, while PFC simulations with millions of particles have already been demonstrated. An additional advantage is that the tools of multiple scale analysis, developed in the context of pattern formation in Rayleigh-Bénard convection, can be straightforwardly applied to the PFC theory, but not to the more complex DFT. This permits development of the coarse-grained complex amplitude PFC models noted earlier.

The simplified PFC $C_2(q)$ tends to favor the most symmetric crystalline structures – triangular lattices in two dimensions and bcc lattices in three dimensions – but it has recently been shown that fcc and hcp crystals become the equilibrium states in the region near $-0.75 \lesssim \bar{n} \lesssim -0.38$ and $-1.60 \lesssim r \lesssim -0.35$ [53, 94]. Slightly more complicated $C_2(q)$ approximations, employing two or three peaks rather than one, have also been shown to produce a wide range of stable crystalline structures [62, 63]. Higher-order correlations (C_3, etc) can be used as well to generate more complex structures, but this approach is in general quite computationally expensive.

The direct connection between PFC and DFT outlined here makes a large number of methods and applications from the relatively well-developed DFT body of work accessible to PFC studies. One can now in many cases step in where traditional DFTs become analytically or numerically intractable and approach problems with an efficient, simplified framework that still generally contains the essential physics of periodic and liquid-solid systems.

Modified versions of this basic PFC formulation have also been proposed. These include extensions to binary alloys [25] (see Section 2.2.4), a model that incorporates long-lived vacancies [95] (see Chapter 6), a model motivated by structural transformations that allows multiple stable crystal structures [62, 63], a higher-order gradient scheme for more accurate $C_2(q)$ matching [58], an anisotropic model for nonspherical particles [61], and orientational vector/tensor models for liquid crystals [84–87], to list a few.

2.2.3 Static model properties

Phase behavior

In the limit of vanishing thermal fluctuations, equilibrium or metastable PFC states may be either constant (homogeneous liquid), periodic (crystalline solid), or aperiodic (disordered solid). We are interested here in the nature of the PFC phase diagram and the basic properties of the various phases. The average free energy of the liquid phase is easily obtained by substituting $n(\vec{r}) = \bar{n}$ into Eq. (2.1),

$$f_\ell = \frac{r+1}{2}\bar{n}^2 + \frac{1}{4}\bar{n}^4. \tag{2.6}$$

In the limit $r \rightarrow 0$, the equilibrium periodic phases are accurately described by a simple one-mode approximation, since the PFC free energy is lowered by only a fairly narrow range of reciprocal lattice vectors near $q = 1$. A general periodic phase in the one-mode approximation can be written

$$n(\vec{r}) = \bar{n} + \sum_{m_1=0}^{1} \cdots \sum_{m_d=0}^{1} a_{m_1,\cdots,m_d} e^{i\vec{G}\cdot\vec{r}} + c.c. \tag{2.7}$$

where d is the dimensionality of the structure, $a_{m_1,\cdots,m_d}$ are Fourier coefficients of the reciprocal lattice vectors, $\vec{G} = m_1\vec{b}_1 + \cdots + m_d\vec{b}_d$, $\vec{b}_i$ are the reciprocal lattice vectors of the lattice structure, and *c.c.* denotes complex conjugate. In the one-mode approximation, the summations over m_i are taken such that $\vec{G}$ always has length equal to that of the shortest or primary reciprocal lattice vector of the lattice structure in question.

For example, the one-mode two-dimensional triangular lattice is written

$$n_{tri}(\vec{r}) = A\left[\cos(qx)\cos\left(\frac{qy}{\sqrt{3}}\right) + \frac{1}{2}\cos\left(\frac{2qy}{\sqrt{3}}\right)\right] + \bar{n} \tag{2.8}$$

where $A_{eq} = -(4/5)[\bar{n} + (|\bar{n}|/\bar{n})(1/3)\sqrt{-15r - 36\bar{n}^2}]$ and $q_{eq} = \sqrt{3}/2$ are the equilibrium amplitude and wavenumber, respectively. These values are obtained by substituting $n_{tri}(\vec{r})$ into the free energy and minimizing with respect to A and q separately. Minimizing the total free energy over a one-mode unit cell then gives the average F of any basic periodic phase as a function of r and $\bar{n}$. For the triangular lattice, one finds

$$f_{tri} = f_\ell + \left(\frac{3(r+1)}{16} - \frac{1}{2}q_{eq}^2 + \frac{1}{3}q_{eq}^4 + \frac{9}{16}\bar{n}^2\right)A_{eq}^2 + \frac{3}{16}\bar{n}A_{eq}^3 + \frac{45}{512}A_{eq}^4. \tag{2.9}$$

Using Maxwell's equal-area construction, the coexistence boundaries between phases can be calculated for conserved $\bar{n}$. Figure 2.2 shows portions of the resulting one-mode or numerically obtained phase diagrams in one, two, and three dimensions. After fitting $C_2(q)$ to match a given set of material parameters, one typically models a known material within some small portion of one of the phase diagrams displayed in Fig. 2.2.

The order of a given transition between phases of different symmetry is primarily a function of proximity to the critical point at $(r, \bar{n}) = 0$, though the addition of thermal fluctuations described in Section 2.3 can lead to more complex behaviors. In general, the transition at $(r, \bar{n}) = 0$ has a second-order mean field nature, and slightly off-critical regions of parameter space exhibit weakly first-order transitions. As the distance from the critical point is increased, bulk transitions become more strongly first-order. Spinodal lines, or boundaries of global instability, also emerge when standard dynamic equations are employed. These can have important effects on transition behavior as will be discussed further in Section 2.3.

Elastic properties

The elastic properties of the periodic phases are also of fundamental importance, as PFC models aim to capture realistic elastic and plastic effects both during crystal growth and within stabilized solid samples. The average free energy of any periodic PFC phase is naturally a minimum at some equilibrium periodicity a_{eq}, and for small

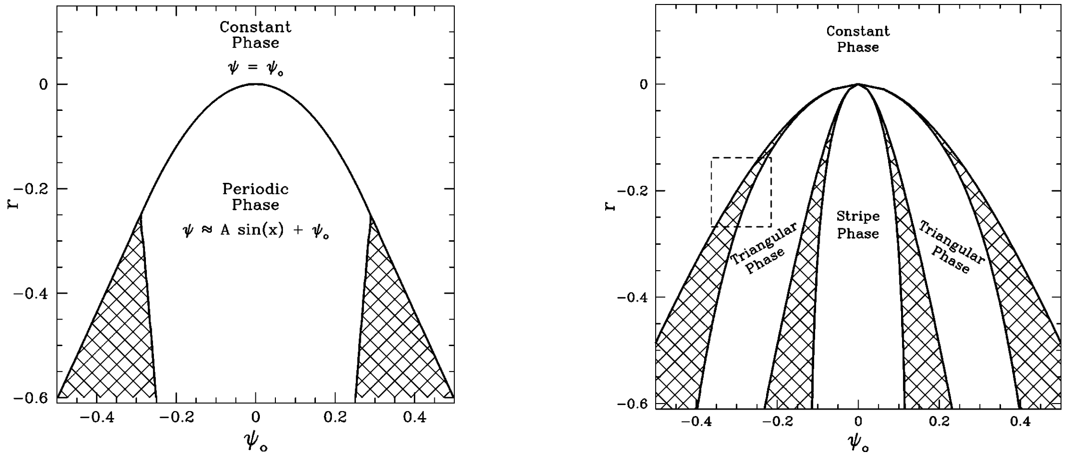

(a) 1D (b) 2D

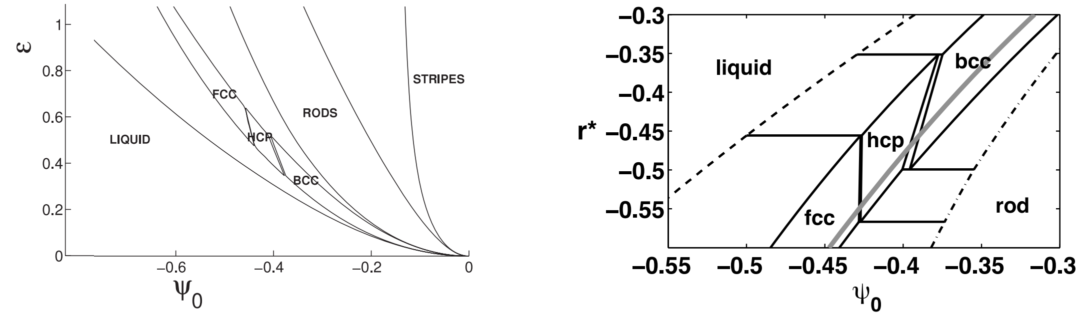

(c) 3D (d) 3D section

Figure 2.2: PFC phase diagrams in one, two, and three dimensions. (a) 1D and (b) 2D diagrams, in the one-mode approximation, from Ref. [4]. Crosshatched regions denote coexistence. The 3D diagrams in (c) and (d) are numerically obtained results from Refs. [94] and [53], respectively. Unlabeled regions denote coexistence, and the gray line denotes the liquid spinodal. $r = r^* = -\epsilon$, $\psi_0 = \bar{n}$.

deformations about a_{eq} varies in a Hooke's law form $[F - F_0 \sim (a - a_{eq})^2]$. The relevant linear elastic constants for a given crystal symmetry can be explicitly calculated in the one-mode limit by determining how $F_{\rm PFC}$ varies under the appropriate deformations ϵ, and relating the $\mathcal{O}(\epsilon^2)$ coefficients to the system's linear elastic constants.

This follows from the definition of the elastic energy of a strained solid [96]

$$F_{el} = \frac{1}{2}\int d^dx\,[K_{ijkl}u_{ij}u_{kl}] = \int d^dx f_{el}(u_{ij}) \tag{2.10}$$

where K_{ijkl} is the elastic constant tensor, $u_{ij} = (\nabla_i u_j + \nabla_j u_i)/2$ is the linearized strain tensor, $\vec{u}$ is the displacement vector, and $f_{el}(u_{ij})$ is the elastic free energy density. A two dimensional triangular crystal, for example, has two independent elastic constants in K_{ijkl}, since symmetry considerations require $K_{ijkl} = \lambda\delta_{ij}\delta_{kl} + \mu(\delta_{ik}\delta_{jl} + \delta_{il}\delta_{jk})$. The Lamé coefficients λ and μ are related to the bulk modulus by $B = \lambda + \mu$ (μ is also the shear modulus). The expression for K_{ijkl} implies that $K_{11} = K_{22} = \lambda + 2\mu$, $K_{12} = K_{21} = \lambda$, $K_{44} = \mu$, and all other $K_{ijkl} = 0$. The standard notation in which $1 = xx$, $2 = yy$, and $4 = xy$ has been used. Writing out the full elastic energy density,

$$f_{el} = \frac{K_{11}}{2}(u_{xx}^2 + u_{yy}^2) + K_{12}(u_{xx}u_{yy}) + 2K_{44}(u_{xy}u_{xy}), \tag{2.11}$$

and substituting $K_{12} = K_{11} - 2K_{44}$ from the relations above gives

$$f_{el} = \frac{K_{11}}{2}(u_{xx}^2 + u_{yy}^2 + 2u_{xx}u_{yy}) + 2K_{44}(u_{xy}u_{xy} - u_{xx}u_{yy}) \tag{2.12}$$

or equivalently

$$f_{el} = \frac{\lambda}{2}(u_{xx}^2 + u_{yy}^2 + 2u_{xx}u_{yy}) + \mu(2u_{xy}u_{xy} + u_{xx}^2 + u_{yy}^2). \tag{2.13}$$

Now consider the energy cost of shear and bulk deformations, defined here by $u_x = \epsilon y$ (shear) and $u_x = \epsilon x$, $u_y = \epsilon y$ (bulk). The elastic energy density becomes

$$f_{el}^{shear} = \frac{K_{44}}{2}\epsilon^2 = \frac{\mu}{2}\epsilon^2, \tag{2.14}$$

$$f_{el}^{bulk} = 2(K_{11} - K_{44})\epsilon^2 = 2B\epsilon^2. \tag{2.15}$$

Performing the same calculations for the one-mode triangular PFC lattice, by substituting $n_{tri}(x+\epsilon y, y)$ (shear) and $n_{tri}(x(1+\epsilon), y(1+\epsilon))$ (bulk) into $F_{\rm PFC}$ and minimizing, one finds

$$f_{el}^{shear} = \frac{3A_{eq}^2}{32}\epsilon^2 + \frac{9A_{eq}^2}{128}\epsilon^4, \tag{2.16}$$

$$f_{el}^{bulk} = \frac{3A_{eq}^2}{4}\epsilon^2 + \frac{3A_{eq}^2}{4}\epsilon^3 + \frac{3A_{eq}^2}{16}\epsilon^4. \tag{2.17}$$

Comparing coefficients gives $\mu = 3A_{eq}^2/16$ and $B = 3A_{eq}^2/8$, fully specifying the small deformation (linear) elastic behavior of the perfect PFC triangular crystal. Note the additional higher order nonlinear elastic terms which are present even in the one-mode approximation of the PFC crystal, including an asymmetric nonlinear ϵ^3 term in f_{eq}^{bulk}. Analogous calculations can be performed for any crystal symmetry of interest. For example, the three independent linear elastic constants in a one-mode bcc crystal are found to be $B = (K_{11} + 2K_{12})/3 = A_{eq}^2/3$, $\mu' = (K_{11} - K_{12})/2 = A_{eq}^2/8$, and $\mu'' = K_{44} = A_{eq}^2/4$, where B is the bulk modulus and μ', μ'' are the two shear moduli.

Topological defects and plasticity

Elastically responsive perfect crystals such as those described above provide a starting point for modeling real solids, but the next level of realism requires defects and their associated strain fields, slip planes, interaction mechanisms, etc. The type of defect generally most relevant to the mechanical behavior of crystalline solids is the dislocation. This is a point defect in two dimensions and a line defect of screw, edge, or hybrid character in three dimensions. Dislocations are represented with atomic-level detail in PFC solids, and it turns out that their long-range stress and strain fields match those of continuum elasticity theory quite well, with the advantage of a more realistic atomistic core region in which stress does not diverge. These defects automatically interact and respond to applied strains with the appropriate atomistic glide, climb, and annihilation mechanisms, as will be shown in Chapter 4.

Edge dislocation structures in a triangular PFC crystal are illustrated in Fig. 2.3, where numerically obtained configurations are compared with those predicted by linear continuum elasticity theory. Figure 2.3(a) shows the equilibrium one-mode crystal before and after application of the linear continuum expressions for the displacement fields of an edge dislocation, u_x and u_y. The result is $n_{tri}(x+u_x, y+u_y)$, where

$$u_x = \frac{b}{2\pi}\left[\phi + \frac{1}{2}\frac{\lambda+\mu}{\lambda+2\mu}\sin(2\phi)\right], \tag{2.18}$$

$$u_y = -\frac{b}{2\pi}\left[\frac{\mu}{\lambda+2\mu}\ln\bar{r} + \frac{1}{2}\frac{\lambda+\mu}{\lambda+2\mu}\cos(2\phi)\right], \tag{2.19}$$

$b = 2\pi/q_{eq}$ is the dislocation Burgers vector, $\phi = \arctan(y/x)$, $\bar{r} = \sqrt{x^2+y^2}$, and the elastic constants λ and μ were calculated above. Figure 2.3(b) shows a simulated PFC edge dislocation before and after reverse application of u_x and u_y, which approximately recovers the equilibrium unstrained crystal. The simulated dislocation was produced by allowing two adjacent crystalline slabs with N and $N+1$ atoms/row, respectively, to equilibrate into a stable configuration. The agreement between automatically generated PFC configurations and continuum elasticity theory is quite good, even very near the dislocation core where strain ultimately diverges in the continuum expressions and where nonlinear elastic effects become more pronounced in the PFC system.

Sequential applications of any continuum defect displacement fields of interest, as demonstrated in Fig. 2.3(a), can provide a useful method for generating complex defect structures in PFC simulations. Figure 2.4 shows an example of a perfect $b = a[100]$ prismatic dislocation loop in a bcc crystal created by a slightly more complex application of this method. Four symmetric edge dislocation lines compose the initial boundary of the loop, which results in an extra unit cell plane of self interstitial atoms in the interior of the loop (a cluster of 392 interstitials in this case). When allowed to relax by evolving in time, the initially square loop becomes octagonal or nearly circular and either grows or shrinks by climb, depending on local strain, temperature, etc. A $b = a[100]$ bcc screw dislocation is illustrated in Fig. 2.5, and common bcc point defects are shown in Fig. 2.6 (self interstitials in split [110]-dumbbell and [111]-crowdion configurations). All of these defects were generated by relaxing an initial PFC state that was created using continuum displacement fields.

Grain boundaries, or periodic arrays of dislocations, also contribute crucially to the properties of polycrystalline solids. Some sample PFC grain boundary structures are shown in Fig. 2.7. Two and three dimensional PFC models have been shown to

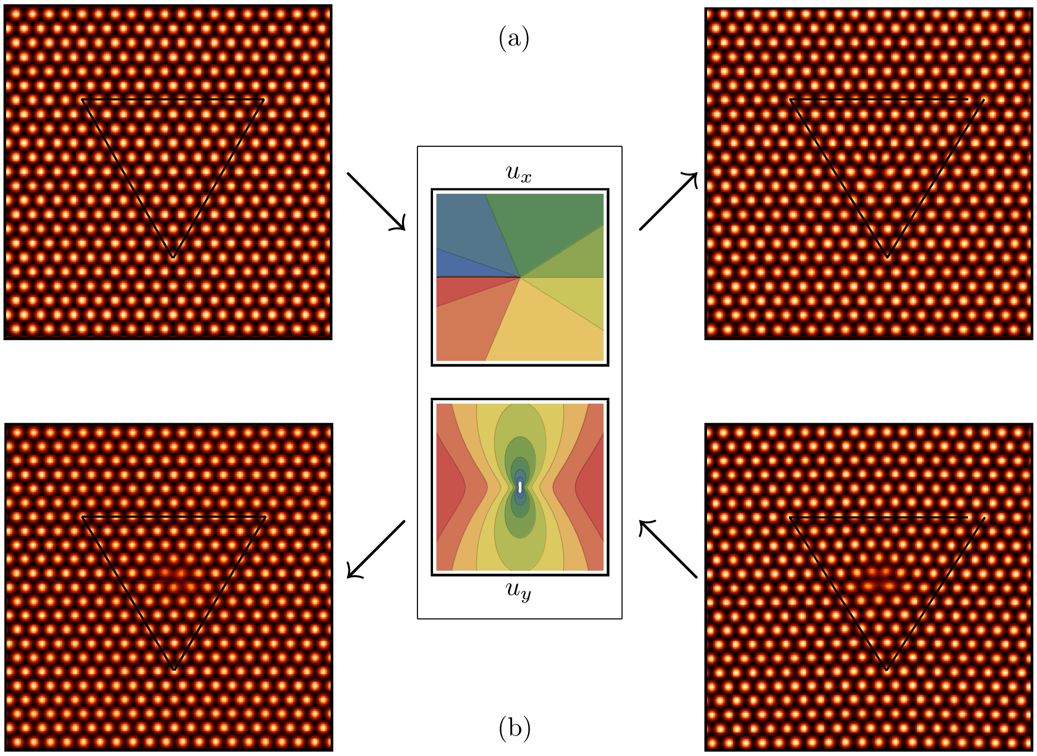

Figure 2.3: (a) The one-mode triangular crystal (left) and the resulting $b = a[10]$ edge dislocation (right) following application of the continuum linear elastic displacement fields u_x and u_y. (b) A simulated $b = a[10]$ PFC edge dislocation configuration (right) and the resulting undislocated state (left) following reverse application of u_x and u_y. The black lines are Burgers circuits, and u_x and u_y are shown as contour plots.

capture known features of grain boundary energetics, such as the low-angle Read-Shockley boundary energy vs. angle (θ) result and the less tractable high θ behavior measured in experiments [4, 71]. The continuum elastic description in which long-range stress fields begin to screen each other as θ is increased, reducing the lateral stress profile from power law to exponential decay, has also been reproduced [31]. Properties related to grain boundary melting are discussed in Chapter 3.

2.2.4 Binary PFC functionals

This outline of static model properties will end with a brief introduction to binary free energy functionals. A much more detailed account can be found in Ref. [25]. The

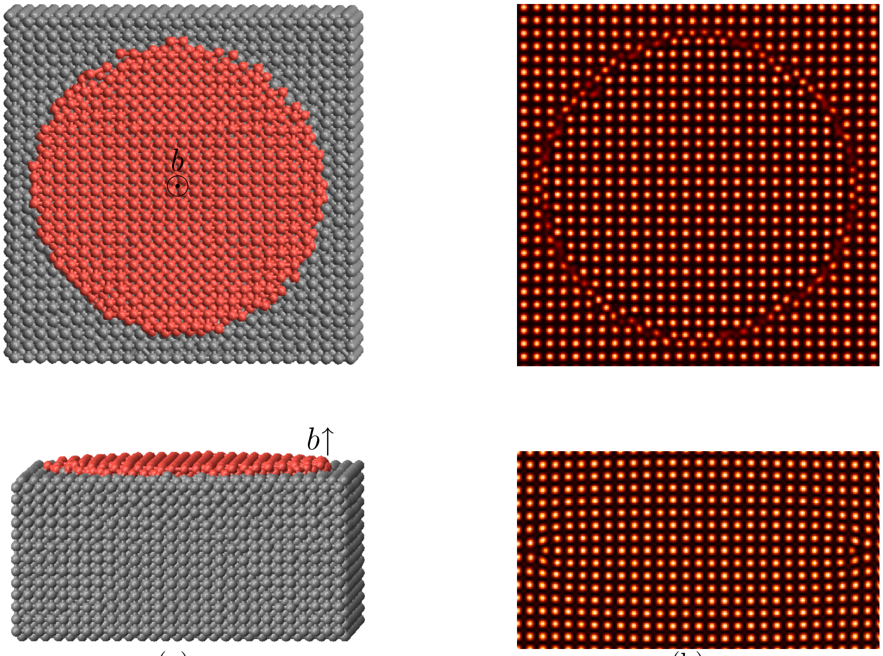

(a) (b)

Figure 2.4: A perfect $b = a[100]$ prismatic dislocation loop in a PFC bcc lattice, generated using continuum elastic displacement fields. (a) Slightly tilted [100] (top) and [010] views (bottom) of the PFC density peak configuration. Red atoms represent self interstitials, gray represents the original unstrained bcc atoms, and all atoms on one side of the loop plane have been blanked. (b) Cross-sectional [100] (top) and [010] (bottom) views of $n(\vec{r})$ through the dislocation loop.

RY functional extended to binary alloys of A and B atoms becomes

$$F^{\mathrm{RY}} = \int d\vec{r} \left[\rho_A(\vec{r}) \ln\big(\frac{\rho_A(\vec{r})}{\rho_l^A}\big) - \delta\rho_A + \rho_B(\vec{r}) \ln\big(\frac{\rho_B(\vec{r})}{\rho_l^B}\big) - \delta\rho_B\right] - \tag{2.20}$$

$$\frac{1}{2}\int d\vec{r}d\vec{r}' \left[\delta\rho_A(\vec{r}) C_2^{AA}(\vec{r},\vec{r}')\delta\rho_A(\vec{r}')\right] - \tag{2.21}$$

$$\frac{1}{2}\int d\vec{r}d\vec{r}' \left[\delta\rho_B(\vec{r}) C_2^{BB}(\vec{r},\vec{r}')\delta\rho_B(\vec{r}')\right] - \tag{2.22}$$

$$\frac{1}{2}\int d\vec{r}d\vec{r}' \left[2\delta\rho_A(\vec{r}) C_2^{AB}(\vec{r},\vec{r}')\delta\rho_B(\vec{r}')\right] + \cdots \tag{2.23}$$

where ρ_i is the number density of species $i = A$ or B, $\delta\rho_i = \rho_i - \rho_{\ell,i}$, $\rho_{\ell,i}$ is the reference number density of species i, and $C_2^{ij}(\vec{r},\vec{r}')$ specifies the isotropic two-point

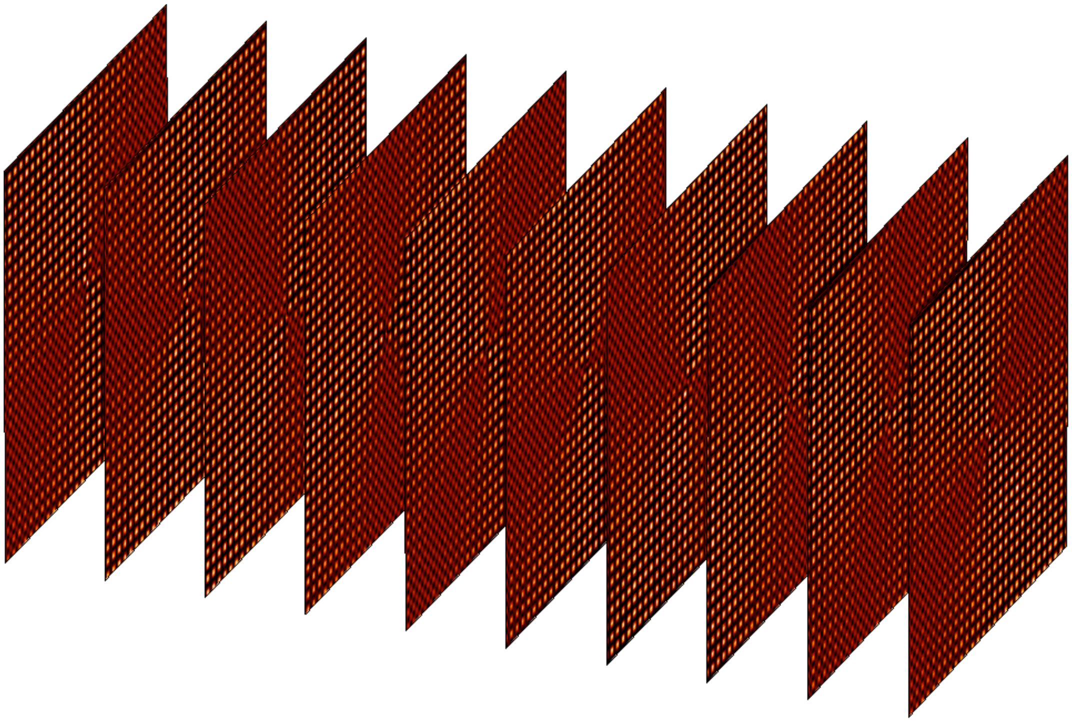

Figure 2.5: Cross sections of $n(\vec{r})$ along one pitch of a $b = a[100]$ screw dislocation in a bcc PFC lattice.

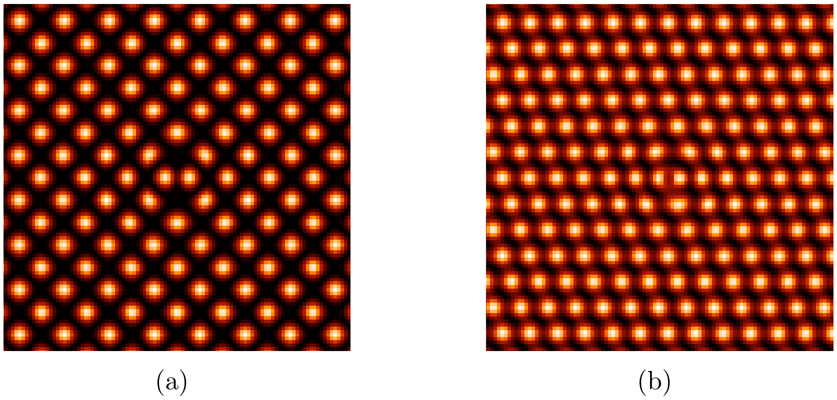

(a) (b)

Figure 2.6: (a) A (200) cross section of $n(\vec{r})$, rotated 45°, showing a bcc self interstitial in the split [110]-dumbbell configuration. (b) A ($\bar{1}10$) cross section, rotated 35.26°, of a [111]-crowdion bcc self interstitial.

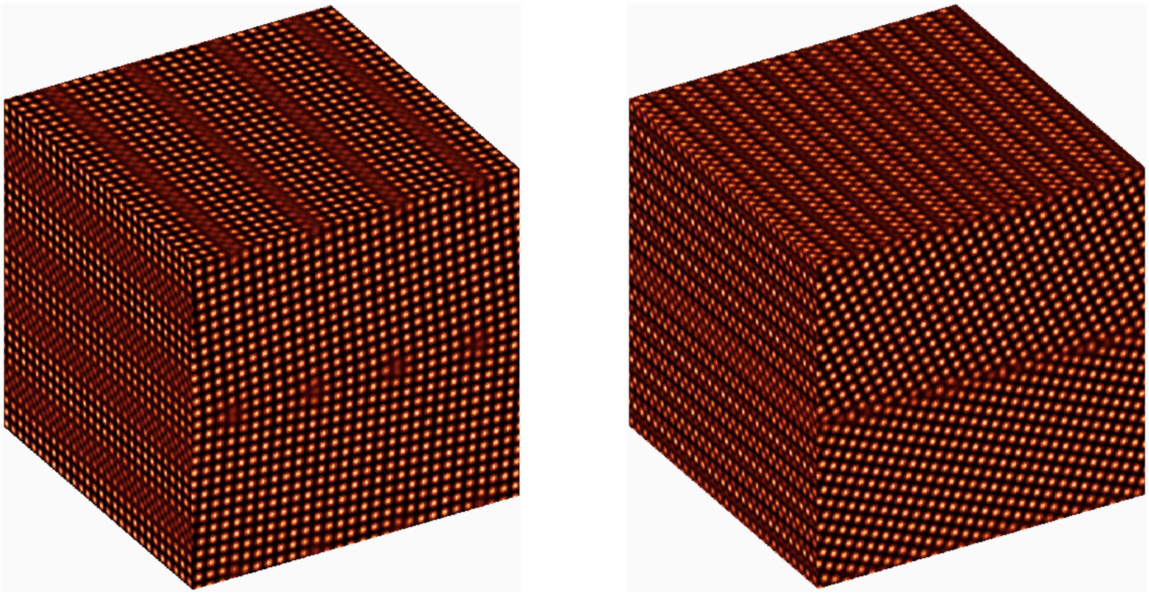
(a) (b)

Figure 2.7: PFC grain boundary configurations. (a) 8.2° and (b) 44.1° symmetric tilt grain boundary pairs in a bcc crystal with periodic boundary conditions.

direct correlation function between i and j particles. The same approximations used to generate the pure PFC functional can be applied to the binary case, giving

$$F_{\text{PFC}} = \int d\vec{r}\,[f_{AA} + f_{BB} + f_{AB}] \tag{2.24}$$

where

$$f_{ii} = \frac{n_i}{2}\left[r_i + (q_i^2 + \nabla^2)^2\right] n_i + \frac{1}{4} n_i^4$$

and

$$f_{AB} = n_A \left[r_{AB} + (q_{AB}^2 + \nabla^2)^2\right] n_B.$$

The f_{ii} terms are simply PFC functionals for independent A and B fields, where $n_i = \rho_i/\rho_{l,i} - 1$ is the species specific scaled number density, q_A and q_B set the AA and BB correlation periodicity, respectively, and r_i is a constant analogous to that of the monatomic model. f_{AB} accounts for AB interactions, with q_{AB} setting the AB correlation periodicity and r_{AB} the interspecies linear coupling constant. In practice it is sometimes simpler to employ only a hard-core-like repulsion term of the form

$f_{AB} = r_{AB}(n_A + 1)(n_B + 1)$ or $f_{AB} = (r_{AB}/2)(n_A + 1)^2(n_B + 1)^2$.

One can also justify additional AB interaction terms on phenomenological grounds, such as $(K/2)|\nabla c|^2$, where $c = n_A/(n_A + n_B)$ is a species concentration field and K is a constant. This term enforces an energy cost for large gradients in c, and it arises naturally when the PFC derivation is performed in terms of, e.g., $n = n_A + n_B$ and c, rather than in terms of n_A and n_B explicitly. Various other levels of approximation in choosing a binary PFC functional can also be defended for specific studies, several of which are discussed in Refs. [25] and [5].

2.3 Dynamics

A closed system's equilibrium thermodynamic information is fully specified by its (exact) free energy functional. A dynamical description requires additional information. Most generally, the dynamics of a closed system should exhibit relaxation toward equilibrium through minimization of F or maximization of entropy S, as required by thermodynamic law. Particle-based theories can be evolved in time through, for example, explicit, discretized Newtonian equations of motion for each particle. A coarse-grained theory such as classical DFT requires, in principle, solution of the full many-body problem at hand to arrive at a coarse-grained, effective equation of motion for n, the averaged atomic density *field*.

This is generally not feasible for interesting systems, thus the simplest approach is often to postulate phenomenological equations of motion for n which obey the fundamental thermodynamic principles of F minimization and any known symmetries or conservation laws. Semi-rigorous derivations can be achieved for some systems by systematically coarse-graining, for example, a particle-based theory such as Brownian dynamics or a fluctuating hydrodynamic theory, to derive alternative equations of motion under relatively controllable limits of approximation. An adiabatic approximation, which assumes a separation of time scales between the (slow) one-particle density field and all other observables, is generally applied in such cases.

Some of the standard dynamic equations from field theory and classical DFT, which will be employed in later chapters, are introduced in this section. All are written here with stochastic thermal noise terms to allow simulations which incorporate activated processes. The question of whether such noise terms are strictly appropriate in an ensemble-averaged theory, which should in principle average all fluctuations into the free energy functional, is an open one [90, 97, 98]. Considering the approximate nature of the PFC functional and the common interpretation of n as a time-averaged, rather than ensemble-averaged, quantity, it seems reasonable at this point to include small amplitude noise terms when phenomenologically justified. For more detailed discussions on how to derive the PFC coarse-grained dynamics, see for example, [15, 50, 60, 82, 99, 100].

With one exception, fluctuating hydrodynamic theories and extensions such as the generalized Langevin equation are not considered here. These approaches explicitly include additional variables in the dynamics, such as velocity or momentum fields, and sometimes energy density and displacement fields. Although such theories in principle apply in the thermodynamic limit, they are commonly fed with quasi-atomistic free energies, and thus numerical studies of these models generally probe the same length scales as PFC. Hydrodynamic and generalized Langevin theories, as a result of the additional (vector) field variables and more complex equations of motion, are considerably more demanding to simulate and ultimately access shorter time scales than numerical PFC studies (see Fig. 1.1). The advantage is a more rigorous framework built on relatively controlled approximations. A goal of PFC modeling is to show that many of the same behaviors emerge from simpler free energies and equations of motion, though this often requires phenomena-specific functional validations. To maintain consistency, the following equations of motion are all written in terms of $n = \rho/\rho_l - 1$.

2.3.1 Nonconserved relaxation: Model A

One of the simplest stochastic phenomenological models for relaxational motion of the field n, when n need not be conserved, is

$$\frac{\partial n}{\partial t} = -\Gamma\mu + \eta \tag{2.25}$$

where t is time, Γ is a mobility constant, $\mu = \delta F/\delta(n+1)$ is the local chemical potential, and η is a Gaussian stochastic noise variable with $\langle \eta(\vec{r}, t)\rangle = 0$ and $\langle \eta(\vec{r}_1, t_1)\eta(\vec{r}_2, t_2)\rangle = 2\Gamma k_B T \delta(\vec{r}_1 - \vec{r}_2)\delta(t_1 - t_2)$. This equation specifies that the field n

evolves locally in whichever direction minimizes F, at a rate proportional to the local chemical potential. This form can be used even when n is conserved to efficiently locate equilibrium states at known, fixed values of $\bar{\mu}$.

2.3.2 An accelerated Model A

An equation of motion that evolves toward equilibrium even more rapidly and efficiently than Eq. (2.25) for nonconserved n is [101]

$$\frac{\partial \ln(n+1)}{\partial t} = -\Gamma\mu + \eta. \tag{2.26}$$

Here n relaxes toward local equilibrium super-exponentially rather than exponentially. One can discretize and take the exponential of both sides of this equation to arrive at an algorithm that is especially efficient when μ contains a $\ln(n+1)$ term, as is the case for the RY functional.

2.3.3 Conserved diffusion: Model B

A conservation law for n implies that

$$\frac{\partial n}{\partial t} = -\vec{\nabla} \cdot \vec{J} \tag{2.27}$$

where $\vec{J}$ is the flux. If the flux is assumed to be driven by gradients in μ,

$$\vec{J} = -\Gamma\vec{\nabla}\mu, \tag{2.28}$$

the resulting equation of motion (for Γ=constant) is known as Model B,

$$\frac{\partial n}{\partial t} = \Gamma\nabla^2\mu + \vec{\nabla} \cdot \vec{\eta}, \tag{2.29}$$

where conserved Gaussian stochastic noise has been added. This is the simplest and probably the most widely used dynamic equation in PFC studies where conserved dynamics are required and fast or highly nonlinear relaxation processes can be safely neglected. It is expected to be particularly relevant for colloidal systems, where relaxation is believed to be dominated by self-diffusion of particles.

Dynamic instabilities, or spinodals, can be mapped onto the PFC phase diagrams when either Eq. (2.25) or Eq. (2.29) is employed. A simple linear stability analysis reveals, for example, that the homogeneous phase becomes globally unstable to perturbations of wavenumber q for $r \leq -(1-q^2)^2 - 3\bar{n}^2$. Thus the liquid phase spinodal begins at $r_s(q=1) = -3\bar{n}^2$, when stochastic noise is ignored. With Eq. 2.29, the liquid structural relaxation times diverge as $\left[2q^2(r+1-2q^2+q^4)\right]^{-1}$ when r_s is approached from above. Spinodal instabilities such as these often play a role in transitions between PFC states, as will be demonstrated in later chapters.

2.3.4 Conserved nonlinear diffusion: Overdamped DDFT

When Γ in the previous scenario is not a constant, but instead depends on position, one obtains

$$\frac{\partial n}{\partial t} = \nabla \cdot (\Gamma(\vec{r})\nabla\mu) + \nu \tag{2.30}$$

where $\langle \nu(\vec{r}_1, t_1)\nu(\vec{r}_2, t_2)\rangle = 2k_BT\nabla\cdot\nabla\left[\Gamma(\vec{r})\delta(\vec{r}_1 - \vec{r}_2)\delta(t_1 - t_2)\right]$. The stochastic noise term used here must be multiplicative to satisfy detailed balance.

The overdamped equation of DDFT corresponds to the case of $\Gamma(\vec{r}) = n(\vec{r}) + 1$. Several researchers have proposed and/or derived this equation with noise [16, 102–104] or without [17, 105, 106], to approximate the dynamics of dense Brownian or classical fluids. It has been argued that the density-dependent mobility term creates 'self-caging' effects which underlie reversible mode coupling behavior and glassy dynamics, while these nonlinearities are absent from Model B [16].

2.3.5 Inertial dynamics

Dynamics in supercooled liquids and in crystalline solids are often dominated by acoustic sound modes or phonons. An equation of motion that incorporates such propagation effects in a qualitative way, by reintroducing faster inertial or wave-like processes, is

$$\frac{\partial^2 n}{\partial t^2} + \beta\frac{\partial n}{\partial t} = \alpha^2\nabla \cdot (\Gamma(\vec{r})\nabla\mu) + \nu \tag{2.31}$$

where α and β are constants related to sound speed and damping rate, respectively. This equation of motion (with $\Gamma(\vec{r}) = 1$) was first applied to PFC dynamics by Provatas *et al.* with a focus on its application to solid elasticity [74], and its derivation has since been discussed in other PFC studies [50, 99, 107, 108]. It has been proposed or derived in various other contexts without the stochastic noise term [109–114].

The fast, oscillating modes generated by the second time derivative combine with the diffusive relaxation term to produce a more rigid, quasiphonon-driven mechanical response than in the overdamped case. These quasiphonons are dissipated over fixed, relatively short length and time scales relative to physical acoustic phonons.

It may be worth noting that the noiseless version of Eq. (2.31) can be written in an equivalent form that somewhat resembles that of Eq. (2.30). Specifically, for $\Gamma(\vec{r}) = 1$, one can rewrite Eq. (2.31) as

$$\frac{\partial n}{\partial t} = \alpha^2 \nabla \cdot \left(\int_{-\infty}^{t} e^{-\beta(t-t')} \nabla \mu \, dt' \right) \tag{2.32}$$

where β^{-1} is seen as the memory time constant or the characteristic time for crossing over from inertial to diffusive dynamics [107].

One might also attempt to extend Eq. (2.31) by noting that the coefficients α and β are in principle functions of wavenumber q. In Fourier space, the form becomes

$$\frac{\partial^2 \hat{n}}{\partial t^2} + \beta(q) \frac{\partial \hat{n}}{\partial t} = \alpha^2(q) \; iq \; \hat{N} \tag{2.33}$$

where $\hat{n}$ and $\hat{N}$ are the Fourier transformed versions of n and $\Gamma(\vec{r})\nabla\mu$, respectively. Common forms for α and β from generalized hydrodynamics are $\alpha(q) = \alpha_0/\sqrt{S(q)}$ and $\beta(q) = \beta_0 + \beta_1 q^2/S(q)$, where α_0, β_0, and β_1 are constants [18]. In the PFC model, we have $S^{-1}(q) \simeq 1 + r + 3\bar{n}^2 + (1-q^2)^2$ or $S^{-1}(\nabla^2) \simeq 1 + r + 3\bar{n}^2 + (1+\nabla^2)^2$ for $r > -1 - 3\bar{n}^2$. Denoting $S^{-1}(\nabla^2) = 1 + \omega(\nabla^2)$, the inertial equation becomes

$$\frac{\partial^2 n}{\partial t^2} + \left[\beta_0 - \beta_1 \nabla^2 \left(1 + \omega(\nabla^2)\right)\right] \frac{\partial n}{\partial t} = \alpha_0^2 \left(1 + \omega(\nabla^2)\right) \cdot \nabla \cdot \left(\Gamma(\vec{r}) \nabla \mu\right). \tag{2.34}$$

The propagating modes in this equation have velocities and damping rates which both depend on wavenumber and reproduce the expected behaviors in the low q limit. Low q waves are weakly damped, with lifetimes $\sim (\beta_0 + S^{-1}(0)\beta_1 q^2)^{-1}$, and have somewhat higher propagation speeds than high q waves, which are rapidly damped out. The specific form of $S(q)$ in the PFC model could lead to singularities since $S(q) \to 0$ for large q, rather than $S(q) \to 1$. The combination of $\alpha(q)$ and $\beta(q)$

should cancel this effect though, as the important quantity is the ratio $\alpha(q)/\beta(q)$ which $\sim 1/q^2$ in the large q limit. This implies that diverging propagation velocities will be suppressed by more rapidly diverging damping rates.

The equation obtained in the limit $\omega(\nabla^2) \rightarrow 0$ has previously appeared in Ref. [99],

$$\frac{\partial^2 n}{\partial t^2} + \left(\beta_0 - \beta_1 \nabla^2\right) \frac{\partial n}{\partial t} = \alpha^2 \nabla \cdot \left(\Gamma(\vec{n}) \nabla \mu\right). \tag{2.35}$$

This form maintains a q-dependent damping rate ($\sim q^2$), and neglects short length scale damping effects due to the structural correlations in $S(q)$ as well as any q dependence of the sound speed. It seems that Eq. (2.35) can also be arrived at from the generalized Langevin equation of fluctuating nonlinear hydrodynamics, by ignoring off-diagonal terms and terms second order in the velocity field. Finally, the limit $\beta_1 \rightarrow 0$ and $\omega(\nabla^2) \rightarrow 0$ reproduces the original inertial dynamics of Eq. (2.31).

2.3.6 Higher-order models: Hydrodynamics of isothermal solids

A more general dynamical model, based on linearized hydrodynamics, and from which the previous equations of motion can be obtained under various approximations, is [50, 99, 100]

$$L_1 \frac{\partial^2 n}{\partial t^2} - \nu L_1 \nabla^2 \frac{\partial n}{\partial t} = \gamma \nabla^2 \left(-\frac{\partial n}{\partial t} + c_2 \nabla^2 n \right) - \alpha_2 L_1 \nabla^2 n + L_1 \nabla \left[\Gamma(\vec{r}) \nabla \mu \right], \tag{2.36}$$

where $L_1 = \partial/\partial t - a_2 \lambda \nabla^2$, λ is an elastic constant, ν_0 is the sum of shear and bulk viscosities, $\gamma = -\lambda/\bar{\rho} + \alpha_2$, $c_2 = \bar{\rho} a_2 \alpha_2$, a_2 is a dissipative prefactor, and α_2 is the linear mass-displacement coupling constant. This equation contains third-order time derivatives, and though it is more complicated than Eq. (2.31), it nonetheless contains only one scalar field n and better describes true hydrodynamic phonons. The phonon damping is correctly proportional to q^2 for $q \rightarrow 0$, as opposed to Eq. (2.31), but similar to Eq. (2.35). Predicted limits of validity for this and the preceding conserved equations of motion are discussed in Refs. [50, 99, 100].

2.3.7 Binary systems: Coupled dynamics

The generalized nonlinear diffusion equations for binary DDFT read

$$\frac{\partial n_A}{\partial t} = \nabla \cdot (\Gamma_A(\vec{r})\nabla\mu_A) + \nu_A \tag{2.37}$$

$$\frac{\partial n_B}{\partial t} = \nabla \cdot (\Gamma_B(\vec{r})\nabla\mu_B) + \nu_B \tag{2.38}$$

where $\langle \nu_i(\vec{r}_1, t_1)\nu_i(\vec{r}_2, t_2)\rangle = 2k_BT\nabla\cdot\nabla\left[\Gamma_i(\vec{r})\delta(\vec{r}_1 - \vec{r}_2)\delta(t_1 - t_2)\right]$ and typically $\Gamma_i(\vec{r}) = n_i(\vec{r}) + 1$. The dynamics of A and B are coupled through the cross terms appearing each species' chemical potential and through the subsequent feedback in the density-dependent mobility terms. It is often more convenient to employ the binary version of Model B when possible,

$$\frac{\partial n_A}{\partial t} = \Gamma_A\nabla^2\mu_A + \eta_A \tag{2.39}$$

$$\frac{\partial n_B}{\partial t} = \Gamma_B\nabla^2\mu_B + \eta_B \tag{2.40}$$

where $\langle \eta_i(\vec{r}_1, t_1)\eta_i(\vec{r}_2, t_2)\rangle = 2\Gamma_i k_BT\nabla^2\delta(\vec{r}_1 - \vec{r}_2)\delta(t_1 - t_2)$.

2.4 Overview and Research Directions

The aim of this chapter has been to provide a sketch of the PFC method by outlining its basic features, properties, and some of the successes realized to date. The approach combining F_{PFC} with coarse-grained Langevin dynamics provides an economical framework for modeling equilibruim and long-time nonequilibrium behaviors of realistic materials systems. Many potential extensions and applications remain to be explored, while the unresolved issues concerning how to rigorously justify the approximations involved and how to properly interpret and connect the parameters of the theory with known observables remain as longer-term challenges. A fuller understanding of the appropriate limits of the theory's validity will require continuing efforts along these lines.

The fundamental approximations inherent to PFC models are introduced during the static and dynamic coarse-graining procedures. As a result of the static coarse-graining, F_{PFC} is not exact. f_{id}^{PFC} is an approximation of the exact f_{id} and f_{exc}^{PFC} is an approximation of the approximate f_{exc}^{RY}. The dynamic coarse-graining which produces either Eq. (2.29) or Eq. (2.30) relies on the assumption of adiabatic relaxation dynamics. Furthermore, hydrodynamic interactions, which may be particularly relevant in colloidal systems, are ignored by the simple dynamic theories. To some degree, a functional validation of the PFC approach must be pursued, based on comparisons of PFC results with known results from more microscopic theories and experiments.

In the remaining chapters, various formulations of the PFC model are applied to problems concerning melting, plasticity, and solidification. It is hoped that the studies presented in the following chapters will help to both assess the capabilities and limitations of PFC models as well as provide insight into new physics within problems that are difficult to model with conventional approaches.

CHAPTER 3

Grain Boundary Melting and Premelting

Dislocation and grain boundary melting are studied in three dimensions using the phase-field crystal method. Isolated dislocations are found to melt radially outward from their core, as the localized excess elastic energy drives a power law divergence in the melt radius. Dislocations within low and intermediate angle grain boundaries melt similarly until an angle-dependent first order wetting transition occurs when neighboring melted regions coalesce. Analytic results employing linear elasticity are derived to describe this behavior from the low angle limit. High angle boundaries are treated within a screening approximation, and issues related to ensembles, metastability, and grain size are discussed.

3.1 Phenomenology and Literature

Freezing and melting transitions in general do not exhibit the degree of universality associated with continuous phase transitions and largely for this reason have eluded a unified theoretical description. The nature of a given melting transition may depend sensitively on the details of the system and experiment, and can involve many distinct processes both within and between multiple forms of excitations. For example, melting may occur abruptly and discontinuously at the melting temperature T_m, or it may initiate well below T_m at surfaces and/or internal defects and proceed up to T_m. This process of premelting has been studied extensively for surfaces [115, 116] and is relatively well understood, but limited and inconsistent experimental evidence for melting at dislocations and grain boundaries leaves a number of issues unresolved.

Premelting in the broadest sense is a process that occurs in periodic systems near a phase transition. Defects in the existing periodic phase act as nucleation sites for the new phase as the transition point is approached, initiating the transition locally before the bulk transition point is reached. The most common example of this process is that which occurs in crystalline materials near their melting temperature. As already described, defects such as vacancies, dislocations, and grain boundaries act as sites for premelting and may significantly affect the properties of the crystal and the melting transition. A slightly different example may be observed in the case of structural phase transitions. Defects in the initial crystal structure will again serve as nucleation sites, but in this case a second crystal structure will emerge rather than a liquid phase. Analogous behaviors are also exhibited, for example, during order/disorder transitions in Raleigh-Bernard convection, magnetic materials, and superconducting systems.

A recent study of colloidal crystals has verified that premelting does occur at vacancies, dislocations, and grain boundaries, and has provided measurements of the localized premelting behavior below T_m [2]. The conditions which determine whether premelting will occur continuously or discontinuously, and whether the width of the premelted region diverges are not fully understood. Grain boundaries in Al have been found to liquify very near T_m, and the width of the melted layer appears to diverge [117]. Discontinuous jumps in grain boundary diffusion coefficients [118, 119], mobility [120], and shear resistance [121] have been found in other metals.

Theoretical studies have been based on either explicitly atomistic methods such as molecular dynamics [122, 123] and Monte Carlo [124], or on continuum phase-field models with uniform phases [24, 125, 126]. Classical DFT has been used to examine surface melting [116, 127], but not grain boundary melting, presumably due to the complexity of the solid-solid interface and the more demanding system size requirements. In this study, dislocation and grain boundary melting are examined using the phase-field crystal (PFC) method [4], which extends the phase-field approach to the level of atomistic resolution and significantly economizes the DFT approach. This permits straightforward identification of stable equilibrium and metastable nonequilibrium atomic structures, while inherently including crystal symmetry and orientation, elasticity/plasticity, and the individual dislocations which compose the grain boundaries. The present description will be most applicable to spherical colloid-like systems and possibly some simple metals.

The melting behavior of dislocation pairs and symmetric tilt grain boundaries of angle $\theta \simeq 4^\circ$, 8°, 16°, 24°, 32°, and 44° are examined numerically for a simple PFC model with bcc symmetry. Analytic results are derived for isolated dislocations and low θ boundaries by combining the PFC equations with continuum linear elasticity. A screening approximation is outlined for high angle boundaries, though somewhat surprisingly, the low θ description is found to remain reasonably accurate for high θ.

3.2 Model Equations and Notation

The PFC free energy functional used in this study is written

$$F = \int d\vec{r} \left\{ \frac{n}{2} \left[r + (1+\nabla^2)^2 \right] n + \frac{n^4}{4} \right\} \tag{3.1}$$

where the relations between model parameters and material parameters as well as their scaling can be found in previous work [25]. Here $n \to n(\vec{r}) + \bar{n}$ is the scaled time-averaged number density, $\bar{n}$ is the average scaled number density, and r is a constant proportional to $T - T_c$. The dynamics are given in dimensionless form by

$$\frac{\partial n}{\partial t} = \nabla^2 \mu + \eta \tag{3.2}$$

where $\langle \eta(\vec{r}_1, t_1) \eta(\vec{r}_2, t_2) \rangle = M \nabla^2 \delta(\vec{r}_1 - \vec{r}_2) \delta(t_1 - t_2)$ and M is a constant proportional to T. This form imposes a constant density and is consistent with the canonical ensemble. The stochastic term η sets the time scale for crossing free energy barriers from dry to wet dislocation configurations locally when the wet state has lower free energy. It may also shift the 'equilibrium' melting behavior to some degree since increasing the fluctuation amplitude M can increase the preferred size of a dislocation core or premelt radius and effectively lower the melting temperature. A relatively small M has been used in the simulations presented here, to minimize the effect of noise on the free energy, yet still allow for barrier crossing.

The semi-implicit pseudospectral algorithm described in Appendix A.2 was used to solve Eq. (3.2) for systems containing either a single dislocation pair or a symmetric tilt grain boundary pair with periodic boundary conditions. The parameters most often used were $\bar{n} = -0.25$ and $M = 0.002$, with a grid spacing of $\Delta x = 0.976031$ and a time step of $\Delta t = 0.5$. These values were chosen because the model behavior has already been well-characterized at this set in previous studies. Effects observed as parameters vary are discussed in Sections 3.5 and 3.6. A system size $V = (512\Delta x)^3 = (56a)^3$ was used for the dislocation pair and 4° grain boundary pair, while $V = (256\Delta x)^3 = (28a)^3$ was used for all other grain boundary pairs, where $a = 8.9237$ is the bcc lattice constant. Finite size effects increase as θ decreases, but were found to be small for all grain boundaries studied. The temperature is taken to be proportional to r since the coefficient of the 2nd order term in F has leading temperature dependence and controls proximity to the critical point at $(r, \bar{n}) = 0$. For $\bar{n} \neq 0$ there is no critical point, and varying r instead passes the system through a first order liquid-solid transition at some melting point $r_m = f(\bar{n})$.

3.3 Simulation Results

To quantify the melting behavior at dislocation sites, the Gaussian width or mean square displacement (D) of each localized density peak was monitored as the temperature r was increased toward the melting point. The local crystallinity ϕ has been defined as

$$\phi(\vec{r}) = \frac{D_L - D(\vec{r})}{D_L - D_X} \tag{3.3}$$

where D_X is the equilibrium D of the crystal phase and D_L is that of the liquid phase for given M. $\phi = 1/2$ is taken to specify a liquid-solid interface.

The radius of melted region around a dislocation core R_m was first measured in this manner for an edge dislocation pair as the temperature was raised toward the bulk melting temperature r_m at which the liquid and crystal free energies coincide. The results are shown in Fig. 3.1, where the data are plotted as $(R_m + R_0)^{-2}$ vs. r to demonstrate that R_m is consistent with a $(r_m - r)^{-1/2}$ form which will be derived later. R_0 is an offset related to the finite size of the dislocation core at zero temperature. The fit to this form predicts a bulk melting temperature $r_m = -0.1407 \pm 0.003$ which

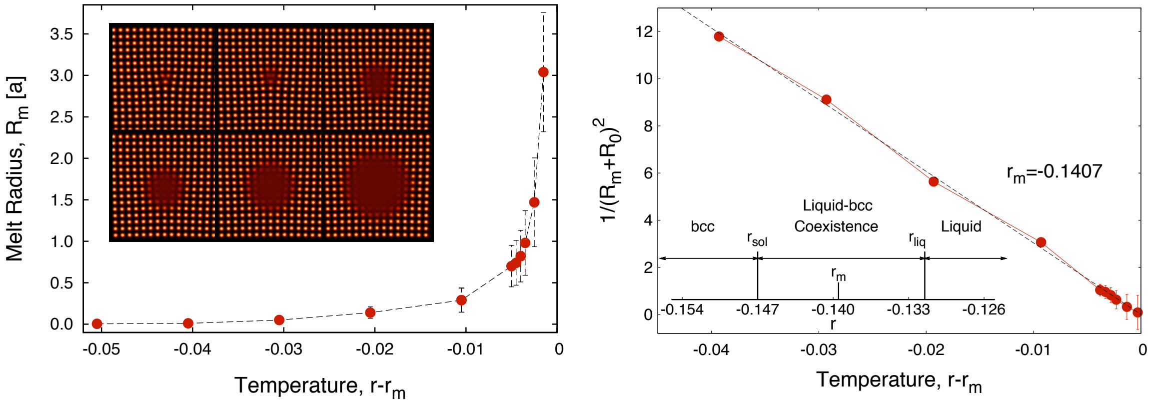

(a) (b)

Figure 3.1: (a) Numerically measured local melt radius R_m around an edge dislocation in a bcc crystal as a function of temperature (units of lattice constant a, $r < -0.1442$ values obtained by extrapolation of $\phi(\vec{r})$). Inset: cross-sectional images of $n(x, y, z)$ from simulations at r = -0.15, -0.144, -0.143, -0.142, -0.1415, -0.141 from top left to bottom right, showing melting at a dislocation core. (b) Same data plotted as $1/(R_m + R_0)^2$. $R_0 = 0.2812a$ is the radius at r = -0.1875, determined by best fit.

is in good agreement with the directly measured value of $r_m = -0.1395$. The upper inset of Fig. 3.1 shows melting around an edge dislocation as $r \rightarrow r_m$.

Measurements of the radially and laterally averaged D due to dislocations and grain boundaries, respectively, are in qualitative agreement with those of Alsayed *et al.* [2] for colloidal crystals. We find that the decay can be fit adequately by either power law or exponential forms, with greater exponential character at large θ and greater power law character at small θ. The radially averaged D for isolated dislocation pairs at various temperatures are shown in Fig. 3.2, the laterally averaged free energies for various grain boundary angles are shown in Fig. 3.3, along with the laterally averaged D for a 44° grain boundary at various temperatures.

Figure 3.4 shows the progression of melting at 8° and 44° grain boundaries. Low angle boundaries were found to first melt radially at each dislocation core, until the melted regions of neighboring dislocations coalesce and a uniform wetting layer is formed along the boundary. In high angle boundaries individual dislocations cannot be distinguished and melting in this case was found to proceed by uniform disordering along the boundary rather than by local radial melting. Similar behaviors are shown

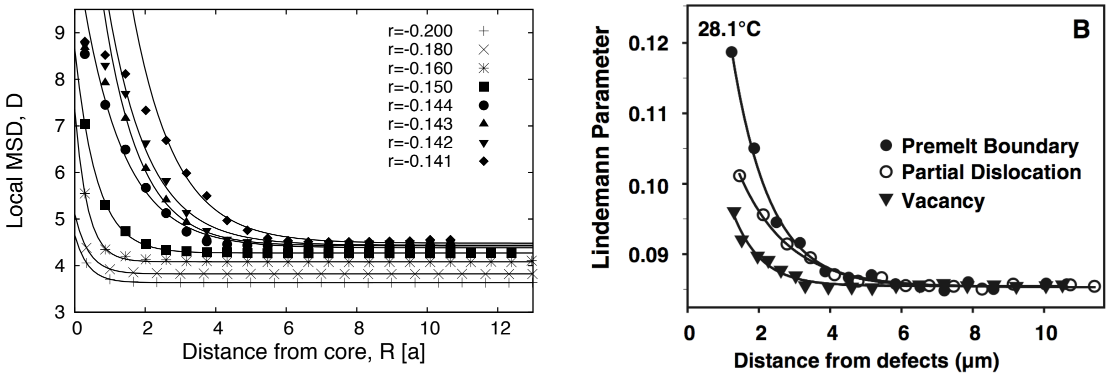

(a) (b)

Figure 3.2: (a) Measured D as a function of distance from the core of a bcc edge dislocation at various values of r. The lines are exponential fits. (b) Experimental data from [2] for partial dislocations, vacancies, and grain boundaries.

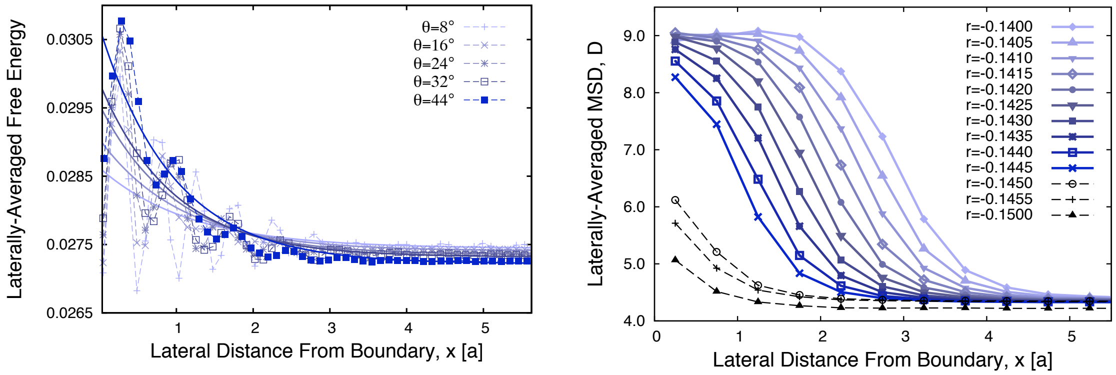

(a) (b)

Figure 3.3: (a) Measurements of the laterally-averaged F away from grain boundaries of various θ at $r = -0.1450$. The solid lines are exponential fits. (b) Measurements of the laterally-averaged D away from a 44° grain boundary as the melting temperature is approached. The notable change in behavior between $r = -0.1450$ and $r = -0.1445$ marks a wetting transition where the metastable dry boundary is replaced by an energetically preferred wet boundary.

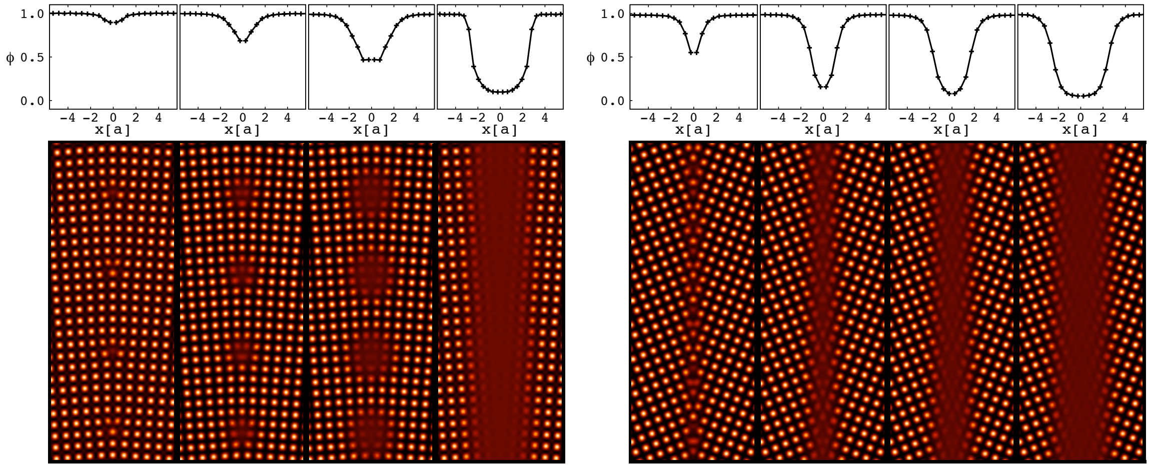

(a) (b)

Figure 3.4: Laterally averaged crystallinity parameter ϕ and cross-sections of $n(x, y, z)$ for (a) 8° and (b) 44° (right) grain boundaries. r = -0.15, -0.142, -0.1415, -0.141 and r = -0.1455, -0.14475, -0.1435, -0.1415 left to right, respectively.

in Fig. 3.5, where the three dimensional most probable instantaneous configurations are displayed for 12° and 44° grain boundaries. Note that Fig. 3.5(a) shows a time sequence during melting after the temperature is raised above the melting point, while Fig. 3.5(b) shows stable configurations at various temperatures as the melting point is approached from below. Interfacial roughening due to thermal fluctuations was negligible in all simulations.

The dependence of the width of the wetting layer (or the liquid volume fraction of the system) on r is shown in the inset of Fig. 3.6 for various grain boundary angles. In all cases the width remains narrow and the boundary relatively dry until above the solidus, at which point a discontinuous jump is observed at some characteristic wetting temperature r_{wet}. The dependence of r_{wet} on θ is shown in the main plot of Fig. 3.6. The fit lines will be discussed in the following, though the axes reveal that the predicted form will be $r_{wet} \sim \sin^2\theta$.

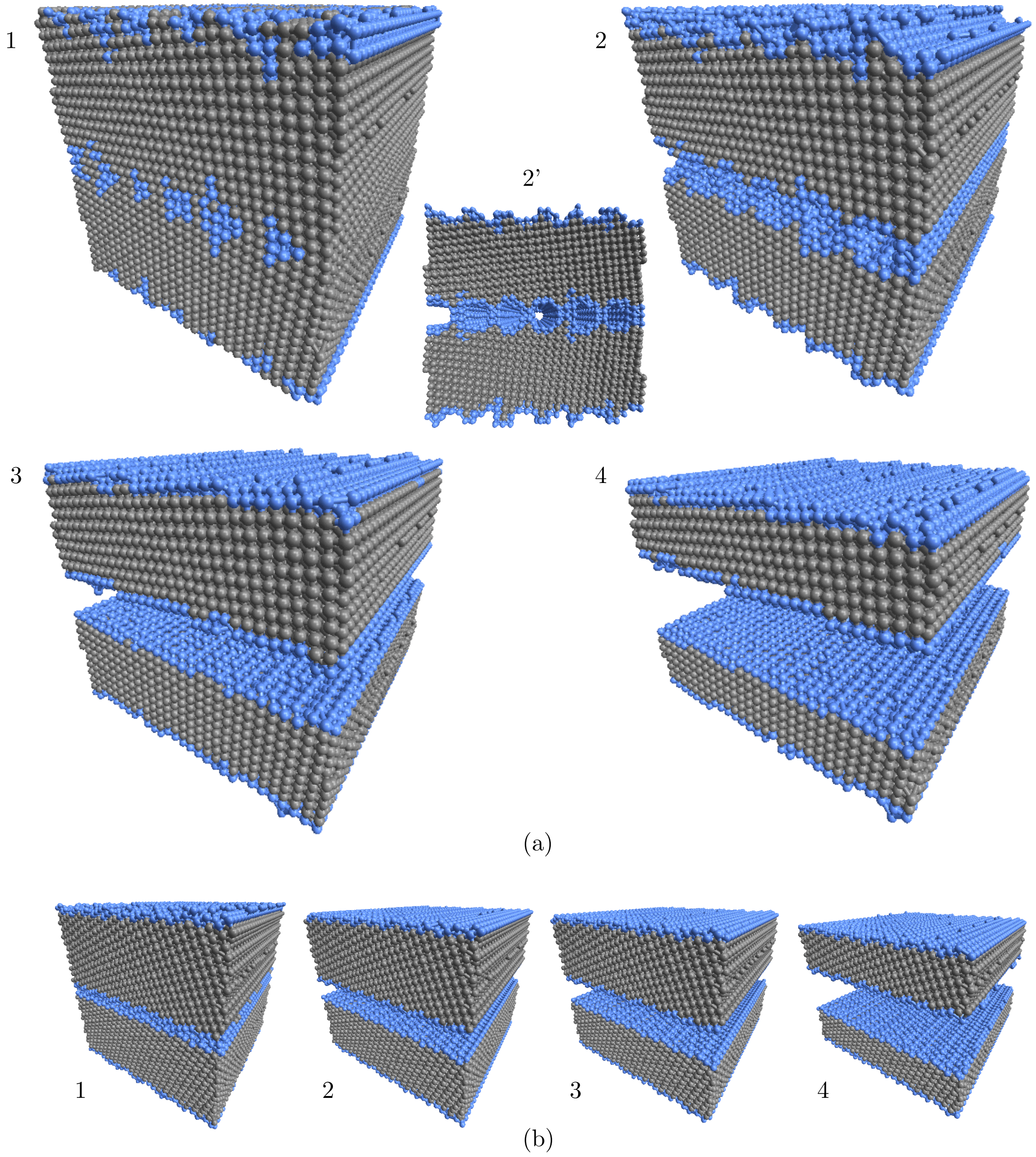

Figure 3.5: (a) Most probable instantaneous structures of a crystal with two 12° grain boundaries as melting progresses at $r = -0.13$. 1) $t = 0$, 2) $t = 90$, 3) $t = 120$, 4) $t = 150$. Bulk atoms are shown in gray, atoms without correct bcc coordination in blue, and empty space between the grains represents liquid. (b) As (a), with 44° grain boundaries shown as the melting temperature, $r_m = -0.1395$, is approached. 1) $r = -0.145$, 2) $r = -0.144$, 3) $r = -0.143$, 4) $r = -0.14$.

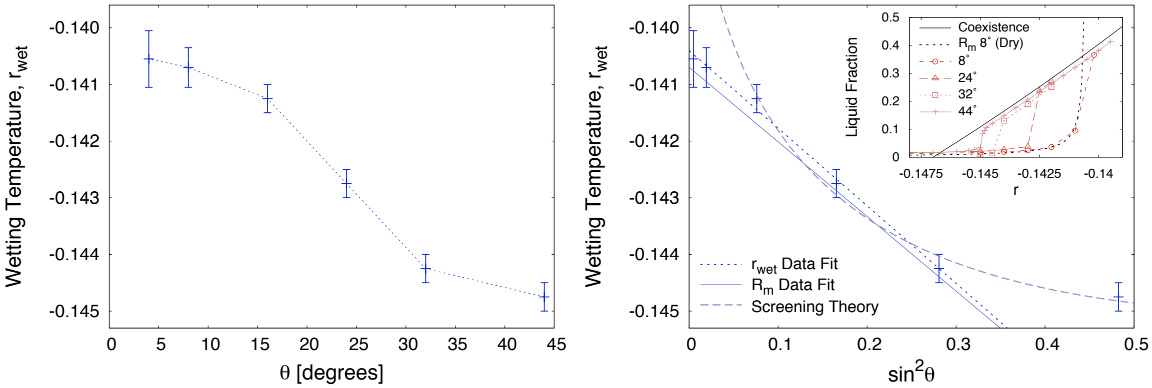

(a)

(b)

Figure 3.6: (a) Grain boundary wetting temperature vs. θ. (b) Grain boundary wetting temperature vs. $\sin^2\theta$. Inset: liquid volume fraction vs. r for various grain boundaries. The dashed line corresponds to the liquid volume fraction predicted for the 8° boundary based on Eq. (3.9) only (ignoring coexistence). Fit lines are discussed in the text.

3.4 Local Melting Equations

Based on these simulation results, we have developed a theory of dislocation-driven melting, which is easily extended to low angle grain boundaries. The low angle results are shown to remain accurate for all but the highest θ where the dislocation spacing d reaches the order of the Burgers vector b. A screening approximation for the spatial grain boundary energy is found to be more applicable for very large θ, with a gradual crossover taking place between these two regimes. Our approach to low angle grain boundaries has similarities to the theory of Glicksman and Vold [128] for 'heterophase' dislocations.

3.4.1 Isolated dislocations

One way to analytically describe defects in a PFC system is to assume that the continuum elastic expressions for the strain fields created by a given defect are reproduced by the PFC model. Then the spatial elastic free energy can in principle be calculated by inserting the continuum expressions into the PFC free energy and minimizing with respect to A and q. Such a calculation is bypassed here by assuming instead that the continuum elastic expression for dislocation free energy holds, and superimposing this result directly onto the PFC free energy. Simulation results indicate that the spatial elastic free energies of PFC dislocations are qualitatively similar to those of continuum theory.

The elastic energy density, $\bar{F}^s_{el}$ around a dislocation core is now approximated using continuum elasticity theory [96]. For a screw dislocation the stress σ^s_{ij} and strain u^s_{ij} tensors are given by

$$u^s_{ij} = \begin{pmatrix} 0 & 0 & -\frac{b}{4\pi}\frac{\sin\phi}{R} \\ 0 & 0 & \frac{b}{4\pi}\frac{\cos\phi}{R} \\ -\frac{b}{4\pi}\frac{\sin\phi}{R} & \frac{b}{4\pi}\frac{\cos\phi}{R} & 0 \end{pmatrix} \tag{3.4a}$$

$$\sigma^s_{ij} = 2\mu u^s_{ij} \tag{3.4b}$$

where $u_{ij} = 1/2\left(\nabla_i u_j + \nabla_j u_i\right)$ is the strain tensor in direction i across a surface oriented in direction j, u_i is the displacement vector in the i direction, μ is the shear modulus of the medium, ϕ is the angle in the x-y plane for a dislocation line in the z-direction, and R is the radial distance in the x-y plane from the core. Superscripts s and e denote screw and edge dislocations, respectively. Eq. (3.4b) holds since a screw dislocation produces only shear stress. The elastic energy density for a screw dislocation is then

$$\bar{F}^s_{el}(R) = \frac{1}{2}\sigma^s_{ij}u^s_{ij} = \frac{\mu b^2}{8\pi^2 R^2}. \tag{3.5}$$

Similarly for an edge dislocation,

$$\bar{F}^e_{el}(R) = \bar{F}^s_{el}(R)/(1-\sigma) \tag{3.6}$$

where σ is the Poisson's ratio.

If we assume this result to hold for an isolated dislocation in the PFC model, at distances approaching the core region, then R_m can be calculated by determining the distance at which $\bar{F}_{el}$ is sufficiently large to destabilize the crystalline phase and melt the dislocation core (Fig. 3.7). To complete this calculation, we need an expres-

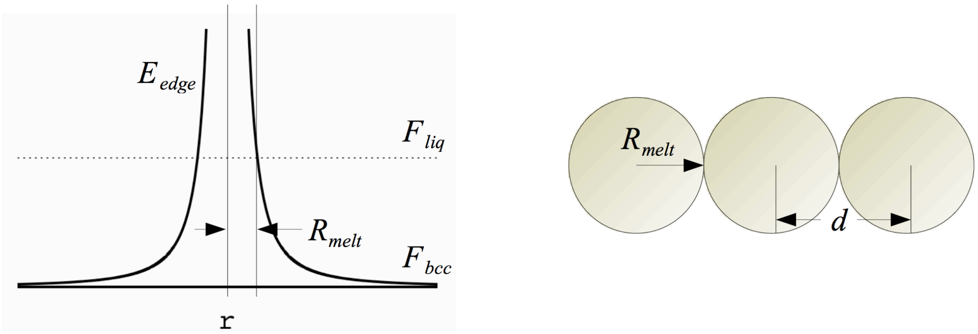

(a) (b)

Figure 3.7: (a) Schematic of spatial dislocation energy illustrating how R_m is estimated. (b) Schematic of liquid coalesence in a low angle grain boundary, the condition which defines when complete wetting occurs.

sion for the free energy of the defect-free crystalline PFC phase, upon which we will superimpose the above local expression for dislocation energy.

It will be assumed that $n(\vec{r})$ can be represented in a one mode approximation for a bcc lattice, i.e., $n(\vec{r}) = A\left(\cos qx \cos qy + \cos qx \cos qz + \cos qy \cos qz\right) + \bar{n}$. Substituting this n into Eq. (3.1) and minimizing with respect to q gives,

$$\Delta f^X = \frac{3}{8}\left(r + 3\bar{n}^2\right) A^2 + \frac{3}{4}\bar{n}A^3 + \frac{135}{256}A^4 \tag{3.7}$$

where $\Delta f^X \equiv (F - F_L)/V$, F_L is the free energy of the liquid, $V = (2\pi/q_{eq})^3$, and $q_{eq} = \sqrt{2}/2$. The continuum elastic result for $\bar{F}_{el}(R)$ assumes an isotropic medium, a condition which is not satisfied for bcc symmetry. To proceed, the isotropic shear modulus μ will be approximated using the average of the two bcc shear moduli reported in Chapter 2, $\bar{\mu} \simeq (\mu' + \mu'')/2 = 3A^2/16$. μ' and μ'' represent upper and lower bounds on bcc shear response, and the ratio $\mu''/\mu' = 2$ gives an indication of the expected deviation from the isotropic limit in which $\mu' = \mu''$.

The equilibrium value of A under uniform strain varies with the magnitude of the strain, indicating that A will vary locally near a dislocation core. Ignoring this generally secondary effect, the (dimensionless) free energy density of the system with a dislocation, $\Delta f^X + \bar{F}_{el}$, can be written

$$\Delta f = \frac{3}{8}\left(r + \frac{E}{\bar{R}^2} + 3\bar{n}^2\right) A^2 + \frac{3}{4}\bar{n}A^3 + \frac{135}{256}A^4 \tag{3.8}$$

where $E^s \equiv 1/(16\pi^2)$ and $E^e \equiv E^s/(1-\sigma)$ for screw and edge dislocations, respectively, and $\bar{R} \equiv R/b$. Equation (3.8) indicates that the elastic energy 'shifts' the effective temperature r by an amount $E/\bar{R}^2$. The implication is that the liquid-solid transition is shifted and instead of occurring globally at $r = r_m$ occurs locally when $r + E/\bar{R}_m^2 \simeq r_m$. The resulting liquid-solid interfacial energy will suppress local melting, but to maintain a simple description, we proceed in the limit of vanishing surface tension to derive upper bounds on the local melting behavior. The bare melt radius is then

$$\bar{R}_m = \sqrt{E/(r_m - r)} \tag{3.9}$$

or $1/\bar{R}_m^2 = (r_m - r)/E$. A more detailed analysis considering the global F condition for melting, rather than this local condition, gives essentially the same result in the limit of zero liquid-solid surface tension.

As shown in Fig. 3.1, this form is consistent with the simulation results for edge dislocation pairs, though the predicted slope $(-1/E^e)$ is smaller in magnitude by a factor of roughly two. A more definitive test would require additional data very near r_m, a region increasingly difficult to access due to system size requirements. The primary source of error in the slope is likely to be overestimation of the strain energy very near the core or premelt radius in the linear elastic approximation, which directly reduces the magnitude of the slope $-1/E^e$. Additional strain energy, independent of the dislocation energy, may also be generated if the cylinder of liquid and the surrounding crystalline matrix have differing densities, an effect neglected in our calculations. This Eshelby strain energy varies as $1/R^2$ and can therefore be absorbed into the prefactor E, though our findings suggest that its contribution is relatively small.

3.4.2 Low angle boundaries

We would now like to describe the melting behavior at low angle grain boundaries by straightforwardly extending the above approach to isolated dislocations, which combines the equations of continuum linear elasticity with PFC free energies. This approach exploits the fact that an isolated dislocation is simply the $d \to \infty$ or $\theta \to 0$ limit of a grain boundary. Such a linear elastic description of grain boundaries therefore rests on the assumption that the stress and strain fields of an isolated dislocation are maintained when that dislocation is part of a larger array, and that these fields can be straightforwardly summed over all dislocations to give the overall stresses and strains. This approach has been successfully applied to the calculation of average energies of low angle grain boundaries [3, 4, 129]. In the following, we first verify the validity of this approach near dislocation cores, the region of interest for premelting, and then proceed to derive an expression for low angle grain boundary wetting and compare with simulation results.

Consider a low angle grain boundary in two-dimensions or a symmetric tilt boundary in three-dimensions, consisting of a periodic array of dislocation lines. The long-range stress and strain fields of the individual edge dislocations aligned parallel to the z axis in the yz plane are given by

$$\sigma_{xy}^{GB}(x,y) = \frac{2\mu b\pi x}{d^2}\sum_{q=1}^{\infty} q\cos\left(\frac{2\pi qy}{d}\right)e^{-2\pi q|x|/d} \tag{3.10a}$$

$$u_{xy}^{GB}(x,y) = \frac{b\pi x}{d^2}\sum_{q=1}^{\infty} q\cos\left(\frac{2\pi qy}{d}\right)e^{-2\pi q|x|/d} \tag{3.10b}$$

where x is the distance from the grain boundary and d is the distance between dislocations. Thus the elastic shear energy, $F_{xy}^{GB} = \sigma_{xy}^{GB}u_{xy}^{GB}/2$ is given by,

$$F_{xy}^{GB}(x,y) = \frac{\mu(b\pi x)^2}{d^4}\sum_{q=1}^{\infty}\sum_{q'=1}^{\infty} qq' e^{-2\pi(q+q')|x|/d}\cos\left(\frac{2\pi qy}{d}\right)\cos\left(\frac{2\pi q'y}{d}\right). \tag{3.11}$$

This equation does not lead to a simple analytic solution for the elastic energy, but a few points are apparent in the limits of large and small distances from the boundary. For $x > d/2$, the $k = 1$ term dominates the sum, indicating that stresses beyond this point will decay exponentially and stresses beyond $x \simeq d$ will be negligible. Near the core, the energy will be dominated by nearby dislocations, meaning that a simple sum of the stresses and strains of the nearest few dislocations will give an accurate

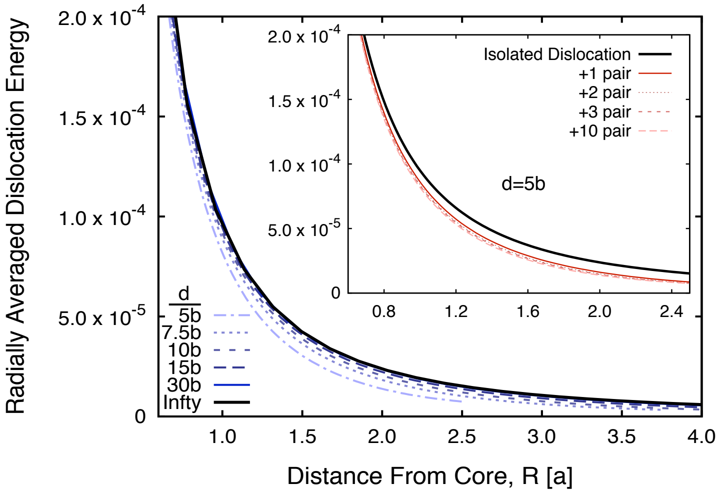

Figure 3.8: Radially averaged elastic energy in the premelting region of a dislocation located within a low angle grain boundary, shown for various dislocation spacings d. In this figure, the 20 nearest dislocations have been considered in the energy calculation. Inset: Radially averaged elastic energy in the premelting region of a central dislocation for increasingly large dislocation arrays. $d = 5b$ to observe the maximum effect from nearby dislocations.

approximation of the energy in this region. This is illustrated in the inset of Fig. 3.8 where the change in *total* radial elastic energy is shown as more dislocations in the array are considered. The change will be greatest for small d so a near-worst-case of $d = 5b$ is shown. The total energy in the premelting region changes only slightly from that of an isolated dislocation, and only $1 - 2$ additional pairs of dislocations are needed to accurately determine the modified energy.

Having verified this, the change in energy near the core can be studied as a function of dislocation spacing d. Figure 3.8 shows the radial elastic energy for various d, indicating that the energy near the core decreases only slightly with dislocation spacing. The decay acquires a slight exponential character (Eq. (3.11)) but changes in magnitude by only a few percent in the region of interest. Closer spacing results in greater stress cancellation, so that the energy per dislocation decreases while the energy per unit length of grain boundary still increases as expected. Thus linear elasticity predicts only a small decrease in the premelt region elastic energy for grain boundary angles $\theta \lesssim 5 - 10°$. One may therefore reasonably expect the melting behavior of dislocations within low angle grain boundaries to be well approximated by the isolated dislocation limit.

Exploiting this expectation, we can proceed to estimate the grain boundary wetting temperature r_{wet} where neighboring dislocations coalesce in low angle boundaries by setting $\bar{R}_m = d/2 = 1/(2\sin\theta)$. Substituting Eq. (3.9) for $\bar{R}_m$ gives

$$r_{wet} = r_m - 4E\sin^2\theta \tag{3.12}$$

which is in good agreement with the data shown in Fig. 3.6. As $\theta \to \theta_{max}$ this approximation loses validity due to the gradual deviation of the dislocation energies from the isolated dislocation result. The observed agreement up to $\theta \simeq 32°$ is somewhat unexpected as the superposition generally loses accuracy for $\theta \gtrsim 10°$. The best fit line predicts $r_m = -0.1404$, again near the measured value.

The solid line in Fig. 3.6 corresponds to the best fit to $\bar{R}_m$ in Fig. 3.1 set equal to $1/(2\sin\theta)$ and solved for r_{wet}. The agreement here clearly indicates that the wetting of low angle and intermediate angle grain boundaries is accurately described by the coalesence of radially melted regions around nearly isolated dislocations.

3.4.3 High angle boundaries

In the limit of large θ ($d \to 0$), the grain boundary energy becomes increasingly uniform along its length (see Fig. 3.4) and can no longer be described linearly in terms of individual dislocations. We expect that elastic fields at long distances are screened by closely spaced 'dislocations', giving rise to exponentially decaying spatial grain boundary energy. Indeed, direct analysis of free energy data from simulations indicates that such an exponential form is qualitatively correct. Solving for r_{wet} using

$$\bar{F}_{el} \sim \mathrm{e}^{-\bar{R}/\ell(\theta)}/\bar{R}^2 \tag{3.13}$$

rather than $\bar{F}_{el} \sim 1/\bar{R}^2$ gives

$$r_m - r_{wet} \sim \mathrm{e}^{-(2\ell(\theta)\sin\theta)^{-1}}\sin^2\theta, \tag{3.14}$$

where the coefficient $\ell(\theta)$ sets the effective screening length. To lowest order in a one-dimensional dislocation density approximation, $\ell(\theta)$ is proportional to $d^{3/2} = 1/\sin^{3/2}\theta$. The wide dashed line in Fig. 3.6 shows that a fit to this general form more accurately captures the behavior for large θ, though a less approximate expression for $\ell(\theta)$ is needed to fit accurately across all angles.

3.5 Coexistence and the Canonical Ensemble

Some comments concerning the influence of liquid-solid coexistence and the canonical ensemble (i.e., conserved density) on grain boundary melting may be helpful at this point. The equilibrium state for a simple system with a grain boundary is most generally either dry if $F_{gb} < 2F_{ls} + \ell(\bar{F}_L - \bar{F}_X)$ or wet if $F_{gb} > 2F_{ls} + \ell(\bar{F}_L - \bar{F}_X)$, where F_{gb} is the grain boundary energy, F_{ls} is the energy of a liquid-solid interface, and ℓ is the width of the liquid region in the wet state. If the wet state becomes favorable below the melting temperature, then a grain boundary wetting transition occurs. In the canonical ensemble as examined here, the effects of liquid-solid coexistence and the subsequent shifts in density of the two phases above the solidus r_{sol} modify this heuristic argument. Now r_m, the temperature at which $\bar{F}_L = \bar{F}_X$, is straddled by a coexistence region. As $r \to r_m$ the system first encounters a solidus above which some volume fraction of liquid will minimize the overall $\bar{F}$ in the thermodynamic limit. For the grain boundary pair geometry, the equilibrium state above r_{sol} is one with a uniform volume of liquid occupying each boundary region. Therefore, an equilibrium first order wetting transition will occur at r_{sol} as long as the grain size is not excessively small. Above r_{sol}, the liquid layer width will be controlled by coexistence rather than local defect energies, since the elastic fields of the grains largely decouple ($\bar{F}_{el} \to 0$) upon wetting.

The results presented for $\bar{n} = -0.25$ show no wetting or strong premelting for $r \leq r_{sol}$, and the equilibrium wetting transition is not observed. Instead, a θ-dependent discontinuous transition from the metastable dry boundary state to the equilibrium wet state occurs at $r_{sol} < r_{wet} < r_m$, as shown in the inset of Fig. 3.6. For large θ this metastability occurs because the uniform wetted state is simply not nucleated in observable times, due to a non-zero free energy barrier (and possible small finite

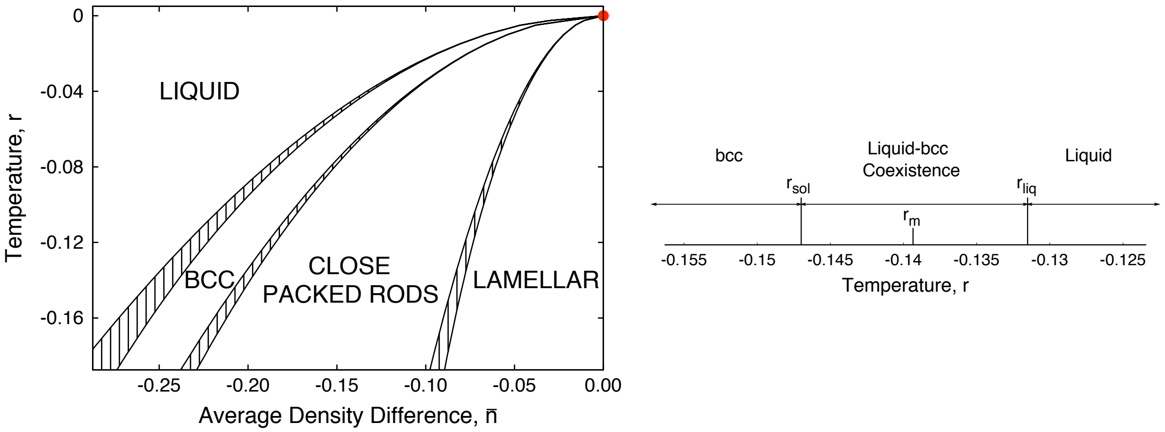

(a) (b)

Figure 3.9: (a) PFC phase diagram in the $(r, \bar{n})$ plane in three dimensions. Hatched areas designate coexistence regions, the red dot denotes the critical point. (b) Slice of the phase diagram at simulated value $\bar{n} = -0.25$ showing location of coexistence bounds and r_m.

size effects). For small θ, when d/R_m is large, a uniform wetting layer cannot be realized, so the system must absorb the free energy cost of many localized cylindrical liquid-solid interfaces. This suppresses the observed liquid volume fraction until R_m finally grows sufficiently large to coalesce and a uniform wetting layer can be formed. Thus in all cases, the dislocations and/or grain boundaries act as nucleation sites for the liquid above r_{sol}, creating well-defined nonequilibrium paths from the metastable dry state to the F minimizing wet state (which all must conserve n). But the effective energy barrier between wet and dry boundaries is largest for small θ, exaggerating small θ metastability.

We can gain some sense of whether wetting will occur below the solidus (canonical premelting or prewetting) by comparing the predicted value of R_m for an isolated dislocation at r_{sol} to that required for coalescence and wetting with a given grain boundary angle, $R_{\text{coalesce}}(\theta)$;

$$R_m(r_{sol}) = R_{\text{coalesce}}(\theta) \tag{3.15}$$

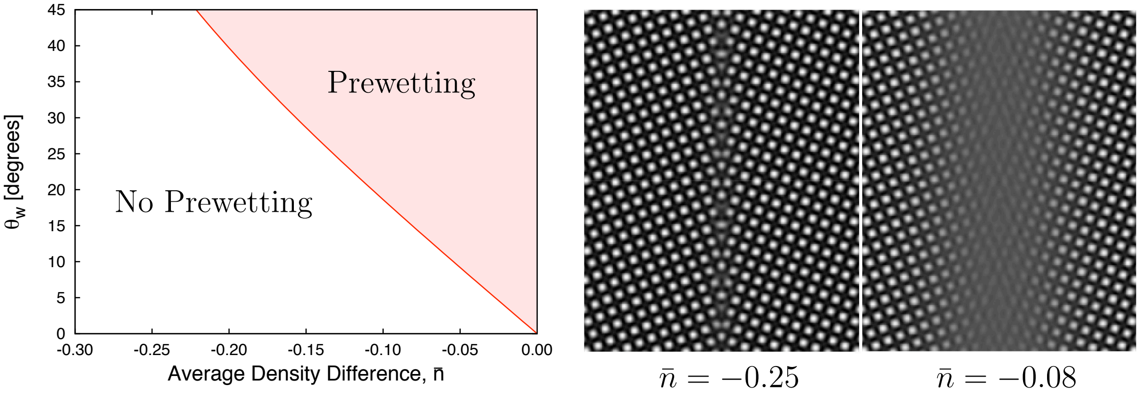

(a) (b)

Figure 3.10: (a) Condition for wetting below the solidus in the canonical ensemble (canonical prewetting), estimated from the low angle limit. (b) Dry 44.8° grain boundary at $r = r_{sol}$, $\bar{n} = -0.25$, and prewetted 44.8° grain boundary at $r = r_{sol}$, $\bar{n} = -0.08$.

or

$$\sqrt{\frac{E}{r_m - r_{sol}}} = \frac{1}{2\sin(\theta_w)}. \tag{3.16}$$

In the one-mode approximation, $r_m \simeq c_m \bar{n}^2$ and $r_{sol} \simeq c_{sol}\bar{n}^2$ where c_m and c_{sol} are constants. Substituting these expressions and solving for θ_w gives

$$\theta_w = \sin^{-1}\sqrt{\frac{c_m - c_{sol}}{4E}\bar{n}^2}. \tag{3.17}$$

Thus for any fixed average density it is expected that canonical prewetting will occur only above the critical grain boundary angle θ_w. If $\theta_w > \theta_{max}$, then no prewetting is expected. This behavior can be mapped out as a prewetting phase diagram in (θ, $\bar{n}$) space, as shown in Fig. 3.10. This result will be most applicable in the small thermal noise limit and as before will likely lose accuracy for large θ, but should serve as a rough guide.

Equation (3.17), as shown in Fig. 3.10, indicates that the likelihood of prewetting increases as the critical point at $\bar{n} = 0$ is approached, or equivalently as the liquid-solid transition shifts from strongly first order to weakly first order. For example, at $\bar{n} = -0.25$ all grain boundaries should remain dry up to the solidus temperature, while at $\bar{n} = -0.08$ all grain boundaries with $\theta \gtrsim 15°$ are expected to undergo a prewetting transition below the solidus temperature. The images of dry and wet 44.8° solidus grain boundaries at $\bar{n} = -0.25$ and $\bar{n} = -0.08$, respectively, shown in Fig. 3.10 are consistent with this prediction. Thus for $\bar{n} \lesssim -0.22$ we expect a sharp transition from nonequilibrium dry boundaries to coexistence satisfying wet boundaries at some θ dependent temperature above the solidus - as seen in the simulations discussed in the previous sections. For $\bar{n} \gtrsim -0.22$ we expect to see a weak, possibly truncated divergence in the boundary premelt width below the solidus, followed by adjustment to coexistence satisfying widths above the solidus.

The condition for wetting in the canonical ensemble also involves the grain size L_g, such that wetting can be suppressed to temperatures above r_{sol} when L_g is finite. The condition can be written as $F_{gb}+L_g\Delta F_X > 2F_{ls}+\ell\Delta F_C$ where $\Delta F_X = \bar{F}_X[\bar{n}]-\bar{F}_X[n_X]$ and $\Delta F_C = \bar{F}_L[n_L]-\bar{F}_X[n_X]$. Here $\ell = (n_X-\bar{n})/(n_X-n_L)$, $\bar{n}$ is the conserved average density, and n_X and n_L are the shifted coexistence densities of the solid and liquid phases, respectively. For $r \leq r_{sol}$, if we assume that $\Delta F_X = 0$ and $n_L = n_X = \bar{n}$ (this is not the case when premelting is strong below r_{sol}), we recover the original inequality $F_{gb} > 2F_{ls} + \ell(\bar{F}_L - \bar{F}_X)$ and L_g is not a significant factor. In the limit $L_g \to \infty$, the wetting condition will always be satisfied for $r > r_{sol}$ and the equilibrium transition occurs at r_{sol}. As L_g decreases, the equilibrium wetting transition is shifted to higher r.

3.6 Grand Canonical Ensemble

Three-dimensional simulations have also been conducted in the grand canonical ensemble, i.e., nonconserved density, where the complications due to liquid-solid coexistence are avoided. In this scenario the dynamics are given by

$$\frac{\partial n}{\partial t} = -\left(\frac{\delta F}{\delta n} + \mu_0\right) + \nu \tag{3.18}$$

where $\langle \nu(\vec{r}_1, t_1)\nu(\vec{r}_2, t_2)\rangle = M\delta(\vec{r}_1 - \vec{r}_2)\delta(t_1 - t_2)$. As the average chemical potential μ_0 is increased, rather than temperature, we find in general for the parameter values chosen that the 'equilibrium' behavior for fixed grain boundaries of all angles is to remain essentially dry up to the melting point μ_0^*, above which the free energy is minimized by complete melting of the solid. This corresponds to a very weakly increasing grain boundary width and discontinuous melting at μ_0^*. The energy barrier to melt the crystal is sufficiently large that considerable superheating is instead observed in the simulations.

The melting behavior at grain boundaries is also influenced by whether the equilibrium bulk melting transition is weakly or strongly first order. For large $|\bar{n}|$ the bulk melting transition is strongly first order and the energy of a liquid-solid interface is prohibitively large to allow any boundary wetting below μ_0^*. Thus the grain boundary melting transition is also strongly discontinuous. As $\bar{n} \to 0$ the bulk transition becomes more weakly first order, both the grain boundary and the liquid-solid interface become increasingly diffuse or ‘soft’ as shown in Fig. 3.11. This allows greater growth in the width of the grain boundary and potentially a weak divergence in width very near μ_0^* before complete melting occurs. Thus, a more weakly discontinuous grain boundary melting transition is observed. This diverging width for small $|\bar{n}|$ may reflect increasing delocalization of the ‘soft’ solid phase rather than the emergence of a fully liquid layer.

It is also apparent from the simulations that many states from dry to varying degrees of wet become metastable for long times near μ_0^*, such as those shown in Fig. 3.11. The states obtained near the melting point may therefore depend on the initial state of the system and the waiting time and may not correspond to the state of lowest free energy. In our simulations, the dry states were found to have lowest free energy up to μ_0^* for all parameter values examined.

We can still quantify the growing width w of a grain boundary, especially for weakly first order systems, regardless of whether the boundary interior can clearly be considered liquid. Such data is shown in Fig. 3.12 for a 44.8° boundary at $r = -0.02$. A weak divergence up to the transition point is apparent, and the form of the divergence is consistent with either a logarithmic form $w/b \sim \ln(\mu_0^* - \mu_0)$ or a power law form $w/b \sim (\mu_0^* - \mu_0)^{-\delta}$, where δ is a positive constant.

Premelting at grain boundaries has also been studied in the grand canonical ensemble by Mellenthin *et al* using the two-dimensional PFC model [72]. Their approach is to compute the effective ‘disjoining potential’ of prewetted grain boundaries as a

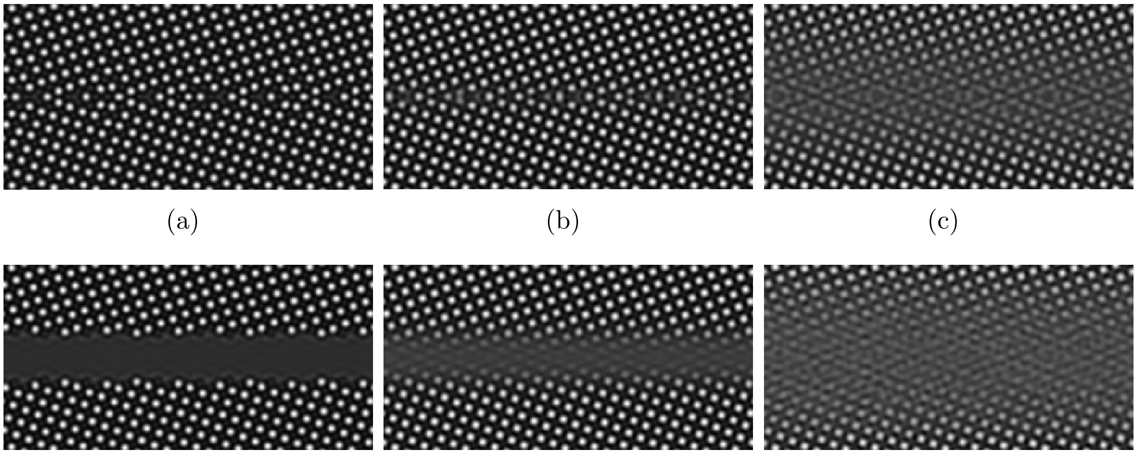

(a) (b) (c)

Figure 3.11: Cross-sections of the time-averaged number density field $n(x, y, z)$ for dry (top) and wet (bottom) 44° grain boundaries simulated with nonconserved density. The images illustrate the increase in boundary/interface diffuseness and loss of distinction between wet and dry states as the transition becomes more weakly first order. (a) $\bar{n} = -0.44$, $r = -0.50$, $\mu_0 = 0.17585$, (b) $\bar{n} = -0.25$, $r = -0.14$, $\mu_0 = 0.06339$, (c) $\bar{n} = -0.066$, $r = -0.01$, $\mu_0 = 0.01596$.

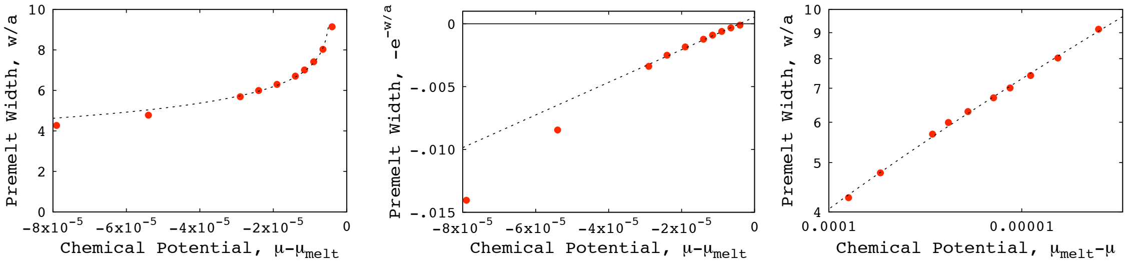

(a) (b) (c)

Figure 3.12: Premelting in the grand canonical ensemble at a 44.8° boundary, $r = -0.02$. (a) Raw data with a logarithmic fit. Tests of (b) logarithmic and (c) power law divergences, showing consistency with both.

function of premelt region width, to determine whether the effective interaction at the interface is repulsive (wet) or attractive (dry) as the melting point is approached. They find a similar weak logarithmic divergence for high angle boundaries and superheating with localized liquid pools for low angle boundaries. Grain boundaries above some critical angle are thus shown to have purely repulsive disjoining potentials for all premelt widths, while lower angle boundaries switch from repulsive at small widths to attractive at large widths, cutting off any divergence. The degree of premelting appears to be slightly enhanced in two dimensions, which may be due to proximity to the critical point ($r = -0.1$ in their study), purely dimensional effects, or some combination of the two. The disjoining potential approach provides a natural framework for high angle grain boundaries which wet uniformly, while the localized radial melting equations presented in this chapter provide a natural description of low angle boundaries with nonuniform melting pathways.

3.7 Conclusions

Three dimensional dislocation and grain boundary melting in PFC bcc crystals have been examined numerically and described in terms of local melting criteria. Isolated dislocations, driven by an excess core elastic energy, melt radially according to a power law in T. Dislocations within low and intermediate angle grain boundaries melt similarly until an angle-dependent first order wetting transition occurs when neighboring melted regions coalesce. A localized theory based on continuum elastic energy expressions for isolated dislocations has been developed in the low angle limit and shown to describe the simulation results for low and mid angle grain boundaries. High angle boundaries have been treated within an elastic screening approximation. Ensemble-specific effects have been discussed, and the different melting pathways to be expected in canonical and grand canonical ensembles highlighted. Premelting has been shown to be generally enhanced as the bulk melting transition becomes more weakly first order, and an approximate low-to-mid angle expression for the critical grain boundary prewetting angle has been derived.

CHAPTER 4

Dislocation Dynamics

The fundamental dislocation processes of glide, climb, and annihilation are studied on diffusive time scales using a two dimensional phase-field crystal (PFC) model. Glide and climb are examined for single edge dislocations subjected to shear and compressive strain, respectively, in a two dimensional triangular lattice. It is shown that the natural features of these processes are reproduced without any explicit consideration of elasticity theory or ad hoc construction of microscopic Peierls potentials. Particular attention is paid to the Peierls barrier for dislocation glide/climb and the ensuing dynamic behavior as functions of strain rate, temperature, and dislocation density. It is shown that the dynamics are accurately described by simple viscous motion equations for an overdamped point mass, where the dislocation mobility is the only adjustable parameter. The critical distance for the annihilation of two edge dislocations as a function of separation angle is also presented.

4.1 Phenomenology and Literature

Plastic flow in periodic systems is typically mediated by the motion of line defects or dislocations. The largest challenge in developing a meaningful theory of plasticity is often linking the microscopic behavior of individual, discrete dislocations to the macroscopic plastic behavior of the system. In atomic and molecular crystals for example, understanding the effect of dislocations on mesoscopic and macroscopic material properties involves the treatment of length and time scales that capture the relevant dynamics of individual dislocations ($\sim 10^{-12}s$,$\sim 10^{-9}m$) through those that describe the macroscopic response of the material ($\sim 10^{1}s$,$\sim 10^{-2}m$). An important approach to the problem of spanning this large range of scales has been to measure the dynamics of individual dislocations and/or small numbers of interacting dislocations on the shortest time scales from molecular dynamics (MD) simulations [130–133]. These results are then used as input into coarse-grained, mesoscopic simulations such as dislocation dynamics (DD) [26, 27], which can provide information on systems with large numbers of dislocations under the action of experimentally accessible strains and strain rates.

In this study, dislocation dynamics are examined on length scales comparable to those encountered in MD simulations, but over diffusive time scales and using experimentally accessible strain rates. This approach provides a single framework that removes the vibrational time scales, while large length scales can potentially be reached using complex amplitude multi-scale expansions of PFC models [35–42] and/or advanced simulation methods [38, 43–49]. In addition to atomic crystals, the results presented here may be interpreted in terms of other periodic systems such as Abrikosov vortex lattices in superconductors [134], magnetic thin films [135, 136], block copolymers [137], oil-water systems with surfactants [138], and colloidal crystals.

4.2 Model Equations and Notation

Some of the basic principles of PFC modeling were discussed in Chapter 2, where the dimensionless free energy functional was introduced,

$$F_{\text{PFC}}[n(\vec{r})] = \int d\vec{r} \left\{ \frac{n}{2} \left[r + (1+\nabla^2)^2 \right] n + \frac{n^4}{4} \right\} \tag{4.1}$$

$n \to n(\vec{r}) + \bar{n}$ is the scaled atomic number density order parameter, $\bar{n}$ is the scaled average number density, and r is a constant related to temperature. The dynamics of n are assumed here to be given by

$$\frac{\partial n}{\partial t} = \nabla^2 \mu + \eta \tag{4.2}$$

where η is a Gaussian random noise variable ($\langle \eta(\vec{r}_1, t_1)\eta(\vec{r}_2, t_2)\rangle = M\nabla^2\delta(\vec{r}_1 - \vec{r}_2)\delta(t_1 - t_2)$. M is a constant proportional to T, which will be largely neglected in this chapter, as will be discussed in Section 4.4.

The objective of this chapter is to uncover the dynamic behavior of dislocations as described by Eqs. (4.1) and (4.2) and to show that basic characteristics of the known dynamics are automatically and realistically reproduced. Rigorous connections between PFC models and traditional microscopic models such as molecular or Brownian dynamics are subjects of current research. That being noted, a few relevant points about the connections can be made on general grounds.

First, the geometry of a given periodic PFC structure ensures, for example, that any energy barriers arising from localized spatial variations in atomic position can be qualitatively represented by the PFC model. In principle this description provides rigorous methods for calculating various quantities associated with dislocation motion, such as saddle point and activation energies, for specific atomic models.

The connection between microscopic and PFC *dynamics* is a bit more difficult to access. The present PFC model maintains only the slow, diffusive part of the dynamics, averaging out collision and phonon time scales for example. This implies that any physical mechanisms that occur on fast time scales (such as brittle fracture) cannot be described by the PFC method. Methods for reintroducing faster time scales were discussed in Chapter 2, and plastic behaviors under such alternative dynamic conditions have since been examined by others [25, 47, 74, 76].

In Section 4.3, the details of how the PFC model is adapted to numerical simulation are outlined, and in Section 4.4 the simulation results for glide, climb, and annihilation are presented and analyzed. Section 4.5 includes a summary, comparison with other recent phase field simulations of dislocations, and discussion of further developments.

4.3 Simulation Method

4.3.1 Discretization, initial and boundary conditions

Equation (4.2) was solved numerically in two dimensions using the 'Spherical Laplacian' approximation for ∇^2 [139] and a forward Euler discretization for the time derivative (see Appendix A.1 for details). Periodic boundary conditions were applied in all directions for glide simulations and mirror boundary conditions were used perpendicular to the climb direction in climb simulations. To create a system with a single edge dislocation, an initial condition consisting of a triangular one-mode solution for $n(x, y)$ was applied with N atoms/row in the lower half and N+1 atoms/row in the upper half. The triangular state is expressed analytically as

$$n(x,y) = A\left[\cos(qx)\cos(\frac{qy}{\sqrt{3}}) + \frac{1}{2}\cos(\frac{2qy}{\sqrt{3}})\right] + \bar{n} \tag{4.3}$$

where

$$A = -\frac{4}{5}\left(\bar{n} + (|\bar{n}|/\bar{n})\frac{1}{3}\sqrt{-15r - 36\bar{n}^2}\right), \tag{4.4}$$

and q here is the numerically determined equilibrium wavenumber for a triangular state at a given value of r. In glide simulations, the triangular state was bounded at its upper and lower edges by a constant, or liquid, state of width approximately $4a_y$, where a_y is the equilibrium lattice parameter in the y-direction (Fig. 4.1). The same approach was used in climb simulations, except that the liquid was placed along the lateral boundaries. Before applying strain, all systems were allowed to equilibrate until their free energy no longer changed with time.

At a given value of r, the value of $\bar{n}$ for the triangular portion of the simulation was set to fall on the phase boundary between the triangular and triangular/constant coexistence regions. The value of $\bar{n}$ for the liquid portion of the simulation was set to fall on the boundary between the triangular/constant coexistence region and the constant phase region. This was necessary to make the interfaces between the triangular and constant phases stable, with no preference toward crystallization or melting. A drawback is that this makes any comparison of results at different r values indirect, since $\bar{n}$ must vary with r. For this reason the boundary conditions were changed when the r dependence of the dynamics was of interest. Details are discussed in the following section.

4.3.2 Strain application

Two methods were used to apply strain to the system. In both, $n(x, y)$ was coupled to an external field along the outer two rows of particles bounding the liquid phase on each side of the system. This external field was set to the one-mode solution given in

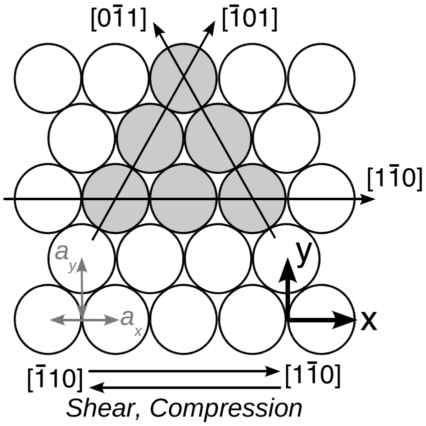

Figure 4.1: Schematic of (111) plane in a FCC crystal corresponding to the 2D system of interest.

Eq. (4.3), and for glide (climb) was moved in the positive x-direction along the lower (left) rows and in the negative x-direction along the upper (right) rows, both at the same constant velocity. The particles in the system are energetically motivated to follow the motion of these fields, giving the effect of a physically applied strain.

In the first method, which will be called rigid displacement, Eq. (4.2) was solved in the presence of the external fields, but in addition, the particles between the external fields were rigidly displaced along with the motion of the fields to ensure a linear strain profile across the width of the system. In the second method, this rigid displacement was not enforced, allowing the strain profile to take whichever form the dynamics of Eq. (4.2) dictate. This method will be called relaxational displacement. In Section 4.4, it will be shown that the dynamic behavior of the dislocations can be significantly influenced by which method is used and that the two methods may be viewed as limiting cases of rigid and diffusive response. From this viewpoint, rigid displacement describes atomic crystals and relaxational displacement applies to 'softer' systems such as colloidal crystals, superconducting vortex lattices, magnetic films, oil-water systems containing surfactants, and block copolymers.

4.3.3 Symmetries and time scales

The crystalline symmetry here is equivalent to the {111} family of planes in a FCC lattice or the {0001} family of planes in a HCP lattice, for example. These close packed planes and the subsequent glide directions compose the primary slip systems in many common types of ductile, metallic crystals. Using the FCC lattice as a reference, application of shear in this geometry results in glide along a $\langle 110\rangle$ direction within a $\{111\}$ slip plane, as shown in Fig. 4.1. The directions in a HCP lattice would fall in the $\langle 11\bar{2}0\rangle$ family. Climb in this geometry was made to occur along a $\langle\bar{1}\bar{1}2\rangle$ direction. Shear and compression were also applied over various other rotations as will be discussed briefly in the following.

System sizes ranging from 676 to 56,952 particles were examined, and strain rates ranging from $2{\times}10^{-7}/t$ to $1{\times}10^{-2}/t$ were used, where t is the dimensionless time introduced in Eq. (4.2). These strain rates can be expressed in physical units by matching the time scales of the model to those of typical metals near their respective melting temperatures. This is done by equating vacancy diffusion constants, D_v, which have been calculated analytically for this model in [4], and which range from $\sim 10^{-8}$–$10^{-13} cm^2/s$ for typical metals [140]. Lattice constants, a, must also be equated to return to physical units. Using Cu at 1063°C as a reference ($D_v \simeq 10^{-9} cm^2/s$, $a \simeq 0.361$nm), and matching to the model at $r = -0.8$ ($D_v = 1.78a^2/t$), the range of strain rates used converts to $.09/s$–$4500/s$. Using these same parameters, the dislocation velocities observed are on the order of 10^{-7}–$10^{-4} m/s$, a range well below the acoustic limit and accessible by experiment. The dislocation densities range from approximately 10^{10}–$10^{12}/cm^2$.

4.3.4 Simulation output: A preliminary example

Before presenting the analysis of all simulation data, the output from a single glide simulation will be presented to clarify various definitions and results that will be of importance in interpreting the data. The collective results from all simulations will be analyzed further in the following section.

Four primary types of output were generated in each simulation, from which all properties of interest were extracted. The variables are the instantaneous position and velocity of the dislocation, and the strain and change in free energy of the system, all recorded as functions of time as shown in Fig. 4.2. The gray lines represent theoretical results which will be presented in Section 4.4. Note that all figures in the following use dimensionless units, though some quantities will be labeled with units of a_x, a_y,

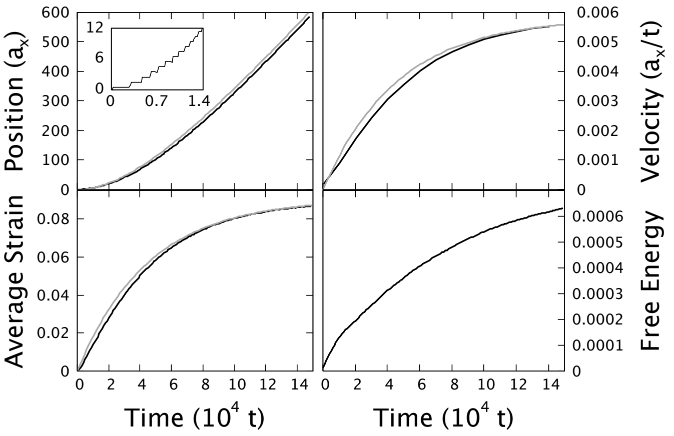

Figure 4.2: One set of simulation data (black lines) and the corresponding theoretical results (gray lines) for glide. Parameters are $r = -0.4$, (L_x, L_y)=(60,56), and $\dot{\gamma} = 2{\times}10^{-6}/t$ The inset in the upper left corner of the upper left plot shows a magnification of the position vs. time data at early times to emphasize the stick-slip nature of the motion at low velocities.

and t for clarity.

The position was determined by locating all maxima of $n(x, y)$ (which will be considered the discrete particle locations) and counting the number of nearest neighbors for each. Any maxima with more or less than six nearest neighbors must be near the dislocation core, and by averaging the positions of all maxima identified in this way, an overall dislocation position was inferred. The velocity was then calculated from the slope of the position versus time data.

The average shear strain in the system, $\bar{\gamma}$, was measured by again locating the peaks in $n(x, y)$, and noting that in equilibrium, each particle will have another particle located a distance of $2a_y$ away in the positive y-direction. If this particle is found to be offset some distance, dx_i, in the x-direction, then the local shear strain is equal to $dx_i/2a_y$. The average shear strain in the system is then given by

$$\bar{\gamma} = \frac{1}{2Na_y} \sum_{i=1}^{N} dx_i \tag{4.5}$$

where N is the number of particles in the system. The fourth variable, the average free energy F, was simply calculated from Eq. (4.1) at regular intervals of time.

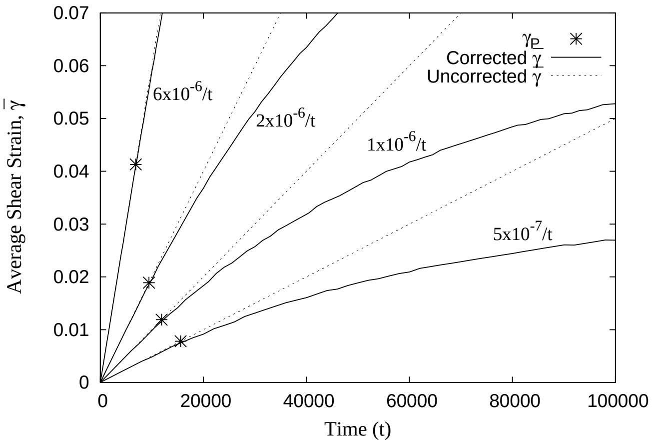

Figure 4.3: Corrected and uncorrected $\bar{\gamma}$ versus time at $r = -0.4$ and $(L_x, L_y) = (60, 56)$ for various values of $\dot{\gamma}$. The strain at which γ_P is defined has been highlighted on each curve.

The Peierls barrier is a measure of the resistance to the onset of motion in a periodic system. In these simulations, the barrier is defined as the amount of strain that has been applied at the instant that the dislocation has precessed a distance of one lattice constant. γ_P and ϵ_P will denote the Peierls barriers for glide and climb, respectively. For clarity, Fig. 4.3 shows $\bar{\gamma}$ as a function of time for a few different values of $\dot{\gamma}$. The strain corresponding to this definition of γ_P is indicated on each curve and can be seen to correspond to the point where the measured strain begins to deviate from the applied strain. The deviation is due to the strain relieved by the motion of the dislocation, as will be discussed in the next section.

4.4 Results and Analysis

4.4.1 Equilibrium dislocation geometry

Following equilibration as described in the previous section, the dislocations were found to reach one of the two stable configurations shown in Fig. 4.4. Which of the two configurations is selected depends sensitively on the details of the boundary conditions as well as on the system size. Systems larger in the x-direction tend to favor Config. 1, and systems larger in the y-direction tend to favor Config. 2, apparently due

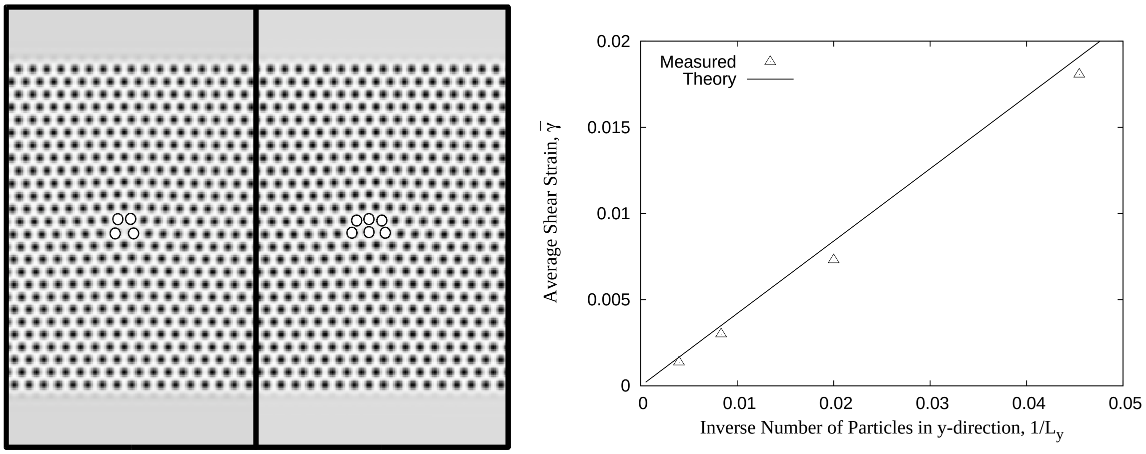

(a) (b)

Figure 4.4: (a) Stable dislocation configurations: The greyscale represents $n(x, y)$ and the particles around the dislocation core have been highlighted for clarity. Left: Config. 1. Right: Config. 2. (b) Equilibrium elastic strain, $\bar{\gamma}$, due to an edge dislocation plotted as a function of inverse system size in the y-direction. L_x was fixed at 56 particles for the data shown.

to the greater strain relief available at larger extensions. Systems with approximately equivalent x and y dimensions that were equilibrated with thermal noise oscillated between Configs. 1 and 2, indicating that the two states are approximately equivalent energetically. It will be shown in the following section that the initial configuration affects γ_P but not the subsequent velocity of the dislocation.

The average shear strain, $\bar{\gamma}$, in each system was measured and the values recorded following equilibration have been plotted in Fig. 4.4 as a function of $1/L_y$, where L_y is the number of particles in the y-direction. A simple analysis reveals that the total $\bar{\gamma}$ due to an edge dislocation in this geometry should be equal to $\sqrt{3}b/(4L_y)$, where b is the Burgers vector of the dislocation. This result agrees well with the measured values shown in Fig. 4.4, indicating that the measurement technique is reliable.

4.4.2 Glide: Constant applied shear rate dynamics

Simulations were conducted using steady shear over a range of applied shear rates ($\dot{\gamma}$), temperatures (r), and system sizes (L_x, L_y). The dependence of the Peierls barrier and the velocity vs. $\bar{\gamma}$ behavior on these variables will be discussed in the following subsections.

Peierls barrier for glide

To test for finite size effects, γ_P was measured as a function of system size, or inverse dislocation density. Within estimated errors, no change was observed under rigid displacement as the system size was increased from 676 to 56,952 particles. Under relaxational displacement, a slight increase with L_y was noted, and is linked to the time required for the strain applied at the edges to diffuse inward to the dislocation core. Diffusion is fast compared to the inverse shear rates required to apply relaxational displacement (rows of particles slip relative to each other at all but the lowest values of $\dot{\gamma}$), so the increase of γ_P with L_y cannot be very large. The nonlinear shear profile that is produced may exaggerate this lag between the applied strain and the strain near the dislocation, but the overall effect was nonetheless found to be relatively small.

Next, the barrier was examined as a function of r, which is proportional to the distance in temperature from T_c. To do this consistently, the boundary conditions were changed to mirror rather than periodic at the top and bottom, and the constant phase was entirely removed from the simulation. This made it possible to vary r at a single value of $\bar{n}$, isolating the temperature dependence in a more realistic manner. Results are shown in Fig. 4.5.

The decrease in γ_P as the melting point is approached is expected since the triangular phase amplitude decreases near T_c. A decreases with increasing r according to Eq. (4.4), and even without thermal fluctuations a distinct temperature dependence is produced. This decrease in A corresponds to an increase in the effective width of the dislocation which, according to the Peierls-Nabarro model [141], lowers the Peierls barrier for glide. With thermal fluctuations, these results did not change significantly, though at low $\dot{\gamma}$, which is where the change would be greatest, it was not possible to include fluctuations and maintain reasonable computation times. Similar linear decreases in γ_P as some effective T_c is approached have been found in experiment [142, 143] and theory [144, 145], along with increases in γ_P with $\dot{\gamma}$ much like those shown in Fig. 4.5.

At temperatures closer to the melting point ($r \simeq -0.18$), the dislocations began to climb at very low strains before any glide had occurred. This is the first evidence that climb is the dominant process at high temperatures, as in real crystals. Further

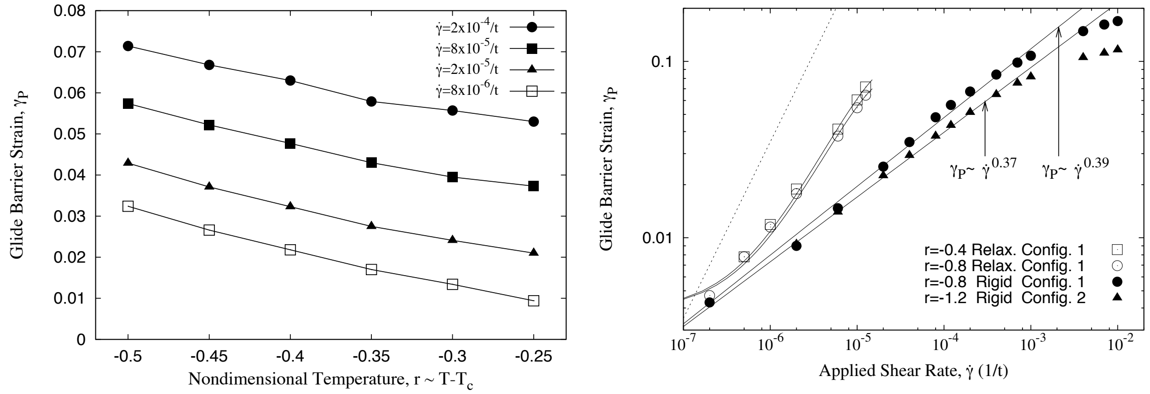

(a) (b)

Figure 4.5: (a) Temperature dependence of the Peierls strain barrier for glide without thermal fluctuations. Data shown is at $\bar{n} = 0.25$ and (L_x, L_y)=(56,56) under rigid displacement. (b) Measured Peierls strain barrier for glide, γ_P, as a function of applied strain rate for the cases of rigid and relaxational displacement. The fits to the rigid data are power laws as indicated in the image. The dotted line shows a linear $\dot{\gamma}$ dependence for reference. Note that γ_P is consistently lower for Config. 2 than for Config. 1, even with the differing r's working toward the opposite effect.

evidence will be presented with the climb results.

The dependence of γ_P on $\dot{\gamma}$ was also explicitly measured (Fig. 4.5). Both methods of shear application result in what appears to be a power law increase in γ_P as the shear rate is increased, where the relaxational displacement data are nearly linear and the rigid displacement data appear to approach a limit γ_P at high $\dot{\gamma}$. The transition to no $\dot{\gamma}$ dependence for large $\dot{\gamma}$ under rigid displacement can be understood by studying the evolution of F under an applied shear. In [4], the change in F for a one-mode approximate triangular solution under the action of shear was found by minimizing F when $n(x, y)$ is replaced with $n(x + \bar{\gamma}y, y)$. The resulting equation, valid for small $\bar{\gamma}$, is

$$\Delta F_{Shear} = \frac{q_{eq}^4 A^2}{6} \bar{\gamma}^2. \tag{4.6}$$

In principle, this represents a rigid displacement of $n(x, y)$ at infinitely large $\dot{\gamma}$. In this limit, γ_P has no explicit dependence on $\dot{\gamma}$;

$$\gamma_P = \sqrt{\frac{6\Delta F_P^{Glide}(\bar{n}, r)}{q_{eq}^4 A^2}}. \tag{4.7}$$

Dislocation dynamics in soft structures such as colloidal crystals are reasonably expected to correspond to the case of relaxational displacement. These systems typically exhibit very little rigidity associated with sound modes or phonons, thus their relative softness. Conversely, dynamics in atomic crystals are believed to better correspond to the case of rigid displacement at large $\dot{\gamma}$. A more constructive way to model atomic crystals would be to explicitly consider a phonon or wave term in the dynamics, as has been done by other authors [47, 74]. When such modes are considered, the collective motion of particles in response to an applied force is enhanced, more closely resembling the case of rigid displacement. It is argued in this sense that the methods of rigid displacement in the large $\dot{\gamma}$ region and relaxational displacement represent limiting cases of response, and that a more rigorous description including effective phonon dynamics would fall between these limits.

Atomistic glide mechanism

The nature of the dislocation motion in these simulations (Fig. 4.6) is stick-slip at low velocities with a transition to a more continuous character at high velocities. This is expected, as the lattice barrier leads to thermally activated motion when ΔF_{Shear} approximately equals ΔF_P^{Glide}, while at large values of ΔF_{Shear} the barrier becomes secondary and the motion assumes a damped character. The shear rate dictates the maximum velocity and therefore the extent to which the motion becomes continuous. Three regimes of motion were observed, with selection depending on the ratio

$$v_{ss} = \frac{\dot{\gamma}}{\rho_d b} \tag{4.8}$$

where ρ_d is the dislocation density dictated here by the system size. The reason for labeling this quantity v_{ss} will soon become apparent.

For large v_{ss} ($\gtrsim 0.016a/t$), the dislocation quickly reaches the overdamped regime and adjacent layers of particles begin to slip relative to each other along the x-direction

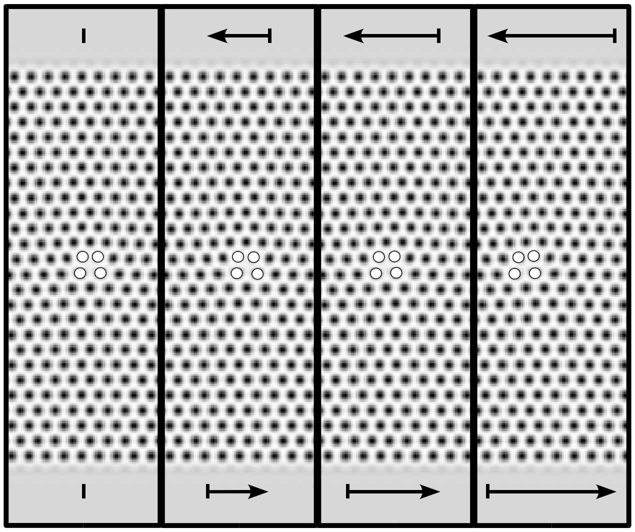

Figure 4.6: Atomistic glide mechanism under constant applied shear rate (the particles around the dislocation core have been highlighted for clarity). From left to right, $n(x, y)$ is shown at t=0, 500, 1000, and 1500, corresponding to $\bar{\gamma}$=1%, 2%, 3%, and 4%. The arrows indicate relative strain magnitudes and directions.

before a steady-state velocity is achieved. Slipping usually occurs when the strain exceeds approximately 20% in rigid displacement or 10–15% in relaxational displacement. At moderate values of v_{ss} ($0.06\gamma_P \lesssim v_{ss} \lesssim 0.016a/t$), the dislocation approaches a continuous glide motion and eventually reaches a steady-state velocity. This velocity can be calculated by equating the Orowan equation

$$\dot{\gamma}_{Plastic} = \rho_d b v \tag{4.9}$$

to the applied shear rate, giving the quantity v_{ss} defined in Eq. (4.8). This is the glide velocity required to plastically relieve strain at exactly the same rate at which it is being applied. Fig. 4.7 shows v_{ss} versus $\dot{\gamma}$ as measured from simulations. The measured values follow a linear trend as Eq. (4.8) predicts, with the slopes in good agreement with the theoretical values. This again shows that the plastic strain relief due to glide is correctly reproduced and that the proper steady-states are achieved.

At low values of v_{ss} ($\lesssim 0.06\gamma_P$), a more surprising type of motion occurs in which the dislocation overcomes the Peierls barrier, glides a short distance, and then comes to a stop. The cycle then repeats itself once enough strain is re-accumulated to

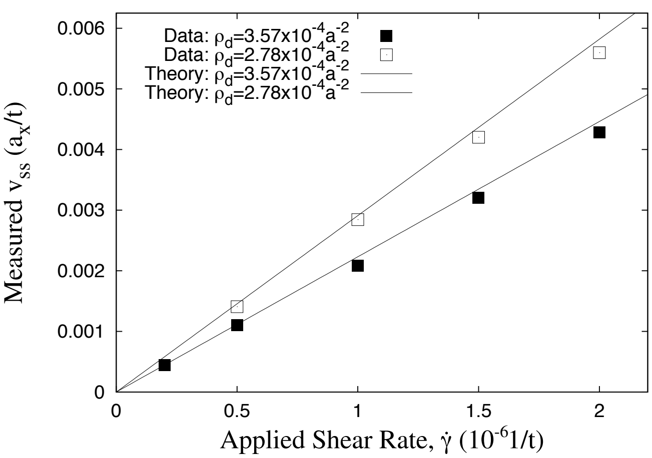

Figure 4.7: Measured steady-state glide velocities for two system sizes. The upper data points are at $r = -0.4$ and the lower data points are at $r = -0.8$.

overcome the barrier again. This oscillatory motion will occur whenever the velocity assumed just above the Peierls barrier is greater than the theoretical v_{ss} for the system. The rate at which the dislocation glide relieves strain is temporarily greater than the applied strain rate, so the energy falls below the Peierls barrier and glide is no longer possible until the strain energy again increases sufficiently.

Viscous dynamics

Empirically, dislocation glide velocity is described by the following equation:

$$v = v_s(\tau_{\text{eff}}/\tau_s)^m \tag{4.10}$$

where v_s is the shear wave velocity, τ_{eff} is the effective shear stress on the dislocation, τ_s is the material stress constant, and m is the stress exponent [26]. The stress exponent has been found to range from less than 1 to over 100 in some cases. For typical pure metals such as aluminum or copper, $m \simeq$ 1–5. These values may change significantly depending on temperature, stress range, and local defect densities. For example, in iron, m falls into one of three regions (m<1, m=1, m>1) depending on the conditions examined [26]. As will be shown in this subsection, the dislocation velocity was found to be approximately linear in both stress and strain ($m \simeq 1$) for all parameter ranges studied. This is not unexpected, as higher values of m are often attributed to effects such as jogs, impurities, and other defects which modify the dynamics from those expected for pure, two-dimensional crystals.

The dynamics of a single gliding dislocation are well described by the equation of motion for a point mass in a damped medium,

$$m_{\text{eff}}\dot{v}(t) = F_0 - \beta v(t) \tag{4.11}$$

where m_{eff} is an effective dislocation mass, F_0 is a constant proportional to $\dot{\gamma}$, and β is a damping constant.

Equations for $v(t)$, $x(t)$, and $\bar{\gamma}(t)$ can easily be derived from this starting point, but first the Orowan equation will be used to write m_{eff}, F_0, and β in terms of more meaningful parameters. It will be shown that the velocity is linear in $\bar{\gamma}$, but assuming this from the start, one can write

$$v(\bar{\gamma}) = M_\gamma(\bar{\gamma}(t) - \bar{\gamma}_0) \tag{4.12}$$

where M_γ is the slope, which can be interpreted as an effective mobility for glide. Next note that $\bar{\gamma}(t)$ is a function of the applied strain and the strain relieved by the gliding dislocation;

$$\bar{\gamma}(t) = \dot{\gamma}t - \rho_d b x(t). \tag{4.13}$$

Substituting Eq. (4.13) into Eq. (4.12) and differentiating gives

$$\dot{v}(t) = M_\gamma\dot{\gamma} - M_\gamma\rho_d b v(t) \tag{4.14}$$

and equating terms in Eqs. (4.14) and (4.11) shows that

$$\frac{F_0}{m_{\text{eff}}} = M_\gamma\dot{\gamma} \tag{4.15}$$

and

$$\frac{\beta}{m_{\text{eff}}} = M_\gamma\rho_d b. \tag{4.16}$$

This analysis indicates that the damping experienced by the dislocation is a result of the strain relief connected to the glide process and is not directly linked to the dynamics of Eq. (4.2). That is, if the second term on the right hand side of Eq. (4.13) were removed then both the velocity and the strain would be linear functions of time, without any effective damping. Including this term means that the effective damping can be controlled by changing ρ_d, with larger values of ρ_d corresponding to increased damping.

Solving Eq. (4.11) in terms of these new parameters, and applying the initial conditions $v(0) = 0$ and $x(0) = 0$ gives

$$v(t) = v_{ss}(1 - e^{-M_\gamma \rho_d b t}) \tag{4.17}$$

and

$$x(t) = v_{ss}\left(t + \frac{1}{M_\gamma \rho_d b} e^{-M_\gamma \rho_d b t}\right) - \frac{\dot{\gamma}}{M_\gamma \rho_d^2 b^2}. \tag{4.18}$$

Substituting Eq. (4.18) into Eq. (4.13) then gives

$$\bar{\gamma}(t) = \frac{v_{ss}}{M_\gamma}\big(1 - e^{-M_\gamma \rho_d b t}\big) + \bar{\gamma}_0. \tag{4.19}$$

Finally, comparing Eqs. (4.19) and (4.17) produces the desired linear relation assumed in Eq. (4.12) and the similar relation $v_{ss} = M_\gamma \bar{\gamma}_{ss}$, where $\bar{\gamma}_{ss} = \dot{\gamma}/M_\gamma \rho_d b$. The data shown in Figs. 4.9 and 4.7 verify that these linear relations are observed.

In all of these equations, the only adjustable parameter is M_γ, the effective mobility of the dislocation. Using values of M_γ measured from simulations, Fig. 4.2 shows excellent agreement between these analytic results and the simulation data for one parameter set, and Fig. 4.8 shows similar agreement for various other parameter sets. If it is assumed that the free energy obeys the relation to $\bar{\gamma}$ given in Eq. (4.6), then Eq. (4.19) can be substituted into Eq. (4.6) to give

$$\Delta F_{Shear} = \frac{1}{6}\left[\frac{q_{eq}^2 A \dot{\gamma}}{M_\gamma \rho_d b}\big(1 - e^{-M_\gamma \rho_d b t}\big)\right]^2 \tag{4.20}$$

which agrees relatively well with the high shear rate data, as shown in Fig. 4.8. The inset in the lower right of Fig. 4.8 shows how the agreement begins to fail at lower shear rates. This anomaly in the low $\dot{\gamma}$ glide data is not fully understood.

It is worth examining the strain dependence of the velocity further. In gradient

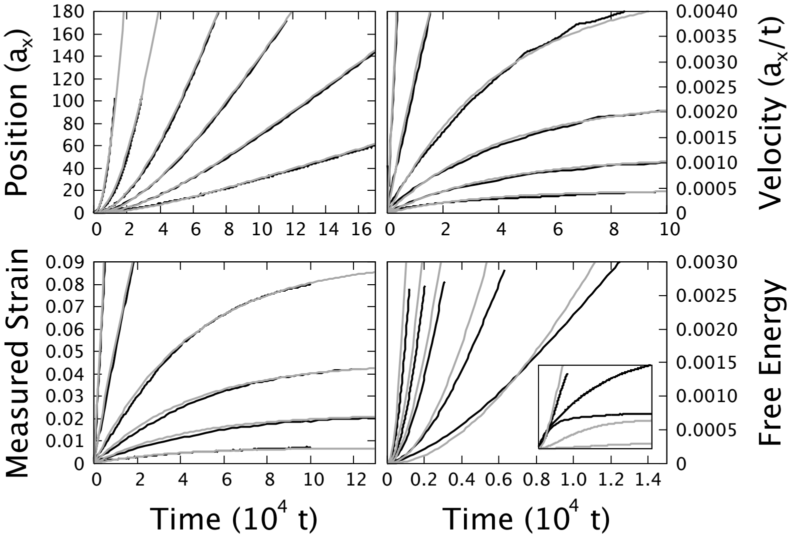

Figure 4.8: Additional comparisons between simulation data (black lines) and viscous motion equations (gray lines) for glide where where M_γ is the only adjustable parameter. From left to right in each plot curves are shown for $\dot{\gamma} = 2 \times 10^{-5}$, 6×10^{-6}, 2×10^{-6}, 1×10^{-6}, 5×10^{-7}, and $2\times10^{-7}/t$ except for the lower right which shows data for $\dot{\gamma} = 2\times10^{-4}$, 1.2×10^{-4}, 8×10^{-5}, 4×10^{-5}, and $2\times10^{-5}/t$. The inset in the lower right corner of the lower right plot shows data for lower shear rates, $\dot{\gamma} = 6 \times 10^{-6}$, 2×10^{-6}, and $5 \times 10^{-7}/t$ where Eq. (4.20) begins to fail. In all plots $r = -0.8$ and (L_x, L_y)=(56,46).

systems, the velocity of finite structures is expected to be proportional to the driving force applied F_D, which in this case can be interpreted as the derivative of the change in free energy due to the application of shear;

$$v \sim F_D = \frac{d\Delta F_{Shear}}{d\bar{\gamma}} \simeq \frac{q_{eq}^4 A^2}{3}\bar{\gamma}. \tag{4.21}$$

Additionally, Eqs. (4.11)–(4.19) indicate that velocity is in general linear in $\bar{\gamma}$ for this type of overdamped system. All simulations resulted in approximately linear velocity (v) vs. $\bar{\gamma}$ behavior for dislocation glide, as shown in Fig. 4.9. It is important to correct the overall strain shown in Fig. 4.9 for that relieved by the glide of the dislocation (Eq. (4.9)), especially when using small system sizes.

Both methods of displacement produce nearly the same value of M_γ under all conditions, though it is more difficult to determine the local strain around the dis-

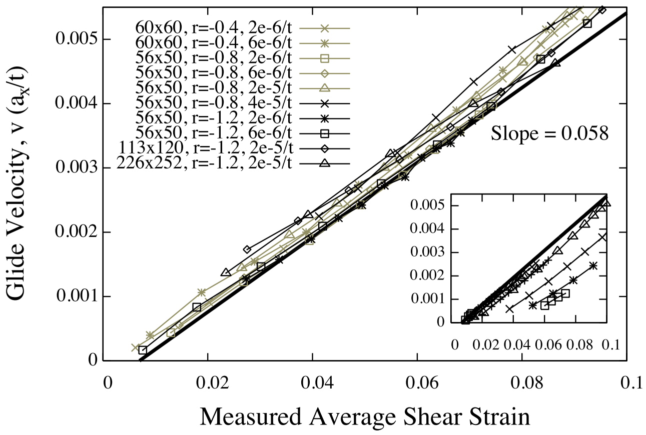

Figure 4.9: Dislocation glide velocity under rigid displacement as a function of the measured average shear strain, $\bar{\gamma}$. A number of system sizes, temperatures, and shear rates are shown to illustrate the uniformity of the dynamics. The heavy line is a representative linear fit. Inset: Dislocation glide velocity under relaxational displacement at various shear rates and two values of r. The strain values are overestimated due to the nonlinear shear profile produced by this type of shearing, but the slopes are relatively unchanged. The heavy line is the same linear fit as in the larger graph.

location for the case of relaxational displacement, due to the nonlinear shear profile. For rigid displacement, the free energy follows the expected form ($\Delta F_{Shear} \sim \bar{\gamma}^2$) and the velocity appears to be linear for $\bar{\gamma}$ less than $\sim 10\%$. For relaxational displacement, the anomaly in the free energy behavior noted above complicates the results, but the velocity remains linear in $\bar{\gamma}$ with values of M_γ similar to those found for rigid displacement. An analytic calculation of M_γ would complete this analysis of the dynamics, but since the simulation results indicate no strong dependencies on any variables, $M_\gamma = 0.06 a_x/t$ is believed to be a reasonable estimate for most cases of interest.

Shear was also applied along directions not lying on one of the axes of symmetry with predictable results. As the angle θ_R is increased (with 0° denoting alignment with a symmetry axis), the Peierls barrier grows but the slip direction remains along the nearest symmetry axis. Once θ_R becomes large enough, approximately $10 - 30°$ depending on the value of r, the dislocation prefers to climb rather than glide, with motion in the general direction of the applied shear.

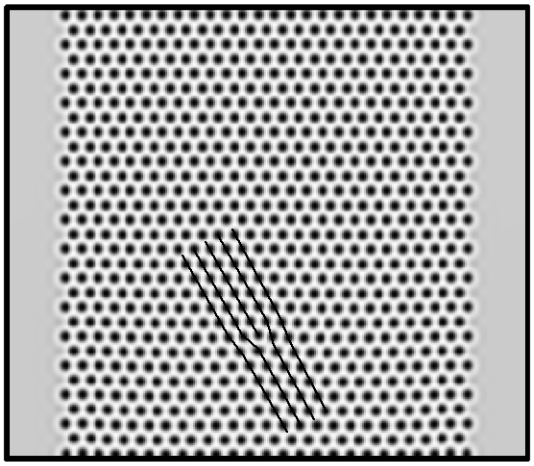

Figure 4.10: A small sample climb simulation setup where $n(x, y)$ has been plotted. The extra row of particles terminating at the core of the dislocation has been highlighted.

A similar analysis to that presented in Eqs. (4.11)–(4.20) can be applied to the case of constant strain by removing the external force from Eq. (4.11). The resulting equations were also found to agree well with simulation data. It is also worth noting that the velocity vs. $\bar{\gamma}$ behavior is essentially the same as that shown in Fig. 4.9 when the shear condition is one of constant strain.

4.4.3 Climb: Constant applied strain rate dynamics

Climb simulations were conducted using steady compression over a range of parameter values similar to those used for glide simulations. Before presenting the results, a caveat on this portion of the study is in order. It was found that the results varied systematically (i.e. the Peierls barrier decreased) with the grid spacing Δx, apparently due to the decrease in relevant dimensions with compression. A grid spacing small enough to overcome this effect could not be reached since the time step must be dramatically decreased with Δx. But the nature of the results and the essential physics remain the same; the data are only shifted by this effect. An example of the climb simulation geometry is shown in Fig. 4.10.

Peierls barrier for climb

The dependence of ϵ_P on ρ_d is of the same nature as that found for γ_P. No change was found under rigid displacement as L_x and L_y were increased, but an increase with L_x was observed under relaxational displacement, again in proportion to the diffusion time from the edge of the sample to the dislocation core.

The r dependence of ϵ_P is shown in Fig. 4.11 for various strain rates. Comparison with the glide Peierls barrier data in Fig. 4.5 confirms the same general linear behavior. ϵ_P is quite large at low r but decreases toward T_c such that there is a crossover close to T_c where ϵ_P becomes less than γ_P. Thus climb is predominant at high temperatures, in agreement with the accepted phenomenology [26]. This was also confirmed in the glide simulations where climb was found be preferred near T_c, even at very low values of applied shear. Note that the data shown in Fig. 4.11 was obtained using modified boundary conditions of mirror on all sides with no liquid phase.

Following [4], the change in F under compression can be calculated by substituting $n(x/(1+\bar{\epsilon}), y)$ into Eq. (4.1) and minimizing with respect to A. The result is similar to that for shear;

$$\Delta F_{Comp.} = \frac{q_{eq}^4 A^2}{2} \bar{\epsilon}^2. \tag{4.22}$$

In this limit, as was also the case for glide, ϵ_P can be written in the form

$$\epsilon_P = \sqrt{\frac{2\Delta F_P^{Climb}(\bar{n}, r)}{q_{eq}^4 A^2}}. \tag{4.23}$$

The strain rate dependence is also similar to that for glide, as shown more clearly in Fig. 4.11. The results show that $\gamma_P \sim \dot{\gamma}^{0.30}$, which is similar to the dependence $\gamma_P \sim \dot{\gamma}^{0.37}$ measured for glide at the same r. The absolute values of ϵ_P are significantly higher than those for glide in this case because of the low value of r that was used.

Atomistic climb mechanism

Dislocation climb is a nonconservative process. It requires either the diffusion of particles away from the dislocation core or toward it, unlike glide which involves only rearrangements of particles around the core. The mechanism of climb is shown in Fig. 4.12, where in these simulations mass diffuses away from the core since the strain is

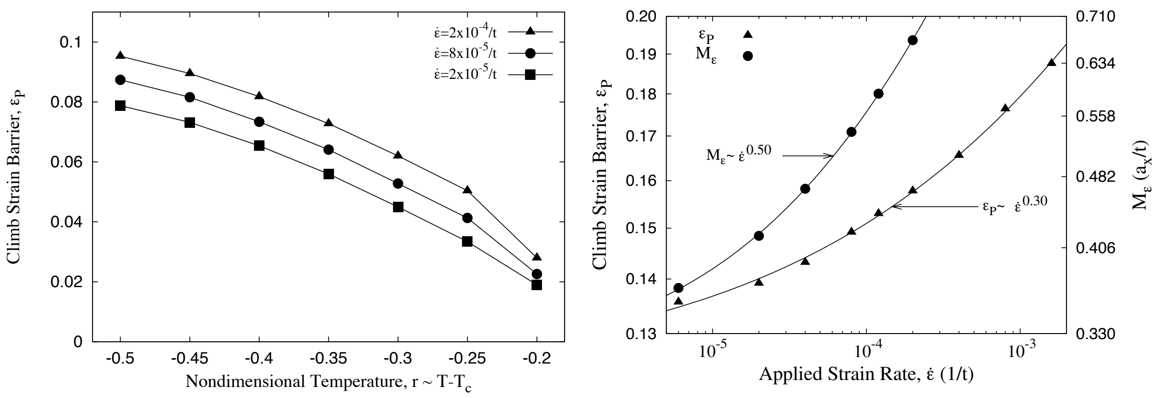

(a) (b)

Figure 4.11: (a) Temperature dependence of the Peierls strain barrier for climb without thermal fluctuations. Data shown is at $\bar{n} = 0.25$ and (L_x, L_y)=(52,103) under rigid displacement. (b) Measured Peierls strain barrier for climb and the subsequent mobilities under rigid displacement at $r = -1.2$ and (L_x, L_y)=$(52, 166)$.

applied through compression.

Again, similar to what was found for glide, the motion has a stick-slip character at low velocities and becomes more continuous at higher velocities. The motion proceeds by alternating between configurations 1 and 2 (Fig. 4.4). Starting from Config. 2, as shown in the upper left image of Fig. 4.12, the particle marked with an 'X' diffuses away, leaving the core in Config. 1 as shown in the next image. The two particles marked with arrows then merge together, returning the dislocation to Config. 2 as shown in the subsequent image. The process repeats as long as there is sufficient strain energy to maintain motion. For climb in the opposite direction, particles diffuse in and split rather then diffuse away and merge, respectively. This merging and splitting of particles may seem unphysical, but in a time-averaged sense these motions simply represent diffusion of mass away from or toward the dislocation core, which is the fundamental limiting process in dislocation climb.

Viscous dynamics

The dynamics of a single climbing dislocation are well described by the same damped equation of motion used to describe glide (Eq. (4.11)). Again, the only adjustable parameter is M_ϵ, the effective mobility for dislocation climb. Fig. 4.13 shows the

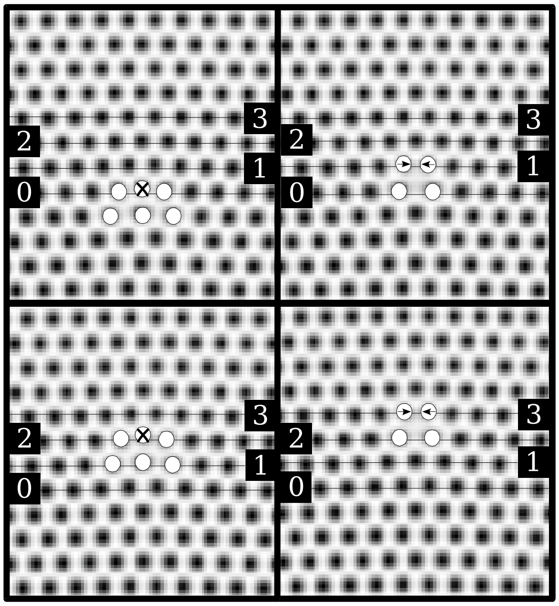

Figure 4.12: Atomistic climb mechanism under constant applied strain rate. From top left to bottom right, $n(x,y)$ is shown at t=300, 600, 800, and 900, corresponding to $\bar{\epsilon}$=2.4%, 4.8%, 6.4%, and 7.2%. The particles around the dislocation core have been highlighted and the rows near the core have been labeled for clarity. The particles marked with an 'X' are those which diffuse away between subsequent images, and those marked with arrows merge together.

agreement between these analytic results and typical sets of simulation data.

The velocity versus $\bar{\epsilon}$ behavior shown in Fig. 4.13 appears to be slightly nonlinear, but this is due to the relatively short range of motion that could be captured with computationally tractable system sizes. An approximate M_ϵ can nonetheless be extracted, and the results indicate first of all that the values of M_ϵ are an order of magnitude higher than those measured for M_γ ($M_\epsilon \simeq 0.5$). The slopes of the v versus $\bar{\epsilon}$ curves are much steeper for climb than for glide, but at the same time the velocities remain zero to much higher strains due to the larger values of ϵ_P (except near T_c). Also, M_ϵ is not quite as unchanging as M_γ, in that relatively weak, though measurable dependencies on r and $\dot{\epsilon}$ were found. The data indicate a slight decrease in M_ϵ with increasing r and an increase with $\dot{\epsilon}$ that goes like $\sqrt{\dot{\epsilon}}$ (Fig. 4.11).

To calculate the dynamics of F, Eq. (4.19) can be substituted into Eq. (4.22) to

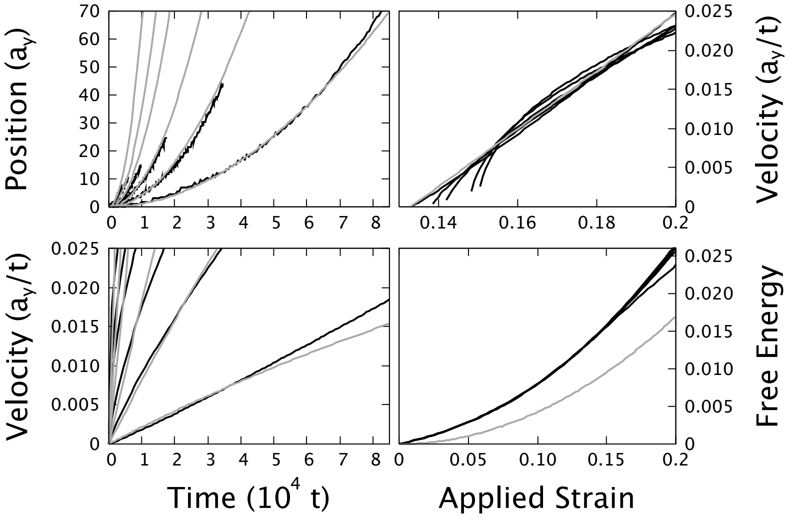

Figure 4.13: Comparisons between simulation data (black lines) and viscous motion equations (gray lines) for climb. From left to right in each plot curves are shown for $\dot{\epsilon} = 2 \times 10^{-4}$, 1.2×10^{-4}, 8×10^{-5}, 4×10^{-5}, 2×10^{-5}, and $6 \times 10^{-6}/t$. In all plots $r = -1.2$ and (L_x, L_y)=(52,166).

give

$$\Delta F_{Comp.} = \frac{1}{2}\left[\frac{q_{eq}^2 A\dot{\epsilon}}{M_\epsilon \rho_d b}\left(1 - e^{-M_\epsilon \rho_d b t}\right)\right]^2 \tag{4.24}$$

which agrees reasonably well with the data shown in Fig. 4.13. The difference is mostly due to the low value of r used, since the one mode approximation loses accuracy away from T_c. No anomaly in F like that found in the glide data was observed in the climb simulations. All curves of the change in F under compression fall onto approximately the same curve when plotted versus $\bar{\epsilon}$.

Compression was also applied along directions not lying on one of the axes of symmetry at $r = -0.8$. As the angle θ_R is increased, the dislocation first glides some distance proportional to θ_R in a direction along the nearest symmetry axis. Then climb begins along the same lattice direction as in the unrotated case, with the value of ϵ_P increasing only slightly with θ_R. Nearer T_c it would be reasonable to expect less tendency toward the initial gliding, as climb becomes the preferred type of motion. Generally, the application of strain along irregular directions relative to the lattice symmetry results in a mixed motion of glide and climb.

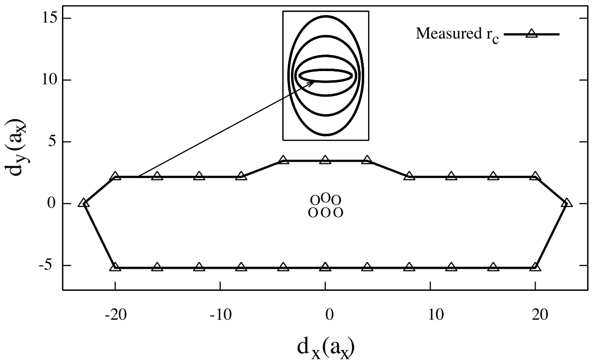

Figure 4.14: Measured critical radii for annihilation at $r = -0.25$ and $\bar{n} = 0.25$. The configuration shown in the center is the reference dislocation at $(0, 0)$ from which θ_0 was measured. The inset shows a schematic of the expected behavior as the temperature is increased above the crossover r at which climb becomes dominant.

4.4.4 Annihilation

Annihilation occurs when two dislocations having opposite Burgers vectors merge and eliminate each other. There exists a critical separation, d_c, at a given angle, θ_0, below which annihilation will occur, and this separation is in principle a function of the crystal symmetry, type of dislocation, temperature, relative velocity, and the local strain field. Results were obtained here for the static case ($v = 0$) at a single temperature and under no applied strain, for two perfect edge dislocations.

Consider one dislocation at some location $(0, 0)$ and another at (d_x, d_y) with opposite Burgers vector. In radial coordinates the separation can be expressed in terms of a distance d_0 and an angle θ_0. At $\theta_0 = 0°$, annihilation occurs by pure glide, and as θ_0 is increased a mixed motion of glide and climb is required, until $\theta_0 = 90°$ where annihilation occurs by pure climb. d_c was determined as a function of θ_0 by increasing the initial separation until annihilation no longer occurred. Periodic boundary conditions were used in all directions and the parameters chosen were $\bar{n} = 0.25$, $r = -0.25$, and $(L_x, L_y) = (56, 43)$. The equilibrium wavenumber at this $\bar{n}$ and r would require 56.5 particles in the $x-$direction, so placing 56/row in the bottom half and 57/row in the top half produces a dislocation with minimal preset bias toward climb in either direction. The results are shown in Fig. 4.14.

Despite the unbiasing, d_c is asymmetric with a preference toward climb in the $-y$ direction. This is apparently a consequence of the asymmetry of the strain field across the $x-$axis of the dislocation core, where there is an enhancement of strain in the lower half-plane. The particle positions around the core clearly reflect this asymmetry. Note that the details of the strain field will be slightly different for a dislocation in Config. 1, but the same argument should nonetheless hold.

The elliptical shape of $d_c(\theta_0)$ is expected since $\gamma_P^0 < \epsilon_P^0$ for this parameter set. As r is increased, eventually $\epsilon_P^0 < \gamma_P^0$, and the primary axis of the ellipse should coincide with the $y-$axis (climb axis), becoming more elliptical as T_c is approached. This expected behavior is shown schematically in the inset of Fig. 4.14. Moving from the inner to the outer ellipse corresponds to increasing r.

Extending the elliptical approximation and assuming that d_c is directly proportional to the Peierls strain, one can write a temperature dependent equation for d_c;

$$d_c(\theta_0, r) \simeq \frac{|A_\gamma A_\epsilon r|}{\sqrt{A_\gamma^2 \sin^2\theta_0 + A_\epsilon^2 \cos^2\theta_0}} \tag{4.25}$$

where A_γ and A_ϵ are the slopes of the Peierls strain versus r curves for glide and climb respectively.

4.5 Conclusions

Three fundamental dislocation processes have been numerically examined in idealized two dimensional settings using a phenomenological PFC model. The diffusive dynamics were measured over a range of temperatures, dislocation densities, and experimentally accessible strain rates. In equilibrium, two stable edge dislocation configurations were found to exist, with one resulting in a slightly lower Peierls barrier for glide than the other. The Peierls barriers for glide and climb, γ_P and ϵ_P respectively, were found to have little or no dependence on dislocation density, and both showed approximately linear decreases with increasing temperature (in the absence of thermal fluctuations). Near T_c, $\epsilon_P < \gamma_P$ verifying the expectation that climb is dominant at high temperatures. A crossover temperature was identified below which $\gamma_P < \epsilon_P$ and glide becomes the preferred type of motion. Both strain barriers also showed essentially power law increases with the applied strain rate, where the exponents are similar for glide and climb at equal r's. Under relaxational displacement (no phonons), γ_P is nearly linear in $\dot{\gamma}$, while under rigid displacement at high strain rates (strong phonons) the deviation from linear is much greater ($\gamma_P \simeq \dot{\gamma}^{0.38}$) with relatively little change in the barrier strain at high strain rates. Physical arguments and some mathematical arguments were given for all of these behaviors.

The motion of a gliding or climbing edge dislocation was found to be stick-slip in character at low velocities and nearly continuous at high velocities. Three possible regimes of motion were observed for glide, depending on the expected steady-state velocity of the dislocation defined in Eq. (4.8). These involve an oscillatory glide, a steady-state glide, and slipping rows of particles, in order of increasing v_{ss}.

A simple viscous dynamic model has been formulated to describe the results obtained for gliding and climbing dislocations, where the only adjustable parameter is M_γ or M_ϵ. Excellent agreement is obtained between these equations and the simulation results, both of which indicate that velocity is linear in strain for both glide and climb. The slope of the v versus $\bar{\gamma}$ curve for glide, M_γ was found to be nearly unchanging across all parameter ranges. The slope for climb, M_ϵ, which is an order of magnitude greater than M_γ, was found to increase approximately as $\sqrt{\dot{\epsilon}}$.

A critical distance for the annihilation of two edge dislocations was also measured, and an asymmetry with preference toward annihilation in the $-y$ direction was found. $d_c(\theta_0)$ approximately takes the form of an ellipse whose major axis is predicted to be along the glide direction at low temperatures and along the climb direction at high temperatures.

Traditional uniform phase-field models have also been used to study dislocation dynamics [144, 146–148]. These approaches differ from the PFC method in that they do not naturally contain atomistic detail. The domains in these models typically differentiate dislocation loops and the interfaces represent dislocation lines. Coarsening of large arrays of lines etc. can be efficiently studied, but atomistic detail is either lost or must be explicitly added through postulated Peierls potentials. The relevant equations of elasticity must also be rigorously applied, unlike in the PFC model which naturally exhibits elastic behavior as well as Peierls potentials.

Other phenomena relevant to dislocation dynamics, such as obstacle and impurity effects, could be studied with a similar approach, and more complicated dynamics involving screw dislocations, dislocation loops, multiplication processes, etc. could be examined in three dimensional simulations. Alternatively, the two dimensional model could provide interesting insights into the problem of dislocation-mediated melting in two dimensions.

CHAPTER 5

Diffusion-Driven Amorphous Solidification and Crystallization

The thermodynamics and dynamics of freezing and glass formation in diffusion-driven three dimensional monatomic liquids are studied using phase-field crystal simulations. At low cooling rates bcc crystals are formed by nucleation and growth from the melt. At large cooling rates a kinetically driven first-order transition from supercooled liquid to a disordered glasslike solid occurs. Though this amorphous solidification process is not dynamically consistent with a true glass transition, the structure and properties of the resulting disordered solid are shown to strongly resemble those of a typical glass. A secondary transition from the amorphous solid precursor phase to the equilibrium crystalline state occurs after some cooling rate dependent waiting time. Consequences of pseudo-critical behavior and heterogeneity near the liquid spinodal are also discussed.

5.1 Phenomenology and Literature

When a simple liquid is cooled below its freezing temperature, a crystalline solid typically becomes the state of lowest free energy and a first-order crystallization transition may occur. If the liquid is cooled very rapidly crystallization can be avoided, with the liquid instead undergoing a characteristic rapid but continuous slowing accompanied by very little two-point structural change – a glass transition. A few introductory notes on the glass transition were provided in Chapter 1. In this section, a brief summary of some of the literature concerning classical DFT and the dynamics of glass formation is given, to outline known results and the general behaviors for which we will be searching. A more thorough discussion is reserved for Chapter 6 where the primary dynamic signatures are observed and reported.

The PFC approach taken here is related to the classical density functional theory of freezing [8, 10] and to the variously proposed dynamical extensions of density functional theory [17, 103, 104, 149–152], as discussed in Chapter 2. The expected utility of dynamic density approaches in modeling the glass transition lies in their combination of coarse-grained free energies with mesoscopic equations of motion, which together provide a thermodynamic description of atomic structure and dynamics over long time scales.

Most density functional studies of glass-formation have focused on the static properties of the free energy functional, using various analytic or numerical approximations to locate and characterize metastable minima with aperiodic or glass-like density structures at large supercoolings [153–159]. Early dynamical simulations of the weakly inhomogeneous supercooled liquid were performed using nonlinear fluctuating hydrodynamics [160]. Despite the insights gained from these DFT studies, results involving dynamics have been limited and there remains a need for advancement in terms of finding less restricted solutions, studying larger systems, and thoroughly examining dynamic behavior in both the ergodic and non-ergodic regimes.

PFC models, when viewed as simplified DFTs, should not suffer from many of these applied limitations and may therefore provide a means of realizing significant advances in terms of late-time modeling of glass formation. Initial work toward this objective is reported upon in this chapter, outlining the first demonstrations of metastable glass-like minima in PFC models and the nature of the transitions by which they are reached. Freezing behavior is studied in three dimensions with simple diffusional dynamics, while more nonlinear free energies and equations of motion are examined in Chapter 6.

The standard PFC free energy evolved with Model B dynamics can be numerically simulated at system sizes several orders of magnitude larger than previous density functional studies and over simulation times on the order of 10^6 or more typical liquid relaxation times. This corresponds to time scales several orders of magnitude longer than those accessible to typical molecular dynamics simulations. The simulated glass-like metastable states are obtained here in a physically meaningful way with no explicit restrictions on the solution set. The packing structure and local density profiles are naturally optimized and are found to exhibit heterogeneity in local mean square displacements.

5.2 Model Equations and Notation

The PFC free energy functional used in this chapter is the same as that examined in Chapters 3 and 4,

$$F = \int d\vec{r} \left\{ \frac{n}{2} \left[r + (1+\nabla^2)^2 \right] n + \frac{n^4}{4} \right\} \tag{5.1}$$

where $n \rightarrow n(\vec{r}) + \bar{n}$ is the scaled atomic number density order parameter, $\bar{n}$ is the average density, and r is a constant related to temperature. The relation of this model to classical DFT was discussed in Chapter 2. Essentially, Eq. (5.1) corresponds to a specific approximate parametrization of the full density functional form. As will be demonstrated, this simplified form exhibits the same qualitative freezing behavior as its DFT counterpart, but is considerably simpler to manipulate and simulate numerically. A consequence of the approximations used may be a restriction on the number of systems and the range of conditions which can be quantitatively described.

The appropriate dynamics for a glass-forming liquid described by a DFT-type free energy has been debated among practitioners of the various forms of dynamic density functional theory and other related field theories. This initial study will focus primarily on the simplest form potentially capable of capturing the relevant behavior,

$$\frac{\partial n}{\partial t} = \nabla^2 \mu + \eta \tag{5.2}$$

where η is a Gaussian stochastic noise term with $\langle \eta(\vec{r}_1, t_1)\eta(\vec{r}_2, t_2)\rangle = M\nabla^2\delta(\vec{r}_1 - \vec{r}_2)\delta(t_1 - t_2)$, M is a constant used to vary the relative magnitude of the thermal fluctuations to the free energy topology, and t is the dimensionless time. This equation describes a conserved density field $n(\vec{r})$ undergoing a purely diffusive free energy minimization in the presence of random thermal fluctuations.

The most common dynamic density functional equation of motion also maintains density conservation and diffusive free energy minimization, but introduces a local density-dependent mobility and multiplicative thermal noise. With the rescaled density n, it has the form

$$\frac{\partial n}{\partial t} = \nabla \cdot ((n+1)\nabla \mu) + \nu \tag{5.3}$$

where $\langle \nu(\vec{r}_1, t_1)\nu(\vec{r}_2, t_2)\rangle = M\nabla\cdot\nabla((n+1)\delta(\vec{r}_1-\vec{r}_2)\delta(t_1-t_2))$. For a small-$n$ expansion, if $n \ll 1$, one has $n+1 \simeq 1$ and Eq. (5.3) reduces to Eq. (5.2), including the noise term. For highly inhomogeneous states the differences may become significant, but all monatomic simulations employing Eq. (5.3) have to this point produced qualitatively similar results to those described in the following for Eq. (5.2).

A semi-implicit pseudospectral algorithm was used to solve Eq. (5.2) in three dimensions with periodic boundary conditions (see Appendix A.2 for details). The parameters used were $\bar{n} = -1/4$, $\Delta x = 1$, and $\Delta t = 1/2$, while system sizes were varied from $V = 64^3$ to $V = 512^3$ (∼686 to ∼390,224 atoms). Sizes of $V \gtrsim 128^3 - 256^3$ are generally required to overcome the finite size effects discussed in Section 6.4.4.

5.3 Freezing Transition

At high temperatures the equilibrium phase for the time-averaged number density $n(\vec{r})$ is a spatially uniform fluid state. For off-critical average densities, as the dimensionless temperature parameter $T \equiv r+1$ is lowered, the liquid passes through a first order phase transition point below which the equilibrium phase is one with periodic density modulations, corresponding to a bcc crystalline state. Due to the nucleation barrier between liquid and solid phases, the liquid can be supercooled until the spinodal temperature T_s is approached and the free energy barrier eventually vanishes.

5.3.1 Coexistence region (nonspinodal)

Previous density functional studies [153–158] and others [161, 162] find that for sufficiently large supercooling, a large number of metastable states with aperiodic density modulations and with $F_{cryst} < F < F_{liquid}$ become accessible by a first-order transition. The simulations described in this chapter show that this discontinuous transition to a glass-like state occurs in the monatomic PFC system and also demonstrate that

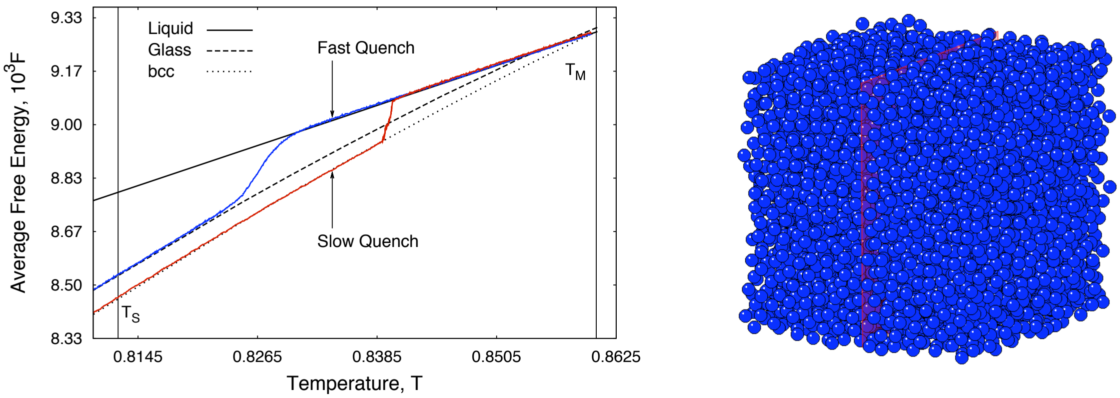

(a) (b)

Figure 5.1: (a) Free energies of various phases vs. T. Disordered solid F is a representative result from a single rapid quench, as F varies significantly only for $\dot{T}$ near $\dot{T}_c$. Example fast and slow quenches are overlaid to illustrate the effect of cooling rate. (b) Disordered solid at $V = 128^3$, where local peaks in $n(\vec{r})$ are represented by spheres, and the highlighted central plane is shown to improve perspective.

the structure of the resulting solid phase depends primarily on the cooling rate $\dot{T}$. Very low cooling rates lead to bcc structures, generally through a two-stage nucleation process involving an initial disordered solid which quickly rearranges into a bcc crystal. As $\dot{T}$ is increased, the stability of the initial disordered solid grows and it persists for longer and longer times. Finally, at cooling rates above the critical cooling rate $\dot{T}_c$, the amorphous solid is relatively stable for times longer than the time scale of the simulations. Here the system is kinetically limited and becomes trapped in the metastable disordered state, unable to organize with the symmetry of lowest free energy.

This cooling rate effect is illustrated in Fig. 5.1, where two examples of the free energy change with temperature are shown, one for high $\dot{T}$ and one for low $\dot{T}$. Sample configurations obtained at various cooling rates are also shown in Fig. 5.2, where the gradual shift toward bcc order is evident. There appears to be no Kauzmann temperature at which the entropies ($S = -\partial F/\partial T$) of the amorphous and bcc phases would cross.

Since the disordered solid forms through a nucleation process, classical nucleation theory should be applicable to some extent near the liquid-bcc coexistence region.

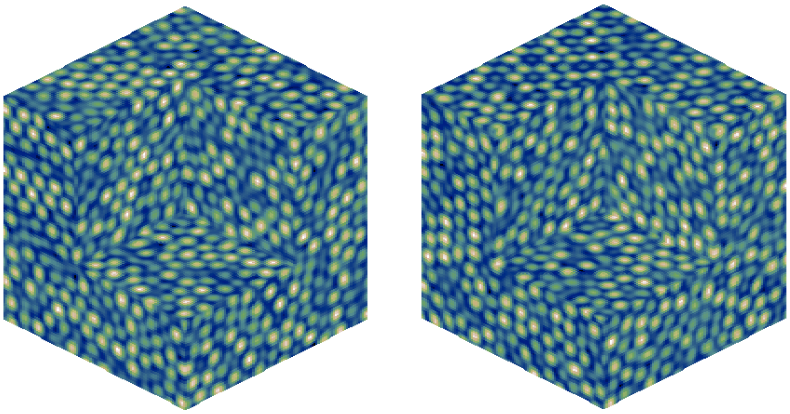

(a) $7.5 \times 10^{-8} T/t$ (b) $3.75 \times 10^{-8} T/t$

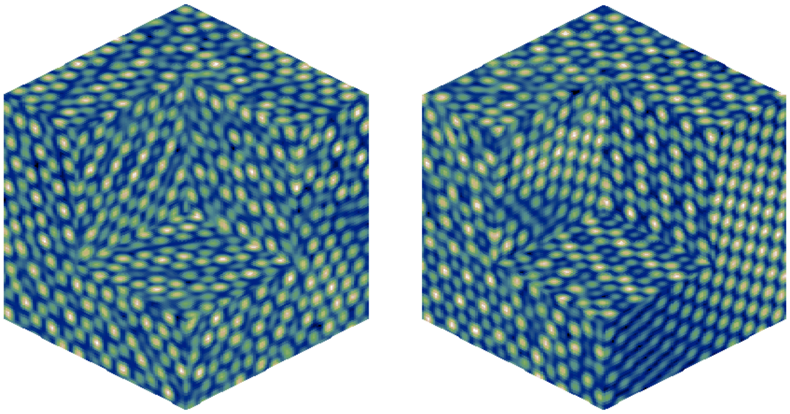

(c) $1.5 \times 10^{-8} T/t$ (d) $3.75 \times 10^{-9} T/t$

Figure 5.2: Sections of $n(\vec{r})$ from systems quenched at various cooling rates. Light areas correspond to high density, dark areas to low density. $T_{\text{init}} = 0.816$, $T_{\text{final}} = 0.810$, and $V = 256^3$. Each cube shown contains a region $V = 96^3$, or $\sim 5\%$ of its system's overall volume.

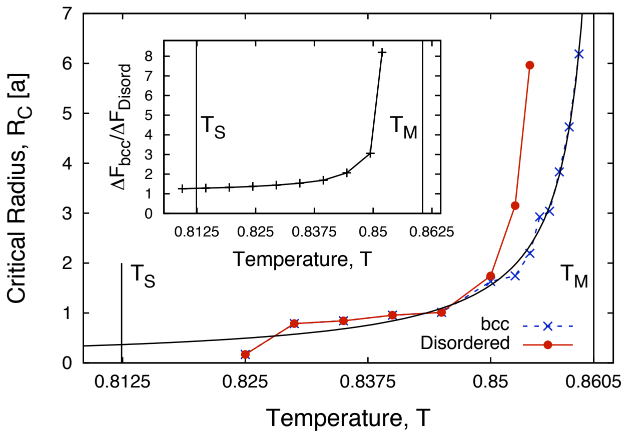

Figure 5.3: Measured critical radii of disordered solid and bcc phases in liquid at various T, in units of the equilibrium one-mode bcc lattice constant a. The dashed line is a fit to classical nucleation theory where $R_c \propto (\mathrm{T_m} - \mathrm{T})^{-1}$. Inset: Calculated ratio of bcc to disordered solid free energy barriers from classical nucleation theory.

Atomistic modifications to the uniform droplet picture are naturally captured by the PFC description, which should remain meaningful at droplet sizes smaller than those below which uniform theories break down. Critical radii R_c have been measured for bcc and disordered solid droplets in liquid at various temperatures, as shown in Fig. 5.3. These measurements were made by evolving various initial spherical seeds of solid with radii R surrounded by liquid, and defining R_c as the initial value of R below which the seed droplet melts and above which the seed droplet grows. The disordered solid results represent an average over several different disordered seeds. The two structures are found to have essentially equivalent R_c, except near the equilibrium bcc melting temperature T_m, where the disordered solid phase is increasingly unstable and tends to crystallize in very short times. For small R_c, the critical radii are discretized to values corresponding approximately to atomic neighbor distances, while the larger R_c diverge more smoothly, following $R_c \propto (T_\mathrm{m} - T)^{-1}$ as predicted by classical nucleation theory.

These results indicate that the free energy barrier between liquid and disordered solid is consistently 10% to several times smaller than the barrier between liquid and bcc (Fig. 5.3 inset). The predicted nucleation times $t_n \propto e^{\Delta F/k_B T}$ are at least one order of magnitude smaller for the disordered solid than for the bcc structure. Thus the initial presence of disordered droplets in all quenching simulations is tentatively attributed to droplet energetics. Since the bulk energy of a disordered solid droplet is always higher than that of a bcc droplet, this would imply that the interfacial energy between liquid and amorphous solid is significantly smaller than the overall liquid-crystal interfacial energy.

5.3.2 Spinodal effects

The preceding discussion of freezing applies to the general case in which the first-order liquid to disordered solid transition occurs at low to moderate supercooling (weak-coupling regime, M not too small). When the liquid can be supercooled very deeply, near its spinodal temperature T_s, pseudo-critical effects emerge due to the underlying continuous instability. Similarities between the near-spinodal liquid and glass-forming liquids have been examined by other authors [161, 163, 164]. Here it is found that, despite the appearance of the onset of glass-formation near T_s – signaled by a diverging relaxation time, stretched exponential decay, and spatial heterogeneity in local relaxations – the pseudo-critical effects play only a secondary role in the freezing process. They have little bearing on whether the resulting solid is disordered or crystalline, and therefore do not appear to be associated with a true glass transition in this system, as discussed in the following.

The liquid intermediate scattering function or density autocorrelation relaxation function $\mathrm{F}(q,t) = \langle \delta n(q,0)\delta n^*(q,t)\rangle / \mathrm{F}(q,0)$ can be calculated at the linear level by solving the equation of motion for the linearized chemical potential ($\delta F/\delta n$) in Fourier space, giving

$$\mathrm{F}(q,t) \simeq e^{-t/\tau} \tag{5.4}$$

where $\tau = \left[2q^2(T - 2q^2 + q^4)\right]^{-1}$ is the density autocorrelation relaxation time. This solution for τ is plotted in Fig. 5.4 along with measurements from numerical simulations. Without fluctuations, τ diverges at $T = T_\mathrm{s}$ for $q = 1$. The Vogel-Fulcher fitting function, widely used to characterize glass forming liquids,

$$\tau = \tau_0 e^{B/(T-T_\mathrm{s})} \tag{5.5}$$

where τ_0 and B are constants, is reasonably accurate near T_s, but the spinodal analysis

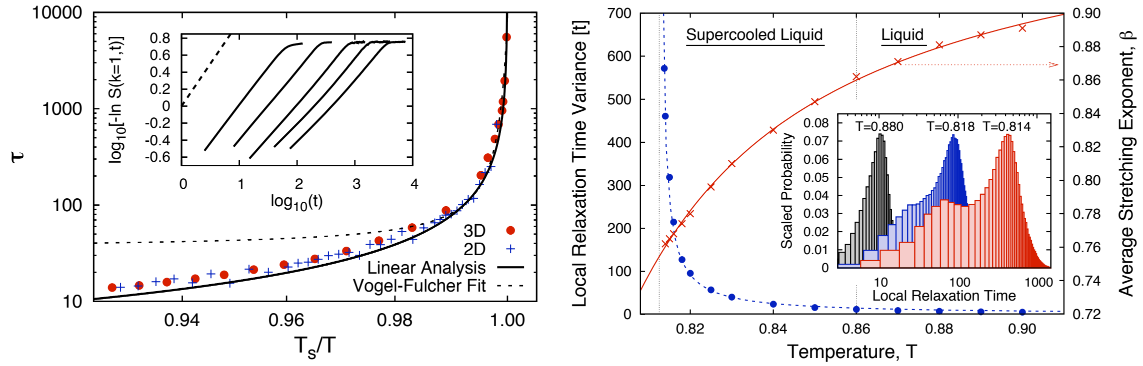

(a) (b)

Figure 5.4: (a) Divergence of the density autocorrelation relaxation time for two- and three-dimensional systems. Relaxation data taken near the first peak in $S(q)$ at $q = 1$. Inset: Stretching relaxation functions as T decreases from left to right. The dashed line corresponds to normal exponential decay ($\beta = 1$). (b) Variance in the distribution of local relaxation times and the resulting average stretching exponent β as $T \to T_s$. The dashed-line fit to the variance data is of the form $(T - T_s)^{-1}$, while that to the β data follows $\beta \sim 1 + \exp\left[A/(T - T_0)\right]/T^{2^{-1/2}}$. The inset shows sample distributions on a log-scale at three values of T.

clearly points to a power law a divergence of the form $\tau \sim (T - T_{\mathrm{s}})^{-1}$.

Measurements of $\mathrm{F}(q, t)$ also indicate that the PFC liquid exhibits increasingly stretched exponential decay as T_{s} is approached. Fits to the form

$$\mathrm{F}(q, t) = e^{-(t/\tau)^{\beta}} \tag{5.6}$$

indicate that the stretching exponent β decreases from ~ 1 to ~ 0.76 near T_{s} (Fig. 5.4). This apparent stretching coincides with, and is in part caused by, the onset of increasing dynamic heterogeneity near the liquid spinodal, as shown in Fig. 5.4(b). Well above T_{s}, the local relaxation times τ_ℓ are fairly homogeneous across all regions of the liquid. Near T_{s} the width of the τ_ℓ distributions increases dramatically (along with the average relaxation time), approximately following a $(T - T_{\mathrm{s}})^{-1}$ divergence. This signifies growing heterogeneity, as different regions in the system are relaxing with a larger and larger disparity of rates. Spatial correlations of local relaxation times will require further examination to discuss conclusively, but it is noted that the most mobile regions tend to be arranged in string-like clusters which surround the less mobile regions.

The preceding pseudo-critical behaviors appear to indicate that the supercooled liquid near T_s is undergoing a continuous transition toward an effectively frozen state, somewhat resembling the behavior of a fragile glass former. Thermal fluctuations eventually truncate this pseudo-critical behavior and near T_s the initially continuous slowing of dynamics is overridden by a clear first-order freezing transition. Therefore, even when spinodal effects are strong, the transition from liquid to disordered solid is ultimately first order in this system, and the suggestive pseudo-critical behavior has relatively little bearing on whether the resulting solid is glass-like or crystalline. Global instability to nucleation for $T \lesssim T_\mathrm{s}$ seems to be one way in which a near-spinodal liquid differs from a glass-forming liquid, which by contrast remains robust to first order discontinuities at all temperatures (for sufficiently rapid quenches).

The appearance of an amorphous solid rather than a crystalline solid upon quenching *below the spinodal* in two dimensions has been discussed in a similar context [162]. Deep quenches below T_s were shown to generate instability across a broad range of wave vectors, preventing the growing droplets from selecting a single wave vector corresponding to the ordered structure. This picture is consistent with simulation results for sub-spinodal quenches presented here, and it is found additionally that sufficiently slow quenches facilitate formation of the equilibrium crystal structure, regardless of proximity to T_s.

5.4 Disordered Phase Structure and Properties

The structure of the PFC disordered solid phase is consistent with that of many known glass formers, having a structure factor $\mathrm{S}^P(q)$ and radial distribution function $g^P(R)$ that are liquid-like and exhibit the characteristic split second peak. $\mathrm{S}^P(q)$ and $g^P(R)$ are the spherically averaged structure factor and radial distribution function, respectively, of the most probable atomic configuration. Examples of $\mathrm{S}^P(q)$ are shown in Fig. 5.5 for various cooling rates $\dot{T}$. The disordered structures obtained at large $\dot{T}$ are qualitatively similar to but quantitatively different from the Bernal packing scheme. As $\dot{T}$ is decreased the structure factor of the resulting solid develops more prominent peaks all corresponding to diffraction peaks in a bcc crystal (see Fig. 5.5

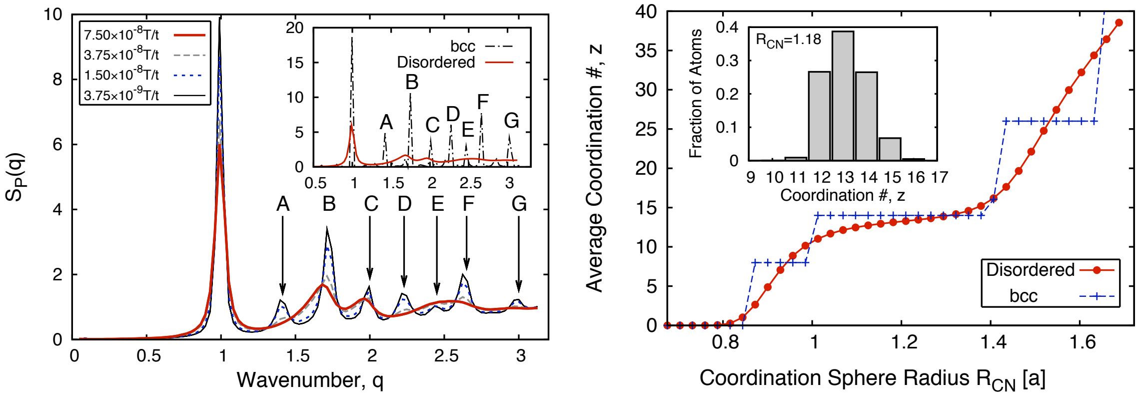

(a) (b)

Figure 5.5: (a) Most probable instantaneous solid structure factors $S^P(q)$ at various cooling rates. Data for systems shown in part in Fig. 5.2. Wavenumbers corresponding to bcc peaks are labeled with letters. Inset: bcc and disordered solid $S^P(q)$. (b) Coordination number vs. coordination sphere radius for most probable atomic structures of representative disordered and bcc systems, in units of the equilibrium one-mode bcc lattice constant a. Inset: Histogram of coordination numbers at $R_{\mathrm{CN}} = 1.18$.

inset), and visual inspection reveals that sizable regions with bcc order have formed, as is clearly seen in Fig. 5.2.

Analysis of local, short-range order was performed on many amorphous configurations, and representative data for the average coordination number z as a function of coordination sphere radius R_{CN} is shown in Fig. 5.5(b). The bcc result exhibits clear steps at values of $z = 8, 14, 26, \ldots$, as required. The disordered solid result shows a much more gradual rise in z, to a near plateau at $z \simeq 13$, and then further increase. A histogram of coordination numbers at $R_{\mathrm{CN}} = 1.18a_{\mathrm{bcc}}$ is shown in the inset of Fig. 5.5(b). These results compare favorably with values for various binary metallic glasses obtained using ab initio molecular dynamics [165].

An effective packing fraction σ can also be defined as

$$\sigma = \frac{N}{N_{\mathrm{bcc}}}\sigma_{\mathrm{bcc}} \tag{5.7}$$

where N is the number of density peaks in the system, N_{bcc} is the number that would be found in an ideal bcc system of the same size, and $\sigma_{\mathrm{bcc}} = 0.68$ is the ideal bcc

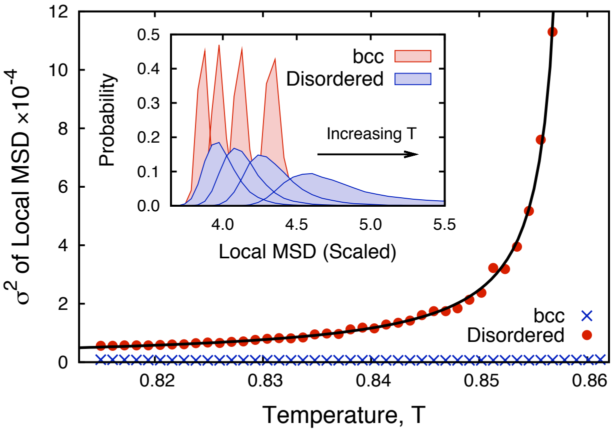

Figure 5.6: Variance in the distribution of local MSDs in disordered and bcc samples vs. temperature. The solid line is a power law fit with exponent -1. Inset: Local MSD distributions at various temperatures.

packing fraction. Measurements indicate that $\sigma \simeq 0.63 - 0.64$, with 0.64 being the apparent limiting value for the disordered phase. This is compared to $\sigma = 0.61$ for the Bennett hard-sphere glass [166] and $\sigma = 0.6366$ for dense randomly packed ball bearings [167]. Thus in many respects, the structure of the disordered solid phase is consistent with that of simple structural glasses as observed experimentally and in atomistic computer simulations.

As noted, the PFC disordered solid also exhibits spatial heterogeneity in local mean square displacements (MSDs), with a distribution of local MSDs several times broader than that of the bcc phase (Fig. 5.6 inset). The variance of this distribution, as shown in Fig. 5.6, is found to diverge approximately as $(T_{\rm m} - T)^{-1}$ as the disordered solid is heated, while the bcc phase shows a much weaker increase in heterogeneity before melting. This behavior is related to the phenomenon of critical softening in glasses, where the relative solidity of a glass, as measured by the Debye-Waller factor, decreases with strong nonlinearity at high temperatures [168].

5.5 System Size and Aging

For relatively small systems ($V \lesssim 128^3 - 256^3$) the gradual sequence of structures leading from the maximally disordered state to the perfect bcc state becomes increasingly restricted. Only highly disordered or highly ordered states are generally observed below this range. Such a restriction on the possible states has significant effects on the relaxation of the disordered solid toward the lower-energy crystalline state. Very little aging of a disordered system is possible when the intermediate phases of mixed character are inaccessible, and the disordered solid is effectively frozen in or near its initial minima for times longer than the simulations. In sufficiently large systems, a more systematic aging behavior is observed. Thermal fluctuations lead to small local rearrangements in $n(\vec{r})$, sometimes cascades of rearrangements, which lower F incrementally toward that of the bcc state. The rate of relaxation is strongly dependent on $\dot{T}$.

Therefore, even though the structural correlation lengths in a glass-like system are expected to be only on the order of a few atomic spacings, the system size here must be considerably larger to avoid finite size effects in the relaxational dynamics of the non-equilibrium state. By comparison, the more homogeneous supercooled liquid phase exhibits finite-size effects only near T_s, where the correlation length becomes large.

5.6 Discussion and Conclusions

Direct numerical simulations have been used to demonstrate that the monatomic PFC model exhibits a range of freezing behaviors which depend primarily on the quench rate and proximity to the liquid spinodal temperature. When freezing occurs well above T_s, the transition is strongly first order and in qualitative agreement with classical nucleation theory. Simulations indicate that the initial nucleites are relatively disordered with high probability, regardless of the cooling rate. As the nucleites grow and coalesce, they either remain disordered and glasslike if the quench is sufficiently rapid, or rearrange locally into the equilibrium bcc structure if the quench is slow. Thus glass formation in this regime is kinetically driven but strongly first order, with no accompanying continuous slowing of liquid dynamics as is characteristic of a typical glass former.

When freezing occurs near T_s, the supercooled liquid exhibits pseudo-critical behaviors which somewhat resemble the onset of a glass transition. These include a diverging relaxation time, stretched exponential decay, and apparent dynamic heterogeneity. These appear not to be associated with a true glass transition in this system, as the kinetically driven first-order transition ultimately intervenes near T_{s}, and the preceding pseudo-critical effects serve only to alter the critical cooling rate and not the qualitative nature of glass formation as described above.

Despite the fact that formation of the disordered solid phase stems from a kinetically driven first-order transition rather than a clear glass transition, the structure and properties of the disordered solid appear to be consistent with those of simple glasses. The monatomic PFC free energy clearly contains inherent glasslike minima but the diffusive model accesses them by a dynamic pathway that does not resemble a glass transition. This could be a peculiarity of simple monatomic systems, which have not been shown to undergo a glass transition experimentally, and which typically exhibit only initial signs of a glass transition on short time scales before rapidly crystallizing in most atomistic simulations. It is possible that the relevant short time scales in this scenario are inaccessible to the coarse-grained PFC description, or that purely diffusive dynamics simply do not capture the localized and highly nonlinear caging processes which are believed to drive the glass transition. If a suitable size and/or mobility difference between species is fundamental to glass formation, or at least strongly enhances glass formability, then the lack of a clear glass transition here would not be surprising.

The primary dynamic signatures of the glass transition are shown in the next chapter to emerge when highly nonlinear free energies are combined with equations of motion which also consider inertial dynamics. The path from these initial results, outlined in Chapter 5, to those presented in the next chapter was not a direct one. Freezing dynamics were examined within several modified PFC models in which the free energy functional and/or equation of motion were/was altered with the aim of generating glassy behavior. Several of these abandoned, though in some cases not entirely unsuccessful, models are recorded in Appendix B. They are all less satisfactory for present purposes than the model described in Chapter 6.

CHAPTER 6

Supercooled Liquid Dynamics and the Glass Transition

The dynamics of glass forming supercooled monatomic and binary liquids are studied numerically using phase-field crystal simulations. A nonlinear stochastic framework combining modified phase-field crystal free energies and inertial dynamic density functional theory is shown to successfully describe several aspects of glass formation over multiple time scales. Agreement with the central predictions of mode coupling theory is demonstrated for underdamped liquids at moderate supercoolings, and a rapidly growing dynamic correlation length is found to be associated with fragile behavior. Aging properties are also examined and shown to scale with time in the same manner as many known experimental and simulated glass forming systems. A postulated time scaling procedure results in a qualitatively correct description of experimentally observed relaxation phenomenology over 12 orders of magnitude in time.

6.1 Phenomenology and Literature

Phenomenology

Any liquid rapidly quenched to a sufficiently low temperature will undergo a glass transition, though the precise meanings of ‘rapidly’ and ‘low’ can vary enormously from material to material. Rather than nucleating crystallites and freezing discontinuously into an ordered crystalline solid, the glass forming liquid slows continuously but very rapidly while the system maintains most of its liquid-like atomic structure. At T_g the structural relaxations become sufficiently slow that the material can be considered a disordered solid or glass. In many ways this solid still resembles a liquid, but one that relaxes with effectively infinite slowness.

Figure 1.2 shows a compilation of viscosity data for several glass formers, highlighting the strong versus fragile classification scheme proposed by Angell [1]. Strong liquids are those which retain an Arrhenius temperature dependence, and therefore constant activation energy, across the full measurable viscosity range. Such systems typically have strongly covalent interactions. Fragile liquids on the other hand are typically dominated by van der Waals or ionic interactions, and are characterized by a region of more rapid super-Arrhenius viscosity growth. This temperature dependence can often be accurately described by the Vogel-Fulcher fitting function introduced in Chapter 5, (viscosity $\eta_v \sim \tau = \tau_0 e^{B/(T-T_0)}$ where τ_0 and B are constants).

Another important feature of glass forming liquids is the stretched exponential relaxation function, also introduced in Chapter 5 ($\mathrm{F}(q,t) = e^{-(t/\tau)^\beta}$ where $\beta < 1$). This feature is generally associated with a distribution of roughly exponential relaxation functions spread throughout the system. It is common as well for glass forming liquids slightly above T_g to exhibit two-step relaxation functions, characterized by rapid (β) relaxation to a non-zero plateau correlation value followed by slower (α) relaxation toward zero correlation. Anomalies in thermodynamic quantities also emerge at the laboratory glass transition temperature T_g, due to a sudden inability to widely sample phase space over the measurement time scale. First order thermodynamic quantities such as entropy show a rapid change in slope in the vicinity of T_g, while second order quantities undergo 'smeared' jumps in value. For example, the specific heat drops rapidly at T_g as shown in Fig. 1.2, with the location of the drop (and thus T_g) strongly dependent on the quench rate.

Glasses, and systems out of equilibrium in general, also usually display aging behaviors. That is, their physical properties vary with time as the system evolves irreversibly through phase space toward lower energy configurations. Such behaviors are most often quantified through dynamic correlation functions. The intermediate scattering function, for example, can be generalized to include a waiting time t_w, which is irrelevant in equilibrium, but becomes important out of equilibrium,

$$\mathrm{F}(q, t_w + t, t_w) = \langle \exp\{iq[n(t_w + t) - n(t_w)]\}\rangle. \tag{6.1}$$

Such relaxation functions can often be separated into two components,

$$\mathrm{F}(q, t_w + t, t_w) = \mathrm{F}_{fast}(q, t) + \mathrm{F}_{aging}(q, t_w + t, t_w), \tag{6.2}$$

where F_{fast} contains rapid processes which do not depend on t_w, and F_{aging} contains the slower processes which do depend on t_w. The aging component often obeys a simple scaling such that

$$\mathrm{F}(q, t_w + t, t_w) = \mathrm{F}_{fast}(q, t) + \mathrm{F}_{aging}(q, t/t_w^{\mu}) \tag{6.3}$$

where $\mu \leq 1$. A simple explanation for this type of behavior is that the free energy landscape in aging systems is roughly divided into two scales, such that the distribution of free energy barriers assumes a bimodal character with a group of relatively small and a group of relatively large barriers. The fast relaxations reflect jumps over the small barriers, which can always be readily overcome and are thus independent of t_w. The slower relaxations are set by the scale of the large barriers and thus exhibit a dependence on t_w as the system gradually evolves within and between the larger scale basins.

Theories of glass formation

A unified theoretical framework within which the glass transition may be understood does not currently exist. Thus many independent approaches continue to be developed and examined, each generally applicable to some finite region of the transition. Some approaches can be classified as thermodynamic or equilibrium theories, while others are based on purely dynamic or nonequilibrium arguments. Since no single theory has proven adequate, it is not yet clear whether the structural glass transition is driven primarily by an underlying thermodynamic transition, by processes of purely dynamic origin, or by some combination of the two scenarios (as was found to be the case for spin glasses).

Two notable early theories include the free-volume model [169] and the Adam-

Gibbs configurational entropy model [170]. The free-volume approach attributes the increase in viscosity to a decrease in the available free-volume distributed throughout the system. The self-diffusion coefficient is related to the free-volume v_f by

$$D_s = ga^* u_v \exp\left(-\gamma_0 v^*/v_f\right), \tag{6.4}$$

where g is a geometrical factor, a^* is a molecular diameter, u_v is the gas kinetic velocity, $1/2 < \gamma_0 < 1$ is an overlap factor, and v^* is the critical free volume below which transport ceases. Specific relations bewteen v_f and T generally lead to expressions such as

$$D_s = ga^* u_v \exp\left(\frac{-\gamma_0 v^*}{\bar{v}_m \alpha_T (T - T_0)}\right) \tag{6.5}$$

where $\bar{v}_m$ is the mean molecular volume, α_T is the mean thermal expansion coefficient, and T_0 is the T at which free volume disappears. This is the Vogel-Fulcher equation, derived here from a scenario based on intuitive physical assumptions. Various aspects of the glass formation process can be reasonably well described with the free-volume approach, but its main drawbacks seem to be that it does not address the specific microscopic dynamic processes associated with rearrangements of v_f and that an unambiguous definition of v_f itself is unavailable.

Thermodynamic approaches generally postulate a vanishing configurational entropy density s_c in glass forming liquids below some critical temperature T_0. s_c is a reflection of the number of disordered microstates accessible to the system at a given T, and this number is assumed to control the time scale for liquid-like relaxation. Dynamic arrest is then driven by an underlying thermodynamic singularity at T_0, when the number of possible states goes to one. Essentially, the system is viewed as a mosaic of cooperatively rearranging regions, wherein the average cooperative volume approaches the system volume at T_0 and further rearrangements become impossible. Relaxation times can be predicted by applying the Adam-Gibbs hypothesis, which states that τ is related to s_c as

$$\tau = \tau_0 \exp \frac{B}{T s_c(T)} \tag{6.6}$$

where τ_0 and B are constants. When $s_c \sim T - T_0$, a Vogel-Fulcher equation is again obtained. Both of these early models provide physical insight into the types of microscopic features and thermodynamic scenarios that may drive glass formation, especially in the deeply supercooled regime, but they are not rigorously justified from a statistical mechanical viewpoint.

The most significant modern theoretical advances have been concentrated near the early stages of slowing. Mode coupling theory [28–30] (MCT) and molecular dynamics [13, 171–173] (MD), for example, have provided insight into the initial regime of slowing above the so-called crossover temperature T_c, but are ineffective when applied to the slower regimes that occupy roughly ten orders of magnitude in time between T_c and the glass transition temperature T_g. MCT provides self-consistent equations of motion for the liquid correlation functions from first principles. The relaxation functions can be shown to obey a non-linear memory equation of the form

$$\ddot{\mathrm{F}}(q,t) + \Omega_0^2(q)\mathrm{F}(q,t) + \int_0^t M(q,t-s)\dot{\mathrm{F}}(q,s)ds = 0 \tag{6.7}$$

where $\Omega_0^2(q) = k_B T q^2/(mS(q))$ is the sound wave vibrational dispersion and $M(q,t-s)$ is the (generally unknown) memory function. If certain simplifying approximations are made, these equations can be solved numerically and have been shown capable of describing the early stages of glass formation in many liquids with excellent accuracy. The MCT transition is purely dynamical, driven by a non-linear feedback mechanism in the relaxation functions. Roughly, the relaxation time of a given dynamic correlation function diverges as its correlation magnitude approaches some critical value at temperature T_c.

A sharp dynamical transition is thus predicted at T_c, with relaxation times diverging as $\tau \sim (T - T_c)^\gamma$. Just above T_c, the correlation functions exhibit two-step relaxations, and the slow α relaxations eventually diverge at T_c. The fast β relaxations (decay toward plateau) are asymptotically described by the so-called MCT critical decay power law, $\mathrm{F}(q,t) = f + At^{-a}$, where f is the nonergodicity parameter or plateau height and A and a are constants. The late β relaxations (initial decay after plateau) are asymptotically described by the von Schweidler law, $\mathrm{F}(q,t) = f - B(t/\tau)^b$, where B and b are constants. The exponents γ, a, and b are related through $\gamma = 1/(2a) + 1/(2b)$. The slow α relaxations are generally well-described by stretched exponentials, with typical values for β near 0.6. These predictions are fulfilled with excellent accuracy during the onset of glass formation in many liquids, but the sharp singularity at T_c is not observed. The liquid instead continues to relax through activated hopping events that are not accounted for in idealized MCT. Thus extending MCT to the later stages of the glass transition remains an open subject of research.

MD simulations have also proven fruitful when applied to the early stages of the transition, but this method reaches its computational limits many orders of magnitude below the time scales relevant to most of the glass formation process. One of the enduring missions of glass modeling has therefore been to extend the reach of atomistic models – through brute force or conceptual advances – further in time and deeper into the slow regimes of the transition.

Time- or ensemble-averaged dynamic density functional theories [17, 102–106, 109–112, 149–152, 174] (DDFTs) have been proposed as an efficient means of describing slow dynamics in dense liquids below T_c, but several key issues concerning such theories remain unresolved: which of the proposed equations of motion are most appropriate, whether the details of the free energy significantly influence the dynamics, and whether the detailed predictions of MCT can be reproduced and eventually improved upon by such theories.

The early classical DFTs of freezing were developed to describe equilibrium properties of discontinuous liquid to crystal transitions, and they typically center on postulated free energy functionals of the ensemble-averaged or time-averaged atomic number density field [7, 8, 10]. Explicit equations of motion for the density field were introduced with the aim of building a coarse-grained dynamical framework for inhomogeneous fluids and liquid-solid systems, now sometimes referred to as DDFTs. Some of the common Langevin equations have been explicitly derived from microscopic dynamics, others are simply plausible phenomenological approximations. These theories in general are considered more fundamental than MCT in that the equations of idealized MCT can be derived from a generic DDFT starting point, and their time-averaged nature means that in principle they can describe dynamics beyond the early stages of the transition, into the proposed activation dominated regime. The simplest, most efficiently simulated variation of this approach, to our knowledge, is the PFC class of free energy functionals [4, 25] which will be examined in this chapter.

Mean field DFT functionals are known to typically produce multivalley free energy landscapes in which an exponential number of aperiodic solid states coexist below a certain T [33, 153–159]. These states have average free energies intermediate between those of the mobile liquid and the underlying crystalline phase. However, the nature of the transition by which a liquid evolves toward and between these aperiodic solid states upon quenching is influenced heavily by the microscopic dynamics and thus, in DDFT, by the equation of motion employed. Approximate analytic results [110, 149, 150] indicate that two DDFT equations of motion may describe a MCT-type glass transition. Numerical confirmations of stretched exponential decay and super-Arrhenius slowing have been reported for related models [151, 160], but no such numerical studies of a proper DDFT seem to exist, and no evidence of plateauing correlators or tests of the associated MCT scaling predictions have been reported for any such models to our knowledge.

Here the results of direct numerical simulations of a candidate DDFT that considers both inertia and damping, and utilizes the PFC class of free energy functionals are presented. The equation of motion for the time-averaged density field contains three dynamic components; ‘slow’ diffusive damping, ‘fast’ inertial propagation, and additive stochastic noise. This is the so-called MPFC form first proposed by Provatas *et al* [74], and used here in combination with a modified highly nonlinear free energy functional due to Chan *et al* [95], which will be denoted as the Vacancy or VPFC form.

This particular stochastic PFC-DDFT framework is shown to successfully describe several aspects of the glass formation process over multiple time scales while sensibly capturing the underlying competition between vitrification and crystallization in both monatomic and binary systems. In Section 6.2 the model is introduced and some connections with other DDFTs of glass formation are briefly established. Issues related to defining and controlling temperature in the given model are discussed, and a minimal temperature quenching procedure is outlined. Results for monatomic systems are presented in Section 6.3, while binary systems are treated in Section 6.4. Monatomic systems are found to exhibit early signs of glass formation at intermediate temperatures and times but ultimately to crystallize unless rapidly quenched to a low temperature. Binary systems are shown to be much less prone to crystallization and to display a rich and accessible range of characteristically glassy dynamics. The nature of the resulting glass transition (strong vs. fragile) is characterized as a function of the balance of inertial and damping terms, and links between the degree of fragility and cooperativity, extended correlations, and memory effects are discussed. It is verified here for the first time that DDFT can describe a fragile MCT-type glass transition in detail, over multiple time scales, and that relatively simple PFC free energies express the relevant physics of dense supercooled liquids. It is hoped that these findings will encourage further study toward determining the degree to which such theories can ultimately extend the temporal reach of atomistic models of glass formation.

6.2 Model Equations and Notation

The dimensionless Helmholtz potential of a two component PFC system can be written

$$F = \int d\vec{r}\,[f_{AA} + f_{BB} + f_{AB}] \tag{6.8}$$

where here the specific forms are given by [175]

$$f_{ii} = \frac{n_i}{2}\left[r_i + (q_i^2 + \nabla^2)^2\right] n_i + \frac{1}{4}n_i^4 + H_i(|n_i|^3 - n_i^3)$$

and

$$f_{AB} = \frac{n_A}{2}(q_{AB}^2 + \nabla^2)^2 n_B + \frac{r_{AB}}{2} n_A^2 n_B^2.$$

In this notation $i = A$ or B, $n_i \to n_i(\vec{r}, t) + \bar{n}_i$ is the scaled time averaged number density of i particles, $\bar{n}_i$ is the species average number density, r_i is related to the liquid bulk modulus, q_i sets the equilibrium distance between particles of the same species, q_{AB} sets that between A and B particles, and H_i and r_{AB} are constants (see Refs. [4, 25] for further discussion of how these parameters relate to material properties). The terms multiplied by H_i discourage $n_i < 0$ and are the distinguishing feature of the Vacancy or VPFC model [95, 175]. A hard $n_i \geq 0$ cutoff enforces the physical interpretation of n_i as a constrained number density and in doing so produces a range of highly nonlinear responses. The resulting solutions take the form of interacting time-averaged density peaks, with local regions of $n_i \simeq 0$ representing unoccupied, or vacancy, sites.

As a first approximation for the dynamics of the density fields, diffusive relaxations can be described through a direct minimization of the local free energy, and all dynamic processes on shorter time scales can be absorbed into an additive stochastic noise term, giving Model B dynamics,

$$\frac{\partial n_i}{\partial t} = \nabla^2 \mu_i + \sqrt{M_i}\eta_i. \tag{6.9}$$

Here t is the dimensionless time, M_i is a constant proportional to temperature, and η_i is a gaussian stochastic noise variable with $\langle \eta_i(\vec{r}_1, t_1)\eta_i(\vec{r}_2, t_2)\rangle = \nabla \cdot \nabla \delta(\vec{r}_1 - \vec{r}_2)\delta(t_1 - t_2)$. The PFC simulations reported in Chapter 5 indicate that Eq. (6.9) supports metastable glass-like states but in general produces a discontinuous, nucleation-driven liquid to glass transition [33]. The dynamic correlators often exhibit stretching, but clear two-step relaxations and Vogel-Fulcher divergences are not readily observed. An earlier study employing non-conserved dynamics and conserved MC-type dynamics similarly concluded that super-Arrhenius slowing does occur but that the overall nature of the slow relaxations are in many ways dissimilar to those of a glass forming liquid [176].

The equation of overdamped DDFT also considers only diffusive time scales but with a spatially varying mobility function and multiplicative noise,

$$\frac{\partial n_i}{\partial t} = \nabla \cdot (\Gamma_i(\vec{r})\nabla \mu_i) + \sqrt{M_i}\nu_i \tag{6.10}$$

where $\Gamma_i(\vec{r})$ is generally set to $n_i(\vec{r}) + 1$ and

$$\langle \nu_i(\vec{r}_1, t_1)\nu_i(\vec{r}_2, t_2)\rangle = \nabla \cdot \nabla \left[(n_i(\vec{r}) + 1)\delta(\vec{r}_1 - \vec{r}_2)\delta(t_1 - t_2)\right].$$

This equation's connection with the MCT of glass formation has been studied by Kawasaki *et al* [149] and by Andreanov *et al* [150]. As noted in Chapter 2, Kawasaki *et al* have suggested that the non-constant mobility term $n_i(\vec{r}) + 1$ in Eq. (6.10) gives rise to caging effects and is therefore essential for describing dense glass forming liquids. In fact, their calculations indicate that the standard equations of the MCT glass transition can be derived from Eq. (6.10) but not from Eq. (6.9). A recent derivation of Eq. (6.10) relevant to PFC colloidal models has been given [60], as well as discussion of its application to binary PFC systems [41].

A third equation reintroduces a 'fast' time scale through an added inertial or wave-like term,

$$\frac{\partial^2 n_i}{\partial t^2} + \beta_i \frac{\partial n_i}{\partial t} = \alpha_i^2 \nabla \cdot (\Gamma_i(\vec{r}) \nabla \mu_i) + \sqrt{M_i} \nu_i \tag{6.11}$$

where α_i and β_i are constants. The introduction of Eq. (6.11) to PFC modeling was discussed in Chapter 2. In the realm of DDFT and glass formation, Archer [109, 110] and Marconi and Tarazona [111, 112] have derived the noiseless version of Eq. (6.11) to describe dense fluids with both inertia and damping, as an extension of the simpler overdamped dynamics of Eq. (6.10). Recent analyses of Eq. (6.11) suggest that it too may recover the class of MCT equations for the liquid dynamic correlators that successfully describe a wide range of glass forming behaviors [110].

In this chapter Eq. (6.11) with $\Gamma_i(\vec{r}) = 1$ is numerically investigated, without approximation. Note that inclusion of stochastic noise implies an interpretation of DDFT in the time-averaged sense rather than in the ensemble-averaged sense [97, 98]. Equations of motion that explicitly consider additional fields such as momentum or energy density are not considered, as the single field description is significantly more tractable in terms of direct simulation, analytic solution, and connection to MCT. An explicit Euler finite difference algorithm was used to solve Eq. (6.11) in three dimensions with periodic boundary conditions (see Appendix A.3).

Since the PFC free energy is generated through a truncated expansion of the Ramakrishnan-Yussouff functional [7], every variable PFC parameter may in principle have some degree of temperature dependence when associated with a particular molecular system. But for the sake of simplicity and of demonstration, temperature will here be associated with only one variable, that specifying the magnitude of stochastic thermal noise, $T = T_N M_i$. This minimal temperature quenching procedure induces all of the glass forming behaviors that have been selected for study. Equilibrium liquid states at high M_i were thus quenched by lowering $T = T_N M_i$ at some rate $\dot{T}$, and the freezing transition was analyzed for onset of vitrification or crystallization. Similar results have been obtained by increasing the average density rather than lowering M_i, as is generally done with hard sphere liquids.

The noise-based method of varying T emphasizes the stochastic nature of the present model, whereas the deterministic versions of DDFT describe a glass transition associated with the temperature dependence of the free energy alone. The effect of varying M_i should be similar to that of varying the *effective* free energy functional generated by renormalization over the stochastic noise contributions.

6.3 Results: Monatomic Liquids

Simple monatomic systems generally have low barriers to crystallization, a property which limits their utility as models for glass formation. Signs of glass formation may nonetheless be observable near the freezing temperature of the crystal, T_f, before the onset of crystallization. Glass states may also be stable for long times when the liquid is quenched very rapidly to temperatures well below T_f, producing a characteristic 'nose' feature in the system's time-temperature-transformation (TTT) diagram. The results presented in this section confirm that these are precisely the freezing behaviors produced by the monatomic VPFC model.

Simulation data relevant to glass formation are shown in Fig. 6.1 for a representative monatomic system. For $T \gtrsim 1.6$ the structure and dynamics are those of a normal liquid. The measured intermediate scattering functions, $\mathrm{F}_{ij}(q,t) = \langle \delta n_i(q,0) \delta n_j^*(q,t) \rangle / \mathrm{F}_{ij}(q,0)$, decay exponentially, the corresponding average relaxation times show an Arrhenius T dependence, and the structure factors are characteristic of an equilibrium liquid state. The function $\mathrm{S}^P(q)$ quantifies the structural correlations of the localized peaks in the density field: $\mathrm{S}_{ij}^P(q) = \langle \delta n_i^P(q) \delta n_j^{P*}(q') \rangle$, where $\delta n_i^P(r)$ is a binary map of the positions of the local number density peaks.

Below $T \simeq 1.6$, the liquid begins to show signs of nonequilibrium behavior and the onset of glass formation. $\mathrm{F}(q,t)$ becomes increasingly stretched and begins to exhibit a shoulder, the average relaxation time briefly begins to grow with a super-Arrhenius T dependence, and a split second peak emerges in $\mathrm{S}^P(q)$. But signs of glass formation persist only to the freezing temperature of the crystal, T_f. Below this point crystallization interrupts the apparent glass transition unless the liquid is rapidly quenched well below T_f. The time-temperature-transformation (TTT) diagram shown in Fig. 6.1(d) demonstrates this behavior. The profile of the nose feature is typical of

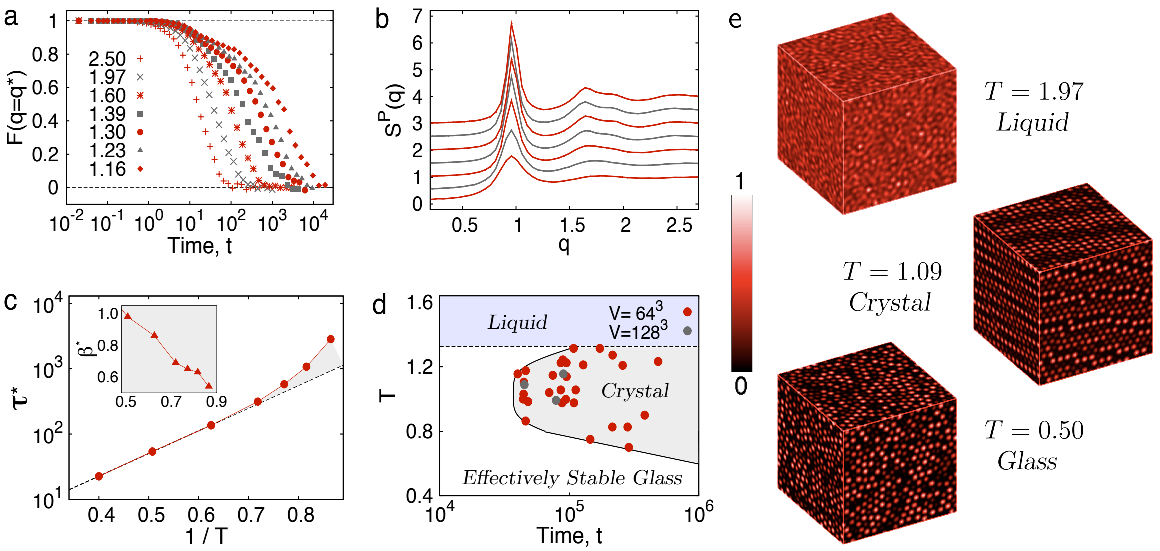

Figure 6.1: Glass formation and crystallization in the monatomic VPFC model. (a) F(q^*, t) at various T where q^* corresponds to the first peak maximum in S$^P(q)$. (b) S$^P(q)$ at same T as in (a), offset vertically by $0.5n$ with $n = 0, 1, ...$ (c) Arrhenius plot of τ^* from F(q^*, t), Inset: stretching exponent β^* from fit to F$(q^*, t) = \exp\left[-(t/\tau^*)^{\beta^*}\right]$. (d) *TTT* diagram: samples quenched from $T = 1.6$ at various $\dot{T}$, points denote where crystallization occurred, the solid line is a guide to the eye. (e) Representative $n(\vec{r})$ configurations for three states, averaged over $4,000t$. Unless specified otherwise, $\bar{n}_A = 0.15$, $r_A = -0.9$, $q_A = 1$, $H_A = 1500$, $T_N = 1000$, $\alpha_A = 1$, $\beta_A = 0.01$, $f_{BB} = f_{AB} = 0$, $\Delta x = 1.0$, $\Delta t = 0.02$, and $V = 128^3$.

materials with relatively marginal glass forming ability, such as metallic glasses. Since long-lived glassy states are not supported in the region $0.6 \lesssim T \lesssim T_f$, one cannot study a gradual dynamic transition from liquid to glass.

Before moving on, it may be worth noting that this example demonstrates one of the advantages of the PFC-DDFT approach to glass formation; that all fundamental aspects of phase behavior in liquid-solid systems are naturally incorporated. The crystallization process is crucial to any description of freezing when the relevant energy barriers are low, and such models automatically account for it. Idealized MCT, for example, does not. It predicts an uninterrupted divergence of the liquid relaxation time below T_f for this system. Even when crystallization does not play an important role, access to thermodynamic variables for liquid, glass, and crystal phases as well as a tangible description of the transformation dynamics between each makes the

PFC-DDFT approach an appealing framework for this problem.

6.4 Results: Binary Liquids

The binary system studied here contains equal number densities of A and B atoms ($\bar{n}_A = \bar{n}_B = 0.075$), and the equilibrium spacing of A atoms is 20% smaller than that of B atoms ($q_B/q_A = 0.8$). Other size and concentration ratios have also been examined, but the discussion here will be limited to the $q_B/q_A = 0.8$, $\bar{n}_A = \bar{n}_B = 0.075$ system. The other model systems show similar qualitative behaviors.

6.4.1 Inertia versus damping

The results presented in the previous section were limited to a single, highly underdamped dynamic condition, $\alpha_A/\beta_A = 100$. In this section the qualitative behavior of the chosen binary model is outlined for a range of dynamic conditions, from highly underdamped ($\alpha_i/\beta_i = 100$) to highly overdamped ($\alpha_i/\beta_i = 0.01$). Then results for the highly underdamped case are presented in greater detail, as this condition produces the widest range of glass forming behaviors.

Only the NN correlations are plotted in Figs. 6.2(a)-(c), where N denotes the full density field $n_A + n_B$. When damping dominates, an effectively stable glass with dynamics resembling those of a strong glass former is generated. The dynamic correlators are generally best fit as a single exponential decay for all accessible T, with increased stretching as T is lowered, but any plateaus are absent or ill-defined in the $\alpha_i/\beta_i \lesssim 1$ data. The relaxation times exhibit a nearly Arrhenius T-dependence over the entire accessible T-range.

At the opposite extreme, when inertia dominates, a transition with dynamics characteristic of fragile liquids is generated. The dynamic correlators show both stretching and clear plateauing as T is lowered, and the divergence of the relaxation time is well fit by the Vogel-Fulcher form ($\tau = \tau_0 \exp[B/(T - T_0)]$). This divergence becomes increasingly super-Arrhenius at higher T as α_i/β_i grows. The underdamped transition at this level of detail qualitatively resembles that described by MCT.

The fragility of the PFC liquid therefore appears to be strongly linked with the balance of inertial and damping terms in Eq. (6.11), α_i/β_i. The degree of fragility is

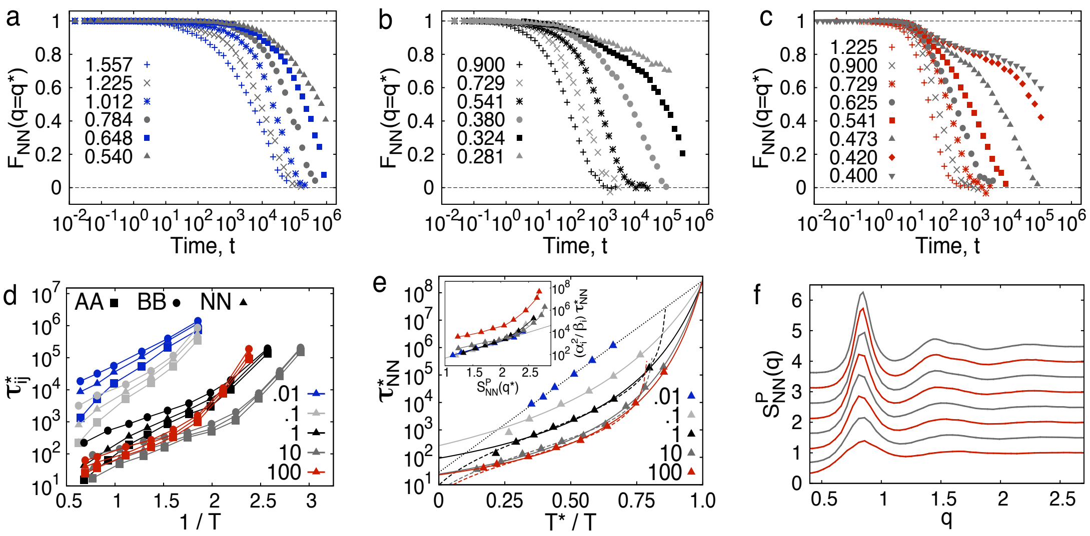

Figure 6.2: Binary VPFC results for various damping conditions. $\mathrm{F}_{NN}(q^*, t)$ at various T are shown for α_i/β_i of (a) 0.01, (b) 1, and (c) 100. (d) Arrhenius plot of the structural relaxation times τ^*_{ij}. (e) the same data (NN only) scaled as an Angell plot to clarify strong vs. fragile behaviors, with Vogel-Fulcher fits shown as solid lines and power law fits as dashed lines. Inset: $(\alpha_i^2/\beta_i)\tau^*_{NN}$ vs. $\mathrm{S}^P_{NN}(q^*)$, demonstrating scaling of overdamped systems and deviation from this scaling when inertial effects become large. (f) $\mathrm{S}^P_{NN}(q)$ for $\alpha_i/\beta_i = 100$. $\bar{n}_A = \bar{n}_B = 0.075$, $r_i = -0.9$, $q_A = 1$, $q_B = 0.8$, $H_i = 1500$, $T_N = 1000$, $q_{AB} = 8/9$, $r_{AB} = 100$, $\Delta x = 1.0$, $\Delta t = 0.025$, and $V = 64^3$, 128^3, or 256^3.

in turn correlated with the nominal spatial extent of cooperative dynamic behavior, which is set by an inherent length scale associated with the inertial term. This term generates wave modes which propagate over a fixed length scale in a crystal before being damped, and the resulting dynamic correlation length follows $\xi_D^{\text{crystal}} \sim \alpha_i/\beta_i$ [74]. In a normal liquid these correlations are largely suppressed by the low density and weak structural correlations, so that $\xi_D^{\text{liquid}} \ll \xi_D^{\text{crystal}}$ and cooperativity is limited. But with greater supercooling, as the system becomes increasingly dense and solid-like, the inertial correlations survive over length scales which likely approach ξ_D^{crystal}. Roughly, $\xi_D^{\text{liquid}} \to \xi_D^{\text{crystal}} \sim \alpha_i/\beta_i$ as $T \to T_g$. (This behavior may signal the onset of a percolation-type transition, wherein the growing correlation volumes eventually form a continuous rigid network persisting over all accessible t. See for example Refs. [177–179].)

The effects of this growing dynamic length scale are therefore especially prominent in highly underdamped systems, where its properties can be observed and quantified through finite size effects in $\mathrm{F}(q, t)$. Its effects are apparent only upon the slow relaxation processes in the glass-like liquid, with the fast, pre-plateau processes remaining effectively independent of system size. As an example, when $\alpha_i/\beta_i = 100$ finite size effects in the post-plateau relaxations become numerically insurmountable below $T \simeq 0.4$. Measurements indicate that the average two point liquid static correlation length ξ_S^{liquid} grows slowly, approximately as $1/T$, while the dynamic correlation length grows more rapidly, as $\xi_D^{\mathrm{liquid}} \sim (T - T_0)^{-1 \pm 0.35}$ (see Fig. 6.5(c)). This distinction indicates that the supercooled liquid exhibits heterogeneous dynamics driven by strong inertial effects. Similar links between slowing dynamics and growing dynamic correlation lengths have been discussed within the random first order theory (RFOT) [180], the Adam-Gibbs-DiMarzio entropic theory [170], MCT [181], MD simulations [171, 182, 183], and colloidal experiments [184, 185], to name a few. Thus, the growing ξ_D^{liquid} that we have identified in underdamped DDFT is consistent with known results from theory and experiment. Whether such a length scale can generally be associated with inertial effects is for now unclear.

A correlation between fragility and the length scale for cooperativity is consistent with existing interpretations of strong and fragile liquids [186]. The cooperative dynamics permitted when oscillations are weakly damped appears to be fundamental to the fragile glass transition or at least sufficient for its existence. A link to recent experiments on colloidal glasses which demonstrate a transition from strong to fragile behavior as the elastic properties of the colloidal particles become increasingly stiff [187] also appears relevant. When overdamped, Eq. (6.11) describes a very soft, viscoelastic solid, while elastic stiffness and fragility both increase as damping is reduced. This is because $\alpha_i \sim v_s \sim \sqrt{E}$, where v_s is a sound speed and E is the relevant elastic modulus. Greater elastic stiffness should therefore correspond to reduced effective damping and an expectation of increased fragility. This agrees with the trend found in Ref. [187]. (Links between fragility and elastic properties have also been discussed in Ref. [188])

A slightly different physical picture can be invoked by considering Eq. (2.32), which suggests that α_i/β_i controls the dynamic memory time rather than the dynamic length scale. Less damping then corresponds to enhanced memory effects, which leads to increased caging and a more rapid slowing of relaxations. This argument is probably limited to the range of dynamics in which cooperativity or memory effects are non-negligible, $\alpha_i/\beta_i \gtrsim 3$, wherein the dynamics become steadily more fragile as damping is reduced. For much smaller α_i/β_i, relaxations become slower in general, presumably due to the loss of a discernible oscillatory relaxation channel, but lose their two-stage and super-Arrhenius features.

6.4.2 Inertia dominated dynamics

The case of $\alpha_i/\beta_i = 100$ will now be examined in greater detail. Figures 6.3 and 6.4 show simulation images of $N(\vec{r}) = n_A(\vec{r}) + n_B(\vec{r})$ for this system averaged over various times at $T = 1.225$, 0.541, and 0.420. Caging is apparent at short times for all T, as the peaks oscillate locally but rarely move large lateral distances. Eventually the time-averages of the smaller A peaks begin to spread as the majority have escaped their initial cages, and the larger B peaks evolve similarly at slightly later times. In the intervening period, the B particles are effectively caged by the A particles. When averaged over very long times, both density fields approach a structureless state with density $\bar{n}_i$.

As T is lowered and the liquid becomes glass-like, the long time averages retain more of their original structure as the peaks exhibit less translational freedom. It is important to note that time averages are shown at equal multiples of each liquid's relaxation time, not at equal t, so that time scales remain normalized as T is varied. The continuous but rapid decline in translational freedom as T is lowered signals a smooth transition from liquid-like to activated dynamics. This is consistent with the postulated crossover at T_c, below which relaxations are expected to be limited by increasingly rare, heterogeneously correlated cage escape events. This transition coincides with the emergence of the plateau in $\mathrm{F}_{ij}(q,t)$ and the split second peak in $\mathrm{S}^P_{NN}(q)$ below $T \simeq 0.6$, as shown in Figs. 6.2(c) and (f).

6.4.3 Comparison with MCT

Figure 6.5 shows data for the $\alpha_i/\beta_i = 100$ system relevant for comparison with the predictions of MCT. The nonergodicity parameter, $f_{ij}(q)$ (height of the plateau in $\mathrm{F}_{ij}(q,t)$), is plotted in Figure 6.5(a) for $T = 0.420$. It follows the normal MCT

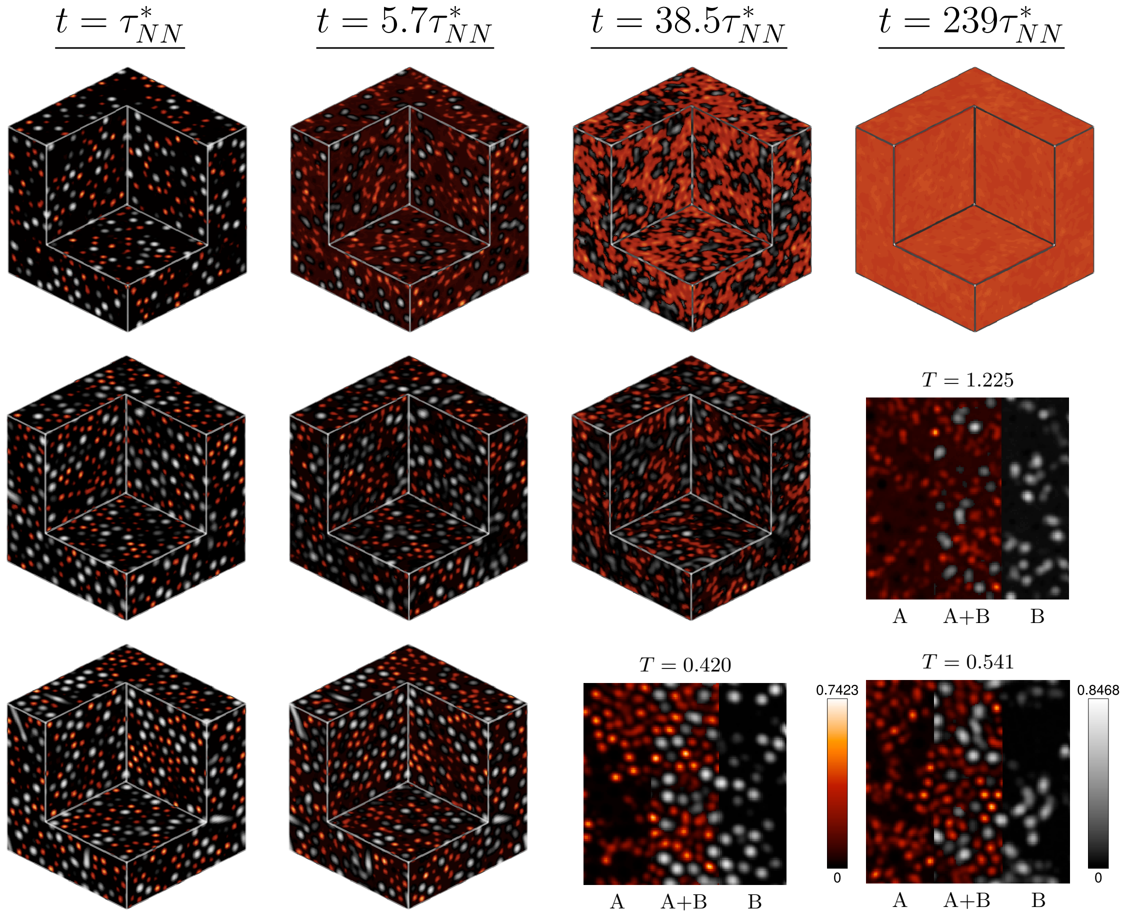

Figure 6.3: Time-averaged density evolution in the supercooled binary liquid. Binary number density field at $T = 1.225$ (top), 0.541 (middle), and 0.420 (bottom) averaged over the indicated multiples of each system's relaxation time. A sub-cubic section of each cell has been removed to reveal a portion of the inner simulation box. $n_A(\vec{r})$ time averages are displayed with a black-orange color scheme, $n_B(\vec{r})$ with black-white. 2D cross-sections from the $t = 5.7\tau^*_{NN}$ images are displayed toward the bottom right. Each shows $n_A(\vec{r})$ time averages (left), overlay of $n_A(\vec{r})$ and $n_B(\vec{r})$ time averages (middle), and $n_B(\vec{r})$ time averages (right).

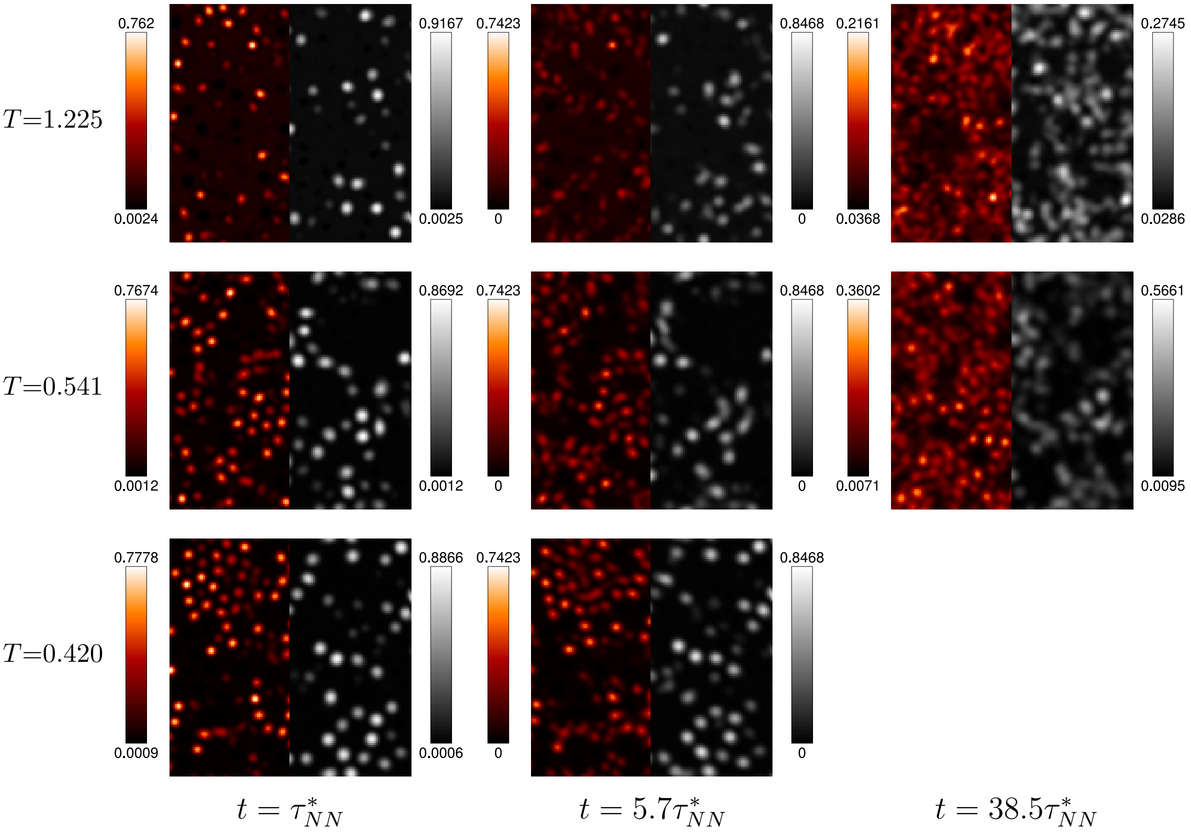

Figure 6.4: 2D cross-sections of the binary number density field at three temperatures, averaged over the indicated multiples of each system's relaxation time. The left half of each image shows $n_A(\vec{r})$ time averages (black-orange) and the right half shows $n_B(\vec{r})$ time averages (black-white).

behavior in which $f_{ij}(q)$ decays while oscillating in phase with $\mathrm{S}_{ij}(q)$.

Some of the dynamic scaling behaviors predicted by MCT are tested in Fig. 6.5(b). The von Schweidler law for late β-relaxations (initial decay after plateau) is an asymptotic approximation of the full MCT master relaxation curve. Present results indicate that the von Schweidler scaling, $\mathrm{F}(q,t) = f - B(t/\tau)^b$, is obeyed reasonably well over 2-3 orders of magnitude in time. The measured von Schweidler exponent $b \simeq 0.45 \pm 0.15$ is comparable to typical values. To within statistical error b is independent of q and T, consistent with asymptotic MCT, though the data suggests a moderate decrease in b with T. The initial decay to the plateau is best fit at intermediate T by a simple

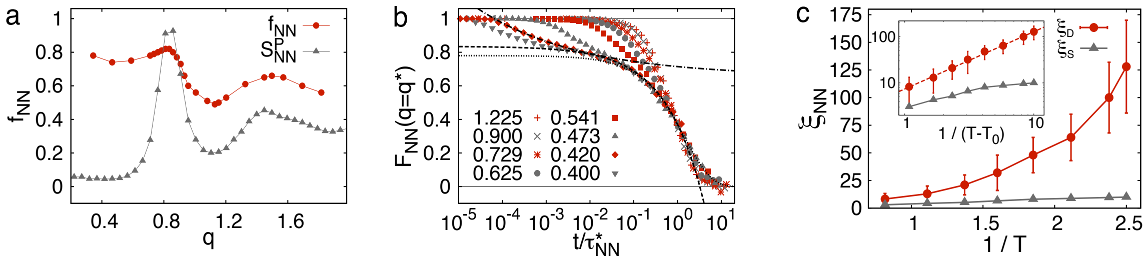

Figure 6.5: Comparison of the highly underdamped model with MCT and other theories. (a) $f_{NN}(q)$ shown with $\mathrm{S}^P_{NN}(q)/2.7$. (b) $\mathrm{F}_{NN}(q, t/\tau^*_{NN})$ with various MCT scaling functions. Dashed: von Schweidler law, Dotted: stretched exponential, Dashed-Dotted: $(1-f_{NN})\exp[-t/\tau_\beta]+f_{NN}\exp[-(t/\tau_\alpha)^\beta]$. (c) Static and dynamic correlation lengths vs. $1/T$. Inset: same data plotted vs. $1/(T-T_0)$ on a log-log scale. The dashed red line has a slope of 1, corresponding to $\xi_D \sim (T-T_0)^{-1}$.

exponential, though the MCT critical decay power law, $\mathrm{F}(q,t) = f + At^{-a}$, becomes the better fitting function once the plateau is well-defined. The measured critical decay exponents vary somewhat with ij, T, and q, but on average $a \simeq 0.3 \pm 0.1$.

The late α-relaxations predicted by MCT are generally well-approximated by a stretched exponential decay. The VPFC data are fit quite well by this form, as shown in Fig. 6.5(b), but with a stretching exponent β that decreases with T from approximately 1 to 0.6. MCT also predicts that the initial divergences of the fast and slow relaxation times follow power laws, $\tau_\beta \sim (T-T_c)^{-1/(2a)}$ and $\tau_\alpha \sim (T-T_c)^{-\gamma}$, respectively, where $\gamma = 1/(2a) + 1/(2b)$. Fits to these forms are shown in Fig. 6.2(e), and though the Vogel-Fulcher fits are superior, the power law fits are reasonably accurate through the early stages of super-Arrhenius growth. The resulting parameters, $\gamma \simeq 2.25 \pm 0.75$ and $a \simeq 0.33 \pm 0.1$, both agree with the values determined from fits to the relaxation functions within estimated error.

6.4.4 Aging properties

The effect of waiting time t_w on the supercooled liquid relaxations is shown in Fig. 6.6. Samples were quenched instantly from $T = 0.9$ to the indicated temperatures, and the $\mathrm{F}_{ij}(q, t_w + t, t_w)$ were then measured for values of t_w=10^0, 10^1, 10^2, 10^3, 10^4, and 10^5. The normal liquid at $T = 0.729$ exhibits only very minor signs of aging, even for values of t_w much smaller than the equilibrium relaxation time. This suggests that

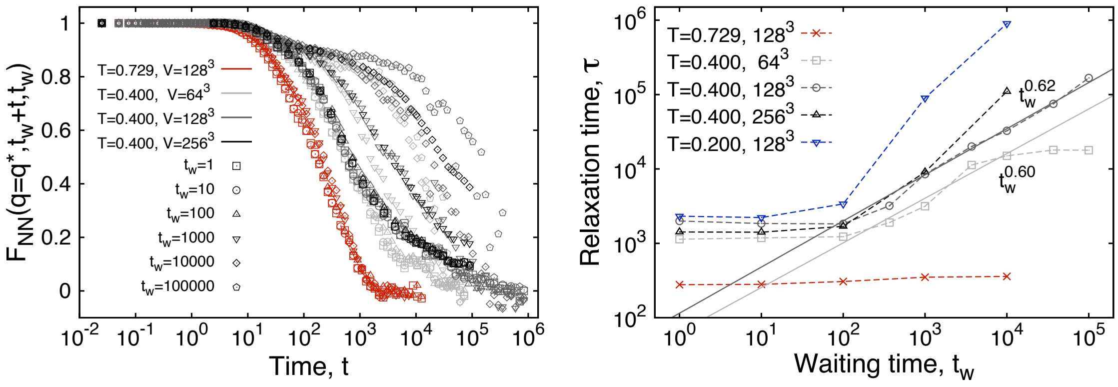

(a) (b)

Figure 6.6: Aging behavior in the underdamped binary VPFC supercooled liquid. Samples quenched from $T = 0.9$ and monitored after various waiting times t_w. (a) $\mathrm{F}_{NN}(q^*, t_w + t, t_w)$ for various t_w, T, and system sizes. (b) Measured relaxation time vs. t_w showing the various scalings with t_w.

the free energy landscape in the normal liquid state is relatively flat, such that any initial liquid-like state will already be close to equilibrium and will very rapidly lose any small initial history dependence.

At $T = 0.4$, well into the glass-like regime, clear aging effects emerge for all values of t_w smaller than the structural relaxation time. The general behavior is very similar to that observed in MD simulations [189] and colloidal experiments [12]. There is an initial range of small t_w values for which the relaxation functions show little or no t_w dependence. This behavior is apparently associated with the fastest possible relaxation process for a given T in this model, which effectively cuts off all faster time scales. Above this T-dependent cutoff, a systematic t_w-dependence becomes apparent, with very good adherence to the predicted $\mathrm{F}_{fast} + \mathrm{F}_{aging}$ decomposition. Short time scales remain independent of t_w, while slow relaxations scale quite well with t/t_w^{μ}. The measured values of μ are in the range of 0.5 to 1, with possible dependences on system size and T.

All of the t_w scalings break down at large t_w as the 'equilibrium' relaxation function is eventually obtained and aging ceases. The 'equilibrium' relaxation function depends on system size when finite size effects are present, as in the $T = 0.4$ and $T = 0.2$ data. Another interesting feature of the data is the long-time tail that appears for small t_w. This seems to be a reflection of the sudden introduction of slow processes and significant local trapping. The slow time scale is immediately evident in the relaxations for all t_w, but takes some finite amount of time to reach a steady state as the system settles into the new, more restrictive free energy landscape.

6.4.5 Bridging time scales

The issue of connecting these PFC results with physical time scales, by defining an effective coarse-graining time, has not yet been discussed in any detail. One way to make this connection, when the model describes two characteristic dynamic scales, is to define the coarse-graining time in terms of the relative separation of the two scales.

In the inertial equation of motion, the chosen separation between phononic and dissipative time scales can be interpreted to set the physical time scales being modeled. Consider the case in which $\alpha = 1$. When $\beta \ll 1$, the two processes are relatively close in time, and the shortest time that can be described by the model should be near the characteristic phononic times. The longest time, given finite computational power, will likely be three to six orders of magnitude above phonon times. When $\beta \gg 1$, the two time scales become widely separated, and the shortest time that can be described should eventually become longer than the characteristic phononic times. Fast processes are effectively integrated out or neglected in such cases, and the longest time described then increases in proportion to β. If the characteristic phononic times are regarded as relatively fixed (in physical units), then increasing β can be interpreted as increasing the physical coarse-graining time. Thus, for the inertial PFC model in the limit of fixed T, the time over which a system is coarse-grained should be roughly proportional to the chosen damping rate β [$t_{\text{actual}} \sim \beta t_{PFC}$]. One can also show that linear vacancy diffusion times in the inertial model scale as βt in the long time limit, which further supports the idea that physical times enter the model through the damping rate.

This simple picture becomes more complicated when T is varied and/or when more realistic phonon dynamics are considered, but it should serve as one possible basis for connecting with physical times. It is also probably reasonable to assume that the accuracy of the description decreases as the coarse-graining time grows, but this should be less of a concern for some systems than for others. For example, the situation described above is similar to that known to occur in glass forming liquids. The characteristic relaxation times grow rapidly over a narrow T range, and the separation between ‘fast’ and ‘slow’ processes becomes quite large. Thus, the proposed ability to telescope our description across time scales should be most valid for systems like glass forming liquids, where there are rapidly varying, well-separated dynamic processes, with late time dynamics dominated by diffusive dissipation.

Figure 6.7 shows the application of these arguments to the binary VPFC glass forming liquid. Scaling t with β spreads the measured relaxation times out over eight orders of magnitude. If T is also scaled such that the curves converge, the envelope of the resulting data set can be well described by a Vogel-Fulcher fit. The corresponding $\mathrm{F}(q, \beta t)$ results can be superimposed in the same way to span 12 complete orders of magnitude in time. A further assumption is made here, that the large β results describe only the post-plateau relaxations and can thus be set to begin from the plateau height measured from small β simulations. Comparison with experimental data from a colloidal glass forming liquid shows striking qualitative agreement in terms of the universal relaxation features of fragile liquids. Quantitative agreement is not expected since the PFC model used here is not intended to describe a polydisperse hard sphere system. It should also be noted that the experimental data shows the self-part of the intermediate scattering function, while the PFC data shows the full $\mathrm{F}(q, t)$. Both forms generally show the same qualitative behaviors in glassy liquids.

Simulating 12 orders of magnitude (or more!) in time in three dimensions is a significant, previously undemonstrated capability and worth emphasizing. If phononic times are $\mathcal{O}(10^{-10}s)$, it is implied that the longest times on the PFC scale approach fully macroscopic values. For colloidal systems, this scale is shifted upward. It would clearly be of interest to examine more closely the accuracy of this description as a function of the coarse-graining time, and to determine more precisely when such a β-scaling might be valid.

An initial test of validity is shown in Fig. 6.7(c), where the MCT time-temperature superposition principle is applied to the scaled data. The detailed MCT functional form is relatively well obeyed by the dynamic correlators for all T and β, when time is scaled by β. This fact and the accurate Vogel-Fulcher envelope fit constitute an initial data-based justification of the proposed time scaling, though further study is

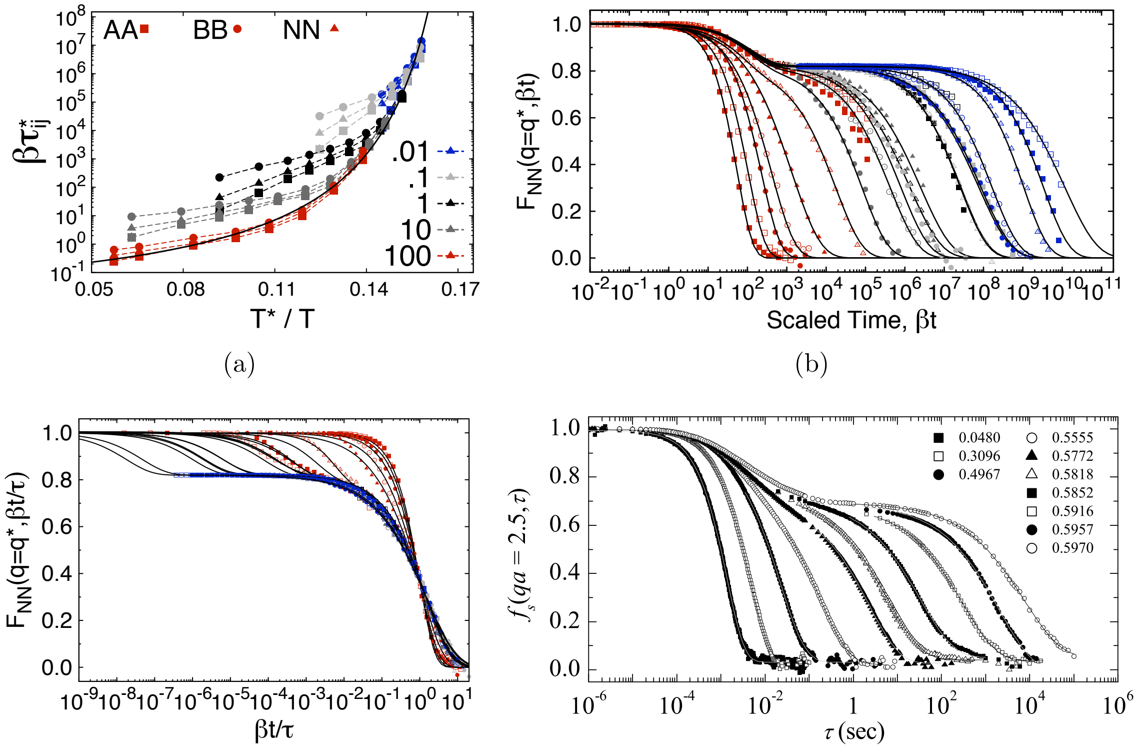

(a)

(b)

(c)

(d)

Figure 6.7: Binary VPFC glass formation in the β-scaled time limit and comparison with experimental colloid data. (a) Arrhenius plot of scaled relaxation times (offset in T) and the envelope Vogel-Fulcher fit (solid line). (b) Dynamic correlators $\mathrm{F}_{NN}(q, \beta t)$ scaled by β. The lines are fits to superimposed stretched exponentials. (c) Same as (b) except with the MCT t/τ scaling, to demonstrate general adherence to the time-temperature superposition principle. The pre-plateau fit for large β is assumed from the small β results. (d) Dynamic correlators for a hard sphere colloidal glass former [190].

clearly in order, considering the implications of such a scale bridging procedure.

6.5 Conclusions

These results confirm that the DDFT equation of motion with inertia does in fact describe a glass transition, and that when damping is weak this transition strongly resembles both the structural glass transition observed for fragile glass formers as well as that predicted by MCT. Relatively simple PFC free energies have also been shown to contain sufficient physics to produce a wide range of glassy behaviors, while still permitting efficient simulation. The necessary ingredients for a comprehensive glass transition in PFC-DDFT models therefore appear to be 1) sufficiently strong local nonlinear effects which act to suppress crystallization, naturally achieved through a simple repulsive coupling of A and B fields with lattice constants that differ by $\sim 10 - 25\%$, and 2) an equation of motion with two well-separated characteristic times, such as the underdamped inertial formulation. The highly nonlinear VPFC penalty term acts to further enhance glassy behaviors by highlighting packing and free volume effects.

Monatomic systems exhibit early signs of glass formation but eventually crystallize unless rapidly quenched to a very low temperature. Binary systems circumvent the crystallization problem and display a range of characteristically glassy behaviors. With overdamped dynamics, the observed relaxations exhibit stretching and the structure becomes increasingly glass-like as T is lowered, but the temperature dependence of the relaxation time is nearly Arrhenius. As the balance in the equation of motion is shifted toward the inertial term, or equivalently, as the propagation length scale is increased or the dynamic memory time is increased, the system becomes increasingly fragile. Plateauing relaxation functions are obtained due to the strong caging effect (a separation of cage rattling and cage escape time scales) as well as a Vogel-Fulcher temperature dependence for the slow relaxations. The transition is accompanied by increased cooperativity in the supercooled liquid and a growing correlation length, which may eventually saturate before T_g is reached.

The findings outlined here are consistent with a picture in which fragility is driven by a large dynamic correlation length, which in some cases can be associated with large elastic moduli. A direct test of this association could be performed using colloidal systems such as those of Ref. [187]. By varying the degree of confinement, one could compare the relative magnitudes and growth rates of any dynamic correlation length as behavior is varied from strong to fragile.

A conservative numerical algorithm was used in this work to demonstrate with maximum confidence that the simulation results are accurate and unbiased, and that the model does in fact produce a glass transition. Thus, the maximum accessible distance below T_c has not yet been probed, but preliminary results obtained using more advanced algorithms indicate that significant improvements in efficiency are at hand. The inclusion of an inertial term in the equation of motion, which allows one to study faster processes and the MCT plateau in the dynamic correlators, may inevitably impact the theory's ability to simulate extremely long relaxation times, but if the proposed time scaling remains valid with overdamped dynamics, then studies examining behavior well below T_c appear to be possible.

CHAPTER 7

Binary Heteroepitaxial Thin Film Growth

The characteristic spatial concentration patterns that develop in growing strained alloy films are outlined from simulation results for a two dimensional binary PFC model. These patterns are either lateral peak-to-valley variations or vertical surface-substrate variations, and the specific behaviors are shown to vary with misfit strain and species mobility ratio. Selected growth issues in simpler monatomic films are also discussed in relation to the predictions of continuum elastic theories. Significant deviations from the continuum limit are observed for relatively small deviations from idealized growth conditions.

7.1 Phenomenology and Literature

A potentially useful application of the PFC model is in the technologically important process of thin film growth. Heteroepitaxy, the growth of a crystalline film exhibiting atomic coherency with a crystalline substrate of differing lattice constant, is a widely encountered type of film growth for which the PFC approach is particularly well-suited. One may define three general stages in the growth of a film from the melt under uniaxial strain. The first is an initial surface roughening stage, described in the continuum limit by the Asaro-Tiller-Grinfeld (ATG) instability [191–193]. The second stage is characterized by strain relief through nucleation of dislocations at locations of strain concentration, typically on the roughened surface. During the third stage, the film surface relaxes back toward a planar morphology and uniform growth, as the initial misfit strain has been relieved by the dislocations.

The ATG theory describes the initial roughening process in terms of a chemical instability in solid films growing under uniaxial lateral strain. The instability is driven by a competition between surface energy and the rising elastic strain energy in the growing solid. Above some threshold, the amount of strain energy relieved by a rough surface will be greater than the corresponding increase in surface energy, so roughness becomes preferred at wavelengths above some critical value. The resulting surface corrugations generally grow unstably – a protuberance at the surface lowers the local chemical potential, increasing the local film growth rate, while a surface valley raises the local chemical potential, either slowing the local film growth rate or encouraging melting. The linear result is a divergence in surface roughness which eventually leads in real films to dislocation nucleation at valleys, followed finally by relaxation of surface roughness.

The ATG theory describes only the onset of the initial morphological instability, not dislocation nucleation and not the subsequent relaxation. It provides predictions for the thickness at which a film initially becomes unstable to roughening $h_{unstable}$, and above this thickness, the linear growth rates $\sigma(q)$ of all unstable surface perturbation wavenumbers q, including the fastest growing wavenumber q_c and the largest unstable wavenumber q_0. All of these results, being linear, apply to the onset of morphological instability and may not provide an accurate description of much of the roughening process.

Heteroepitaxy has been examined in previous PFC studies of monatomic films [3, 4]. These initial works showed that the three general growth stages of morphological instability, dislocation nucleation at the film surface, and relaxation are all naturally reproduced without the numerical singularities at cusp tips encountered in most continuum models. Another important effect in alloy films, compositional instability (phase separation in the growing film), requires consideration of multiple atomic species and their interaction. The purpose of this chapter is to illustrate how the binary PFC model addresses such compositional effects in alloy heteroepitaxy, focusing on the spatial dynamics of phase separation over diffusive time scales.

In traditional applications, crystal growers desire flat, uniform film surfaces with a minimal number of dislocations and a homogeneous composition throughout the film. In other cases, such as the epitaxial growth of quantum dots, it is important to carefully control the surface morphology and composition profile to produce the desired spatial patterns. Some devices incorporate continuous or discontinuous compositional grading so that electronic properties can be customized to meet a specific need. In all of these cases, it is important to understand the individual and cooperative roles of misfit strain (ϵ), solute expansion (η), and species mobilities (Γ_A, Γ_B) in the dynamic evolution of the phenomena listed above.

To date, a number of models of single component film growth incorporating surface roughening, dislocation nucleation, or both have been proposed [191, 192, 194–211], and models of binary film growth incorporating surface roughening and phase separation have been proposed as well [212–224]. However, there appear to be no existing models of binary film growth which capture all of the above important phenomena, and it would be reasonable to expect that new insights into the nature of film growth could be gained through the simultaneous investigation of all of these growth characteristics.

A unified treatment of this sort is justified for the following reasons. There is clearly a strong link between surface roughening and dislocation nucleation, as dislocations nucleate at surface cusps when the film becomes sufficiently rough. It is also known that phase separation in the film is significantly influenced by local stresses, which are inherently coupled to surface morphology and dislocation nucleation. The dynamics of the growth process must then be influenced by the cooperative evolution of all three of these phenomena. Numerical simulations will be presented in this chapter which show that the binary PFC model produces all of the growth characteristics described above, and that each is influenced by misfit strain and atomic size and mobility differences between species.

7.2 Model Equations and Notation

The binary PFC free energy used in this study is a simplified version of the general binary PFC formulation outlined in [25]. With a slight change in notation relative to

Chapter 6, it can be written in the form

$$F = \int d\vec{r}\Big(\frac{N}{2}\left[r + (1 + R_{AB}^2\nabla^2)^2\right] N + \frac{1}{4}N^4 + \frac{v}{2}c^2 + \frac{w}{4}c^4 + \frac{L^2}{2}|\vec{\nabla}c|^2 - A_0N^2c^2\Big) \tag{7.1}$$

where F is the dimensionless Helmholtz potential, $N = n_A + n_B$ is the scaled total number density field, $c = n_A - n_B$ is the scaled concentration field, $n_i \rightarrow n_i(\vec{r}, t) + \bar{n}_i$ is the scaled density field for i particles, $\bar{n}_i$ is the average scaled number density of i particles, $r + 1 = T$ is proportional to an offset temperature, $R_{AB} = 1 + \eta c$ sets the relative lattice constants of A and B particles, η is the solute expansion coefficient which defines the relative size difference of the two atomic species (a positive value of η corresponds to larger A atoms than B atoms), and v, w, L, and A_0 are additional constants. The system evolution is given by

$$\frac{\partial n_A}{\partial t} = \Gamma_A \nabla^2 \mu_A \tag{7.2}$$

$$\frac{\partial n_B}{\partial t} = \Gamma_B \nabla^2 \mu_B \tag{7.3}$$

where Γ_A and Γ_B are the diffusive mobilities of species A and B, respectively.

The physical problem recreated in these simulations is that of growth of a symmetric (i.e. 50/50 mixture, or average density difference $c_0 = \bar{n}_A - \bar{n}_B = 0$) binary alloy film from a liquid phase or from a saturated vapor phase above the bulk coherent spinodal temperature. Growth at temperatures above the miscibility gap is typical of experimental conditions and should ensure that phase separation is driven by local stresses and is not due to spinodal decomposition. Initial conditions consisted of a binary, unstrained crystalline substrate, eight atoms in thickness, placed below a symmetric supercooled liquid of components A and B. A typical phase diagram produced using parameters representative of those used in the present study is shown in Fig. 7.1, and the location of the supercooled liquid has been noted.

In all results presented, parameters are the same as in Fig. 7.1 except η, Γ_A, and Γ_B are varied as specified. $T = 0.89$ is used throughout. In what follows the misfit strain is defined as $\epsilon = (a_{film} - a_{sub})/a_{sub}$, where $a_{film} \approx a_A(1 + \eta c)$ in the constant concentration approximation. For a symmetric mixture of A and B atoms (i.e., $c_0 = 0$) $a_{film} = (a_A + a_B)/2$.

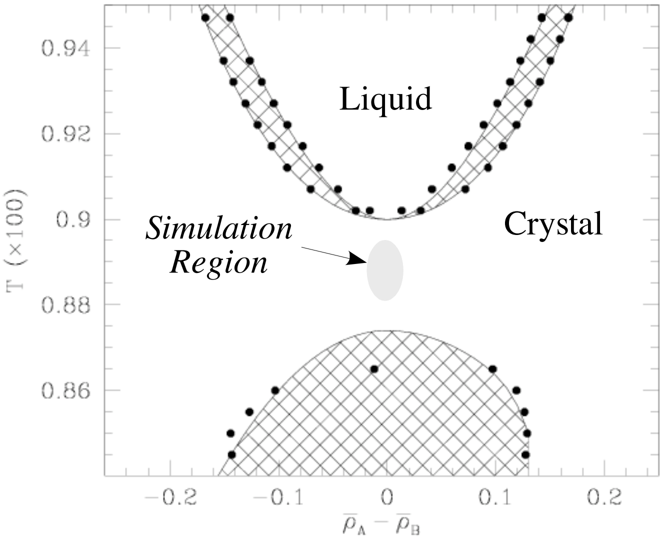

Figure 7.1: Binary PFC phase diagram for (η, v, w, L, A_0)=(0.25, 0.16, 4, 1, 0.9). Crosshatched areas correspond to regions of coexistence.

Periodic boundary conditions were used in the lateral directions, while a mirror boundary condition was applied at the bottom of the substrate. A constant flux boundary condition was maintained along the top boundary, $120\Delta x$ above the film surface, to simulate a finite deposition rate. Misfit strain was applied to the system by setting $R_{AB} = 1$ in the substrate and $R_{AB} = 1 + \epsilon + \eta c$ in the film. This approach yields a film and substrate that are essentially identical in nature except for this shift in lattice parameter in the film. Complexities resulting from differing material properties between the film and substrate are therefore eliminated, isolating the effects of misfit strain, solute strain, and mobility differences on the film growth morphology. The substrate was permitted to strain elastically, but was prevented from decomposing compositionally except near the film/substrate interface.

7.3 Simulation Results

7.3.1 Roughening, dislocation nucleation, and relaxation

One advantage of using the PFC method to simulate film growth is that singularities at cusp tips are suppressed, allowing simulations to continue to and beyond the point

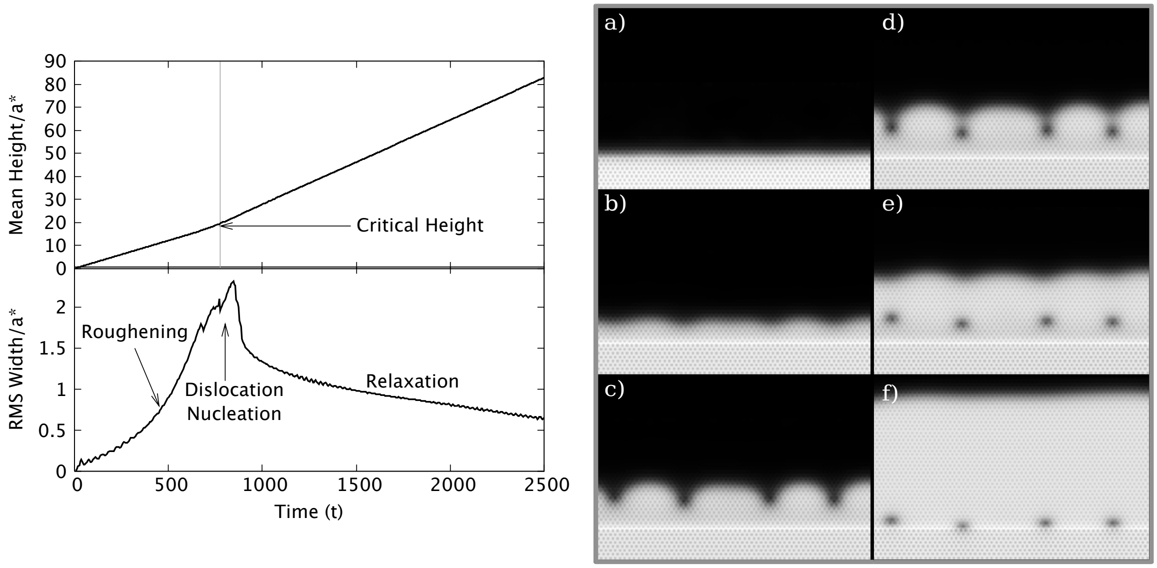

(a) (b)

Figure 7.2: (a) Sample plots of average film thickness (upper) and RMS surface roughness (lower) vs. time. (b) Plots of the smoothed local free energy showing the progression of the buckling instability, dislocation nucleation and climb toward the film/substrate interface. From a) to f) times shown are t=150, 600, 1050, 1200, 1500, and 2550. Note the nearly planar film surface in the last frame, after the dislocations have relieved most of the misfit strain. $\epsilon = 0.04$, $\eta = -1/4$ and $\Gamma_A = \Gamma_B = 1$.

of defect nucleation. This allows us in the present case to systematically investigate the effects of misfit strain, solute strain, and mobility differences on the critical height h_c of growing films. Here h_c is linked to dislocation nucleation and will be defined as the average height of the film at the time of maximum average defect height. In simulations exhibiting more than one wave of dislocation nucleation, the maximum average defect height during the first wave is used.

The well-documented evolution of film surface morphology due to the ATG morphological instability is naturally reproduced by the binary PFC model, resulting in the destabilization of planar films for nearly all non-zero values of misfit strain. Figure 7.2(a) shows typical plots of the mean film thickness and RMS surface roughness as functions of time, where the time corresponding to the critical height has been noted. Figure 7.2(b) shows the corresponding spatial progression of the local free energy as a growing film exhibits instability, dislocation nucleation, and relaxation.

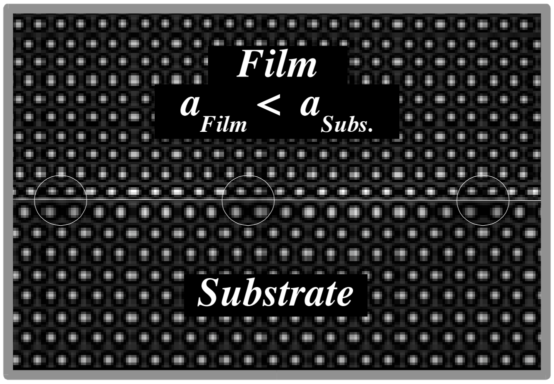

Figure 7.3: Plot of the local density field N showing loss of coherency between film and substrate, resulting from dislocation nucleation and climb.

Typically, several dislocations (perfect edge dislocations in this system) are nucleated at approximately the same time, relieving nearly all stress due to misfit with the substrate and/or differing species sizes. Following nucleation, the dislocations climb toward the film/substrate interface, locally relieving stress in the layers above (Fig. 7.2). In the present model, with a triangular lattice structure, this motion is purely climb and is largely perpendicular to the interface (and opposite the growth direction). Once the dislocations reach the film/substrate interface, coherency of the film with the substrate is lost (Fig. 7.3).

7.3.2 Phase separation

The nature of phase separation within the bulk film and at the film surface was found to vary with model parameters, but a number of generalizations applicable to all systems studied have been identified. For the case of equal mobilities (Γ_A=Γ_B) it is found that, in the presence of misfit strain and solute strain, the component with less misfit relative to the substrate preferentially segregates below surface valleys, while the component with greater misfit relative to the substrate preferentially segregates below surface peaks (see Fig. 7.4(a)). This lateral segregation is logical when one considers the physical coupling of the ATG instability with the compositional instability. According to the ATG theory, valleys become regions of stress concentration as the roughening instability proceeds, while the film relaxes near peaks, allowing larger film growth rates in these preferred regions. Larger (smaller) atoms will be driven

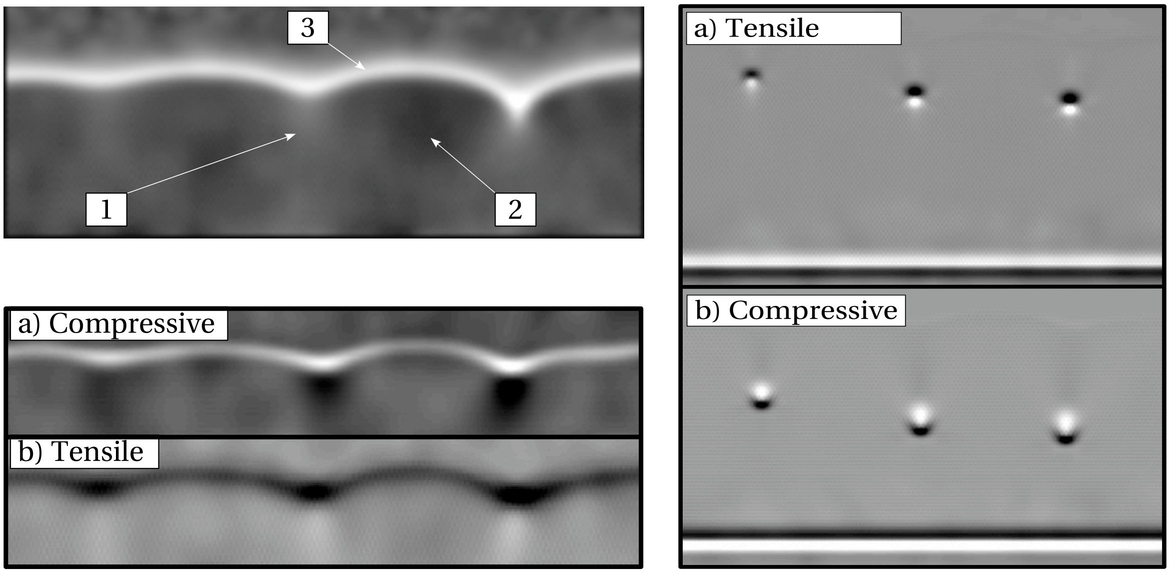

(a) (b)

Figure 7.4: (a) Top: Plot of the smoothed local concentration field c showing lateral phase separation between surface peaks and valleys. White: Component A (large, fast), Black: Component B (small, slow). $\epsilon = -0.02$, $\eta = 0.4$, $\Gamma_A = 1$, $\Gamma_B = 1/4$, and $t = 3500$. See text for discussion of the numbered arrows. In this case, the greater misfit component (B) does not accumulate at the film surface because of the greater mobility of the lower misfit component (A). Bottom: Same as Top, but highlighting the nature of phase separation under opposite signs of ϵ. Here η=0.25, Γ_A=1, Γ_B=1, a) ϵ=0.04, b) ϵ=-0.025. In both cases, the component with greater misfit is driven toward the film surface and below surface peaks, while the lower misfit component segregates below surface valleys. (b) Same as (a), but highlighting the complementary phase separation at the film/substrate interface and around defects (η=0.25).

toward regions of tensile (compressive) stress, which correspond to peaks (valleys) in a compressively strained film and to valleys (peaks) in a film under tensile strain. This coupling creates a lateral phase separation on the length scale of the surface instability and has been predicted and verified for binary films [212–220, 225–229], and analogous behavior has been predicted and verified in quantum dot structures [230–232]. The extent of this type of phase separation is of course dependent upon the relative atomic size and mobility differences of the two components.

Second, again for the case of equal mobilities, the component with greater misfit relative to the substrate is driven toward the film surface (see Fig. 7.4(a)). This behavior can also be explained in terms of stress relaxation and is somewhat analogous to impurity rejection in directional solidification. The greater misfit component can be viewed as an impurity that the growing film wishes to drive out toward the interface. Experimental evidence from SiGe on Si [225] and InGaAs on InP [226, 227] verifies this behavior as an enrichment of the greater misfit component was detected at the film surface in both systems. Other models [213, 214, 217, 220] have not produced this type of vertical phase separation, possibly a result of neglecting diffusion in the bulk of the film.

The third generalization that can be made is that, in the case of sufficiently unequal mobilities, the component with greater mobility accumulates at the film surface (see Fig. 7.4(a)). It was found that when the two components have a significant mobility difference, typically greater than a 2:1 ratio, the effect of mobility is more important than the combined effects of misfit and solute strains in determining which component accumulates at the surface. Since Ge is believed to be the more mobile component in the SiGe system, the findings of Ref. [225] for SiGe on Si provide experimental support for this claim. They find a significant enrichment of Ge at the film surface, a result that is likely due to a combination of this mobility driven effect as well as the misfit driven effect described in the second generalization.

Experimental evidence also indicates that segregation of substrate constituents into the film may occur during film growth [233, 234]. Binary PFC simulations similarly reveal a vertical phase separation near the film/substrate interface, which is complemented by a phase separation mirrored in direction near defects (Fig. 7.4(b)). The extent of this phase separation is controlled largely by the bulk mobilities of the two constituents, and to a lesser degree by η. The complementing phase separation near climbing defects is a transient effect, any traces of which are dulled once the defect reaches the film/substrate interface.

7.3.3 Additional findings

Growth temperature and deposition rate also have important effects on the growth characteristics of these systems. In Molecular Beam Epitaxy (MBE), it is expected that higher (lower) temperatures will result in decreased (increased) values of h_c [206, 207]. Though a detailed study spanning a wide range of temperatures was not conducted in the present work, it was found, as a general rule, that lowering the growth temperature (increasing the film growth rate) does result in increased values of h_c, while increasing the growth temperature (decreasing the film growth rate) results in decreased values of h_c. This behavior has been seen experimentally [206, 207, 235] and can be explained in terms of the dynamics, where one can argue that slower film growth rates allow additional time to relax toward an equilibrium state, which according to the ATG instability will be a state in which the surface roughness has increased. This translates to increased roughening at a given height for a system growing at a higher temperature or slower rate. Defect nucleation is then energetically favorable at a lower film height in comparison to a film grown at a lower temperature. The energy barrier for dislocation nucleation also decreases with increasing temperature, which can only strengthen the preceding argument.

7.4 Aside: Monatomic Heteroepitaxy – Beyond Linear Continuum Theory

The results presented in this chapter give a qualitative overview of the concentration patterns that emerge when strain and composition fields are coupled in growing alloy films. The quantitative details of this process are bound to be richly complex, with strong dependences on several variables. In fact, there is sufficient complexity in terms of the morphological instability alone, that a number of issues within the scope of monatomic heteroepitaxy remain relatively unexplored. A few additional points concerning the morphological instability in heteroepitaxially grown monatomic films will be briefly examined here, with the modest intent of emphasizing some of the open issues and presenting a few initial results.

Of particular interest is whether the predictions of continuum theory are relevant under non-idealized growth conditions. For example, how does a finite substrate with distinct elastic properties influence the instability? How does the instability change as the film growth rate increases from the quasi-static limit toward relatively large values? How does the simultaneous interaction of many perturbation wavemodes at the film surface, combined with the preceding complications, modify the evolution of the instability near the regime of dislocation nucleation?

7.4.1 Linear continuum predictions

The linear instability predictions of continuum theory were discussed in Section 7.1. Specifically, it has been shown that $q_c \sim \epsilon^2$ and $\sigma(q_c) \sim q_c^{2\gamma}$ in the linear regime [236], where γ assumes integer values for specific dominant transport mechanisms (2 for evaporation-condensation, 3 for bulk diffusion, 4 for surface diffusion). The continuum result for $h_{unstable}$ depends on the properties of the substrate. Two specific cases will be considered here: a perfectly rigid substrate ($h_{unstable} \sim 1/\epsilon^2$ [236]), and a substrate with elastic properties identical to those of the growing film ($h_{unstable} = 0$ [236]). Thus the effect of a rigid substrate is in general stabilizing within continuum theory. The effect of a non-zero film growth rate k_v on the predictions of continuum theory is unclear but is generally expected to be stabilizing as well [236].

The first PFC studies of film growth outlined the natural progression and coupling of surface instability, dislocation nucleation, and relaxation in two dimensions, focusing on the implications of this coupling in terms of h_c [3, 4]. Huang and Elder have since applied the PFC amplitude equation approach to systematic studies of morphological instability and island wavelength selection, also in monatomic two dimensional films [40, 65]. They examined strained, free-standing, static films (no substrate, $k_v = 0$) perturbed at a single wavenumber at a time. The evolution of instability is thus relatively slow and nearly linear, conditions valid for comparison with the predictions of ATG theory. Their results showed that even under idealized conditions the continuum theory is not always valid. In particular, the prediction for dominant wavenumber selection was found to break down at sufficiently large misfits due to atomistic effects and/or non-zero interface widths [77]. They also found that the maximum instability growth rate has a somewhat more complicated dependence on misfit than indicated by ATG-type theories, especially for large misfits. Interestingly, instability growth rate dispersions consistent with simple bulk diffusion have been obtained from direct (non-amplitude) PFC simulations [77]. Thus, the continuum predictions for perturbation growth rates and wavenumber selection at sufficiently small ϵ seem to be at least approximately correct in idealized PFC simulations. It will be shown in the following that this agreement is quickly destroyed by non-ideal growth conditions, such as non-zero film growth rates, explicit finite-size substrates, and highly nonlinear evolution dynamics.

7.4.2 Simulation results

For this study, monatomic film growth was simulated using a substrate eight monolayers thick, with periodic lateral and mirror horizontal boundary conditions. Equations (2.1) and (2.29) with $r + 1 = T$ were used. Temperatures of $T = 0.835$, 0.826, and 0.818 were used to produce three distinct film growth rates k_v, and small thermal noise perturbations were applied to the inital liquid region. Misfit strain was applied by varying the substrate lattice parameter from the equilibrium value at each T, while keeping the film properties constant. The rigid substrate condition was simulated by strongly coupling the substrate to an external field with appropriate periodicity. Other numerical parameters used were $\Delta x = 0.65$, $\Delta t = 0.002$, $L_x = 8198\Delta x$, $\bar{n} = -0.25$, and $\Gamma = 1$.

Critical film thickness for onset of instability

Initial simulation results are shown in Fig. 7.5. First consider the case of an elastically matched film and substrate, where continuum theory predicts $h_{unstable} = 0$. $h_{unstable}$ is defined here as h at which the film surface RMS roughness first begins to grow exponentially, typically near a RMS value of 1.0. The continuum predictions in general should be most valid in the regime of small ϵ and small k_v. The data in this regime indicate that $h_{unstable}$ does approach a constant at small ϵ, but that this constant is much larger than zero. This limiting value in fact appears to be associated with a Mullins-Sekerka (MS) dendritic instability, without which $h_{unstable}$ would apparently continue to grow rapidly as $\epsilon \rightarrow 0$. A similar MS-ATG coupling at slow film growth rates has been found in previous PFC simulations [54].

For small ϵ and small k_v, the film surface morphology is dominated by the MS instability, which presumably selects a wavenumber based on k_v rather than ϵ. Simulations show that dendrite-like morphologies emerge for small ϵ and small k_v, in which the spacing approaches a constant value independent of ϵ. Thus more dislocations are nucleated than required to relieve the misfit strain in the MS-dominated regime. For sufficiently large k_v the MS instability is suppressed and the ATG-like instability dominates. Nonetheless, the regime in which continuum ATG results should be most valid is obscured by a separate phenomena, limiting its relevance to these simulations.

Elastically matched film/substrate systems at large misfits appear to obey the

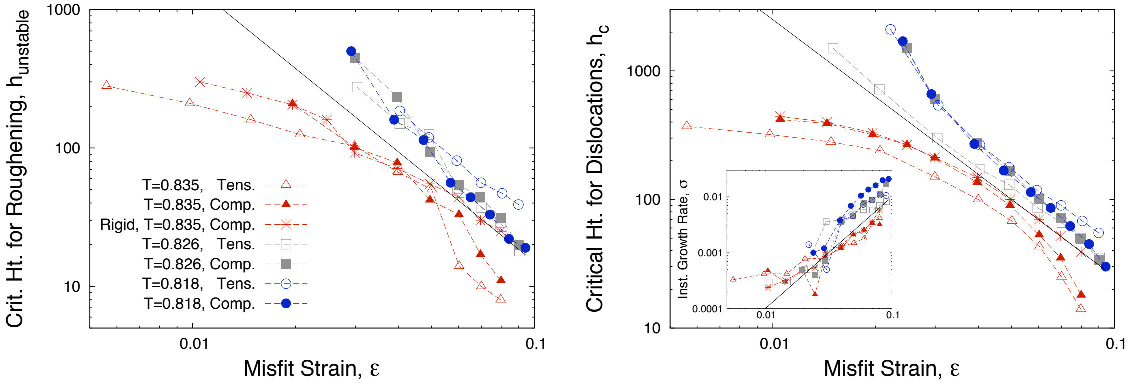

(a) (b)

Figure 7.5: (a) Film critical height for roughening onset vs. misfit strain at various T. The solid line has a slope of -2. (b) Film critical height for dislocation nucleation vs. misfit strain at various T. The solid line has a slope of -2. Inset: Film RMS roughness growth rate vs. misfit strain at various T. The solid line has a slope of $+2$.

rigid substrate prediction in which $h_{unstable} \sim 1/\epsilon^2$. For small ϵ and large k_v, $h_{unstable}$ appears to grow with a stronger than $1/\epsilon^2$ dependence, but the detailed behavior at large h has not been accessed in these initial simulations. The results for rigid substrates are qualitatively similar to those for matched substrates, with a slightly enhanced stability. Thus, the predicted $1/\epsilon^2$ dependence is observed only for large misfits, which may be coincidental. The linear ATG predictions for $h_{unstable}$ therefore do not appear to be satisfied in most PFC systems with non-infinite substrates, non-zero film growth rates, and fully nonlinear dynamic evolution. The expectation of kinetic stabilization [236], resulting in larger values of $h_{unstable}$ for large k_v is observed to a modest degree, as is the prediction of enhanced stability when rigid substrates are employed.

Critical film width for onset of instability

There are in general lower limits on the film lateral dimension L_x and ϵ, below which the ATG instability is predicted to not occur. Simulations confirm that there is indeed no instability below some critical value L_x^*, where L_x^* is generally the value of L_x at which the ideal number of dislocations required to perfectly relieve the misfit strain is 0.5. There may be a weak divergence in h_c as $L_x \to L_x^*$ from above, but further simulations would be required to confirm the nature of any such divergence.

Instability growth rate

The overall growth rate of the morphological instability is reflected in the RMS surface roughness. An average rate for each film can be extracted from an exponential fit in time, over the period spanning from initial instability to dislocation nucleation. This average rate as a function of ϵ is shown in Fig. 7.5(b). All films are found to roughen with nearly the same ϵ^2 rate dependence, except possibly in the MS regime where the ϵ dependence tends to vanish. The maximally unstable growth rate from the linear analysis for the onset of roughening under ideal conditions has a much stronger $\epsilon^{2\gamma} \simeq \epsilon^6$ form. Thus, if one attempts to compare the ATG predictions with the large ϵ simulation data, the growth rate of the morphological instability appears to be significantly suppressed by non-zero film growth rates, surface mode coupling effects, and explicit substrates. The small ϵ regime is again obscured by the MS instability.

Critical film thickness for dislocation nucleation

The results to this point indicate that the simulated conditions, though not terribly extreme, place us well beyond the regime in which the linear ATG description of morphological instability is valid. A nonlinear dynamic description appears necessary to capture the full range of roughening from onset to dislocation nucleation. There could potentially be agreement with linear ATG in the small ϵ, small k_v region, but the MS instability dominates this regime in the diffusive PFC model. Obviously then, an extrapolation of the linear theory to predict h_c, the critical height for dislocation nucleation, is bound to fail. However, if the linear predictions are replaced with the general forms inferred from Fig. 7.5, a reasonable, though incomplete, description is easily written down.

Generally, $h_c \simeq h_{unstable} + h_{disloc}$, where h_{disloc} is the amount of film growth between initial instability and dislocation nucleation. Simulations indicate that $h_{unstable} \sim \epsilon^{-2}$ for sufficiently large ϵ, and $h_{disloc} \sim \ln[\bar{\sigma}^* + 1]/\bar{\sigma}$ where $\bar{\sigma}^* \sim k_v^{-1}$ is the observed average film roughness at nucleation and $\bar{\sigma} \sim \epsilon^2$ is the observed roughness growth rate. Therefore we expect that $h_c \sim 1/\epsilon^2$ roughly, for large misfits, as found in the simulations. For small ϵ and small k_v, $h_{unstable}$ and h_{disloc} both approach constant values due to MS dominance, and h_c must necessarily approach a constant value as well. For small ϵ and large k_v, a possible accelerated divergence in $h_{unstable}$ causes h_c to grow rapidly out of measurement range.

This variety of behavior as a function of film growth rate, misfit strain, and substrate properties highlights the complexity of dynamic heteroepitaxy when non-idealized growth conditions are considered. The $1/\epsilon^2$ dependences at large misfits do appear consistently and hint at some unity for Volmer-Weber or island growth processes, but the intervening MS instability at small misfits and growth rates obscures the layer-by-layer growth regime. In general, linear continuum theories tend to break down quickly when non-infinite substrates are employed and as the evolution of the surface profile becomes highly nonlinear, with coupling between surface modes and stabilizing kinetic effects at non-zero k_v. Atomistic effects also become important at large misfits, further limiting the applicability of continuum theories.

7.5 Conclusions

Three general features of phase separation in growing films have been identified from the simulation results outlined here, as a function of misfit strain and species mobility ratio. Lateral patterns emerge on the length scale of the surface roughness, with the lower misfit component segregating below surface valleys and the higher misfit component below surface peaks. A vertical separation also occurs, with one component accumulating at the film surface. When both species have the same mobility, the higher misfit component will be driven toward the film surface, but if the lower misfit component is sufficiently mobile, then it will tend to accumulate most at the surface. Vertical phase separation patterns at the film-substrate interface and around dislocations have also been identified.

A few issues that arise in simpler monatomic films have also been discussed relative to the predictions of continuum elastic theory. In addition to atomistic causes, significant deviations from the linear continuum limit appear at large misfits, apparently due to nonlinear coupling of surface modes, kinetic effects, and non-infinite substrates. For low film growth rates, a Mullins-Sekerka-type dendritic instability is found to dominate the morphological evolution of growing films in the diffusion-dominated PFC model.

CHAPTER 8

Summary and Future Work

It is hoped that the studies described in this dissertation provide useful physical insights into the various phenomena addressed, but also that they serve in exploring and validating the capabilities of PFC modeling. The problem of extending the time scale in atomistic simulations is a fundamental and challenging topic, with far-reaching implications for any successful methodologies. Our understanding of nonequilibrium processes in hard and soft liquid-solid systems has been and will continue to be closely linked with an ability to model across time scales.

The PFC approach, as demonstrated here as well as by many others, appears to have much promise in this regard, and has now advanced from a conceptual validation, proof-of-concept stage toward targeted, applied research. Nonetheless, many open issues and unexplored applications remain on both the fundamental and applied levels. Brief summaries of the findings concerning each of Chapters 3-7 are included in the following, along with lists of issues which remain open to various degrees and/or suggestions for future work.

8.1 Melting and Premelting

Summary

Both the localized and generalized nature of dislocation and grain boundary melting have been examined in Chapter 3. Numerical and analytical results are provided for the spatial features of defect melting, along with outlines of some of the general transition features to be expected as a function of ensemble and order of the bulk transition. Since premelting is expected to proceed only logarithmically as $T \rightarrow T_m$, it is generally difficult to conclusively detect its existence in experiments. Measurable effects only occur very near T_m, which leads to difficulty in distinguishing between true premelting and uncertainty in the value of T_m (even in colloids). Thus, both the metastable pathway (superheating) and premelting scenarios examined in Chapter 3 may aid in understanding experiments, but conclusive experimental data will be needed to determine which scenario is most relevant in a given system.

Future Work

A more detailed treatment of interfacial energies in the local melting analysis should produce more accurate results. High angle grain boundaries are often reduced to a continuum description in which a uniform disjoining potential is used to characterize the local melting behavior. It would be interesting to connect the low-mid angle description developed in Chapter 3 with the disjoining potential approach. This might help to address another eventual need, which would be to refine the expression for the critical prewetting angle, perhaps by approaching the calculation from the opposite, high angle side. Application of the three dimensional bcc complex amplitude formulation to premelting would allow larger scale simulations and also provide a means of comparing and validating specific amplitude equation models.

8.2 Dislocation Dynamics

Summary

It is shown in Chapter 4 that defect motion under applied strain in the diffusion-dominated PFC model can be accurately described in terms of simple viscous motion equations for overdamped point masses. The natural features of glide, climb, and annihilation, including Peierls barriers and elastic defect interactions, automatically emerge from the theory. These behaviors are characterized across various temperatures, applied strains, applied strain rates, and dislocation densities.

Future Work

The diffusion-dominated model describes a relatively soft, viscoelastic crystalline state, much like that created by colloids. More rigid atomic and molecular crystals are better described by the inertial PFC model, which has been shown to produce effectively instantaneous long-range elastic interactions. It may be useful to repeat the characterization of Chapter 4 using the inertial model. It might also be interesting to examine the effects of the VPFC formulation on dislocation dynamics and/or to take a closer look at grain boundary effects in monatomic and binary polycrystalline materials. Larger-scale problems such as nanoindentation could also be addressed in future studies.

8.3 Freezing, Amorphous Nucleation, and Spinodals

Summary

Freezing in diffusion-dominated monatomic PFC systems is shown in Chapter 5 to occur with high probability through a first-order nucleation transition to an amorphous solid precursor state in three dimensions. Crystalline states are then obtained through a subsequent first-order amorphous crystallization transition, wherein the lifetime of the amorphous solid is correlated with the cooling rate. The structure of the disordered PFC solid is consistent with that of known simple glass formers. Liquid spinodal effects are shown to produce apparent glassy dynamics in the supercooled liquid, but are ultimately not associated with a true glass transition.

Future Work

The amorphous precursor phase is shown to emerge away from the liquid spinodal for primarily energetic reasons - the free energy barrier for nucleating an amorphous critical droplet is smaller than that of the critical crystalline droplet. Since the bulk free energy of the equilibrium crystal is always lower than that of the amorphous solid, this result implies that liquid-amorphous solid interfacial energy is significantly smaller than the liquid-crystal interfacial energy. A closer quantification of interfacial energies in small solid phase droplets might provide interesting insights into solid phase nucleation.

Near the liquid spinodal, amorphous solids appear to be preferred for primarily kinetic reasons. One might expect the supercooled liquid free energy minima to be ‘closer’ to the amorphous solid minima than to the crystalline minima, leading to a kinetic trapping effect. An investigation of the reasons for this behavior might lead to some interesting analogies between glass forming liquids and spinodal systems.

It is not entirely clear whether inertial dynamics significantly change the behavior reported in Chapter 5. It may also be worthwhile to perform a closer examination of freezing and nucleation behavior in the monatomic VPFC model, where spinodal effects are avoided and free volume effects are enhanced. Finally, there would also be value in extending the amplitude equation formulation to amorphous solids, to enable large scale simulations of glassy materials.

8.4 The Glass Transition

Summary

The results presented in Chapter 6 demonstrate clearly for the first time that PFC and DDFT models can describe the dynamics of glass forming liquids to the level of two-step relaxation functions, Vogel-Fulcher divergences, and agreement with established MCT and experimental results. The success of this description is associated with strong local nonlinearities in the free energy and the combination of inertial and dissipative dynamic processes, all of which lead to strong caging and enhanced dynamic correlations. A physically motivated time scaling extends the reported simulation results to a span of 12 orders of magnitude in time, providing access to nearly the entire glass formation process. A correlation between liquid fragility and a rapidly growing dynamic correlation length is also established.

Future Work

The results established in Chapter 6 open the door to a number of potential PFC studies of glass forming materials. These include aging properties, annealing/melting behaviors, mechanical response to strain, nongaussian dynamics, and dynamic heterogeneity in the deeply supercooled regime. It should also be possible now to formulate PFC models of well-known glass forming systems for comparative studies. It may be worthwhile as well to examine two dimensional liquids for the potential of reaching longer times in both the underdamped and overdamped descriptions. Fully optimized numerics, employing operator splitting methods, filtered spectral operators, and an appropriate stochastic noise wavenumber cutoff, would also assist to this end. Open issues regarding the specific results of Chapter 6 include better quantifying how and why the dynamic correlation length grows in the supercooled liquid, clarifying the thermodynamic behavior near T_g, and determining to what degree the results depend on the form of the VPFC cutoff term. Other equations of motion, such as Eqs. (2.36) and (2.34), may prove necessary for studies of selected dynamic behaviors.

8.5 Epitaxial Growth

Summary

The characteristic spatial concentration patterns that develop in growing strained alloy films are outlined in Chapter 7 as a function of misfit strain and species mobility ratio. These patterns are either lateral peak-to-valley variations or vertical surface-substrate variations. Significant deviations from the continuum limit appear for relatively small deviations from idealized growth conditions. These may stem from atomistic effects (at large misfits), nonlinear coupling of surface modes, kinetic effects, non-infinite substrates, or crossover to a Mullins-Sekerka dendritic instability dominated regime (at small misfits and growth rates).

Future Work

The findings summarized above highlight certain challenges in modeling monatomic heteroepitaxy. Effects due to growth rate, substrate elastic properties, substrate thickness, large misfit strains, and combined ATG-Mullins-Sekerka instabilities need further characterization and connection with the continuum limit. More detailed atomistic phase separation effects in binary heteroepitaxy might also be well-described by VPFC models.

APPENDIX A

Numerical Methods

A.1 Method 1: Diffusive PFC, Euler Real Space

The simplest, most direct scheme for simulating the diffusive PFC model is the forward Euler, real space finite difference method. This method was used for the two-dimensional simulations presented in Chapters 4 and 7. The discretization of the monatomic model, Eqs. (2.1) and (2.29), can be written

$$n^{t+1} = n^t + \Delta t \left(\Gamma \nabla^2 \mu^t + \vec{\nabla} \cdot \vec{\eta} \right)$$

$$\mu^t = \left[r + (1 + \nabla^2)^2 \right] n^t + (n^t)^3$$

where Δt is the time step, and n^t and μ^t are $n(\vec{r})$ and the chemical potential, respectively, at time step t on a given grid location.

Laplacians can be calculated quasi-isotropically in two dimensions as [139]

$$\begin{aligned} \nabla^2 n_{i,j} = [&-3n_{i,j} + 0.5(n_{i+1,j} + n_{i-1,j} + n_{i,j+1} + n_{i,j-1}) + \\ &0.25(n_{i+1,j+1} + n_{i-1,j+1} + n_{i+1,j-1} + n_{i-1,j-1})]/(\Delta x)^2 \end{aligned}$$

and in three dimensions as

$$\nabla^2 n_{i,j,k} = \frac{-24n_{i,j,k} + 2\sum' n_{i',j',k'} + \sum'' n_{i'',j'',k''}}{6(\Delta x)^2}$$

where $\sum'$ and $\sum''$ represent summations over nearest neighbor and next nearest neighbor grid points, respectively.

When a gaussian stochastic noise term $\vec{\eta}$ is used, it is applied to the updated density field at each time step. It can be calculated by producing d independent gaussian random numbers at each grid point and operating on each point with $\vec{\nabla}\cdot$. In three dimensions, a simple discretization for $\vec{\nabla}\cdot$ gives

$$\vec{\nabla} \cdot \vec{\eta}_{i,j,k} = \frac{\eta^{(1)}_{i+1,j,k} - \eta^{(1)}_{i,j,k} + \eta^{(2)}_{i,j+1,k} - \eta^{(2)}_{i,j,k} + \eta^{(3)}_{i,j,k+1} - \eta^{(3)}_{i,j,k}}{\Delta x}$$

where

$$\langle \eta^{(a)}_{i,j,k}(p)\eta^{(b)}_{l,m,n}(q)\rangle = \frac{M\Delta t}{(\Delta x)^d}\delta_{i,l}\delta_{j,m}\delta_{k,n}\delta_{p,q}\delta_{a,b}.$$

A.2 Method 2: Diffusive PFC, Semi-Implicit Pseudospectral

In three dimensions, a semi-implicit pseudospectral algorithm results in potentially several orders of magnitude improvement in computational efficiency compared to the real space finite difference Euler scheme. This method was used in the three dimensional simulations presented in Chapters 3 and 5. The noiseless algorithm for the monatomic model of Eqs. (2.1) and (2.29) is written in Fourier space as

$$\hat{n}_{t+1} = \frac{\hat{n}_t - \Gamma q^2 \Delta t \widehat{n_t^3}}{1 + \Gamma q^2 \Delta t\,[r + 1 - 2q^2 + q^4]}$$

where $\hat{n}_t$ is the Fourier transform of $n(\vec{r})$ at time step t and q is wavenumber. Stochastic noise can be applied as described in Method 1, after the updated density field is transformed back into real space.

A.3 Method 3: Inertial PFC, Euler Real Space

A real space finite difference scheme was used to solve the inertial PFC models of Chapter 6 in three dimensions, allowing direct implementation of quasi-isotropic ∇, $\nabla\cdot$, and ∇^2 operators. This was done to prevent both drift effects and the directional preferences along the simulation cell axes sometimes observed with less isotropic operators. Relaxations in the liquid state were found to be slower in general when less isotropic first and second order operators were used, but to converge in the vicinity of the order employed below. The method used for the binary model of Eqs. (6.8) and (6.11) with $\Gamma_i(\vec{r}) = 1$ is written

$$n_i^{t+1} = n_i^t + \Delta t g_i^t$$

$$\begin{aligned}
g_i^{t+1} &= (1 - \Delta t\beta_i)g_i^t + \Delta t\alpha_i^2\nabla^2\mu_i^t + \Delta t\vec{\nabla}\cdot\vec{\eta}_i^t \\
\mu_A^t &= \left[r_A + (q_A^2 + \nabla^2)^2\right] n_A^t + (n_A^t)^3 + 3H_A(|n_A^t| - n_A^t)n_A^t + \\
&\quad r_{AB}n_A^t(n_B^t)^2 + \frac{1}{2}(q_{AB}^2 + \nabla^2)^2 n_B^t \\
\mu_B^t &= \left[r_B + (q_B^2 + \nabla^2)^2\right] n_B^t + (n_B^t)^3 + 3H_B(|n_B^t| - n_B^t)n_B^t + \\
&\quad r_{AB}n_B^t(n_A^t)^2 + \frac{1}{2}(q_{AB}^2 + \nabla^2)^2 n_A^t
\end{aligned}$$

where n_i^t is $n_i(\vec{r})$ at time step t and grid location (i, j, k), $g_i = \partial n_i/\partial t$ is a local average velocity, and Δt is the time step. Laplacians were calculated quasi-isotropically as in Method 1.

The gaussian stochastic noise terms $\vec{\eta}_i$ were calculated as in Method 1, except with a quasi-isotropic discretization for $\vec{\nabla}\cdot$:

$$\vec{\nabla}\cdot\vec{\eta}_{i,j,k} = \sum_{m=1}^{3} \frac{4\sum'\Delta\eta^{(m)} + \sum''\Delta\eta^{(m)}}{16\Delta x}$$

where

$$\sum{}'\Delta\eta^{(1)} = \eta^{(1)}_{i+1,j,k} - \eta^{(1)}_{i-1,j,k},$$

$$\sum{}' \Delta\eta^{(2)} = \eta^{(2)}_{i,j+1,k} - \eta^{(2)}_{i,j-1,k},$$

$$\sum{}' \Delta\eta^{(3)} = \eta^{(3)}_{i,j,k+1} - \eta^{(3)}_{i,j,k-1},$$

$$\begin{aligned}\sum{}'' \Delta\eta^{(1)} = {} & \eta^{(1)}_{i+1,j+1,k} - \eta^{(1)}_{i-1,j-1,k} + \eta^{(1)}_{i+1,j-1,k} - \eta^{(1)}_{i-1,j+1,k} + \\ & \eta^{(1)}_{i+1,j,k+1} - \eta^{(1)}_{i-1,j,k-1} + \eta^{(1)}_{i+1,j,k-1} - \eta^{(1)}_{i-1,j,k+1} \quad ,\end{aligned}$$

$$\begin{aligned}\sum{}'' \Delta\eta^{(2)} = {} & \eta^{(2)}_{i+1,j+1,k} - \eta^{(2)}_{i-1,j-1,k} + \eta^{(2)}_{i-1,j+1,k} - \eta^{(2)}_{i+1,j-1,k} + \\ & \eta^{(2)}_{i,j+1,k+1} - \eta^{(2)}_{i,j-1,k-1} + \eta^{(2)}_{i,j+1,k-1} - \eta^{(2)}_{i,j-1,k+1} \quad ,\end{aligned}$$

$$\begin{aligned}\sum{}'' \Delta\eta^{(3)} = {} & \eta^{(3)}_{i+1,j,k+1} - \eta^{(3)}_{i-1,j,k-1} + \eta^{(3)}_{i-1,j,k+1} - \eta^{(3)}_{i+1,j,k-1} + \\ & \eta^{(3)}_{i,j+1,k+1} - \eta^{(3)}_{i,j-1,k-1} + \eta^{(3)}_{i,j-1,k+1} - \eta^{(3)}_{i,j+1,k-1} \quad .\end{aligned}$$

Simulations unintentionally included an extra weighting factor of 2 on the next-nearest-neighbor terms, which leads to a slight biasing toward diagonal differences and an underreporting of the actual effective noise strength by a factor of 3/2.

A.4 Method 4: Nonlinear Diffusive PFC, Euler Real Space

The overdamped nonlinear diffusion equation of DDFT, examined in three dimensions in Chapter 6, was also discretized using a forward Euler real space finite difference method. The algorithm used for the monatomic version of Eqs. (6.8) and (6.10) is written

$$n^{t+1} = n^t + \Delta t \left[\nabla \left(\Gamma^t(\vec{r}) \nabla \mu^t \right) + \vec{\nabla} \cdot \left(\sqrt{M \Gamma^t(\vec{r})} \vec{\eta} \right) \right]$$

$$\mu^t = \left[r + (q_i^2 + \nabla^2)^2 \right] n^t + (n^t)^3 + 3H(|n^t| - n^t) n^t.$$

On the grid, with lowest order operators, this becomes

$$\begin{aligned} n^{t+1}_{i,j,k} = n^t_{i,j,k} + \Delta t \Big[& \frac{\Gamma^t_{i+1,j,k} + \Gamma^t_{i,j,k}}{2} \left(\mu^t_{i+1,j,k} - \mu^t_{i,j,k} \right) - \frac{\Gamma^t_{i,j,k} + \Gamma^t_{i-1,j,k}}{2} \left(\mu^t_{i,j,k} - \mu^t_{i-1,j,k} \right) + \\ & \frac{\Gamma^t_{i,j+1,k} + \Gamma^t_{i,j,k}}{2} \left(\mu^t_{i,j+1,k} - \mu^t_{i,j,k} \right) - \frac{\Gamma^t_{i,j,k} + \Gamma^t_{i,j-1,k}}{2} \left(\mu^t_{i,j,k} - \mu^t_{i,j-1,k} \right) + \\ & \frac{\Gamma^t_{i,j,k+1} + \Gamma^t_{i,j,k}}{2} \left(\mu^t_{i,j,k+1} - \mu^t_{i,j,k} \right) - \frac{\Gamma^t_{i,j,k} + \Gamma^t_{i,j,k-1}}{2} \left(\mu^t_{i,j,k} - \mu^t_{i,j,k-1} \right) \Big] / (\Delta x)^2 + \\ & \sqrt{\Delta t} \Big[\sqrt{M \frac{\left| \Gamma^t_{i+1,j,k} + \Gamma^t_{i,j,k} \right|}{2}} \eta^{(1)}_{i+1,j,k} - \sqrt{M \frac{\left| \Gamma^t_{i,j,k} + \Gamma^t_{i-1,j,k} \right|}{2}} \eta^{(1)}_{i,j,k} + \\ & \sqrt{M \frac{\left| \Gamma^t_{i,j+1,k} + \Gamma^t_{i,j,k} \right|}{2}} \eta^{(2)}_{i,j+1,k} - \sqrt{M \frac{\left| \Gamma^t_{i,j,k} + \Gamma^t_{i,j-1,k} \right|}{2}} \eta^{(2)}_{i,j,k} + \\ & \sqrt{M \frac{\left| \Gamma^t_{i,j,k+1} + \Gamma^t_{i,j,k} \right|}{2}} \eta^{(3)}_{i,j,k+1} - \sqrt{M \frac{\left| \Gamma^t_{i,j,k} + \Gamma^t_{i,j,k-1} \right|}{2}} \eta^{(3)}_{i,j,k} \Big] / \Delta x \end{aligned}$$

where $\eta^{(a)}_{i,j,k}$ is defined as in Method 1.

APPENDIX B

Freezing Transitions in Selected PFC and DFT Models

Several PFC and DFT models that were investigated but not reported upon in Chapters 5 and 6 are noted here. The basic aim was to begin formulating general conditions under which PFC systems exhibit the central dynamic features of glass forming liquids, and with this end in mind several approaches were adopted. These involve modifications to the basic free energy functional, the purely diffusive equation of motion, or both. The models studied are described in the following, along with brief discussions and illustrations of some of the characteristic results. Unless specified otherwise, the results apply to three dimensional systems.

B.1 Monatomic Liquids

A progressive introduction of nonlinearities into the free energy functional and equation of motion for monatomic PFC liquids is outlined in this section.

B.1.1 Free energy functional

Weak-coupling regime

Freezing behavior in the standard monatomic PFC model for various $\bar{n}$ and r appears to remain qualitatively similar to that outlined in Chapter 5. The transition becomes more strongly first order away from the critical point, but in the small noise amplitude limit remains a spinodal-driven nucleation process. The resulting disordered solids evolve too slowly to measure any significant relaxations, making numerical studies of glassy dynamics impractical. The other parameter that may be tuned in the basic PFC model is the noise amplitude, which effects the phase diagram as well as the dynamic evolution. For sufficiently large noise amplitude, the liquid relaxations begin to deviate from the predictions of the linear spinodal analysis, and nucleation barriers may be efficiently overcome at nearly any point from coexistence down. Significant nonlinear effects due to stochastic noise could conceivably modify the freezing dynamics, or could speed relaxation processes in the disordered solid states such that their full dynamic range becomes more accessible. Two-stage relaxations might also emerge if the noise effects generate a significant 'fast' evolution component which superimposes onto the 'slow' diffusive relaxations.

Simulation results indicate that the freezing transition remains nucleation-driven with large noise amplitudes and that disordered solids exhibit one-stage, though highly-stretched relaxation functions. Crystallization also continues to intervene over significnat portions of the potential glass transition region. Freezing behaviors associated with modified free energy functionals are therefore discussed in the following subsections, to demonstrate the degree to which nucleation persists and to which relatively simple relaxation processes dominate in simple monatomic models with Model B dynamics.

PFC/DFT comparison

The monodisperse hard sphere (HS) liquid was modeled to examine effects of the basic PFC functional form on freezing behavior. Two-body correlations were assumed to be given by the analytic Percus-Yevick (PY) result for the HS C_2,

$$
\begin{aligned}
C_2(q) = \frac{4\pi}{q^3}[&a(y\cos y - \sin y) + \frac{6\eta b}{y}(y^2\cos y - 2y\sin y - 2\cos y + 2) + \\
&\frac{\eta a}{2y^3}(y^4\cos y - 4y^3\sin y - 12y^2\cos y + 24y\sin y + 24\cos y - 24)]
\end{aligned}
$$

where $y = q\sigma$, σ is the hard sphere radius, $\eta = \pi n/6$ is the hard sphere packing fraction, n is the average number density, $a = (1+2\eta)^2/(1-\eta)^4$, and $b = -(1+\eta/2)^2/(1-\eta)^4$. This C_2 was inserted into the RY-DFT functional, Eq. (2.4), and

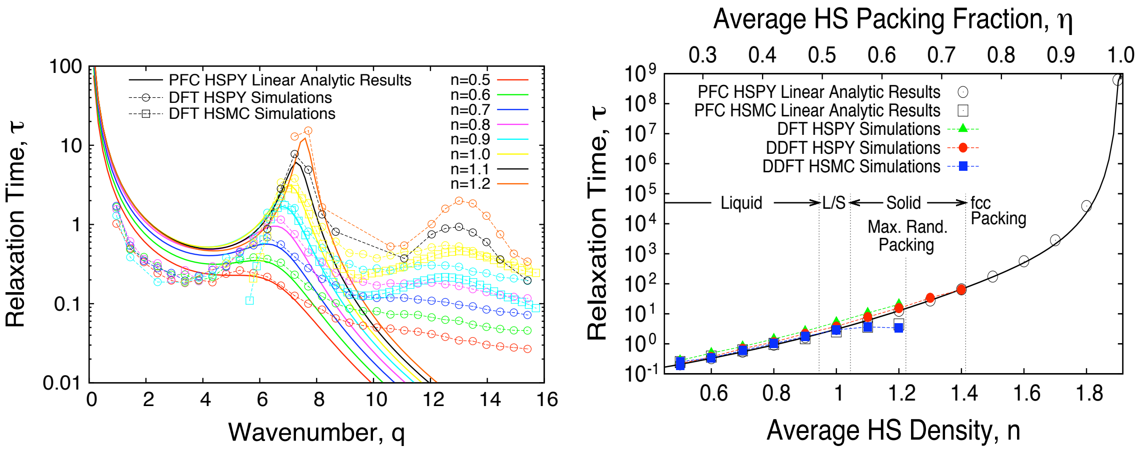

(a)

(b)

Figure B.1: DFT and PFC hard sphere simulation results for supercooled liquid dynamics. (a) Relaxation time versus wavenumber at various densities. (b) Arrhenius plot of relaxation time at the structure factor first peak maximum versus average density.

simulated using both Model B and overdamped DDFT dynamics.

Some results concerning the liquid relaxations are shown in Fig. B.1. As density is increased through the liquid-solid coexistence region, the relaxation time grows with a weakly super-Arrhenius form, but no strong divergence at or near the predicted glass transition density is observed. The relaxation functions are somewhat stretched at high densities but do not plateau. As shown in the figures, the DFT simulation results are well-described by the corresponding linearized PFC model, in which the relaxation time does not diverge until the unphysical PY singularity at $\eta = 1$ is reached.

Since the PY approximation loses accuracy at high densities, more appropriate high density forms for the HS C_2, calculated using Monte Carlo (MC) simulations, were also examined [237]. These produced no noteworthy qualitative changes to the freezing behavior described above. The two functionals intermediate between RY-DFT and standard PFC (RY-DFT with expanded logarithm and PFC with unexpanded logarithm) have also been simulated, with similar results for supercooled liquid dynamics. The same can be said concerning dynamics when the PFC gradient expansion is continued to higher order,

$$C_2(q) = -r - \left(\sum_{m=0}^{\ell} a_{2m} (iq)^{2m} \right)^2$$

or is substituted with the alternate analytic form

$$C_2(q) = \frac{-a_0}{1 + a_1 \exp\left(-q/q_d\right) \sin\left(q_0 q + d\right)}, \qquad q \gtrsim 1$$

where $\ell \geq 1$ is an integer and a_i, q_i, and d are constants. Together, these findings indicate that the PFC approximations in this case (with weakly nonlinear Model B or DDFT evolution) do not significantly modify the supercooled liquid dynamics from the RY-DFT model. This suggests that monatomic glass formation requires qualitatively different free energy functionals from the standard RY-DFT and PFC forms, and/or that qualitatively different equations of motion are needed.

Three-body correlations

Three-body correlations are known to have important consequences in some glass forming materials, especially those with highly directional bonding. The RY-DFT free energy with three-body interactions is given by

$$\begin{aligned} \frac{F}{k_B T} \;&=\; \int d\vec{r}\, [\rho(\vec{r}) \ln\left(\rho(\vec{r})/\rho_\ell\right) - \delta\rho(\vec{r})] - \\ \tfrac{1}{2} &\int d\vec{r}_1 d\vec{r}_2 \delta\rho(\vec{r}_1) C_2(\vec{r}_1, \vec{r}_2) \delta\rho(\vec{r}_2) - \\ \tfrac{1}{6} &\int d\vec{r}_1 d\vec{r}_2 d\vec{r}_3 \delta\rho(\vec{r}_1) C_3(\vec{r}_1, \vec{r}_2, \vec{r}_3) \delta\rho(\vec{r}_2) \delta\rho(\vec{r}_3). \end{aligned}$$

To extend three-body effects to the PFC model in a numerically efficient scheme, an *effective* three-body term has been added to the free energy which encourages or discourages certain bond angles around a ring (in 2D) or a sphere (in 3D) of radius $R \simeq a_t$ centered at each grid point (a_t is the equilibrium lattice constant of the two-dimensional triangular lattice). This approach is more efficient than considering interactions over the entire system at each grid point. The discretized free energy in two dimensions then takes the form

$$F'(i,j) = F(i,j) + n(i,j) \sum_{n=1}^{N} c_n \sum_{\langle R \rangle} n(R) n(R+\theta_n)$$

where (i,j) denotes coordinates on the discretized grid, $F(i,j)$ is the unmodified PFC free energy, N is the number of bond angles being either penalized or encouraged, θ_n are the values of the bond angles, and c_n is the constant specifying the strength of the penalty or encouragement for θ_n. $\langle R \rangle$ implies summation around a ring of radius R, $n(R)$ is the number density at the current location on the ring, and $n(R+\theta_n)$ is the number density at the point on the ring θ_n degrees away from the current location. This functional form for three-body interactions was first introduced in Ref. [238].

To generate a disordered structure, bond angles of $\theta_1 = 60^\circ$ are penalized energetically ($c_1{<}0$) to discourage the equilibrium triangular lattice, and bonds of some irregular angle such as $\theta_2 = 41^\circ$ are made energetically favorable ($c_2{>}0$). When the c_n are tuned properly, a relatively disordered solid is produced upon quenching of the liquid, as shown in Fig. B.2(a). Nonetheless, the observed freezing transition remains discontinuous and the large computational demands make such simulations generally impractical.

B.1.2 Equation of motion

Nonlinear diffusion equations

Standard PFC functionals evolved with the overdamped equation of DDFT appear to produce supercooled liquid relaxations similar to those found with Model B dynamics. The region of liquid metastability is increased in some cases, but the transtion remains discontinuous and the relaxation processes continue to be described by highly stretched single exponentials.

Several related classes of equations with highly nonlinear density- and space-dependent mobilities, including

$$\frac{\partial n}{\partial t} = \nabla \cdot \big((n+1)^{\ell} \nabla \mu \big) + \nu, \tag{B.1}$$

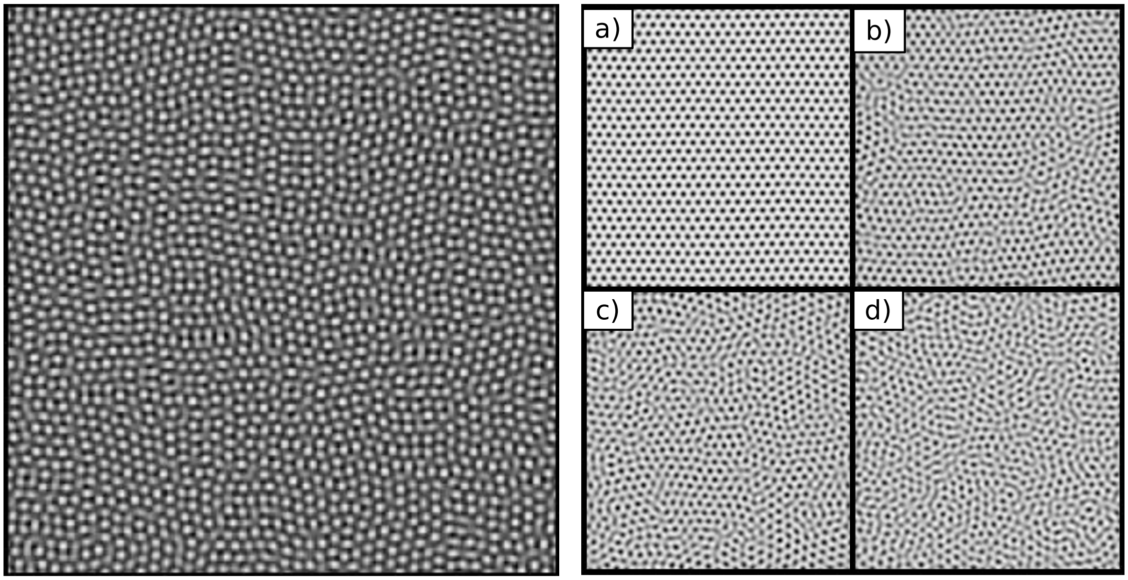

(a) (b)

Figure B.2: (a) Density configuration $n(\vec{r})$ after quenching a liquid with three-body interactions. $\theta_1 = 60°$, $\theta_2 = 41°$, $c_1 = -0.0185$, and $c_2 = 0.0185$. (b) Pinning transition: density configurations $n(\vec{r})$ at various pinning strengths. $V_0 = 0.005, 0.015, 0.02$, and 0.035 in a), b), c), and d) respectively.

$$\frac{\partial n}{\partial t} = \nabla \cdot \Big((n+1)(1 - \exp\left[-(n/\bar{n})^{\ell}\right])\nabla\mu\Big) + \nu, \tag{B.2}$$

and

$$\frac{\partial n}{\partial t} = \nabla \cdot \Big((n+1)\exp\left[-(n/\bar{n})^{\ell}\right]\nabla\mu\Big) + \nu, \tag{B.3}$$

where ℓ is an integer greater than or equal to 1, have also been simulated and found not to produce behavior indicative of a glass transition.

Inertial dynamics

Standard monatomic PFC liquids evolved using the inertial equation of motion, Eq. (2.31), do seem to exhibit a nearly continuous transition from liquid to glass, with signs of plateauing correlators, but suffer from rapid crystallization as in the non-inertial case. Heavily oscillating relaxation functions also tend to appear under the conditions required for continuous glass formation. Thus, the introduction of two well-separated time scales into the equation of motion appears to promote dynamics characteristic of glass forming liquids, but simple monatomic systems suffer from pathologies which limit their utility as models for glass formation.

B.1.3 Quenched disorder

Stochastic pinning potentials

Certain physical systems, such as weakly adsorbed quasi-two-dimensional monolayers on periodic or amorphous substrates [239, 240] or charge-density waves in solids [241, 242], can be modeled as thermodynamic systems driven by sources of quenched or externally imposed disorder. Though the structural glass transition is controlled by mechanisms distinct from quenched disorder, useful insights may come from comparison of the two scenarios.

PFC systems pinned to disordered external fields exhibit dynamical arrest into structurally disordered 'pinned' states as the magnitude of the coupling to the external field is increased. The free energy is modified by terms of the form

$$F = F_{PFC} + HP(\vec{r},t)n(\vec{r},t) \tag{B.4}$$

where H is a constant and $P(\vec{r},t)$ is the pinning field, which here is given at any point in space by a Gaussian random number, $\langle P(\vec{r}_1)P(\vec{r}_2)\rangle = \delta(\vec{r}_1 - \vec{r}_2)$. $P(\vec{r},t)$ may in principle be governed by its own dynamic behavior, but in the limit of zero t-dependence, arbitrarily slow relaxations can be generated by simply increasing the magnitude of H, and/or a transition from the periodic lattice to a disordered solid can be induced as shown in Fig. B.2(b).

Quenched cage models

Slow relaxations in glass forming liquids are driven by caging effects at the level of individual particles. These cages are formed by neighboring particles and are thus transient and self-organized, but quenched cage structures can be used to mimic this behavior in PFC liquids. Stretched and plateauing correlators can be shown to emerge when the liquid is partitioned into boxes separated by pinned walls at which $H > 0$, or when the mobility coefficient Γ is given a spatial dependence wherein each box is assigned a mobility chosen at random from a superposition of 'fast' and 'slow' distributions. It is somewhat interesting that such crude reconstructions of the caging mechanism generate the primary relaxation features of glass forming liquids, but this schematic type of approach is only useful as an illustrative exercise.

B.1.4 Overview

These results indicate that monatomic glass-like structures are generally accessible and often quite stable, but that a comprehensive monatomic glass former in terms of dynamic and thermodynaic behavior is not easily obtained without the use of unsatisfactory complications such as quenched disorder. Other modifications such as anisotropic unit structures or interactions may produce the desired behaviors, but the somewhat simpler route through binary systems is instead pursued in the following section.

B.2 Binary Liquids

Most systems with two or more atomic species are known to have greatly enhanced glass forming ability relative to monatomic systems. It is shown in this section that a minimal binary PFC model with Model B dynamics and purely repulsive interspecies interactions produces many of the central dynamic and thermodynamic behaviors of glass forming liquids. This result indicates that a simple coupling between two diffusively relaxing fields with slightly different equilibrium periodicities is a sufficent condition for the appearance of a glass transition. A different model binary glass former is also investigated and shown to lack a glass transition when the repulsive coupling is weak and stochastic noise is minimized.

B.2.1 Free energy functional

Minimal mutually repulsive binary model

Perhaps the simplest possible binary PFC model is a combination of standard monatomic models for A and B atoms, coupled by a single repulsive-type interaction term,

$$F_{\text{PFC}} = \int d\vec{r}\,[f_{AA} + f_{BB} + f_{AB}] \tag{B.5}$$

where

$$f_{ii} = \frac{n_i}{2}\left[r_i + (q_i^2 + \nabla^2)^2\right] n_i + \frac{1}{4} n_i^4$$

and

$$f_{AB} = \frac{r_{AB}}{2}(n_A + 1)^2(n_B + 1)^2.$$

The constant r_{AB} sets the strength of the mutual repulsion, which discourages peaks in either field from overlapping with those in the other field. When $q_A = q_B$, interpenetrating bcc lattices are quite easily nucleated upon quenching with Model B dynamics (Eq. (2.40)). When $q_B/q_A = 0.8$, the time required to nucleate the equilibrium crystalline structure becomes very large, and the system freezes rapidly but continuously into a disorder solid phase. This is the case for quenches in which only the noise amplitude is decreased (non-spinodal) and for quenches in which only r_i is decreased (spinodal), as shown in Fig. B.3.

The structure factors of the resulting disordered states are glass-like, and the relaxation times appear to diverge smoothly rather than with the sharp increase that indicates a nucleation-driven freezing transition. The relaxation functions do not clearly plateau, but become highly stretched or weakly shouldered. Thus, other than plateauing correlation functions, this simple coupling of geometrical frustration (due to inefficient crystalline packing) with simple dissipative evolution generates a significant range of glass forming behaviors.

The importance of the hard-sphere-type repulsive interaction in terms of glass formation becomes apparent when either r_{AB} is small or other expressions for f_{AB}, such as the RY-DFT form of Eq. (2.23), are used. The binary PFC liquid of Chapter 7, for example, appears to freeze very much as the monatomic PFC liquid studied in Chapter 5. The binary RY-DFT model and its direct PFC approximation (Eq. 2.24) have been simulated as well using Model B dynamics, with parameters chosen to match those of a known MD model glass former. The model is a binary Lennard-Jones system with $\sigma_{AA} = 1$, $\sigma_{BB} = 0.88$, $\sigma_{AB} = 0.8$, $\epsilon_{AA} = 1$, $\epsilon_{BB} = 0.5$, $\epsilon_{AB} = 1.5$, and a concentration of $N_A/(N_A + N_B) = 0.8$ [243]. This parameter set suppresses crystallization in MD simulations, allowing uninteruppted access to the glass-like moderately supercooled liquid.

The $C_2^{ij}(q)$ terms were taken directly from MD simulation data, with first peak fits used to construct the PFC interaction terms. No qualitative differences were observed between the RY-DFT and PFC results, with both systems exhibiting first order freezing transitions to disordered solid states. The weakly nonlinear binary models

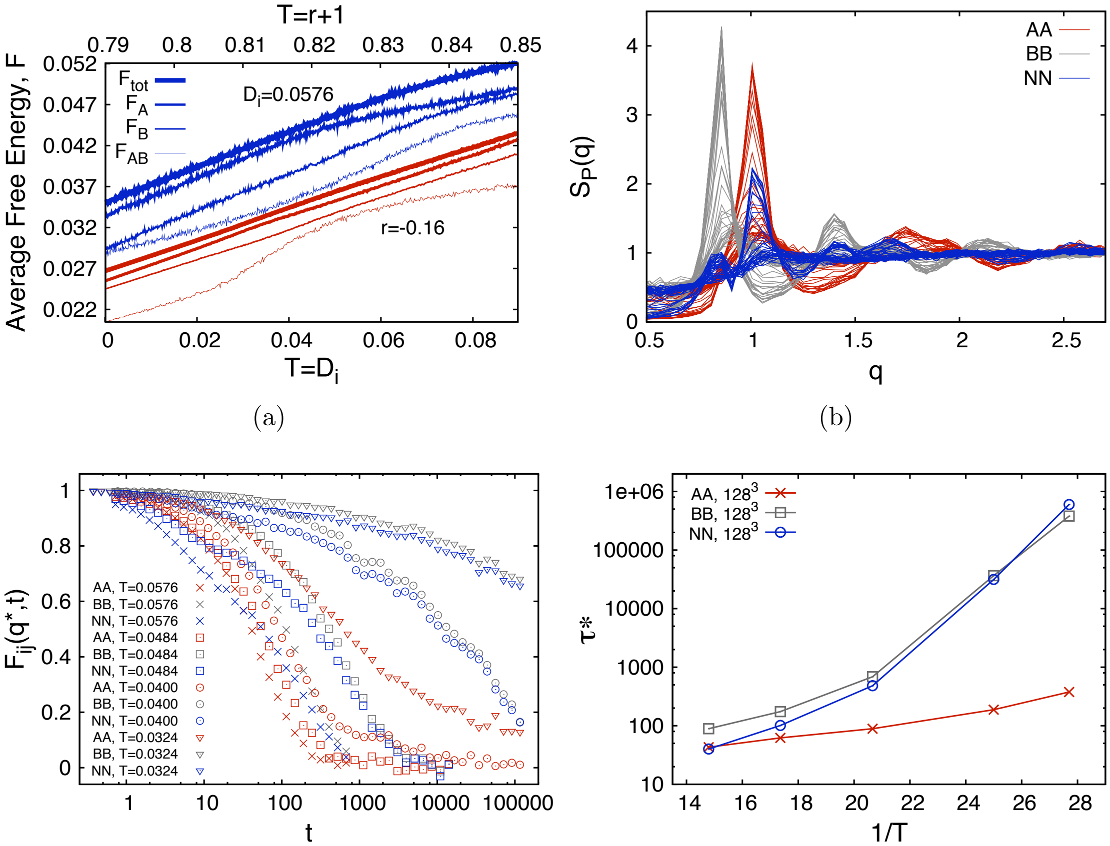

(a) (b)

(c) (d)

Figure B.3: Transition behavior of the minimal mutually repulsive binary PFC glass former. (a) Free energy vs. temperature during glass formation, (b) Emergence of glassy structure factors, (c) Glassy relaxations, (d) Arrhenius plot of relaxation times. $r_{AB} = 0.2$, $q_A = 1$, $q_B = 0.8$, and $r_i = -0.16$ (unless specified otherwise).

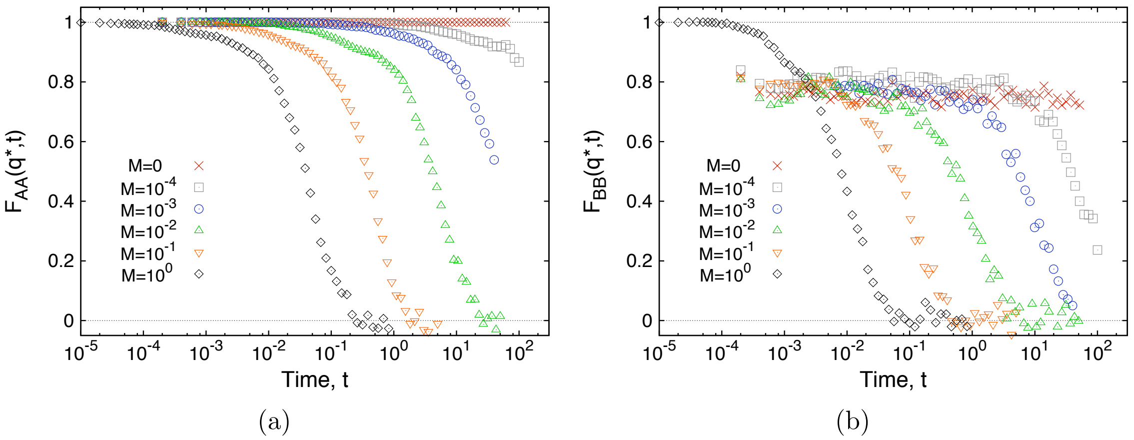

Figure B.4: Two-body relaxations in the binary LJ RY-DFT supercooled liquid. Intermediate (a) AA and (b) BB scattering functions for various mobility ratios.

therefore appear to lack complex glass forming dynamics, much like the standard monatomic models.

B.2.2 Equations of motion

Anomalous mobility ratios

Glassy dynamics can be produced within the binary LJ model described above by imposing a large difference in species mobilities $M = \Gamma_A/\Gamma_B \ll 1$. The BB relaxations begin to exhibit plateaus as M becomes small, as shown in Fig. B.4. The nominally mobile B field is effectively caged by the slow A field, which as $M \to 0$ amounts to a source of quenched disorder and is therefore not justifiable as a model for structural glass formation.

Inertial dynamics

The results for monatomic systems evolved with inertial dynamics indicate that certain glass forming behaviors are promoted in the underdamped regime. Unfortunately, crystallization and oscillating correlators prevented a clean study of the glass transition region for the monatomic liquid. It thus seems likely that the repulsive binary model described earlier in this section would offer more suitable framework for testing the effects of inertial dynamics on glass formation. Simulations of this model will be the subject of a future study.

B.2.3 Overview

Two primary ingredients for glass formation are suggested by the models studied in this appendix: underdamped inertial dynamics and strong local nonlinear free energy components, such as a binary hard-sphere-type repulsion term. A model which combines these two components, along with an additional highly nonlinear barrier term, is studied in Chapter 6. A wide range of glass forming behaviors are shown to naturally emerge from such a description, with little need for parameter tuning.

Bibliography

[1] Angell, C. A. *Science* **267**, 1924 (1995).

[2] Alsayed, A. M., Islam, M. F., Zhang, J., Collings, P. J., and Yodh, A. G. *Science* **309**, 1207 (2005).

[3] Elder, K. R., Katakowski, M., Haataja, M., and Grant, M. *Phys. Rev. Lett.* **88**, 245701 (2002).

[4] Elder, K. R. and Grant, M. *Phys. Rev. E* **70**, 051605 (2004).

[5] Provatas, N. and Elder, K. *Phase-Field Methods in Materials Science and Engineering.* WILEY-VCH Verlag GmbH & Co. KGaA, Weinheim, Germany, (2011).

[6] Evans, R. *Advances in Physics* **28**(2), 143–200 (1979).

[7] Ramakrishnan, T. V. and Yussouff, M. *Phys. Rev. B* **19**, 2775 (1979).

[8] Singh, Y. *Phys. Rep.* **207**, 351 (1991).

[9] Löwen, H. *Physics Reports* **237**(5), 249 – 324 (1994).

[10] Oxtoby, D. *Annu. Rev. Mater. Res.* **32**, 39 (2002).

[11] Kahl, G. and Löwen, H. *J. Phys.: Condens. Matter* **21**(46), 464101 (2009).

[12] Barrat, J.-L. and Hansen, J.-P. *Basic Concepts for Simple and Complex Fluids.* Cambridge University Press, (2003).

[13] Voter, A. F., Montalenti, F., and Germann, T. C. *Annu. Rev. Mater. Res.* **32**, 321 (2002).

[14] Marconi, U. M. B., Tarazona, P., Cecconi, F., and Melchionna, S. *J. Phys.: Condens. Matter* **20**(49), 494233 (2008).

[15] Espanol, P. and Löwen, H. *J. Chem. Phys.* **131**(24) (2009).

[16] Kawasaki, K. *Physica A* **208**, 35 (1994).

[17] Marconi, U. M. B. and Tarazona, P. *J. Chem. Phys.* **110**(16), 8032 (1999).

[18] Boon, J. P. and Yip, S. *Molecular Hydrodynamics.* McGraw-Hill Inc., (1980).

[19] Pusztai, T., Tegze, G., Tóth, G. I., Környei, L., Bansel, G., Fan, Z., and Gránásy, L. *J. Phys.: Condens. Matter* **20**(40), 404205 (2008).

[20] Emmerich, H. *Advances in Physics* **57**(1), 1–87 (2008).

[21] Karma, A. In *Encyclopedia of Materials: Science and Technology*, 6873 – 6886. Elsevier, Oxford (2001).

[22] W.J. Boettinger, J.A. Warren, C. B. and Karma, A. *Annu. Rev. Mater. Res.* **32**, 163–194 (2002).

[23] Chen, L.-Q. *Annu. Rev. Mater. Res.* **32**, 113–140 (2002).

[24] Rappaz, M., Jacot, A., and Boettinger, W. J. *Metall. and Mater. Trans. A* **33A**, 1 (2002).

[25] Elder, K. R., Provatas, N., Berry, J., Stefanovic, P., and Grant, M. *Phys. Rev. B* **75**, 064107 (2007).

[26] Amodeo, R. J. and Ghoniem, N. M. *Phys. Rev. B* **41**(10), 6958 (1990).

[27] Bulatov, V. V., Abraham, F. F., Kubin, L., Devincre, B., and Yip, S. *Nature* **391**, 669 (1998).

[28] Götze, W. *Complex Dynamics of Glass-Forming Liquids: A Mode-Coupling Theory.* Oxford University Press, Oxford, UK, (2009).

[29] Das, S. P. *Rev. Mod. Phys.* **76**, 785 (2004).

[30] Reichman, D. R. and Charbonneau, P. *J. Stat. Mech.* , P05013 (2005).

[31] Berry, J., Elder, K. R., and Grant, M. *Phys. Rev. B* **77**, 224114 (2008).

[32] Berry, J., Grant, M., and Elder, K. R. *Phys. Rev. E* **73**, 031609 (2006).

[33] Berry, J., Elder, K. R., and Grant, M. *Phys. Rev. E* **77**, 061506 (2008).

[34] Berry, J. and Grant, M. *Phys. Rev. Lett.* **106**, 175702 (2011).

[35] Goldenfeld, N., Athreya, B. P., and Dantzig, J. A. *Phys. Rev. E* **72**(2), 020601 Aug (2005).

[36] Athreya, B. P., Goldenfeld, N., and Dantzig, J. A. *Phys. Rev. E* **74**(1), 011601 Jul (2006).

[37] Wu, K.-A. and Karma, A. *Phys. Rev. B* **76**(18), 184107 Nov (2007).

[38] Athreya, B. P., Goldenfeld, N., Dantzig, J. A., Greenwood, M., and Provatas, N. *Phys. Rev. E* **76**, 056706 (2007).

[39] Yeon, D., Huang, Z., Elder, K. R., and Thornton, K. *Philos. Mag.* **90**(1), 237–263 (2010).

[40] Huang, Z.-F. and Elder, K. R. *Phys. Rev. B* **81**(16), 165421 Apr (2010).

[41] Huang, Z.-F., Elder, K. R., and Provatas, N. *Phys. Rev. E* **82**(2), 021605 Aug (2010).

[42] Spatschek, R. and Karma, A. *Phys. Rev. B* **81**(21), 214201 Jun (2010).

[43] Cheng, M. and Warren, J. A. *J. Comp. Phys.* **227**, 6241–6248 (2008).

[44] Wise, S. M., Wang, C., and Lowengrub, J. S. *SIAM J. Numer. Anal.* **47**, 2269–2288 June (2009).

[45] Hu, Z., Wise, S., Wang, C., and Lowengrub, J. *J. Comp. Phys.* **228**(15), 5323 – 5339 (2009).

[46] Tegze, G., Bansel, G., Tóth, G. I., Pusztai, T., Fan, Z., and Gránásy, L. *J. Comp. Phys.* **228**(5), 1612 – 1623 (2009).

[47] Stefanovic, P., Haataja, M., and Provatas, N. *Phys. Rev. E* **80**, 046107 (2009).

[48] Wang, C. and Wise, S. M. *Meth. and App. of Analysis* **17**(2), 191–212 (2010).

[49] Wang, C. and Wise, S. M. *unpublished* (2011).

[50] Majaniemi, S., Provatas, N., and Nonomura, M. *J. Phys.: Condens. Matter* **22**(36), 364111 (2010).

[51] Brazovskii, S. A. *Sov. Phys.-JETP* **41**(1), 85 (1975).

[52] Swift, J. and Hohenberg, P. C. *Phys. Rev. A* **15**(1), 319 (1977).

[53] Tóth, G. I., Tegze, G., Pusztai, T., Tóth, G., and Gránásy, L. *J. Phys.: Condens. Matter* **22**, 364101 (2010).

[54] Tegze, G., Gránásy, L., Tóth, G. I., Podmaniczky, F., Jaatinen, A., Ala-Nissila, T., and Pusztai, T. *Phys. Rev. Lett.* **103**, 035702 (2009).

[55] Gránásy, L., Tegze, G., Tóth, G. I., and Pusztai, T. *arXiv* (2010).

[56] Backofen, R. and Voigt, A. *J. Phys.: Condens. Matter* **21**, 464109 (2009).

[57] Backofen, R. and Voigt, A. *J. Phys.: Condens. Matter* **22**, 364104 (2010).

[58] Jaatinen, A. and Ala-Nissila, T. *Phys. Rev. E* **82**, 061602 (2010).

[59] Hubert, J., Cheng, M., and Emmerich, H. *J. Phys.: Condens. Matter* **21**, 464108 (2009).

[60] van Teeffelen, S., Backofen, R., Voigt, A., and Löwen, H. *Phys. Rev. E* **79**, 051404 (2009).

[61] Prieler, R., Hubert, J., Li, D., Verleye, B., Haberkern, R., and Emmerich, H. *J. Phys.: Condens. Matter* **21**, 464110 (2009).

[62] Greenwood, M., Provatas, N., and Rottler, J. *Phys. Rev. Lett.* **105**, 045702 (2010).

[63] Greenwood, M., Provatas, N., and Rottler, J. *Phys. Rev. E* **83**, 031601 (2011).

[64] Provatas, N. and Majaniemi, S. *Phys. Rev. E* **82**, 041601 (2010).

[65] Huang, Z.-F. and Elder, K. R. *Phys. Rev. Lett.* **101**, 158701 (2008).

[66] Elder, K. R. and Huang, Z.-F. *J. Phys.: Condens. Matter* **22**(36), 364103 (2010).

[67] Muralidharan, S. and Haataja, M. *Phys. Rev. Lett.* **105**, 126101 (2010).

[68] Elder, K. R., Thornton, K., and Hoyt, J. J. *Philos. Mag.* **91**(1), 151–164 (2011).

[69] Jaatinen, A., Achim, C. V., Elder, K. R., and Ala-Nissila, T. *Phys. Rev. E* **80**, 031602 (2009).

[70] Backofen, R., Voigt, A., and Witkowski, T. *Phys. Rev. E* **81**, 025701(R) (2010).

[71] Jaatinen, A., Achim, C. V., Elder, K. R., and Ala-Nissila, T. *Technische Mechanik* **30**, 169–176 (2010).

[72] Mellenthin, J., Karma, A., and Plapp, M. *Phys. Rev. B* **78**, 184110 (2008).

[73] Olmsted, D. L., Buta, D., Adland, A., Foiles, S. M., Asta, M., and Karma, A. *Phys. Rev. Lett.* **106**, 046101 (2011).

[74] Stefanovic, P., Haataja, M., and Provatas, N. *Phys. Rev. Lett.* **96**, 225504 (2006).

[75] Hirouchi, T., Takaki, T., and Tomita, Y. *Comp. Mat. Sci.* **44**(4), 1192 – 1197 (2009).

[76] Chan, P. Y., Tsekenis, G., Dantzig, J., Dahmen, K. A., and Goldenfeld, N. *Phys. Rev. Lett.* **105**, 015502 (2010).

[77] Wu, K.-A. and Voorhees, P. W. *Phys. Rev. B* **80**, 125408 (2009).

[78] Chan, P. Y. and Goldenfeld, N. *Phys. Rev. E* **80**, 065105(R) (2009).

[79] Achim, C. V., Karttunen, M., Elder, K. R., Granato, E., Ala-Nissila, T., and Ying, S. C. *Phys. Rev. E* **74**, 021104 (2006).

[80] Ramos, J. A. P., Granato, E., Achim, C. V., Ying, S. C., Elder, K. R., and Ala-Nissila, T. *Phys. Rev. E* **78**, 031109 (2008).

[81] Achim, C. V., Ramos, J. A. P., Karttunen, M., Elder, K. R., Granato, E., Ala-Nissila, T., and Ying, S. C. *Phys. Rev. E* **79**, 011606 (2009).

[82] Ramos, J. A. P., Granato, E., Ying, S. C., Achim, C. V., Elder, K. R., and Ala-Nissila, T. *Phys. Rev. E* **81**, 011121 (2010).

[83] Xu, Y.-C. and Liu, B.-G. *J. Phys. D: Appl. Phys.* **42**, 035402 (2009).

[84] Mkhonta, S. K., Vernon, D., Elder, K. R., and Grant, M. *arXiv:0806.3445v2 [cond-mat.soft]* (2008).

[85] Mkhonta, S. K., Elder, K. R., and Grant, M. *Eur. Phys. J. E* **032**, 349–355 (2010).

[86] Löwen, H. *J. Phys.: Condens. Matter* **22**, 364105 (2010).

[87] Wittkowski, R., Löwen, H., and Brand, H. R. *Phys. Rev. E* **82**, 031708 (2010).

[88] Guttenberg, N., Goldenfeld, N., and Dantzig, J. *Phys. Rev. E* **81**, 065301(R) (2010).

[89] Provatas, N., Dantzig, J. A., Athreya, B., Chan, P., Stefanovic, P., Goldenfeld, N., and Elder, K. R. *JOM* **59**(7), 83 (2007).

[90] Haataja, M., Gránásy, L., and Löwen, H. *J. Phys.: Condens. Matter* **22**(36), 360301 (2010).

[91] Emmerich, H. *Curr. Op. in Sol. State and Mat. Sci.* **15**(3), 83 – 86 (2011). Applications of Phase Field Modeling in Materials Science and Engineering.

[92] Roth, R. *J. Phys.: Condens. Matter* **22**(6), 063102 (2010).

[93] Kalikmanov, V. I. *Statistical Physics of Fluids: Basic Concepts and Applications.* Springer Verlag, (2001).

[94] Jaatinen, A. and Ala-Nissila, T. *J. Phys.: Condens. Matter* **22**, 205402 (2010).

[95] Chan, P. Y., Goldenfeld, N., and Dantzig, J. *Phys. Rev. E* **79**, 035701(R) (2009).

[96] Chaikin, P. M. and Lubensky, T. C. *Principles of Condensed Matter Physics*. Cambridge University Press, Cambridge, UK, (1995).

[97] Archer, A. J. and Rauscher, M. *J. Phys. A: Math. Gen.* **37**, 9325 (2004).

[98] Kawasaki, K. *Physica A* **362**, 249 (2006).

[99] Majaniemi, S. and Grant, M. *Phys. Rev. B* **75**, 054301 (2007).

[100] Majaniemi, S., Nonomura, M., and Grant, M. *Euro. Phys. Jour. B - Condens. Matter and Complex Sys.* **66**, 329–335 (2008).

[101] Dasgupta, C. *Europhys. Lett.* **20**(2), 131–136 (1992).

[102] Munakata, T. *Phys. Rev. E* **50**, 2347 (1994).

[103] Dean, D. *J. Phys. A: Math. Gen.* **29**, L613 (1996).

[104] Pérez-Madrid, A., Reguera, D., and Rubí, J. *J. Phys.: Condens. Matter* **14**, 1651 (2002).

[105] Marconi, U. M. B. and Tarazona, P. *J. Phys.: Condens. Matter* **12**, A413 (2000).

[106] Archer, A. J. and Evans, R. *J. Chem. Phys.* **121**, 4246 (2004).

[107] Galenko, P., Danilov, D., and Lebedev, V. *Phys. Rev. E* **79**(5), 051110 May (2009).

[108] Ramos, J. A. P., Granato, E., Ying, S. C., Achim, C. V., Elder, K. R., and Ala-Nissila, T. *Phys. Rev. E* **81**, 011121 (2010).

[109] Archer, A. J. *J. Phys.: Condens. Matter* **18**, 5617 (2006).

[110] Archer, A. J. *J. Chem. Phys.* **130**, 014509 (2009).

[111] Marconi, U. M. B. and Tarazona, P. *J. Chem. Phys.* **124**, 164901 (2006).

[112] Marconi, U. M. B. and Melchionna, S. *J. Chem. Phys.* **126**, 184109 (2007).

[113] Galenko, P. *Phys. Lett. A* **287**, 190 (2001).

[114] Koide, T., Krein, G., and Ramos, R. O. *Phys. Lett. B* **636**, 96 (2006).

[115] Oxtoby, D. W. *Nature* **347**, 725 (1990).

[116] Löwen, H. *Phys. Rep.* **237**, 249 (1994).

[117] Hsieh, T. and Balluffi, R. *Acta Metall.* **37**, 1637 (1989).

[118] Budke, E., Surholt, T., Prokofjev, S. I., Shvindlerman, L. S., and Herzig, C. *Acta Mater.* **47**, 385 (1999).

[119] Divinski, S., Lohmann, M., Herzig, C., Straumal, B., Baretzky, B., and Gust, W. *Phys. Rev. B* **71**, 104104 (2005).

[120] Demianczuk, D. W. and Aust, K. T. *Acta Metall.* **23**, 1149 (1975).

[121] Watanabe, T., Kimura, S.-I., and Karashima, S. *Philos. Mag. A* **49**, 845 (1984).

[122] Nguyen, T., Ho, P. S., Kwok, T., Nitta, C., and Yip, S. *Phys. Rev. B* **46**, 6050 (1992).

[123] Broughton, J. Q. and Gilmer, G. H. *Phys. Rev. Lett.* **56**, 2692 (1986).

[124] Kikuchi, R. and Cahn, J. W. *Phys. Rev. B* **21**, 1893 (1980).

[125] Tang, M., Carter, W. C., and Cannon, R. M. *Phys. Rev. B* **73**, 024102 (2006).

[126] Lobkovsky, A. E. and Warren, J. A. *Physica D* **164**, 202 (2002).

[127] Ohnesorge, R., Löwen, H., and Wagner, H. *Phys. Rev. E* **50**, 4801 (1994).

[128] Glicksman, M. E. and Vold, C. L. *Surf. Sci.* **31**, 50 (1972).

[129] Read, W. T. and Shockley, W. *Phys. Rev.* **78**, 275 (1950).

[130] Chang, J., Bulatov, V. V., and Yip, S. *J. Computer-Aided Materials Design* **6**, 165 (1999).

[131] Chang, J., Cai, W., Bulatov, V. V., and Yip, S. *Comp. Mat. Sci.* **23**, 111–115 (2002).

[132] Bailey, N. P., Sethna, J. P., and Myers, C. R. *Mat. Sci. & Eng. A* **309-310**, 152–155 (2001).

[133] Rodary, E., Rodney, D., Proville, L., Bréchet, Y., and Martin, G. *Phys. Rev. B* **70**, 054111 (2004).

[134] Pardo, F., de la Cruz, F., Gammel, P. L., Bucher, E., and Bishop, D. J. *Nature (London)* **396**, 348 (1998).

[135] Sagui, C. and Desai, R. C. *Phys. Rev. E* **52**, 2807 (1995).

[136] Orlikowski, D., Sagui, C., Somoza, A., and Roland, C. *Phys. Rev. B* **59**, 8646 (1999).

[137] Harrison, C., Adamson, H., Cheng, Z., Sebastian, J. M., Sethuraman, S., Huse, D. A., Register, R. A., and Chaikin, P. M. *Science* **290**, 1558 (2000).

[138] Laradji, M., Guo, H., Grant, M., and Zuckermann, M. J. *Phys. Rev. A* **44**, 8184 (1991).

[139] Oono, Y. and Puri, S. *Phys. Rev. A* **38**, 434–453 (1988).

[140] Lubensky, T. C., Ramaswamy, S., and Toner, J. *Phys. Rev. B* **32**, 7444–7452 (1985).

[141] Phillips, R. *Crystals, Defects and Microstructures: Modeling Across Scales.* Cambridge, (2001).

[142] Wasserbäch, W. *Phil. Mag.* **A53**, 335 (1986).

[143] Lachenmann, R. and Schultz, H. *Scripta Metall.* **4**, 33 (1970).

[144] Cuitino, A. M., Stainier, L., Wang, G., Strachan, A., Cagin, T., III, W. G., and Ortiz, M. *Caltech Tech. Report.* **112** (2001).

[145] Tang, M., Devincre, B., and Kubin, L. P. *Mod. and Sim. in Mat. Sci. and Eng.* **7**, 893 (1999).

[146] Koslowski, M., Cuitino, A. M., and Ortiz, M. *J. Mech. Phys. of Solids* **50**, 2597 (2002).

[147] Wang, Y. U., Jin, Y. M., Cuitino, A. M., and Khachaturyan, A. G. *Appl. Phys. Lett.* **78**, 2324–2326 (2001).

[148] Wang, Y. U., Jin, Y. M., and Khachaturyan, A. G. *Phil. Mag.* **85**, 261–277 (2005).

[149] Kim, B. and Kawasaki, K. *J. Phys. A: Math. Theor.* **40**, F33 (2007).

[150] Andreanov, A., Biroli, G., and Lefèvre, A. *J. Stat. Mech.* , P07008 (2006).

[151] Fuchizaki, K. and Kawasaki, K. *J. Phys.: Condens. Matter* **14**, 12203 (2002).

[152] Munakata, T. *Phys. Rev. E* **67**, 022101 (2003).

[153] Singh, Y., Stoessel, J. P., and Wolynes, P. G. *Phys. Rev. Lett.* **54**(10), 1059 (1985).

[154] Dasgupta, C. and Ramaswamy, S. *Physica A* **186**, 314 (1992).

[155] Kaur, C. and Das, S. P. *Phys. Rev. Lett.* **86**(10), 2062 (2001).

[156] Kim, K. and Munakata, T. *Phys. Rev. E* **68**, 021502 (2003).

[157] Singh, S. P. and Das, S. P. *J. Phys.: Condens. Matter* **19**, 246107 (2007).

[158] Kirkpatrick, T. R. and Wolynes, P. G. *Phys. Rev. A* **35**, 3072 (1987).

[159] Dasgupta, C. and Valls, O. T. *Phys. Rev. E* **59**, 3123 (1999).

[160] Lust, L. M., Valls, O. T., and Dasgupta, C. *Phys. Rev. E* **48**(3), 1787 (1992).

[161] Klein, W., Gould, H., Ramos, R. A., Clejan, I., and Mel'cuk, A. I. *Physica A* **205**, 738 (1994).

[162] Jin, Y. M. and Khachaturyan, A. G. *J. Appl. Phys.* **100**, 013519 (2006).

[163] Johnson, G., Mel'cuk, A. I., Gould, H., Klein, W., and Mountain, R. D. *Phys. Rev. E* **57**, 5707 (1998).

[164] Klein, W., Gould, H., Tobochnik, J., Alexander, F. J., Anghel, M., and Johnson, G. *Phys. Rev. Lett.* **85**, 1270 (2000).

[165] Sheng, H., Luo, W., Alamgir, F., Bai, J., and Ma, E. *Nature* **439**, 419 (2006).

[166] Bennett, C. *J. Appl. Phys.* **43**(6), 2727 (1972).

[167] Finney, J. *Proc. Roy. Soc. (London)* **319A**, 479 (1970).

[168] Götze, W. In *Liquids, Freezing and Glass Transition,* Hansen, J., Levesque, D., and Zinn-Justin, J., editors. North-Holland, Amsterdam, (1991).

[169] Turnbull, D. and Cohen, M. H. *J. Chem. Phys.* **34**(1), 120 (1961).

[170] Adam, G. and Gibbs, J. H. *J. Chem. Phys.* **43**, 139 (1958).

[171] Glotzer, S. C. *J. of Non-Cryst. Solids* **274**, 342 (2000).

[172] Binder, K., Baschnagel, J., Kob, W., and Paul, W. In *Bridging Time Scales: Molecular Simulations For the Next Decade,* Nielaba, P., Mareschal, M., and Ciccotti, G., editors. Springer-Verlag Berlin Heidelberg, (2002).

[173] Binder, K., Horbach, J., Knoth, H., and Pfleiderer, P. *J. Phys.: Condens. Matter* **19**, 205102 (2007).

[174] Kirkpatrick, T. R. and Thirumalai, D. *J. Phys. A: Math. Gen.* **22**, L149 (1989).

[175] Chan, P. Y. *Scaling and Pattern Formation in Condensed Matter Systems.* PhD thesis, Univeristy of Illinois at Urbana-Champaign, (2007).

[176] Geissler, P. L. and Reichman, D. R. *Phys. Rev. E* **69**(2), 021501 Feb (2004).

[177] Conrad, J. C., Dhillon, P. P., Weeks, E. R., Reichman, D. R., and Weitz, D. A. *Phys. Rev. Lett.* **97**, 265701 (2006).

[178] Baeurle, S. A., Hotta, A., and Gusev, A. A. *Polymer* **47**, 6243 (2006).

[179] Lubchenko, V. and Wolynes, P. G. *Annu. Rev. Phys. Chem.* **58**, 235 (2007).

[180] Kirkpatrick, T. R., Thirumalai, D., and Wolynes, P. G. *Phys. Rev. A* **40**(2), 1045 (1989).

[181] Biroli, G. and Bouchaud, J. P. *J. Phys.: Condens. Matter* **19**, 205101 (2007).

[182] Tanaka, H., Kawasaki, T., Shintani, H., and Watanabe, K. *Nature Mater.* **9**, 328 (2010).

[183] Kim, K. and Yamamoto, R. *Phys. Rev. E* **61**(1), R41 (2000).

[184] Weeks, E. R., Crocker, J. C., Levitt, A. C., Schofield, A., and Weitz, D. A. *Science* **287**, 627 (2000).

[185] Nugent, C. R., Edmond, K. V., Patel, H. N., and Weeks, E. R. *Phys. Rev. Lett.* **99**, 025702 (2007).

[186] Angell, C. A., Ngai, K. L., McKenna, G. B., McMillan, P. F., and Martin, S. W. *J. Appl. Phys.* **88**(6), 3113 (2000).

[187] Mattsson, J., Wyss, H. M., Fernandez-Nieves, A., Miyazaki, K., Hu, Z., Reichman, D. R., and Weitz, D. A. *Nature* **462**, 83 (2009).

[188] Novikov, V. N., Ding, Y., and Sokolov, A. P. *Phys. Rev. E* **71**, 061501 (2005).

[189] Kob, W. and Barrat, J. *arXiv:9905248v1 [cond-mat.dis-nn]* (1999).

[190] Brambilla, G., El Masri, D., Pierno, M., Berthier, L., Cipelletti, L., Petekidis, G., and Schofield, A. B. *Phys. Rev. Lett.* **102**(8), 085703 Feb (2009).

[191] Asaro, R. J. and Tiller, W. A. *Metall. Trans.* **3**, 1789 (1972).

[192] Grinfeld, M. *J. Nonlin. Sci.* **3**, 35 (1993).

[193] Srolovitz, D. J. *Acta metall.* **37**(2), 621–625 (1989).

[194] Matthews, J. W. and Blakeslee, A. E. *J. Cryst. Growth* **27**, 118 (1974).

[195] Matthews, J. W. *J. Vac. Sci. Technol.* **12**, 126 (1975).

[196] People, R. and Bean, J. C. *Appl. Phys. Lett.* **47**, 322 (1985).

[197] Haataja, M., Muller, J., Rutenberg, A. D., and Grant, M. *Phys. Rev. B* **65**, 165414 (2002).

[198] Muller, J. and Grant, M. *Phys. Rev. Lett.* **82**, 1736 (1999).

[199] Cantat, I., Kassner, K., Misbah, C., and Muller-Krumbhaar, H. *Phys. Rev. E* **58**, 6027 (1998).

[200] Kassner, K., Misbah, C., Muller, J., Kappey, J., and Kohlert, P. *Phys. Rev. E* **63**, 036117 (2001).

[201] Yang, W. and Srolovitz, D. *Phys. Rev. Lett.* **71**, 1593 (1993).

[202] Fischer, A., Kuhne, H., Eichler, M., Hollander, F., and Richter, H. *Phys. Rev. B* **54**, 8761 (1996).

[203] Zou, J. and Cockayne, D. J. H. *J. Appl. Phys.* **79**, 7632 (1996).

[204] Freund, L. B. and Nix, W. D. *Appl. Phys. Lett.* **69**, 173 (1996).

[205] Gao, H. and Nix, W. D. *Annu. Rev. Mater. Sci.* **29**, 173 (1999).

[206] Hull, R., Gray, J., Wu, C. C., Atha, S., and Floro, J. A. *J. Phys.: Condens. Matter* **14**, 12829 (2002).

[207] Gray, J., Hull, R., and Floro, J. A. *Mat. Res. Soc. Symp. Proc.* **696**, N8.3.1 (2002).

[208] Dong, L., Schnitker, J., Smith, R. W., and Srolovitz, D. J. *J. Appl. Phys.* **83**, 217 (1998).

[209] Schulze, T. P., Smereka, P., and Weinan, E. *unpublished* (2002).

[210] Mou, C. and Hsu, J. W. P. *Phys. Rev. E* **56**, 1522 (1997).

[211] Tersoff, J. and LeGoues, F. K. *Phys. Rev. Lett.* **72**, 3570 (1994).

[212] Spencer, B. J., Voorhees, P. W., and Tersoff, J. *Phys. Rev. B* **64**, 235318 (2001).

[213] Spencer, B. J., Voorhees, P. W., and Tersoff, J. *Phys. Rev. Lett.* **84**, 2449 (2000).

[214] Guyer, J. E. and Voorhees, P. W. *Phys. Rev. B* **54**, 10710 (1996).

[215] Guyer, J. E. and Voorhees, P. W. *Phys. Rev. Lett.* **74**, 4031 (1995).

[216] Guyer, J. E. and Voorhees, P. W. *J. Cryst. Growth* **187**, 150 (1998).

[217] Huang, Z. and Desai, R. C. *Phys. Rev. B* **65**, 195421 (2002).

[218] Huang, Z. and Desai, R. C. *Phys. Rev. B* **65**, 205419 (2002).

[219] Leonard, F. and Desai, R. C. *Phys. Rev. B* **56**, 4995 (1997).

[220] Leonard, F. and Desai, R. C. *Phys. Rev. B* **57**, 4805 (1998).

[221] Venezuela, P. and Tersoff, J. *Phys. Rev. B* **58**, 10871 (1998).

[222] Glas, F. *Phys. Rev. B* **55**, 11277 (1997).

[223] Ipatova, I. P., Malyshkin, V. G., Maradudin, A. A., Shchukin, V., and Wallis, R. F. *Phys. Rev. B* **57**, 12968 (1998).

[224] Blanariu, M. and Spencer, B. J. *unpublished* (2003).

[225] Walther, T., Humphries, C. J., and Cullis, A. G. *Appl. Phys. Lett.* **71**, 809 (1997).

[226] Okada, T., Weatherly, G. C., and McComb, D. W. *J. Appl. Phys.* **81**, 2185 (1997).

[227] Peiro, F., Cornet, A., Morante, J. R., Georgakilas, A., Wood, C., and Christou, A. *Appl. Phys. Lett.* **66**, 2391 (1995).

[228] Millunchick, J. M., Twesten, R. D., Follstaedt, D. M., Lee, S. R., Jones, E. D., Zhang, Y., Ahrenkiel, S. P., and Mascarenhas, A. *Appl. Phys. Lett.* **70**, 1402 (1997).

[229] Perovic, D. D., Bahierathan, B., Lafontaine, H., Houghton, D. C., and McComb, D. W. *Physica A* **239**, 11 (1997).

[230] Liu, N., Tersoff, J., Baklenov, O., Jr., A. L. H., and Shih, C. K. *Phys. Rev. Lett.* **84**, 334 (2000).

[231] Tersoff, J. *Phys. Rev. Lett.* **81**, 3183 (1998).

[232] Ratto, F., Rosei, F., Locatelli, A., Cherifi, S., Fontana, S., Heun, S., Szkutnik, P. D., Sgarlata, A., Crescenzi, M. D., and Motta, N. *Appl. Phys. Lett.* **84**, 4526 (2004).

[233] Joyce, B. A. *Jpn. J. Appl. Phys.* **36**, 4111 (1997).

[234] Krishnamurthy, M., Lorke, A., Wassermeier, M., Williams, D. R. M., and Petroff, P. M. *J. Vac. Sci. Technol. B* **11**, 1384 (1993).

[235] Anan, T., Nishi, K., and Sugou, S. *Appl. Phys. Lett.* **60**, 3159 (1992).

[236] Spencer, B. J., Voorhees, P. W., and Davis, S. H. *Phys. Rev. Lett.* **67**(26), 3696 (1991).

[237] Groot, R. D., van der Eerden, J. P., and Faber, N. M. *J. Chem. Phys.* **87**(4), 2263 (1987).

[238] Tupper, P. and Grant, M. *Europhys. Lett.* (2007).

[239] Thomy, A., Duval, X., and Regnier, J. *Surf. Sci. Rep.* **1**, 1 (1980).

[240] Pandit, R., Schick, M., and Wortis, M. *Phys. Rev. B* **26**, 5112 (1982).

[241] Karttunen, M., Haataja, M., Elder, K., and Grant, M. *Phys. Rev. Lett.* **83**, 3518 (1999).

[242] Gruner, G. *Rev. Mod. Phys.* **60**, 1129 (1988).

[243] Kob, W. and Andersen, H. C. *Phys. Rev. Lett.* **73**(10), 1376 (1994).